DUAL-CURING THIOL-ACRYLATE-EPOXY THERMOSETS FOR FUNCTIONAL APPLICATIONS

Claudio Russo

UNIVERSITAT
ROVIRA i VIRGILI

Dual-curing thiol-acrylate-epoxy thermosets for functional applications

---

Claudio Russo

DOCTORAL THESIS

2021

DUAL-CURING THIOL-ACRYLATE-EPOXY
THERMOSETS FOR FUNCTIONAL APPLICATIONS
Claudio Russo

Claudio Russo

DUAL-CURING THIOL-ACRYLATE-EPOXY THERMOSETS FOR FUNCTIONAL APPLICATIONS

DOCTORAL THESIS
Tarragona, Spain (2021)

Supervised by:
Prof. Silvia De la Flor and Prof. Xavier Fernàndez-Francos

Department of Mechanical Engineering

UNIVERSITAT ROVIRA i VIRGILI

DUAL-CURING THIOL-ACRYLATE-EPOXY
THERMOSETS FOR FUNCTIONAL APPLICATIONS
Claudio Russo

Departament d'Enginyeria Mecànica
Campus Sescelades, Edifici E4
Avinguda dels Països Catalans, 26
43007 Tarragona, Spain

Professor Silvia De la Flor of the Department of Mechanical Engineering at the Universitat Rovira i Virgili and Professor Xavier Fernàndez-Francos of the Department of Heat Engines at ETSEIB, Universitat Politècnica de Catalunya.

Certify:

that the Doctoral Thesis, entitled "DUAL-CURING THIOL-ACRYLATE-EPOXY THERMOSETS FOR FUNCTIONAL APPLICATIONS" presented by Claudio Russo to obtain the title of Doctor, has been carried out under our direction and meets the requirements to qualify for the European Mention.

Tarragona, June 2021

Prof. Silvia De la Flor

Prof. Xavier Fernàndez-Francos

DUAL-CURING THIOL-ACRYLATE-EPOXY
THERMOSETS FOR FUNCTIONAL APPLICATIONS
Claudio Russo

Acknowledgement

"I thank whatever gods may be
For my unconquerable soul."
(Invictus, W. E. Henley)

After more than three years the time has thus come to thank all the people that have helped and supported me throughout this arduous race.

First and foremost, my sincere gratitude goes to my director Silvia De la Flor for having been a reference point during all these years. Thank you for your invaluable guidance and support that have allowed me to grow up both as a person and researcher. My sincere gratitude goes also to my co-director Xavier Fernandez-Francos for his huge contribution to the research project and to my professional growth. The knowledge and dedication of you both have been crucial in this path, and I will be forever grateful.

I would also like to thank the head of the Funcmat group, Angels Serra, for kindly welcoming me in the research group. Your everyday passion and commitment in keeping our group at the highest level have been for me an inspiration. I want to also thank Xavi Ramis, Osman Konuray and all the other group members based in Barcelona.

A special thanks goes to Veronica Ambrogi for her great support during my stay in Naples, and for her dedication in teaching me chemistry, ever since I was one of her three best chemistry students. I also want to thank Piero Cerruti for his great support and his precious advice during my stay in Naples.

I want to extend my sincere gratitude to all the people I have met during these long years in Tarragona. Many thanks to Marta and Toni for their welcome and support ever since I was an Erasmus student. Thank you to my Catalan friends and colleagues, Adrià, Isaac, and Xavi for all the time spent together in the lab and for the beers para desconectar. Thank to Dailyn and David, your help and advice have been really precious. Thanks to all the lab mates I had during these years, Ruben, Alberto, Federico, Alireza, Aina, Jordi, and to the ones I forgot to mention.

I would also like to thank all the people I have met during my stay in Naples: Noemi, Angela and Libera, no matter what happens Aperitivo at 17h. Giovanni Filippone and Martina Salzano de Luna for kindly welcoming me in their research group.

Thank you to my Italian family in Tarragona, Gianmarco, Mario, Rita and Mimmo for the amazing time we spent together. A special mention to Francesco, you have been a great

friend, lab mate, family, and flat mate. It was a pleasure to share this journey with you and I wish you all the best.

Now is the turn of my family and my hometown supporters. My deep and sincere gratitude to my family, Zio Aldo, Zio Erminio, Zia Anna, Zia Elena, Gianlorenzo, Stefano and my family from Cilento for their continuous help and support. I am grateful to my sister for always being there for me. I am forever grateful to my parents for giving me the opportunities and experiences that have made me who I am. You have been my role models and inspiration; no words could ever express how grateful I am. A deep gratitude to my beloved grandparents, even though you are gone all my achievement are dedicated to you.

Thank you to my lifelong friends, my oldest friend Gianmarco, Roberto, Mario, Davide, Luigi, Gabriele; we grew up together and I hope we will get old together too. Thank you to Sara for the psychological support, Fiorella for her constant concern about my hair and Claudia.

Lastly, I would like to thank You. Besides you are no longer part of my life, a beautiful part of this achievement is still yours. You will always have a big piece of my heart.

Ringraziamenti

"I thank whatever gods may be
For my unconquerable soul."
(Invictus, W. E. Henley)

Sono passati più di tre anni ed arrivato il momento di ringraziare tutte le persone che mi hanno aiutato e supportato durante questa difficile corsa.

Prima di tutto, la mia sincera gratitudine va alla direttrice della tesi Silvia De la Flor per essere stata un punto di riferimento durante questi anni. Grazie per la tua preziosissima guida e il costante supporto, che mi hanno permesso di crescere sia come persone che come ricercatore. La mia sincera gratitudine va anche al co-direttore della tesi Xavier Fernandez-Francos per il suo enorme contributo al progetto di ricerca e alla mia crescita professionale. La competenza e dedizione di entrambi sono stati cruciali durante questo percorso, e ve ne sarò per sempre grato.

Mi preme anche ringraziare la responsabile del gruppo Funcmat, Angels Serra, per avermi amabilmente accolto nel gruppo di ricerca. La tua enorme passione e il tuo impegno nel mantenere il gruppo ai suoi massimi livelli sono stati per me una fonte d'ispirazione. Voglio anche ringraziare Xavi Ramis, Osman Konuray e gli altri membri del gruppo che sono a Barcellona.

Un ringraziamento speciale va a Veronica Ambrogi per il grandissimo supporto durante il mio periodo a Napoli, e per il suo impegno nell'insegnarmi la chimica, sin da quando ero uno dei suoi tre migliori studenti di chimica. Voglio anche ringraziare Piero Cerruti per il suon grandissimo supporto e i suoi preziosi consigli durante il mio periodo a Napoli.

Desidero estendere la mia sincera gratitudine a tutte le persone che ho incontrato durante questi lunghi anni a Tarragona. Mille grazie a Marta e Toni per l'accoglienza e il supporto sin da quando ero uno studente Erasmus. Grazie ai miei amici e colleghi catalani, Adrià, Isaac e Xavi per tutto il tempo trascorso insieme in laboratorio e per le birre para desconectar. Grazie a Dailyn e David, il vostro aiuto e i vostri consigli sono stati davvero preziosi. Grazie a tutti i compagni di laboratorio che ho avuto in questi anni, Ruben, Alberto, Federico, Alireza, Aina, Jordi, e a quelli che ho dimenticato di menzionare.

Vorrei anche ringraziare tutte le persone che ho incontrato durante il mio periodo a Napoli: Noemi, Angela e Libera, qualunque cosa accada Aperitivo alle 17h. Giovanni

Filippone e Martina Salzano de Luna per avermi gentilmente accolto nel vostro gruppo di ricerca.

Grazie alla mia famiglia italiana a Tarragona, Gianmarco, Mario, Rita e Mimmo per il fantastico tempo trascorso insieme. Una menzione speciale per Francesco, sei stato un grande amico, compagno di laboratorio, famiglia e coinquilino. È stato un piacere condividere questo viaggio con te e ti auguro tutto il meglio.

Ora è il turno della mia famiglia e dei sostenitori della mia città natale. La mia profonda e sincera gratitudine alla mia famiglia, Zio Aldo, Zio Erminio, Zia Anna, Zia Elena, Gianlorenzo, Stefano e la mia famiglia Cilentana per il loro continuo aiuto e supporto. Sono grato a mia sorella per essere sempre stata lì per me. Sarò per sempre grato ai miei genitori per avermi dato le opportunità e le esperienze che mi hanno reso quello che sono. Siete stati i miei esempi da seguire e la mia fonte d'ispirazione; nessuna parola potrebbe mai esprimere quanto ve ne sono grato. Una profonda gratitudine ai miei amati nonni, anche se non ci siete più tutti i miei traguardi li dedico a voi.

Grazie ai miei amici di una vita, il mio più vecchio amico Gianmarco, Roberto, Mario, Davide, Luigi, Gabriele; siamo cresciuti insieme e spero che invecchieremo anche insieme. Grazie a Sara per il supporto psicologico, Fiorella per la sua costante preoccupazione per i miei capelli e Claudia.

Infine, vorrei ringraziare te. Sebbene tu non faccia più parte della mia vita, una bellissima parte di questo traguardo è comunque tua. Un pezzo del mio cuore sarà per sempre tuo.

Ob la di, Ob la da
Life goes on, bra
(The Beatles)

DUAL-CURING THIOL-ACRYLATE-EPOXY
THERMOSETS FOR FUNCTIONAL APPLICATIONS
Claudio Russo

Abstract

Nowadays, more and more applications demand materials with complex shape designs which is a difficult task when working with thermosetting polymers. The curing or fabrication of thermosets is a complex process involving drastic physical changes, from a liquid-like mixture to rigid covalently crosslinked networks. This makes difficult to control the processing of complex shapes. In addition, the final shape cannot be processed anymore due to the presence of crosslinks within the network. The rise of 3D printing procedure has provided a viable way to cope with thermosets conformability issues but its characterized by a long processing time and low productivity.

In this context, dual-curing processing has emerged as an extremely valuable tool for the design of thermosets. It consists in the combination of two independent crosslinking processes that can be carried out both sequentially and simultaneously. The benefits of dual-curing processing rely on its processing flexibility and the possibility of enhancing the properties of cured parts in single- or multi-stage processing scenarios. In particular, well-separated sequential systems are characterized by an intermediate stable material which can be exploited in two-stage applications and to obtain complex shaped final thermosets without using complex processing techniques. Control of the curing sequence can be obtained combining two curing reactions triggered by different stimuli (i.e., heat and light) or by kinetic control of the reactions. Once a suitable combination of polymerization reactions has been established, a family of thermosets with different intermediate and final properties can be obtained by selecting monomer structure and functionality and altering the monomer feed ratio.

In view of the increasing needs of easy and versatile curing process, we developed a novel dual-curing system based on the combination of two “click” reactions: the thiol-acrylate Michael addition (first stage) and thiol-epoxy reaction (second stage). Dual-curing systems combining these two reactions were recently reported in the literature, but the reaction was activated with UV-light and the curing mechanism and sequence were not studied in detail. The novelty of our work is represented by the thermal activation of both reactions using a single catalyst, and the elucidation of the curing sequence and the conditions that make it possible to control it in multi-stage processing scenarios. Furthermore, the developed system was oriented towards the development of functional applications by adjusting the network structure to the final task.

To begin with, the dual-curing chemical mechanism was comprehensively studied and a curing procedure ensuring a good separation between two process was developed. Both the thiol-acrylate and thiol-epoxy reactions can take place under similar temperature conditions. Nevertheless, a safe and robust control of the curing sequence was achieved by choosing a suitable e temperature for the first curing process and taking into consideration the different intrinsic reactivity and the temperature dependence of the two reactions. A wide range of properties was attainable with this dual-curing system just by modifying the proportion between the thiol-acrylate and thiol-epoxy bonds in the network. Furthermore, the intermediate materials were found to present a large stability time window during which they can be safely stored or processed.

Once the dual-curing system was characterized we proceeded to study possible advanced applications. First of all, we characterized the shape-memory properties of thermosets obtained introducing new components to make network structural changes addressed to the enhancement of the shape-memory effect (SME). We were able to develop shape-memory thermosets with optimal SME in all recovery conditions. Due to their remarkable behaviour in partially and fully constrained recovery conditions we propose their possible application as mechanical actuators.

In addition, we tested the suitability of the dual-curing to the preparation of two-stage adhesives taking advantage of the system developed. Adhesive strength of single-lap joints (SLJs), obtained using both liquid-like and solid-like intermediate materials, were determined. Dual-curing processing was proved to have high potentiality in adhesive bonding applications, in particular with solid-like intermediate materials. An accurate control of the bondline thickness was achieved, while liquid-like intermediate led to stronger joints with respect to the joint obtained with the direct curing of the same reactive system. A beneficial effect of the incorporation of boron nitride (BN) fillers on adhesion was also evidenced.

Finally, thiol-acrylate-epoxy dual-curing system was used to develop electro-responsive shape-memory polymers. The capability to recover the shape under an electrical stimulus was studied by combining the thermal SME of these materials with an electrically conductive heater layer incorporated into them. When a voltage is applied, the heat released by Joule effect in the conductive heater increases the temperature and activates the shape-memory response. In this case BN fillers were used to enhance the thermal conductivity of the shape-memory thermoset in order to obtain faster recovery process. Unconstrained recovery experiments based on direct heating in oven and internal joule heating were performed. The electro activation of the SME resulted

in significantly faster recovery and, using a custom-made thermoelectric control, an accurate control of the recovery process was achieved.

In the final part of the investigation, we proposed the application of the developed electro-responsive design to a free-standing actuator design. It consists in the addition of a shape-changing layer that can be provide a bi-directional motion to the actuator. In this way, a reversible motion activated by on/off cycles of the electric stimulus can be obtained, leading to a significant step towards an efficient and autonomous operation of this actuators.

DUAL-CURING THIOL-ACRYLATE-EPOXY
THERMOSETS FOR FUNCTIONAL APPLICATIONS
Claudio Russo

TABLE OF CONTENT

List of Abbreviations

SMP	Shape-Memory Polymer
SCP	Shape-Changing Polymer
SCC	Shape-Changing capability
SME	Shape-Memory Effect
SMC	Shape-Memory Cycle
SMPC	Shape memory polymer composites
LCN	Liquid-Crystalline Networks
SMP	Shape-Memory Polymer
SCC	Shape-Changing capability
SMC	Shape-Memory Cycle
SMPC	Shape memory polymer composites
LCE	Liquid-Crystalline Elastomer
LC	Liquid-Crystalline
P-M	Polydomain-to-Monodomain
T_{trans}	Transition Temperature
T_g	Glass Transition Temperature
T_m	Melting Temperature
T_{iso}	Isotropization Temperature
T_{aniso}	Anisotropization Temperature
T_{peak}	Peak Temperature
T_{prog}	Programming Temperature
ε_D	Strain after Deformation
ε_u	Programmed Strain
ε_P	Permanent Strain
T_r	Recovery Temperature
σ_{rec}	Recovery Stress
σ_D	Programmed Stress

σ_{break}	Stress at Break
ε_{break}	Strain at Break
E	Flexural Modulus
FWHM	Full width at half maximum
SED	Strain energy density
R_r	Shape-Recovery Ratio
R_f	Shape-Fixation Ratio
W_a	Work Output
DMA	Dynamic-Mechanical Analysis
DSC	Differential Scanning Calorimetry
ESEM	Environmental Scanning electron microscopy
TMA	Thermomechanical Analysis
FTIR	Fourier Transform Infrared Spectroscopy
r_c	Critical ratio
r_a	Acrylate ratio
G' / E'	Storage Moduli
G'' / E''	Loss Moduli
SLJ	Single lap joint
G	Shear Modulus
GT	Glassy thermoset
TC	Thermal conductivity
CTE	Coefficient of thermal expansion
c_p	Heat capacity
PWM	Pulse width modulation
D_{cycle}	Duty cycle
R_{Heat}	Heating resistance
I_{Heat}	Heating current

DUAL-CURING THIOL-ACRYLATE-EPOXY
THERMOSETS FOR FUNCTIONAL APPLICATIONS
Claudio Russo

DUAL-CURING THIOL-ACRYLATE-EPOXY
THERMOSETS FOR FUNCTIONAL APPLICATIONS
Claudio Russo

Chapter 1

Introduction & Objectives

DUAL-CURING THIOL-ACRYLATE-EPOXY
THERMOSETS FOR FUNCTIONAL APPLICATIONS
Claudio Russo

Chapter 1 : INTRODUCTION & OBJECTIVES

1.1. Overview of thermosetting materials

A conventional way to classify polymeric materials relies on their thermal behaviour, which is defined by the existence of different transition temperatures, depending on their molecular architecture. The glass transition is a second order thermodynamic transition from the glass to the rubbery state, and the temperature at which this transition occurs is named glass transition temperature (T_g). Microscopically, this transition implies the cooperative movement of the polymeric chains sliding to each other when subject to an external force. Thermoplastics are made of a tangle of linear polymeric chains which, in the solid states, can be arranged either in a semicrystalline or amorphous structure. Thermoplastic polymers are able to flow when heated above a characteristic transition temperature; amorphous polymers will flow when heated sufficiently above their glass transition temperature (T_g) while semicrystalline polymers will retain mechanical consistency until they are further heated above their melting temperature (T_m), after which linear chains are free to move and flow takes place. In contrast, Thermosets can only be softened by increasing temperature above T_g and they remain solid until thermal degradation. The reason behind this different behaviour lies in their different molecular architecture. Thermosets have a crosslinked network structure made of strong covalent bonds which impede the material to flow. When heated to elevated temperatures, degradation occurs, leading to the permanent breakage of bond and destruction of the structure. Moreover, thermosets cannot be dissolved in any solvent owing to the interconnection of the crosslinked structure throughout the whole sample. Therefore, a thermoset can be better defined as a polymer network crosslinked by covalent bonds that percolates the whole mass [1,2]. Finally, there are also significant differences in processing between thermoplastics and thermosets. Thermoplastics can be reprocessed and reshaped when heated above T_m (or T_g) while thermosets are irreversibly formed by curing the proper formulation in a specific mould or a desired surface. As will be later discussed, T_g is a crucial parameter during the entire thermoset life cycle (manufacturing, processing, and use). However, the boundary between thermoplastic and thermosets is currently questioned by an emerging new class of polymer networks designed as Vitrimers by Leibler [3]. Vitrimers are capable to interchange covalent bonds within a permanently crosslinked network. The exchange is triggered above a characteristic temperature (T_v), higher than T_g. Below

T_v, these materials act as a conventional thermoset while, above T_v, they can be recycled or reprocessed thanks to the exchange of covalent bonds.

From the discovery of Bakelite in 1907, polymers were undergoing to an exponential growth with applications covering every aspect of our life; from the most insignificant PET bottle to the most advanced high temperature PEEK used in the aerospace industry. Global plastic production has continuously increased from 15 million tonnes in the sixties to 368 million tonnes in 2019 with over 1.5 million people employed in the European plastics industry and a turnover of more than 350 billion euros [4]. Although thermoplastics constitute the majority, thermosetting resin production also shares the growth rate of the industry. In 2014 estimate of global annual thermoset production was 53 million tons [4]. The first man-made polymer discovered by Baekeland [5] was a phenol-formaldehyde thermoset made of chemically crosslinked chains. Since then, a large variety of different thermosets families have been developed: urea-formaldehyde resins, unsaturated polyesters and epoxy resins occupies the largest market share. Other typical examples are the alkyds, vinyl esters and allyl resins. Despite the great gap in global production between thermoplastics and thermosets, their global production worth is estimated around 10 billion dollars [6]. The large usage of thermoset is due to their characteristic properties such as superior mechanical and thermal properties and the high chemical resistance. The reason behind their unique characteristics can be found in the covalent bonds that forms their network.

Thermoset networks are formed by a characteristic polymerization process called “curing”, during which molecules of monomers or prepolymers are linked together to assemble the final polymer network. The starting formulations used to prepare thermosets are typically made of two main components: a monomers mixture and one or more crosslinking agents. Different kind of catalysts can be also used to either activate the curing reaction or tune the reactivity depending on processing conditions. In some other cases, initiators can be used to activate the homopolymerization of the monomers. The final properties of the cured materials do not only depend on the selected monomers, but they can also be tailored by the quantity of catalyst, the curing conditions, the proportion between monomer and crosslinker and the functionality of the curing agent. The functionality of reactive species is one of the most important parameters in polymer science since it defines the final topology of the network. According to IUPAC, “functionality” is defined as the number of bonds that a single monomer is able to form with the other species involved in the reaction mechanism. The functionality does not always match the number of reactive functional groups because it strongly depends on the reaction mechanism: monomers can have functional groups which do not take part to the reaction, thereby decreasing the number of bonds

the monomer can form. In order to obtain non-linear 3D networks, the functionality of at least one formulation component has to be higher than two. Bifunctional monomers promote the formation of linear polymers with higher flexibility due to the decrease of the crosslinking density. On the other hand, monomers with higher functionality promote the formation of branched crosslinked structures with higher crosslinking density and more rigid behaviour. The higher the crosslinking density the higher the resistance when exposed to heat or chemical attacks. In the same way, the mechanical strength and hardness improve with the crosslinking degree, at expenses of brittleness. Some fibbers or fillers are also commonly added to the formulation, which can respond both to obtain the desired final properties and to reduce the production cost.

The two main transitions taking place during the curing process of thermosets are gelation (liquid-to-rubber transition), and vitrification (liquid or rubber-to-glass transition). Gelation refers to the unique point, named "gel point", at which the molecular weight became infinite [7], evidencing the existence of a giant macromolecule, i.e. with infinite molecular weight, percolating the bulk of the material. This physical transition from liquid to crosslinked gel is a constant conversion event and occurs always at the same degree of cure, regardless of the curing conditions [8]. It is an irreversible process and, from this point forward, the materials start to behave like a solid and can no longer be reshaped. The other important transition that can take place during curing is the Vitrification which is the point at which the material starts to behave like a glass. It is strongly affected by the curing temperature (T_{cure}) and, unlike gelation, it is a thermo reversible process. Vitrification occurs when T_g reaches the Tcure, leading to a dramatic slowdown of curing and the reaction becomes diffusion controlled. At this point, the T_{cure} has to be increased in order to complete the polymerization process and to finally achieve the ultimate glass transition temperature ($T_{g,\infty}$). The sequence of events the reacting system will undergo depends on the cure temperature (T_{cure}). Thus, when T_{cure} is above the ultimate glass transition temperature ($T_{g,\infty}$) of the cured material, the system will only gel. If T_{cure} is below $T_{g,\infty}$ but above the glass transition temperature of the material at the gel point ($T_{g,gel}$), the system will first gel and then vitrify. Finally, when T_{cure} is below $T_{g,gel}$ the system will first vitrify and then, if given enough time, undergo gelation. In many systems the mobility in the vitrified state is too low to permit further reaction, in which case only vitrification occurs [9,10]. However, some studies have reported results that do not agree with this general picture. Gelation has been found to occur before vitrification at all cure temperatures where it could be observed, i.e., also below $T_{g,gel}$ [11].

Thermosets can be divided in different types, depending on the monomers used, the curing agents and the chemistry implied. Phenolic or phenol formaldehyde resins are

synthesized from the condensation reaction of phenol with formaldehyde in the presence of a catalyst. Although they were the first truly synthetic resins to be commercialized, phenolic resins continue to be used for a wide variety of applications, such as moulding powders, laminating resins, adhesives, binders, and surface coatings. For their excellent mechanical resistance, high heat resistance under load, and high impact resistance, phenolic resins are used as impregnant in structural composite materials manufacture. Phenolics main features are their superior fire, smoke and toxicity properties compared to other polymeric matrices for fire-resistance applications [12]. Urea-formaldehyde thermosets are obtained from the urea and formaldehyde reaction. Varying the conditions of reaction and preparation countless varieties of condensed structures can be produced. Their main advantages are the final hardness, the good thermal properties, the low flammability together with their relatively inexpensive production. On the other and their major drawback is the hydrolytic degradation at which they are subjected in presence of moisture and/or acids [13]. Polyurethanes (PUs) are a wide family of thermosets made by of bi- or trifunctional isocyanates with polyols. By varying the starting reagents and their relative amounts PUs can be obtained in different forms and with different properties achieving a huge variety of possible applications. Because of its extraordinary adaptability to meet the most diverse requirements, PUR technology has become established throughout the world in many coatings and adhesives applications. Moreover, the most extended use of PUs is in form of foams, ranging from flexible to rigid, giving products with good insulating characteristics at considerably low density. Unsaturated polyesters are produced by condensation of polyols with saturated or unsaturated anhydrides or dibasic acids. The unsaturation of this type of polyesters provides the subsequent crosslinking in an exotherm reaction. They are characterized by low cost, adequate environmental resistance, light weight, rigidity, electrical resistance, and good wetting to glass fibres. Unsaturated polyesters main applications consist of ship hull, pipelines, vehicles parts, storage tanks, building components and laminated panels. From the esterification of an epoxy resin, typically formulated with styrene, vinyl esters resins are composed [14]. The polymerization process of that resins is initiated by radicals, induced by UV radiation of by peroxides [15,16]. The low viscosity of these formulations makes them highly adequate to produce polymer composites, even though the volatility of styrene is a drawback to be considered and operators must be suitable protected. Alkyd resins are derived from polyesters modified with components such as fatty acids, which confers a tendency to form flexible coatings. Extensively used in paints, they can also be casted in moulds. Alkyds are one of the most inexpensive thermosets. Even if the low durability

in outdoors surfaces and the presence of organic solvents has limited their use, Alkyds are still employed in low performance industrial coatings and for interior paints.

Finally, Epoxy thermosets are one of the most consumed thermosets together with PUs, and their production is largely aimed to electronics, coatings, and composite matrix. They took their name from the characteristic “epoxy” functional group of the monomers which consists in an oxygen atom bonded to two carbon atoms to form a cycle. One of the most commercialized epoxy resins since 1940 is the well-known diglycidyl ether of bisphenol A (DGEBA), a resin based on the reaction of bisphenol A with epichlorohydrin in strong basic conditions. The properties of the epoxy thermosets are strongly affected by the type of curing agent (also known as hardener) and by the reaction mechanism associated to the hardener. Epoxies cannot be polymerized by chain growth mechanism, but they are polymerized by polycondensation and ring-opening. They can be cured with many hardeners or curing agents, among them: amines, acids, anhydrides, phenols, dihydrazides and thiols [2,17,18]. These curing agents are usually added in stoichiometric amounts to the formulation to reach the maximum crosslinking degree. However, in some cases, off-stoichiometric proportions can be exploited to act on the crosslinking density, thereby diversifying the final mechanical characteristics. In addition, epoxy thermosets can be also obtained by means of homopolymerization, either by anionic or cationic reactions (ring-opening polymerization). Nucleophilic or electrophilic initiator are needed in order to take advantage of the highly polar oxygen-carbon bonds and the strain of oxiranic cycle [2,19,20].

Epoxy materials possess a large number of properties that make them valuable both for everyday use products and advanced engineering application: the easy tailoring of final properties; the absence of volatile matter on curing; good mechanical properties thanks to the covalent bonds network, even at high temperature; a high resistance to chemical attack; the strong adhesive bonding produced during curing on many different substrates; electrical and thermal insulation characteristics, owed in part to their amorphous structure [21]. However, they also exhibit major drawbacks such as the shrinkage during the curing process and the difficulty of been conformed after curing, which are common shortcomings of all thermoset polymers [22,23]. The thermal shrinkage can be reduced adjusting the curing temperature profiles, allowing a better relaxation of the network. On the other hand, the so-called expanding monomers (i.e., cyclic orthoesters or orthocarbonates) and hyperbranched modifiers can be used to reduce chemical shrinkage [24–26]. Another extremely valuable way to retain both type of shrinkage is the dual-curing procedure, a multi-stage curing which can be also exploited to obtain complex-shaped pieces overcoming the lack in conformability of the cured pieces.

1.2. Dual-curing thermosets

Multi-stage curing of thermosets has always been an extremely valuable tool to enhance the curing degree and to control final properties. The combination of different curing reaction in a multi-stage processing was found to have interesting advantages that can be exploited for the preparation of materials with advanced properties. The dual-curing concept (**Scheme 1.1**) involves the combination of two polymerization processes in a single thermosetting formulation, which can be activated simultaneously or in a sequential and controlled way, using selective triggers such as UV light or temperature or by differences between the curing kinetics of the two processes [21].

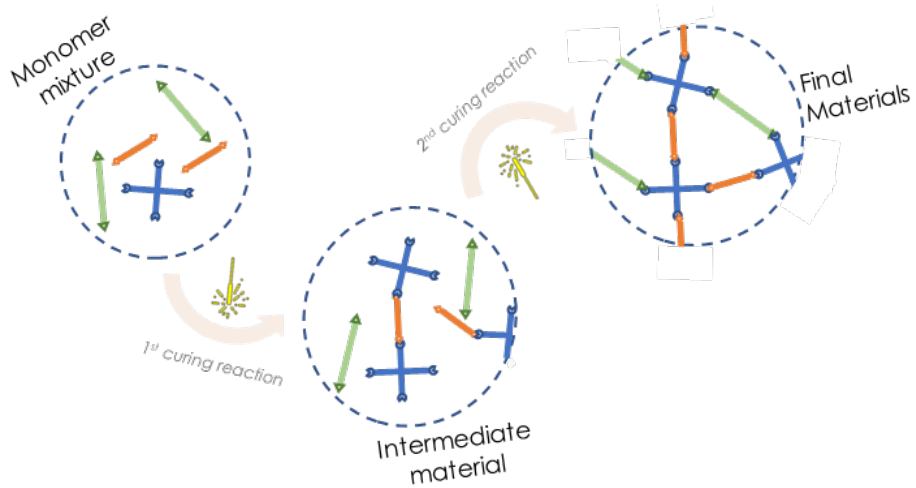

Scheme 1.1. General representation of dual-curing processing.

Although the combination of separated sequential reactions is more attractive, due to the possibility of being exploited for application that requires a multi-stage manufacture, the control of the curing sequence is not always essential when such combination only aims to the improvement of the final properties. For instance, polymerization of excess groups in off-stoichiometric stepwise curing systems is used to enhance the thermal-mechanical properties of thermosets [27,28]. In other cases, when visible or UV light curing is employed, an additional thermal curing stage is used to ensure full conversion of reactants even at deeper layers or shadowed areas [29,30]. However, sequential dual-curing systems are more attractive because they enabled substantial breakthrough in multi-stage processing. In this respect, sequential dual-curing represented an evolution of well-established procedure, such as prepolymer crosslinking [31,32] and B-stage processing [33,34]. The extent of both curing reactions can be easily controlled by merely changing the composition of the formulation. Further

curing is only allowed when the second stage is triggered, differently from B-stage processing, which is subjected to tight time-temperature specifications to minimize the risk of overcuring. In consequence, it is straightforward to obtain intermediate stable materials with desired structure and properties. In comparison with prepolymer synthesis approach, dual-curing allows an easier processing and compounding because it is obtained from low molecular weight monomers formulations. In consequence, sequential dual curing procedures paves the way to simplified development of custom-tailored materials with a flexible processing ability that makes them highly useful for a number of advanced, high-added-value applications [35–37].

The precise control of the material properties in the intermediate stage (i.e., low T_g, low crosslinking density and high deformability) can be exploited as a pre-processing methodology for the development of complex three-dimensional structures without the requirement of complex moulds. In this way, a common drawback in thermosets, which cannot be easily processed after curing, can be easily overcome. Application and patterning of the resin in a persistent shape prior to attachment and full cure is a desirable feature in microelectronics or coatings applications, and this can be easily accomplished following a dual-cure processing thanks to the existence of a stable intermediate material with tailored structure and properties. Besides, the cost in transport or storage steps during the processing of a piece of thermoset can be considerably reduced. Intermediate materials with high deformability and malleability can be cured and then folded into a reduced shape for the transport/storage stage and further unfolded on-situ trough the elastic recovery of the network. Moreover, the low T_g in the intermediate stage considerably improves the impact resistance (energy absorption), thus avoiding irrecoverable damages that may take place during these intermediate stages.

1.2.1. Design of dual-curing systems

In order to be successful, sequential dual-curing systems have to meet three important requirements: (i) both polymerization reactions are selective and compatible so that no undesired inhibition or reactivity effects take place; (ii) reactions are activated by different stimulus, or else they have sufficiently different reaction rates so that they can be controlled from a kinetics point of view; (iii) final and intermediate materials properties can be custom-tailored. The intermediate and final properties of dual-curing materials depend strongly on the network structure at the end of each polymerization process. Network structure at the intermediate and final stages is controlled by monomer functionality, structure, and feed ratio. Significant structural parameters, such

as mass-average molecular weight, gel-point conversion, or cross-linking density or gel fraction, which are strongly correlated with the rheological or thermomechanical properties of partially or fully cured materials, can be analysed. Moreover, a deep understanding of the underlying reaction mechanisms is crucial to obtain tailor-made materials through curing sequences with well-established kinetics. Network build up in multistage processing has been studied using stochastic models in the past [38]. Recently, some criteria for designing dual-curing systems and preliminary network structure analysis were developed based on ideal network build up models [39,40]. However, in certain cases, idealized stepwise network build up models are not able to precisely predict the intermediate and final network properties due to the complex structure-property relationships. A more profound understanding of the effects of monomer structure, functionality, and feed ratio on the intermediate and final properties can be carried out by rheological and/or thermomechanical analysis [41]. The influence of monomer functionality and feed ratio on the gel point can be evaluated by means of rheological analysis on uncured formulations, while thermomechanical analysis provides values of structural parameters (i.e., Storage modulus in glassy and rubbery state, the width of the relaxation process) that can be used to understand the structural changes behind the material properties alteration [41,42].

The catalyst used also have an important role in the network formation. The use of photolatent and thermally-latent catalysts, for base- or acid-catalysed reactions or radical polymerization reactions [43,44] can contribute to the design of efficient one-pot dual-curing formulations. These formulations have good storage stability of the uncured system and stable intermediate properties. The use of blocked species can also be exploited for the design of dual-curing formulations [45]. Careful control of the exothermicity of polymerization is a general concern in composites processing for control and quality purposes [23]. It is also a factor to be taken into consideration in dual-curing processing schemes, especially in the case where the second polymerization process is thermally activated [46].

There are a lot of polymerization reactions which meets all the requirements of a dual-curing procedure. Among them, the so-called “Click” reaction are extensively used as they are orthogonal, selective, efficient and take place in mild and solventless conditions.

1.2.2. Click reaction based dual-curing system

The term Click Chemistry was introduced by Sharpless in 2001 to describe high-yield reactions easy to perform, which can generate complex substances by bringing together

smaller units via heteroatoms [47]. Their main characteristics includes: (i) orthogonality; (ii) regio and stereospecificity; (iii) high yields; (iv) mild, solventless or aqueous conditions; (v) wide range of available starting reactive groups [48,49]. Click reactions led to a new modular construction approach in polymer chemistry as their orthogonality has been exploited, combining two or more click reactions, to prepare complex structures [50,51].

Click reactions are strongly appreciated in the field of thermosets because they permit the preparation of well-defined network structures. As these reactions are tolerant to a wide range of functional groups, they were successfully combined to obtain a wide variety of dual-curing methodology. In particular, they resulted to be an extremely valuable tool for dual-curing system development thanks the above-mentioned characteristics. Click reactions have been classified in the following categories: (i) cycloadditions of unsaturated compounds (e.g., Diels–Alder reaction); (ii) nucleophilic attacks to strained heterocycles (epoxides, aziridines, etc.); (iii) carbonyl chemistry of the non-aldol type (formation of ureas, thioureas, hydrazones, etc.) and (iv) additions to carbon–carbon multiple bonds (thiol–ene, Michael additions, etc.) [52,53]. In **Scheme 1.2** are resumed the reaction schemes of several click reactions. The orthogonality, the specificity and the high yields allows to combine different reaction mechanism without interfere with each other, reaching high conversion rates. Although a wide variety of reaction mechanisms are available, the most explored in dual-curing process are the ones involving thiols as comonomers. Thiols can participate in thermal nucleophilic and radical UV-initiated reactions. Taking into account that dual-curing systems were initially proposed as the combination of an initial photochemical polymerization followed by a second thermal process, thiol chemistry plays an important role in dual methodologies. One advantage that should be considered in these reactions is that the materials obtained have, in general, good transparency, and the cross-linking is accompanied by a low shrinkage, resulting in reduced internal stresses. Generally, high functionality monomers and the introduction of rigid segments are employed to compensate the higher structure flexibility attributed to the longer S – C bond with respect to the C – C bond [54].

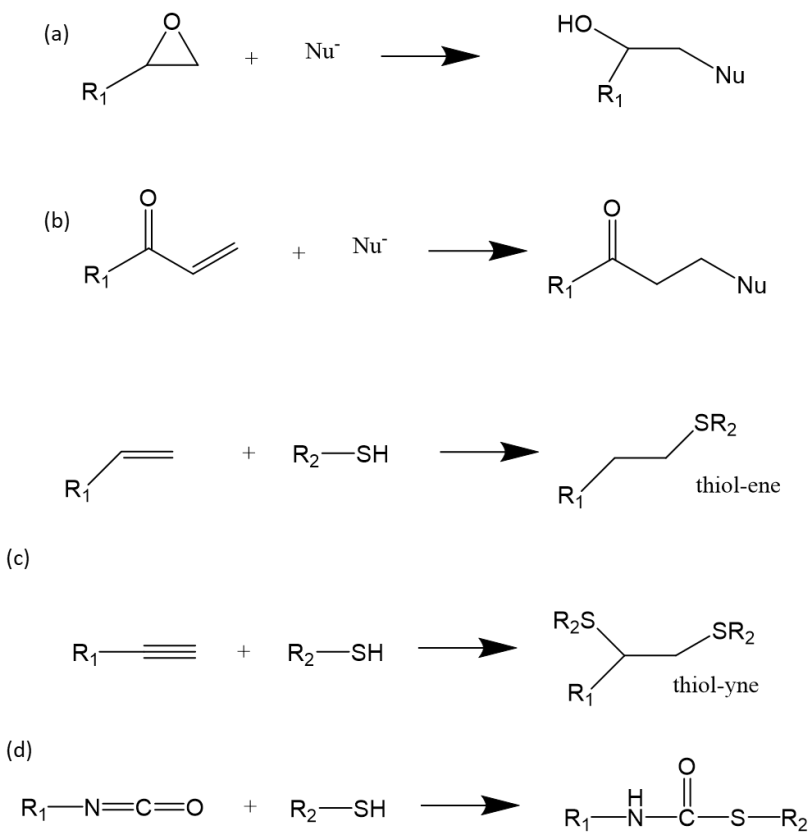

Scheme 1.2. Reaction schemes of several click reactions: (a) Nucleophylic ring-opening reactions; (b) Michael addition reactions; (c) Photochemical addition of thiols to alkenes and alkynes; (d) Carbonyl addition of thiols to isocyanates.

Some examples of dual-curing procedures based on only one reaction can be found in literature. In these cases, monomers with different reactivities are used in order to enable the two-stage curing to be performed at different curing conditions. As an example, Chatani et al. [55] prepared shape-memory thermosets by selective thiol-Michael additions of vinyl sulfones and acrylates which reacts at different temperatures due to their different electrophilic characters. Methacrylates are less reactive than acrylates in Michael additions due the steric hindrance of the methyl group. Therefore, selective dual-curing system can be obtained with acrylates and methacrylates choosing the adequate combinations of monomers and catalysts [56,57].

A common strategy to obtain dual networks is by the combination of two sequential click reactions. One of the earliest dual-click procedures was described by Chan et al., who prepared highly functional materials by a sequential curing process involving a thiol-ene and thiol-yne reactions as first and second stages, respectively [58]. One of the

most studied dual-curing system is based on the combination of an initial photoinitiated thiol-ene and a thermal activated thiol-epoxy reaction [37,59]. This procedure is advantageous, since the use of multifunctional thiols allows covalently connecting both thioether networks. The thiol-ene reaction follows a step-growth polymerization mechanism which results in slow and homogeneous network build-up process with delayed gelation and reduced shrinkage stress as compared with chain-growth polymerizations [60]. The major drawback of this system is the difficult control of the curing reaction. Recently, the use of latent amine precursors that liberates amine by heating at a defined temperature made it possible to establish a true dual photoinitiated-thermal curing with intermediate materials stable for several days [61]. Versatile thiol chemistry was utilized by Shin et al. [62] to design a thiol-isocyanate-ene dual-curing system. In their system, thiol-isocyanate and thiol-ene reactions took place either simultaneously or sequentially, when the thiol-isocyanate is thermal or photo initiated, respectively. Processing flexibility was achieved by the control of curing sequence and, the incorporation of thiourethane groups in thiol-ene networks, improved the physical and mechanical properties thanks to hydrogen bonding.

An extensively used dual-curing procedure consists in the combination of a click reaction followed by an homopolymerization. In order to obtain storable and processable polymers at the final of the first stage of curing and final networks with optimum properties for different applications, the preparation of dual materials from off-stoichiometric formulations has recently gained interest. The monomer in excess should be able to experiment homopolymerization reaction, without any interference. The first stage process is a self-limiting click reaction between two multifunctional monomers with an excess of one of the two monomers. The second stage reaction is a thermally or UV-induced polymerization of the excess of unreacted groups. The materials obtained after the first curing stage can be gelled or ungelled and loosely or tightly cross-linked at the end of the second curing stage, depending on the functionality and the ratio between the first reaction monomers. A critical value, known as critical ratio (r_c) can be identified following theoretical or experimental procedure. The r_c sets a boundary line between ungelled and gelled intermediate materials (**Figure 1.1**) and it is a crucial parameter to evaluate in order to correctly address each monomer ratio to the suitable application. In such systems, the stepwise polymerization at the first curing stage, imparts advantages such as network homogeneity, high gel point conversion, and low curing shrinkage to the material. Later, the secondary chain-wise polymerization stage increases the material crosslinking density, glass transition temperature, strength and hardness, thereby improving its mechanical properties significantly. A common example

of these kind of set-up is the combination of a stepwise Michael additions are combined with chain-wise homopolymerization such as acrylate photopolymerization [35,63]. Interpenetrated covalent bonded polymer networks can be obtained by a mixture of acetoacetates and acrylates: a first stage curing consist of Michael additions is then followed by photoactivated homopolymerization of the acrylate excess. During the second stage, the soft Michael network was converted into a hard cross-linked material with high values of hardness [64,65].

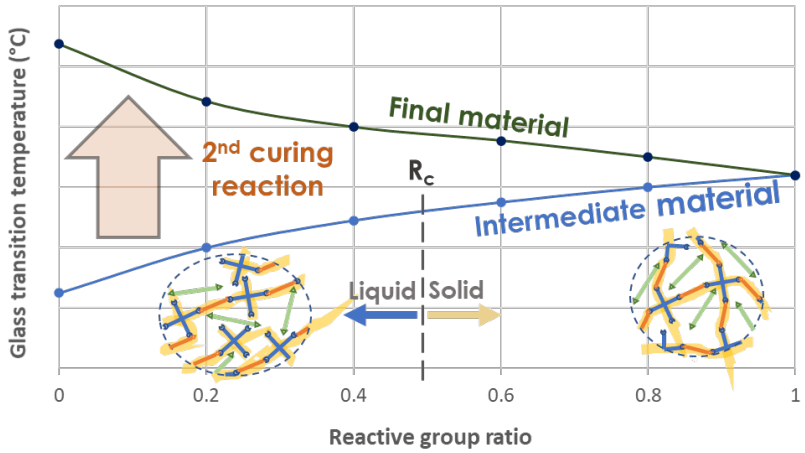

Figure 1.1. Schematical representation of the variation of the glass transition temperatures of the intermediate and final material with the reactive group ratio.

1.2.3. Thiol-acrylate Michael addition

The Michael additions is a prominent click reaction of acrylates which is defined as the 1,4-addition or conjugate addition of resonance-stabilized carbanions to activated double bonds. Michael-type addition reactions are widely used in dual curing processes, because of the variety of commercially available nucleophiles (Michael donors) and activated double bond compounds (Michael acceptors) that can be used in such processes. Of all possible acceptors, acrylates have a suitable combination of reactivity, versatility, availability, and cost while, the most common and clickable co-reactants for acrylates are thiols. Acrylates react with thiols via two distinct mechanisms: (i) Radical mediated thiol–acrylate reaction; (ii) Thiol–acrylate Michael addition. The radical mediated reaction cannot be considered click since, the existing competition between the chain-growth homopolymerization of the acrylate and the step-growth mechanism of the thiol-ene polymerization, leaves partially unreacted thiol monomers [66,67]. On the other hand, the thiol–Michael addition reaction starts with the formation of a

thiolate anion via base catalysed mechanism or nucleophilic path, depending on the pK_a and nucleophilic strength of the catalyst (**Scheme 1.3**). The nucleophilic path is favoured when strong nucleophiles, such as *4-(N,N-dimethylamino)pyridine* (DMAP), are used as catalyst [68]. There are no competing reactions within the mechanism, thereby allowing quantitative conversions of both reactants. As a result, this reaction has been combined with many other click reactions to develop dual-curing systems over the years.

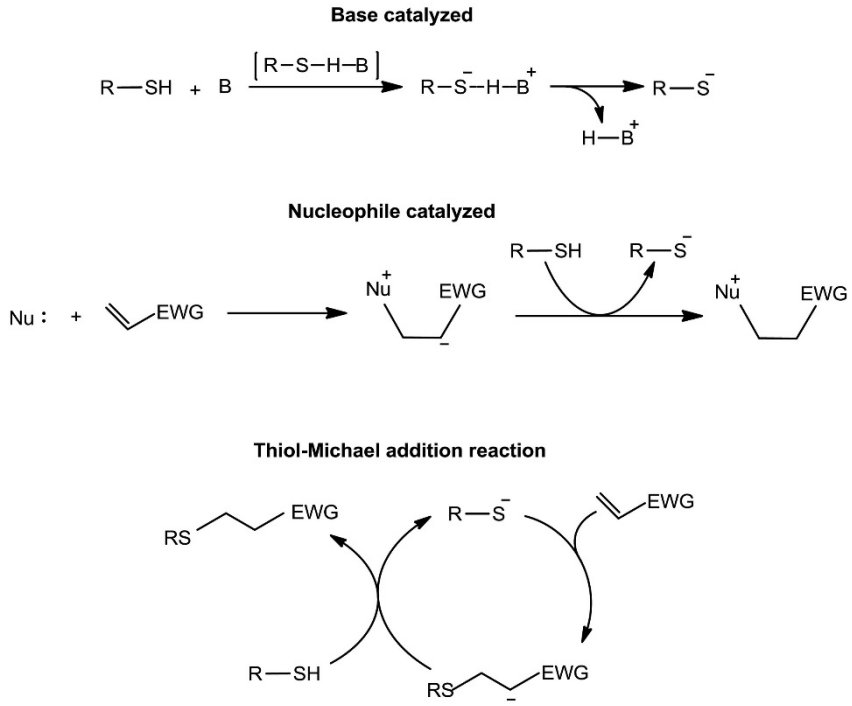

Scheme 1.3. Thiol-acrylate Michael addition reaction via two distinct mechanisms: catalysis by base, or nucleophile. Reported in [68].

Valuable example of dual-curing system based on the combination of thiol-acrylate with thiol-ene or thiol-yne. Sequential dual-curing system were proposed by Peng et al. using a tertiary amine for the thiol–Michael addition and a radical photo initiator for the thiol–ene reaction. In the same way, thiol-Michael was combined with thiol-yne reaction [69,70]. Recently, Konuray et al. developed a thiol-acrylate and thiol-ene dual curing system using a novel set of tertiary amines comonomers with allyl functionality to catalyse the first stage. Then, the allyl moieties later undergo a radical thiol–ene reaction to yield fully crosslinked dual-networks [71]. The same research group also developed sequential dual-curing mechanism consisting of thiol-Michael addition to acrylates at room temperature followed by Michael addition of acetoacetates to acrylates at

moderately elevated temperature. The curing sequence can be controlled with the help of the different acidities of the protons on thiol and acetoacetate groups, the favourable pKa of the base used as catalyst and the self-limiting character of Michael additions. The latency of the curing steps can be regulated by selection of the right catalysts, temperature and curing conditions. Thiol-Michael addition was also combined with thiol-isocyanate reaction to obtain thermosets with tuneable mechanical properties. Thiol-isocyanate co-catalysed by phosphine and acrylate was faster than the thiol–Michael addition at low-phosphine concentration allowing a good separation between the two steps [72]. Taking advantage of the behaviour associated with click reactions, Nair et al. developed a novel dual-curing system based on off-stoichiometric thiol-acrylate formulations [35,73]: stoichiometric base-catalysed thiol-acrylate Michael addition is followed by a photoinitiated free-radical polymerization of the excess of acrylate groups.

1.2.4. Thiol- epoxy

Another prominent click reaction is the amino catalysed thiol-epoxy reaction. The amine can act directly as a base, extracting the thiol proton and enhancing the nucleophilicity by forming thiolate active groups, or as a nucleophile, attacking to the epoxide and finally generating thiolate (**Scheme 1.4**) [74]. The reaction can be thermally, or photo initiated and is characterized to an extremely fast reaction due to the amine catalyst. In order to obtain longer pot-life latent catalysts can be employed [75].

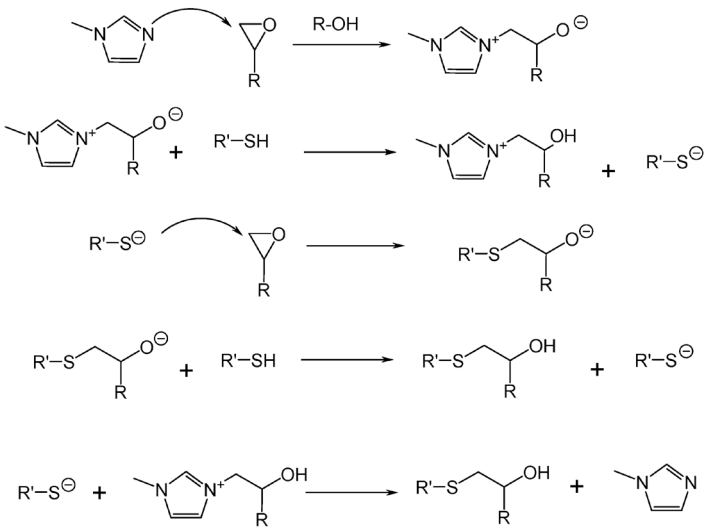

Scheme 1.4. Thiol-epoxy reaction catalysed by 1-methylimidazole as tertiary amine as reported in [74].

Base-catalysed click thiol-epoxy thermosets have a broad range of applications even if their major drawback is the low glass transition temperature and low rigidity. In order to enhance the final properties thiol-epoxy reaction has been successfully combined with other click reaction in numerous dual procedures. A new dual-curing system based on off-stoichiometric thiol-epoxy formulations was recently developed [76]. Sequential two-step process could be achieved using a single tertiary amine catalyst due to the selectivity and faster kinetics of thiol-epoxy polycondensation over epoxy homopolymerization. Materials were stable in the intermediate state, after thiol-epoxy reaction, allowing the safe storage and manipulation before the second stage of the curing began, leading to final thermosets with enhanced thermomechanical properties. Hybrid thiol-ene/epoxy networks have been prepared by combining radical click thiol-ene reaction and epoxy homopolymerization in photocurable formulations, through a dual UV-thermal curing process. Formation of thioether species is very fast, and the interaction of thioether or thiol species with oxonium cations leads to the formation of stable trialkyl sulfonium cationic species [77] that act as latent thermal catalysts that are able to activate epoxy curing at temperatures higher than 100°C [77,78]. In general, the materials obtained show a glass transition temperature between the pristine thiol-ene and epoxy UV-cured [78,79]. The use of allyl terminated hyperbranched polyesters as -ene monomer made it possible to reach glass transition temperatures higher than the epoxy homopolymer [79]. Recently, Gamardella et al. [80] developed a new family of thermosets by means of a thiol-isocyanate-epoxy dual-curing system. The sequential dual behaviour of the new system proposed here is based on the faster reaction kinetic of the isocyanate-thiol at a relatively low temperature, compared to the thiol-epoxy reaction. The thiol-epoxy second stage is then triggered at higher temperature leading to thermosets with a wide range of properties depending on the ratio between the isocyanate and epoxy groups.

1.2.5. Dual Thiol-Michael and Thiol-epoxy systems

A few examples of dual-curing procedure obtained combining thiol-Michael addition with thiol-epoxy click reaction can be found in literature. Although the radical-mediated thiol–acrylate reaction does not generally exhibit click characteristics, it has been combined with other click reactions to obtain materials with significantly low soluble content. Jian et al. [81] obtained hybrid organic networks by thiol–epoxy/thiol–acrylate polymerization processes in which both reactions proceeded sequentially without clear separation. The curing was triggered by irradiation with UV light by the use of a photobase generator 1,5,7-triazabicyclo[4.4.0]dec-5-enyl tetraphenylborate (TBD·HBPh4) capable of in situ generating a strong base and free radicals, with

isopropylthiolxanthone (ITX) as photosensitizer to extend the wavelength absorption range of the catalyst. The free radicals facilitated both thiol–acrylate radical polymerization as well as acrylate homopolymerization, leading to materials with unreacted thiol groups. However, as the photobase generator also liberated a strong base (TBD), thiol–Michael addition also took place and compensated partly for the stoichiometric imbalance. The researchers found that thiol–acrylate reactions and acrylate homopolymerization were faster and more efficient than the thiol–epoxy reactions (>95% conversion in a matter of seconds and minutes, respectively), and the thiol conversion increased with an increase in the epoxy content. Recently, Konuray et al. presented a novel photolatent dual-cure thiol–acrylate–epoxy system [68]. Under UV light, the photobase generator liberates a strong base that catalyses the thiol–Michael reaction at room temperature. To initiate the second curing reaction between epoxy and remaining thiols, the system is heated above 80°C. The use of a radical inhibitor ensured that no radical mediated acrylate homopolymerization took place. The final material properties suggested potential applications such as chemically resistant industrial coatings, adhesives, and electronic materials. It is also reported in the literature the preparation of hybrid polymer networks (HPNs) from one-pot thiol–acrylate–epoxy mixtures. Jin et al. [82] cured a stoichiometric combination of a diacrylate and a diepoxide using difunctional or multifunctional thiol crosslinkers. The nucleophilic thiol–acrylate reaction and thiol–epoxy reaction was carried out simultaneously at 80 °C in the presence of 1,8-diazabicyclo[5,4,0]undec-7-ene (DBU). Depending on the functionality of the thiol, resulting materials exhibited a wide range of properties characterized by differential scanning calorimetry (DSC), dynamic mechanical analysis (DMA) and scanning electron microscopy.

In Chapter 3, a novel sequential dual-curing system obtained by the combination of thiol-acrylate and thiol-epoxy reaction, both thermally triggered, is proposed. The possibility of obtaining a chemically stable intermediate material based exclusively on the differences in reaction kinetics is demonstrated.

1.2.6. Advanced application of dual-cured thermosets

Over the last few years, dual-cured materials have been exploited for numerous advanced applications thanks to their characteristic features. These systems are very advantageous because of the two distinct and largely independent sets of properties achievable by the two stages. Moreover, dual-curing mechanisms enable a fine tuning of the materials properties through the control of relative contribution of the two curing

reactions; starting from one set of monomers and catalyst a wide range of intermediate and final properties can be obtained and adjusted to the desired application (**Figure 1.2**).

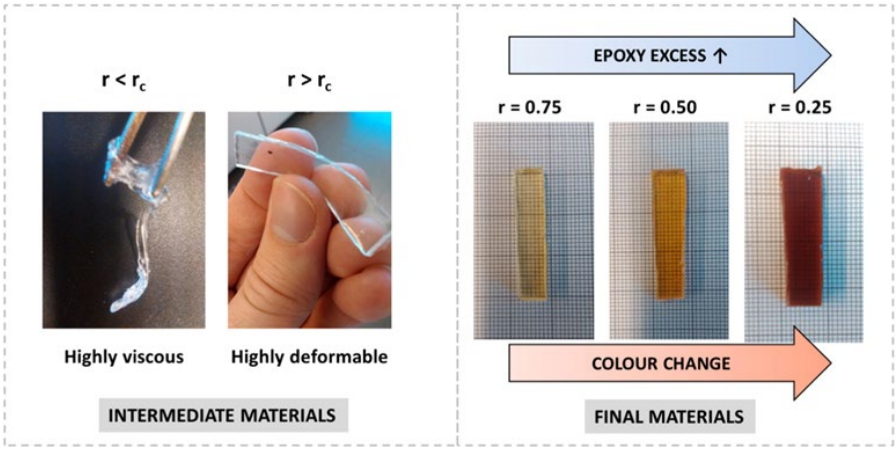

Figure 1.2. Example of different intermediate and final materials obtained at different thiol-epoxy ratios in off-stoichiometric thiol-epoxy systems. Reproduced from [41].

Different applications have been described in the literature where dual-curing reactions are smartly applied. The advanced applications range from shape-memory polymers, energy-absorbing devices, photopatterning and coatings technologies through the recently emerged in composites prepreg and 3D printing materials [21,36].

One of the most investigated application of dual-cured thermosets are the shape-memory materials. Click based dual-curing mechanism generally results in thermosets with good shape-memory properties, thanks to the narrow glass transitions favoured by the high conversions and the absence of side reactions associated to the click behaviour. In this field the intermediate stage can be easily exploited to obtain complex shaped actuators [76] or to obtain well-defined triple shape-memory thermosets as made by Chatani et al. [55]. The developed material was proved to be stable in its intermediate temporary shape for an extended time thanks to its two distinct networks, each holding separate temporary shapes.

Dual-curing sequential system which combines thiol-ene and thiol-isocyanate click reaction was found to have high performance in energy absorbing applications [83]. Thiol-ene network was being investigated for their potentially high non-destructive energy absorption which were limited by their low toughness. Incorporating (thio)-urethanes into the networks increased strain at break and toughness while decreasing cross-link density, making these materials to outperform common materials used to mitigate concussive events from impact.

Thiol-isocyanate-methacrylate dual-curing networks were used to obtain well-defined surface patterns and functional geometric shapes. In the first stage rigid thiourethane networks with methacrylate functionalized ends were obtained. Methacrylate functionalized network, incorporating photoinitiator and photoabsorber, were irradiated with UV light to generate a final network with complex property gradients. Combining suitable photomask and properties, researchers were able to mechanically program specific 3D shapes and surface topographies. Subsequentially, 3D geometries and topographies could be erased by temperature or fixed by UV irradiation, thus obtaining functional or smart materials [84].

Interesting examples of dual-processing applications can be also found in advanced coatings applications. Self-healing dual cured polyurethane elastomeric coatings were prepared via Diels-Alder and urethane formation reactions. These two orthogonal reactions were performed combining functionalized of hydroxyl-terminated polybutadiene with furan dangling groups, a synthetized bismaleimide compound and isophorone diisocyanate. Evaluating the microscopic and macroscopic scales showed that the prepared coatings exhibited good healing properties as well as their mechanical properties. Additionally, the healed samples were displayed at least 50 % of their initial strength in the tensile test. Recently, dual-curing processes combining UV-initiated curing process with sol-gel reactions were investigated for the preparation of hybrid organic-inorganic materials. A photo-initiated polymerization is followed by a thermal treatment for promoting sol-gel reactions of suitable alkoxy precursors already embedded in the UV-curable system. In doing so, it is possible to exploit the advantages connected to this fast and solvent-free radiation-induced polymerization, with the sol-gel benefits, leading to the formation of structures (usually in form of thin coatings) that show interesting peculiarities, like enhanced scratch endurance, improved abrasion, heat and radiation resistance, and suitable mechanical and optical features [85].

Dual-curable formulation was used to prepare epoxy prepregs with tailored tack and drape [86]. The obtained formulation had enhanced stability during the storage which eliminates the instability as the main drawback of prepregs. The dual-curing exploited is an off-stoichiometric epoxy-amine system catalysed by two catalyst with different reactivities. Tack and drape as main parameters of epoxy prepreg were tailored by adjusting the degree of cure based on using different amount of double curing agents.

Dual-curing thermosetting systems are recently being developed as an alternative to conventional curing systems due to their processing flexibility and the possibility of enhancing the properties of cured parts in single- or multi-stage processing scenarios

[36]. Most dual-curing systems currently employed in three-dimensional (3D) printing technologies are aimed at improving the quality and properties of the printed parts. However, further benefit can be obtained from control in the curing sequence, making it possible to obtain partially reacted 3D-printed parts with tailored structure and properties, and to complete the reaction by activation of a second polymerization reaction in a subsequent processing stage. Konuray et al. [87] developed dual-curable formulations based on commercial acrylate resins for stereolithography modified with diepoxy monomer, with storage stability of up to 2 months at 32°C, making it suitable for the preparation of stable one-pot formulations. Storage stability and control of the curing sequence were achieved by means of the use of (1) a radical photoinitiator for the 3D-printing stage and (2) a latent cationic initiator based on quaternary ammonium salts stabilized with a tertiary amine for the thermal cationic homopolymerization of the epoxy resin. A latent thermal radical initiator was also added in order to maximize the degree of cure of the acrylate fraction and therefore ensure final uniform material properties. Materials with IPN structure and good compatibility between the two polymeric networks were obtained after the 3D-printing and thermal post curing process. An increase in the elastic modulus of the material was reported due to a systematic increase of the glass transition of the resulting IPNs with increasing epoxy content.

1.3. Shape-Memory Polymers

Shape-memory polymers (SMPs) are a class of actively moving polymers that are able to change shape in response to a stimulus [88]. SMPs can undergo a shape-transformation from a temporary but stable shape, programmed by deformation, to a “memorized” permanent shape. A variety of stimuli can be used to activate the transformation, such as heat, light, electric or magnetic fields, solvents, and mechanical force. The first appearance of the shape recovery effect was proposed by Vernon in 1941 in a US patent [89], describing a material with “elastic memory” that could recover its original shape upon heating. However, it was not until the 1960s, before the terminology was being used, when appeared the first applications of SMPs which consisted of heat shrinkable polyethylene tubes and films. The term “shape-memory” was officially first used in 1984 with the development of a polynorborene based SMP by CdF Chimie Company (France). Starting from the late 1980s the interest in SMPs has increased significantly. One of the reasons of this trend was the discovery of segmented polyurethane SMPs by Mitsubishi Heavy Industries Ltd. due to the versatility of urethane chemistry and its practical potential. The developments in nanotechnology and biotechnology have enabled the

use of SMPs in many applications. In biomedicine, SMPs have been applied in form of cardiovascular stents or smart sutures; deployable structures and morphing skins are used in the aerospace field and the possibility of activating the shape recovery with various stimuli (heat, electricity or magnetism) enables the use of SMPs as sensors [90–92].

The classic one-way shape-memory cycle is schematically represented in **Figure 1.3**. Starting from an original "permanent" shape obtained by conventional processing techniques, the temporary shape is obtained by means of a thermomechanical procedure. This "programming" step consists of heating the polymer to a temperature higher than the transition temperature of the SMP (T_{trans}) and deforming it by a mechanical force to the desired temporary shape. This new shape is fixed by cooling the SMP to a low temperature, lower than T_{trans}. The SMP will show its new temporary shape when an appropriate stimulus is applied. In the case of heat-triggered SMPs, the "recovery" process will be induced by reheating the SMP above its T_{trans} and, if the SMP is constrained during heating, it will exert a force instead of moving. After recovering the original or permanent shape the SMP can be re-programmed to a new temporary shape by re-applying the external stimulus.

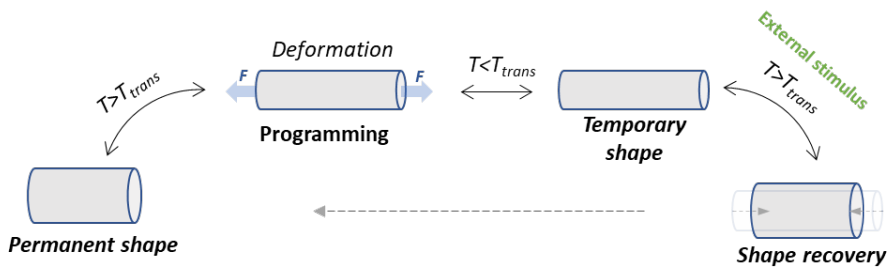

Figure 1.3. Schematic representation of a one-way shape-memory cycle activated by heating.

1.3.1. Shape-memory effect

From an internal energy viewpoint, the shape-memory effect (SME) relies upon the storage and release of strain energy by utilizing a change in entropy [90]. In the glassy state the movement of the polymer chains are highly impeded and the SMP is in a random coil conformation (highest entropy). When increasing the temperature above the transition temperature of the polymer, it acquires a rubber-elastic state, and the molecular dynamics are greatly enhanced. In this state the polymer can be easily deformed, and the polymer chains are aligned in the direction of the applied external force. Therefore, the polymer goes from an equilibrium high entropy random coil state

to a non-equilibrium low entropy aligned state. If the external force is released, the polymer springs back and recovers its original shape. However, if the polymer is cooled down while maintaining the external applied force, the recovery of the polymer chains is prohibited because of the formation of reversible secondary crosslinking points. These crosslinking points are able to fix the temporary shape when the external force is released. This non-equilibrium low entropy temporary shape will remain stable until the temperature surpasses the transition temperature of the polymer. When heated above T_{trans}, the reversible secondary crosslinking points which fix the temporary shape disappear and the strain energy stored during cooling is liberated. This energy provides the polymer the driving force to recover its equilibrium high entropy original shape. Since the SME is an entropy changes driven process, the recovery process is usually referred as entropic elasticity.

Shape-memory polymers are elastic polymer networks that are equipped with suitable stimuli-responsive switches. Two fundamental elements must be present within the polymer network: (i) molecular switches or soft phase; (ii) netpoints or hard phase. The netpoints determine the permanent shape of the polymer network and consists of covalent chemical bond or intermolecular physical interactions while the molecular switches are deformable network elements which allow the shape distortion. In block copolymers, consisting in two different polymeric phases, the domains related to the highest thermal transition temperature act as netpoints (a hard segment), while the chain segments in domains with the second highest thermal transition (T_{trans}) behave as molecular switches (a switching segment). In case of crosslinked thermosets (**Figure 1.4**), there are not two distinct polymer phases, therefore the netpoints are embodied by the covalent bonds while the polymeric chains act as the soft phase. The molecular motion of the network depends on the temperature. Below T_{trans}, the motion of the polymer chains (blue lines) is partially impeded (1) whereas above the T_{trans} the polymer chains can move freely (red lines) (2) and can be easily deformed into a new temporary shape (3). The temporary shape is fixed by the formation of reversible secondary crosslinks points (grey stripes) resulting from the vitrification (or crystallization for semicrystalline thermoplastics) of the molecular switches (4). Therefore, the transition temperature of the SMP can be a glass transition temperature (T_g) (or a melting temperature T_m). The vitrified network prevents the rearrangement of the polymer chains and the recovery of the applied deformation until the polymer is heated above the T_{trans} (5). The network in the rubbery state is free to move and the permanent shape is recovered thanks to the driving force exercised by the netpoints (black dots). So, for thermosetting SMPs the crucial role is played by the covalent bonds which memorize

the original shape and are responsible for the elastic response which drives the recovery process.

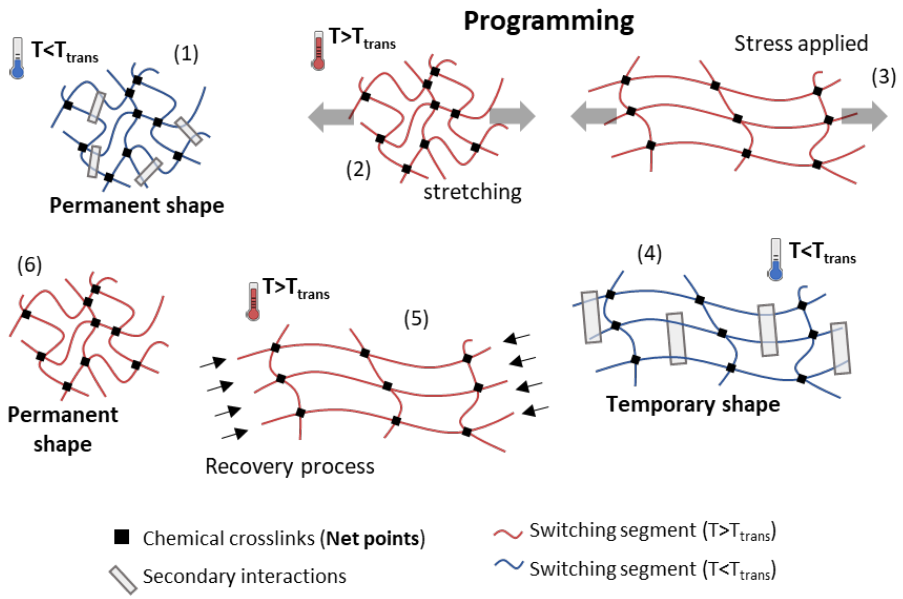

Figure 1.4. Schematic representation of the molecular mechanism of the thermally induced shape-memory effect for covalently crosslinked thermosets.

Essentially, the SME consists of a programming and recovery cycle, commonly called shape-memory cycle (SMC), that can be repeated several times and is the most important procedure to determine the shape-memory properties. Shape-memory cycling can be divided into two modules: *programming the temporary shape* and *recovery of the permanent shape*.

The *programming of the temporary shape* firstly involves a deformation step carried out at a temperature close to T_{trans}, the programming temperature (T_{prog}). Li et al. [93] classified the programming in cold (glassy region), warm (transition region) and hot programming (above the transition region) depending on where the T_{prog} is situated respect to the transition region. The main difference relies on the type of forces involved. Indeed, cold programming mainly involves energetic forces, whereas hot programming are mostly entropic forces. This results in different performances during fixation and recovery processes: cold programming leads to stress relaxation and chains friction resulting, in some cases, in irrecoverable structural damages, negative affecting both fixation and recovery processes. Contrariwise, hot programming leads to more efficient and homogeneous recovery processes but lower stress/strain limits during the

deformation step. Finally, warm programming combines both, energetic and entropic forces due to the viscoelastic response of the network at the vicinity of T_{trans}. Yakacki et al. [94] and Rousseau et al. [95] found that at a certain temperature below T_g related to the onset point of the modulus drop in thermo dynamic-mechanical analysis (the onset temperature $T_g^{E'}$), the stress/strain limits are three-to-five times enhanced in many polymeric materials. Nevertheless, warm programming also promotes stress relaxation and viscous friction between the chains that may worsen the recovery performance. Belmonte et al. comprehensively studied the influence of T_{prog} on both programming and recovery processes of thiol-epoxy shape-memory thermosets: the shape-memory response for a specific operational design can be optimized by choosing the correct programming conditions and accurately designing the network structure. When programming at a high temperature ($T>T_g$), under high network mobility conditions, high shape-recovery ratios and homogeneous shape-recovery processes are obtained for the network structure and the programmed strain level. However, considerably lower stress and strain levels can be achieved. Meanwhile, when programming at temperatures lower than T_g, considerably higher stress and strain levels are attained but under low network mobility conditions. After the deformation step, the temporary shape is stabilized by cooling down the network below T_{trans}. In order to avoid any effect of aging behaviour and effectively fixate the temporary shape, high cooling rates are strongly required [96,97].

The *recovery of the permanent shape* can be carried out in three different conditions: unconstrained, partially constrained and fully constrained.

Although SMP are predominantly employed under partially and fully constrained conditions (i.e., in chirurgical stents their action is aimed to the blood vessel expansion or in actuators like open-valve systems a work releases is needed), unconstrained (free-recovery) experiments are important to characterize the genuine shape-memory behaviour.

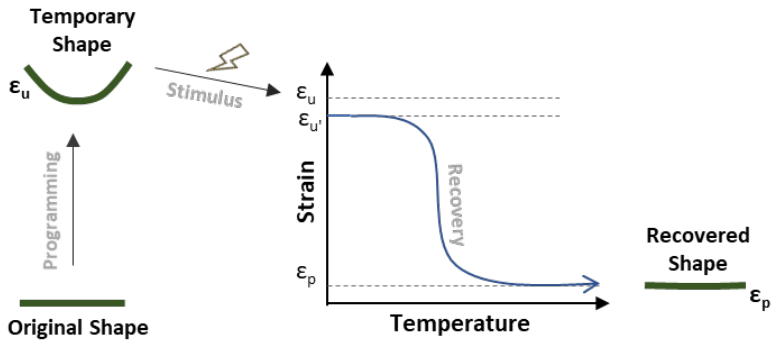

Figure 1.5. Idealized scheme of unconstrained recovery process.

In **Figure 1.5** a conventional unconstrained recovery experiment is represented: the sample in its original shape is deformed to a level of strain ε_u which depends on the applied load. Generally, SMPs are able to retain almost the 100% of the ε_u, and the fixed deformation is indicated as $\varepsilon_{u'}$. After the application of the external stimulus (heating) the sample is able to freely recover the shape; this recovered shape may suffer a permanent strain (ε_p) related to plastic or irrecoverable deformation. Commonly, high performance SMPs, under adequate programming and recovery conditions, result in minimum irrecoverable deformations with $\varepsilon_{u'} \approx \varepsilon_u$. The dynamics of the relaxation mechanism are widely acknowledged as the key factor controlling the free recovery process; it is responsible of the entropic change behind the SME. For this reason, many researchers demonstrated the close relation between the network structure and the unconstrained performances by obtaining tailored free recovery behaviours varying network design and properties (i.e., T_g, homogeneity and crosslinking density) [98–100].

Partially constrained recovery experiments consist in an external force (F_{rec}) or stress (σ_{rec}) applied to the SMP while it is trying to recover the original shape (**Figure 1.6**). The SMP struggle against the stress applied resulting only in a partial recover of the shape but a work output is generated. The work generated during the recovery depends on the stress applied and on the amount of deformation the SMP is able to recover when acting against the stress [101].

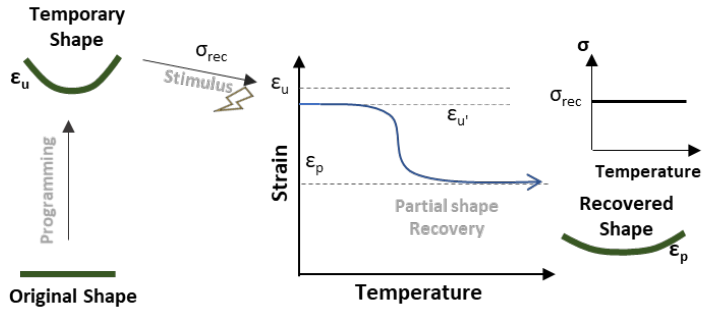

Figure 1.6. Idealized scheme of partially constrained recovery process.

Few studies have focused on the effect of the SMP structural properties on σ_{rec} in the constrained or partially constrained recovery process in comparison with under unconstrained conditions. Santiago et al. [101] studied the influence of the network mobility with the recoverable strain in partially-constrained conditions using hyperbranched-modified epoxy-based SMPs. While the observed trend for the recoverable strain was like Yakacki et al. [102], the decreasing trend in recovery ratio was found to be more pronounced in formulations with more hyperbranched polymer and lower network mobility.

During fully constrained recovery scenarios the recovery of the shape is impeded and the capability of the SMP to generate a recovery stress can be tested. This scenario is generally used to investigate the upper limit capability of the SMP as mechanical actuator. In **Figure 1.7** the fully constrained experiment is schematized. The limit of actuation capability of the SMPs strongly depends on the programming conditions since it is a direct consequence of the energy stored when the sample is programmed. Therefore, it was found that the recoverable stresses are directly proportional to the rubbery modulus which, in turn, is directly proportional to the crosslinking density according to the rubber elasticity theory [42,98]. The explanation can be found in the nature of the forces driving the shape recovery. The recoverable stress is dominated by thermodynamic driving forces attempting to recover the lowest achievable network entropy state, dictated primarily by the shape formed during polymerization. Networks with higher crosslinking densities have larger driving forces to return to their lowest entropy state according to the theory of rubbery elasticity [98].

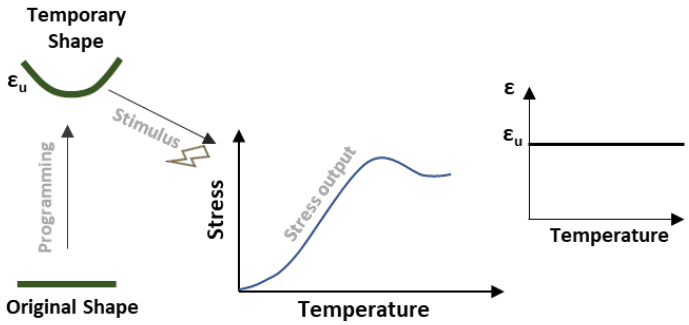

Figure 1.7. Idealized scheme of fully constrained recovery process.

Arrieta et al. found that the ideal conditions to improve the stress generation with the less damage for the network structure are low fixation temperatures, well below the T_{trans}, together with high cooling rates, increasing the pre-strain without being too close to the strain at break limit and reducing the stress relaxation in all the programming steps. Moreover, Belmonte et al. found an increase of the stress generated increasing the crosslinking density of off-stoichiometric thiol-epoxy dual cured SMPs [103].

1.3.2. Classification of shape memory polymers

SMPs can be classified into four different classes depending on their chemical structure and transitions temperatures [104].

Covalently crosslinked glassy thermosets. This class of SMPs consists of covalently crosslinked networks with a glass transition temperature T_g as T_{trans}. They show high degree of shape fixity due to the high modulus at the glassy region and a high degree of shape recovery due to an excellent rubber elasticity at the rubbery region and the absence of chain slippage. Epoxy-based SMPs and acrylate-based SMPs are the most common examples of this class of SMPs. Epoxy-based SMPs are widely used for their excellent mechanical properties, electrical insulation, chemical resistance and thermal stability. The major drawback is their inherent rigidity which limits the programming process. To overcome this limitation, flexible elements can be introduced in the network structure by crosslinking agents with long aliphatic chains [105]. The deformation limits are also improved but the ultimate strength is reduced. Another approach relies on warm programming at $T_g^{E'}$ without directly acting on the network structure.

Epoxy based SMPs can be obtained by curing with differently crosslinking agents. A lot of shape-memory studies were performed on epoxy-amine thermosets [106–108]. Curing with amine compounds results in tough SMPs with high glass transition temperatures that can be addressed to aerospace deployable structures [108]. In our group, epoxy based SMPs have been obtained curing with multifunctional thiol agents

in order to obtain SMPs with considerably increased ultimate strain without significant losses in terms of mechanical strength. High level of actuation were obtained working on the network structure and the programming conditions and high potentiality mechanical actuators have been developed [42,100,103]. Acrylate-based SMPs have attracted a lot of interest due to their high degree of biocompatibility, which make them suitable for biomedical applications [109,110]. The primary backbone of acrylate-based shape-memory networks are formed through free radical polymerization of crosslinking monomers and pendant segments formed by mono-functional chain builder monomers.

Covalently crosslinked semi-crystalline thermosets. This class of SMPs are covalently crosslinked polymers with a melting temperature T_m as T_{trans}. This class is characterized by a high dependence of the shape-memory properties on the degree of crystallinity and the crosslinking density. They exhibit a one-way SME, as well as the glassy one, due to the covalent nature of the crosslinks. The SME is based on a first-order transition leading to faster recoveries than the glassy SMPs [104]. In this class of SMPs the switching unit consist in the crystalline domains, which are responsible of the shape fixation, while the netpoints are still the covalent bonds. Semi-crystalline rubbers are the most common example of this SMPs. This class includes bulk polymers, such as semi-crystalline rubbers, LCNs and hydrogels with phase separated crystalline domains. Examples include the chemically crosslinked trans-polyisopropene, polycycloctene-based polymers and poly-(ε-caprolactone)-based polymers [111,112].

Physically crosslinked glassy copolymers. In this case the network is made of, at least, two different segregated phases: a hard segment, acting as netpoints, and a soft segment which acts as molecular switch. The transition temperature of the hard-segment (T_{perm}) can be either a melting temperature (T_m) or a glass transition temperature (T_g). The temporary shape is obtained by deforming the SMP at a temperature $T_g < T < T_{perm}$, in which the soft-segment is in a rubbery state and is fixed by cooling to $T < T_g$. The glassy domains of the soft phase formed during cooling prevent the rearrangement of the polymer chains. Due to the absence of chemical crosslinks, they show lower shape-memory performance but when the temperature surpasses the transition temperature of the hard segment (T_{perm}) the SMP flows and can be reshaped [104]. Amorphous polyurethanes represent the majority of this class of SMPs [113,114].

Physically crosslinked semi-crystalline block copolymers. They are similar to the physically crosslinked glassy copolymers, though they have semi-crystalline switching domains and the melting temperature of the soft phase act as T_{trans}. The temporary shape is programmed when the soft phase is in the molten state and then fixed upon cooling by the recrystallization of the soft phase domains. Their main drawback is that on optimized behaviour is only achieve after several shape-memory prior to utilization. Moreover, significant irrecoverable deformations are generated during the first cycles

due to the high chain mobility. Semi-crystalline polyurethane-based SMPs represent the most common examples of this class of SMPs [115,116].

In present work a new SMP belonging to the chemically crosslinked glassy thermoset group has been obtained by dual-curing procedure and the SME was extensively characterized under unconstrained, partially constrained, and fully constrained conditions as it will later presented in Chapter 5.

1.3.3. Shape-changing polymers

Shape-changing polymers (SCPs) are another class of actively moving polymers which are able to reversibly change their shape while an appropriate stimulus is applied. According to the definitions gave by Behl and Lendlein [117], SCPs change their shape gradually, (i.e., shrink or bend), as long as they are exposed to a suitable stimulus. This motion is reversible, and the geometry of the new shape is limited by its original three-dimensional shape. As an example, in liquid crystalline networks (LCN) the shape-changing capability (**Figure 1.8**) is activated by applying and external load at high temperatures (higher than the clearing temperature of the mesogens). Then, upon cooling below the T_{trans}, the stress applied promotes the alignment of the mesogenic domains which results in the macroscopic elongation of the sample. Heating up the sample above T_{trans} leads to a recovery of the elongation owing to the disordering of the LC domains and the elastic response of the crosslinked network. The shape-changing remains active as long as the load is applied. A similar mechanism is obtained for light-responsive molecules, such as azobenzene, coupling small scale deformations and light exposure [118].

Essentially, SCPs present a single and reversible shape transformation in response to a stimulus (i.e., thermomechanical and photomechanical stimuli) which is limited to their network structural architecture (fixed geometry), whereas SMPs can adopt different shape-transformation protocols, with higher freedom degree motion, in response to a stimulus (i.e., heat or UV-light), but a shape programming procedure is required each time.

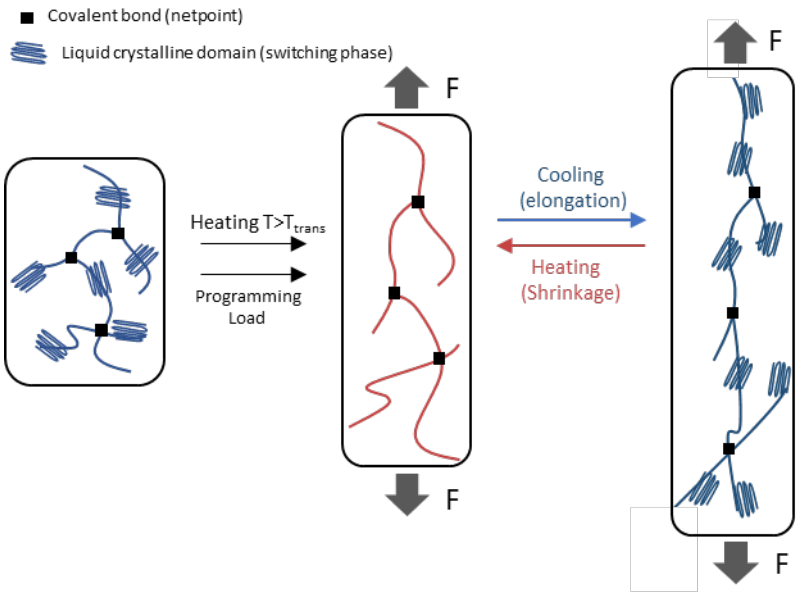

Figure 1.8. Scheme of the shape-changing mechanism in thermoresponsive liquid crystalline network.

Among the different SCPs, liquid crystalline elastomers (LCEs), or liquid crystalline networks (LCN), are the most common class. A LCE presents segregated ordered phases made of rigid-rod moieties, also called mesogens, which arrange themself in a side by side ordered structure, forming several locally aligned LC domains surrounded by an amorphous phase [119]. The main liquid crystalline classes are: (i) nematic, in which the mesogens are ordered along one direction; (ii) smectic, in which several stacked layers made of ordered mesogens are present; (iii) cholesteric, where the aligned mesogens are organized in layers, but with a different orientation in each one of them. In addition, they can be also classified by their position with respect to the polymer backbone. In this case two main class can be found: If the mesogen is part of the polymer backbone, then a main-chain LCE is formed. Instead, if the mesogens are grafted to the backbone, the resulting LCE is classified as a side-chain polymer. Different kind of LCNs for both classifications are illustrated in **Figure 1.9**. Moreover, side-on or end-on bonding is possible, depending on how the mesogens are connected to the backbone [120]. The polydomain structures described above present a percentage of orientationally ordering measured by the ordering parameter (S), that considers an orthogonal axis to quantify the degree of orientation of the domains in respect to this axis within the network. Upon stretching the LCN along the axis director, the LC domains are oriented and aligned increasing S and promoting large deformation processes with minimal force. This

process is called soft elasticity and refers to the ability of the polymer to be stretched at near zero-stress [121]. During this process, there is a transition from a polydomain to an oriented monodomain structure, P-M transition, that begins at a critical strain level which depends on the structural properties of the LCN (crosslinking density, chains mobility, the structure of the mesogenic units and the configuration of the mesophase) and is enhanced at high strain levels [122]. The mechanical and thermal behaviours are influenced by the LC domains. The strength to fracture and plastic deformation are increased thanks to the presence of liquid crystallinity. Moreover, tuning the curing conditions, applying a mechanical stress, a magnetic or an electric field, it is possible to act on the LC domains organization.

From a thermal point of view, LCNs exhibit two different characteristic temperatures. The first one, usually occurring at lower temperature, is the glass transition (T_g), at which the amorphous structure changes from glassy to rubbery. The second one, typically at higher temperature, is relative to the isotropization transition (T_{iso}), where the ordered liquid crystalline (LC) arrangement is lost and the material becomes “isotropic”, resulting in a homogeneously disordered matrix. Upon cooling, a transition from an isotropic to anisotropic organization (reordering in LC domains) occurs at a characteristic anisotropization temperature (T_{aniso}), which do not necessarily match the T_{iso}.

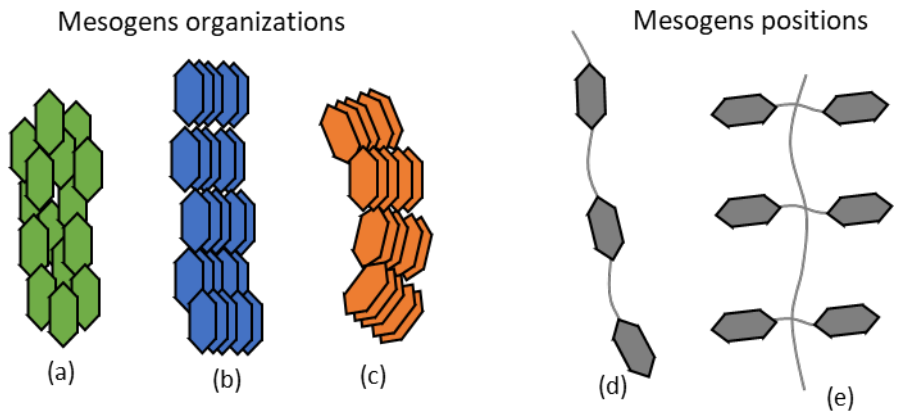

Figure 1.9. Schematic representation of (a) nematic, (b) smectic and (c) cholesteric arrangements of the mesogens. Different position of the mesogens units: (d) main-chain; (d) side-chain.

LCEs show excellent mechanical and physical properties, such as high fracture toughness, high moduli when oriented, low moisture adsorption and good thermal behaviour, properties that are not observed in materials like amorphous or semi-crystalline polymers [123]. In particular, epoxy based LCN presents excellent properties

suitable for high performance applications [124]. They are commonly lightly crosslinked elastomers produced by curing an epoxy monomer, usually having a stiff structure, with carboxylic acids having flexible aliphatic backbone[125,126].

The shape-changing capability (SCC) of LCNs relies on two main phenomena: the macroscopic changes in volume produced by the ordering/disordering of the LC domains and the soft elasticity which allows large deformations with minimal forces. The combination of these phenomena can be exploited to obtain large recoverable strains under the appropriate external stimulus. In thermoresponsive epoxy-based LCN the isotropization of the mesogens units can be triggered by the appropriate thermomechanical stimulus. If an external force is applied during the anisotropization (upon cooling), a stress-aligned LC phase is formed, leading to a highly oriented monodomain structure promoted by the soft elasticity phenomenon. This results in a large macroscopic deformation along the stress director. Subsequently, heating above the T_{iso} cause the disordering of the LC domains and an elastic shrinkage promotes the recovery of the pre-deformed shape [127]. The induced-elongation strongly depends on the topographical configuration of the network and the liquid crystallinity [128,129]. On the other hand, since the crosslinks are responsible of the elastic shrinkage, the crosslinking density is a crucial parameter for mechanical stress generation [130].

1.3.4. Shape-memory polymers applications

In the last decades SMPs have been exploited in a large variety of commercial and industrial applications. Together with the ability to respond to a stimulus, they possess many advantages compared to traditional materials: “soft” nature, the light weight, low cost and large deformation and tailorable properties. Moreover, the large research efforts aimed to adjust the chemical structure design to the desired application have significantly broadened their field of application.

The availability of biocompatible and biodegradable shape-memory polymers has favoured their extensive use in the biomedical field which count numerous examples of materials and devices with the regulatory approval for use. One of the first example of biomedical applications was reported by Lendlein et al. in 2002 [131]: a shape-memory PU monofilament in slack state that was used to suture wounds. When the temperature reaches the body temperature the filament returns to its original shape closing the wound. The SMP was also biodegradable. In recent years SMP staple were developed in order to meet the increasing use of staplers as surgical tools in minimally invasive surgery. A shape memory material staple is able to shrink to fit the exact thickness of the tissue, so that only one sized staple is required, and to provide gentle force to close

the wound. Self-tightening staples were obtain using a commercial biodegradable PLA [132]. A significant amount of research (both preclinical and clinical) has been conducted on SMP cardiovascular devices. For this devices research effort were addressed to the replacement of shape-memory alloys, such as Nitinol which are not biodegradable. Instead of introducing new materials, new ways to trigger SME in biomedical materials was preferred to simplify the R&D process [132]. The Igaki-Tamai SMP biodegradable stent [133] received approval for human use in peripheral vascular applications in 2007 (approval in the European Union only). The stent was reported to be capable of continued expansion over a 3-month time period at body temperature and in response to physiological remodelling of the target vessel. Other example are a triple shape-memory polyurethane that was used to develop an instant retractable stent [134]. Moreover, polymer membrane stents capable of drug eluting were developed to effectively prevent tissue in-growth and infection [135,136]. In addition to stents, numerous cardiovascular-related technologies have been under development utilizing SMPs. Research has been conducted by the authors into SMP aortic valves. These valves utilized the PEEK Altera material for both a mechanically deployable valve base and leaflets. Finally, applications are found in more specialized fields, such as orthopaedics (high strength SMPs can serve to heal the anterior cruciate ligament), tissue engineering (SMP scaffolds to treat cranio-maxillofacial defects) or prothesis (biodegradable and self-deployable SMPs are used for minimal invasion when inserting the prothesis) [137,138].

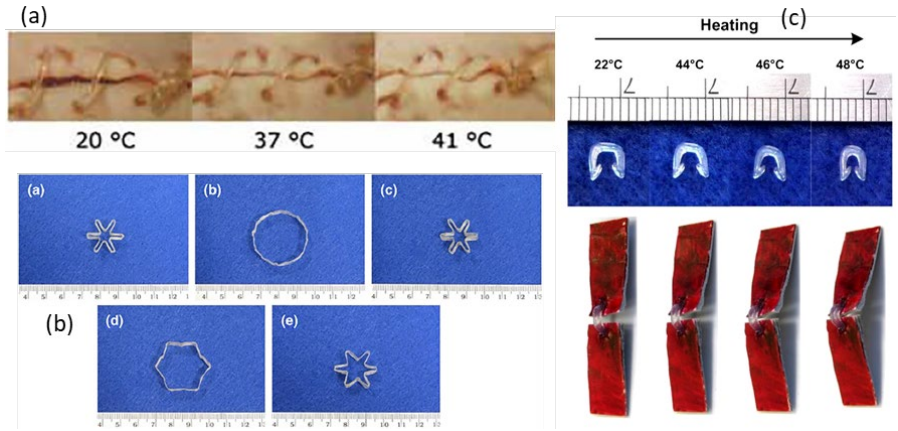

Figure 1.10. (a) Wound closure biodegradable shape-memory polymer by Lendlein et al. [131];(b) instant retraction property of a polyurethane SMP stent [134]; (c) Self-tightening staple based on shape memory PLA bringing two pieces of tissue closer [132].

In aerospace applications SMP and their composites are interesting because of the combination of their properties and their light weight. They are widely used for deployable structures with a different applicability [139]. There are a variety of applications of SMP/SMPC on space structures, such as trusses, radiators, and solar arrays which also underwent to spaceflight experiments. Composite Technology Development Inc. [140] has produced a shape-memory hinge, called elastic memory composite (EMC) hinge, for the deployment of reflectors, radiators, and solar arrays [140]. The EMC hinge is composed of four parts, two carbon-fibre EMC parts with internal heaters and two end-fittings for attachment to the Device body. An EMC hinge experiment was tested on the ISS and was composed of six hinges. The ISS crew deployed these hinges with 7 W over 5 minutes and monitored the deployment accuracy. More recently, Yakacki et al. demonstrated the possibility to reverse the deployment of aircraft pieces with a small airplane origami made of free-standing bidirectional SCPs (stress-induced LCEs), 3D printing and printed electronics [141]. The LCE was obtained through dual-cure of thiol-acrylate systems and the stress-induced was achieved by pre-stretching the LCE in the intermediate stage. 3D printing was used to build up a soft substrate and pattern the silver wire on it. Afterwards, the stretched LCN was anchored to the soft substrate and the airplane device mounted piece-by-piece. Upon heating, the airplane morphs due to the bending of the soft actuators and upon cooling it goes back to the original flat shape. In the same study, other smart structures were presented, from a crawling strip to a folding box always based on an LCN moving element.

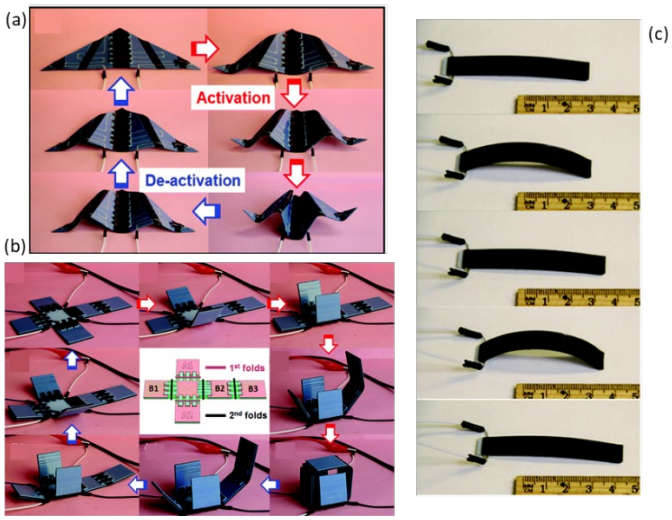

Figure 1.11. (a) activation and deactivation process of an LCN assisted morphing wing; (b) Folding and unfolding LCN assisted of a deployable box; (c) LCN based soft crawler locomotion [141].

SMPs-based flexible electronics has become an attractive area of research. SMPs are flexible and can be combined with electronic devices as the substrate maintaining their properties after multiple programming-recovery cycles, a crucial characteristic for wearable devices. Liu et al. developed a transformable smart energy harvester and self-powered mechanosensation sensor based on a SMP. The device is based on the mechanism of a flexible triboelectric nanogenerator using the thermally triggered shape transformation of organic materials for effectively harvesting mechanical energy [142]. SMPs can also work as information carriers, without additional electronic elements. Li and co-workers [194] combined different Morse codes in one epoxy-based SMP composites. The epoxy substrate was divided into four separate areas containing Fe3O4, CNT, p-aminodiphenylimide, and neat epoxy polymer. Each Morse code had its corresponding embossed area, and the stimulus under UV light, electromagnetic, and radiofrequency fields activated the corresponding areas according to the embedded material [143].

1.4. Shape memory actuation

1.4.1. Activation methods of shape-memory polymers

Although most of the SME are based on thermal transitions, other types of activation mechanism can be exploited. Heating in air is standard for many applications; however, using an aqueous environment allows for faster recovery due to enhanced heat transfer. Thermal activation can be relatively fast but requires an appropriate heat or energy source nearby and an efficient heat transfer. The SME activation can be slow down by the distance between the transition temperature and the testing temperature. Moreover, in case of external heating, the environment has to be heated up in order to activate the SME which is time and energy consuming.

Different alternatives to thermally activated SME by temperature exchange can be found. On one side, another stimulus, such as light, magnetic field or electrical current can be used to increase the temperature and trigger the thermal transition. On the other hand, athermal activation methods such as solvent-induced or light-induced mechanism can be exploited. In both cases, the use of functional fillers and SMPC have become popular. The functional elements within SMP nanocomposites not only provide an opportunity to improve the strength and modulus of the material, but can also be utilized to impart the materials with stimuli-responsive characteristics [144].

The most investigated alternative activation is the photo-induced SME which is based on certain molecular structures that change their configurations upon irradiation to

specific wavelength. For example, cinnamic acid, which undergoes to reversible dimerization, or azobenzene molecules, which undergo to cis-trans isomerization upon irradiation, can be exploited to obtain light-responsive SMP [145,146]. Solvent-induced SME is showed by the so-called chemo-responsive materials, materials capable to respond at chemical signals. The absorbed solvent molecules of the chemo-responsive SMP enable shape recovery at a significantly lower temperature with disrupting intermolecular hydrogen bonds, plasticizing, and reducing the T_g. This activation mechanism is of particular interest in applications where the material is immersed in an aqueous medium or exposed to humid climate. The most common example are polyurethanes that response to water, ethanol or other chemical solvents [147].

As mentioned before, various type of fillers can be used to enable different ways of SME activation. Polyvinyl alcohol (PVA) reinforced with graphene oxide (GO) can exhibit water induced SME. The hydroxyl group of hydrophilic PVA exhibited high affinity with water molecules which could weaken the primary hydrogen bonding of the PVA/GO composites [148].

Functional fillers are also used to enable alternative triggering stimuli in thermal transition based SMP. Besides the activation is based on a thermo-induced SME, fillers or other functional elements provides an alternative way to heat the SMP, consequently, a classical thermally-activated SMP can be turned into other stimuli-responsive material. This approach can be also used to provide an internal heating source exploiting well known physical effects, such as Joule heating, photothermal heating or magnetic-induced heating, leading to efficient activation independent from external heat sources. The photothermal effect of nanoparticles, such as gold nanoparticles, GO or carbon nanotubes (CNTs) can be used to absorb light energy and transform it into heat, thus, activating the SME [144]. The absorbing microwave materials are able to absorb microwave energy and to transform it into thermal energy by means of molecular friction and collision [149]. CNTs, silicon carbide (SiC), ferroelectric nanoparticles and water molecules can be used as microwave energy absorbers to prepare microwave-induced SMP nanocomposites [144]. Magnetic nanoparticles, such as Fe_3O_4, can be used as inductive heaters in order to produce magnetically sensitive shape-memory polymer nanocomposites. Bai et al. used super-paramagnetic iron oxide nanoparticles (SPIONs) as macromolecular network crosslinking points and magnetic-inductive heating elements to construct norbornene-based magnetically sensitive nanocomposites [150].

1.4.2. Electric control of the actuation

Electro-responsive materials can be obtained by combining thermally triggered SMP with some kind of conductive element. When the latter is activated by an electrical current, the amount of heat required for the SME activation is generated by Joule heating. This thermoelectrical effect is a process in which the flow of an electric current through a conductor produces an amount of heat proportional to its resistance and the square of the current intensity. The electric conductivity of the heating element is important but, to facilitate and promote a fast recovery, the thermal conductivity of the SMP is also crucial. For this reason, in light of the thermal insulator character of polymers, efforts to increase the thermal conductivity of the SMP are commonly associated to electroresponsive actuation.

Different types of conductive elements can be found in literature: from conductive wires to conductive fillers, passing through conductive fibres and conductive layer patched on the SMP surface.

The deployable or crawling devices developed by Yakacki et al. mentioned in the previous section, were activated by Joule heating of a 3D printed silver ink wire printed on the tangoblack substrate. The preprogrammed LCN moving element was then placed onto the actuator structure. The movement is than triggered by turning on and off the power source (**Figure 1.12**).

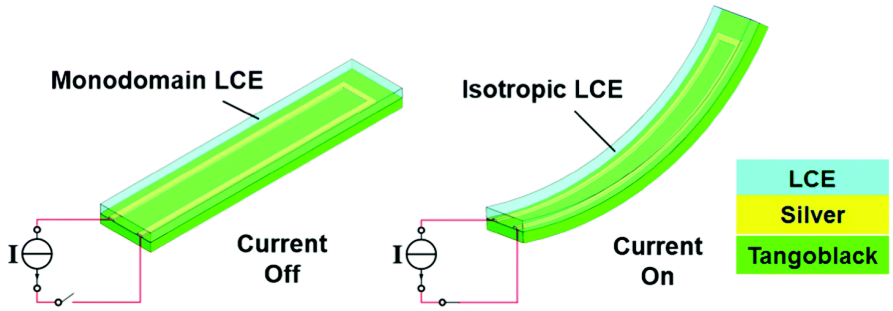

Figure 1.12. Illustration of the electrical activation (right) and deactivation (left) of the printed actuator developed by Yakacki et al. [141].

Quadrini et al. [151] developed a SMPC laminate with an embedded heater. The laminate was obtained by stacking alternative layer of Carbon fibres reinforced plies (CFR) and SMP epoxy foam. The heater was placed in the mid-plane immersed between two SMP layer (**Figure 1.13**). In this case, the conductive element was an actual layer consist of a micro-heater circuit encapsulated between two layers of polyimide film.

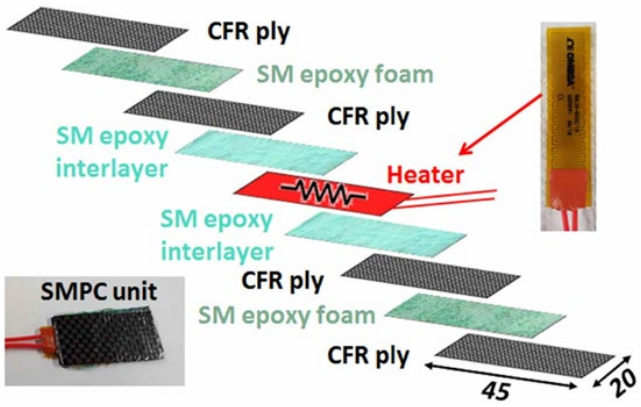

Figure 1.13. Layer configuration of the electroactive SMPC laminates developed by Quadrini et al. [151].

Self-assembled layer of carbon nanofibers (CNF) nanopaper coated on an epoxy based SMP were also used to obtain electroresponsive composites. In particular Lu et al. developed a functionally graded nanopaper by self-assembling CNF and Boron Nitride (BN) on a thermoresponsive epoxy SMP (**Figure 1.14.a**). The BN layer was added to enhance the thermal conductivity of the assembly, allowing a more efficient heat transfer between the conductive CNF layer and the SMP layer [152]. Another interesting way to impose electroresponsive capability to classical thermo activated SMP was proposed by Wang et al. [153]: spray deposition modelling (SDM) technique was develop to fabricate CNT/ SMP composites with desirable self-heating and actuation properties (**Figure 1.14.b**). A CNTs layer of controlled shape and thickness was deposited on SMP polyurethane obtaining a resistive heating-based SME without the need of external heating.

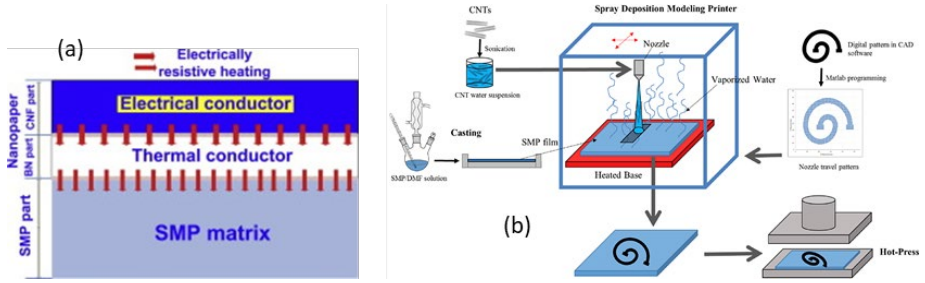

Figure 1.14. (a) Schematic illustration of the functionally graded and self-assembled CNF and BN in nanopaper for electrical actuation of SMP nanocomposite [152]; (b) Schematic of the fabrication process of CNT/SMP nanocomposites developed by Wang et al. [153].

In addition, a common way to obtain the electro activation is providing electrical conductivity to the SMP itself. Conductive fillers can be dispersed in an appropriate SMP matrix in order to significantly increase the almost null intrinsic electrical conductivity of the matrix. In order to achieve the Joule heating various functional fillers were used: CNTs [154], TiO_2 whiskers [155], graphene nanoplatelets (GNP) [156] and aligned Nickel particles [157]. Most of these fillers present also a high thermal conductivity leading to additional beneficial effects in terms of heat transfer through the sample. However, the filler approach presents a major drawback related to the high amount of filler required to reach the percolation threshold. In order to obtain an effective increase of electrical conductivity percolation is crucial because it means that a continuous conductive path made of filler particles is obtained. The high viscosity associated with the high amount of filler can result not only in no homogenous filler distribution but also in difficulties in processability and imperfect transfer of the fillers properties to the SMP matrix. For this reason, conductive layer approach seems to be more efficient and easier to manufacture. In this approach, a crucial aspect is the low thermal conductivity of the SMP which needs to be enhanced in order to obtain fast actuation and to avoid any issue at the interface between the layers.

In Chapter 7 of present work, an electroresponsive SMC has been developed taking advantage of the dual-curing procedure of thiol-epoxy-acrylate SMP to incorporate a conductive layer between two SMP layers. The electro-activation advantages were pointed out by comparing the shape memory performances with those of the same SMP but thermally activated.

1.4.3. Free-standing actuation

LCNs present bidirectional (two-way) actuation when the LC domains are stress-aligned under external mechanical load. Moreover, the SCC is limited by the original three-dimensional configuration of the network structure and the direction of the applied stress, in most cases leading to simple unidirectional motion mechanisms. To overcome this drawback, the most common approach is the incorporation of an elastic component into an already stretched LCN, thus, impeding the LCN shrinkage during the isotropization, but adopting a metastable state-of-ease shape, that is further recovered due to the stress generated in the elastic component [158,159]. The combination of a shape-changing element, that is the LCN, and a stress-applying elastic element can result in a free-standing bidirectional actuation driven by the isotropization of LCN. The “stress-applying” component can be internally incorporated through the crosslinking of

a new network structure or externally incorporated by embedding an elastic matrix onto the stretched LCN. Dual-curing processing represent a valuable tool in both approaches.

As reported in section 1.2 a dual-curing processing allows to obtain two networks, simultaneously or sequentially, by the combination of two compatible reactions. The formation of each network can be controlled autonomously and by a different reaction activation stimulus. In view of this, the internal incorporation (**Figure 1.15**) is achieved by curing an initial LCN network that is further stretched inducing the P-M transition towards high strain levels. If the imposed deformation is maintained during the formation of the 2nd elastic network, the already stretched LC network is physically and, in some cases, covalently interlaced with the new elastic network. Triggering the LC transition of the LCN in the resulting polymer will cause disorder of the LC domains, leading to a contraction of the elastic network (energy storage), to further promote the formation and stress-alignment of the LC domains through the elastic recovery of the contracted elastic network (energy release). Meng et al. [160] achieved 15% of uniaxial free-standing actuation via internal incorporation: a semi-crystalline poly(ε-caprolactone) network was partially cured (1st curing stage), stretched up to 650% of strain and stabilized by UV-crosslinking (2nd curing stage). The photo-crosslinked network was the responsible of generating the stress due to the elastic response during the LC transition. Yakacki & co-workers [161] enhanced the actuation up to 110% by using dual-cured "thiol-acrylate" networks with crosslinks of different functionality.

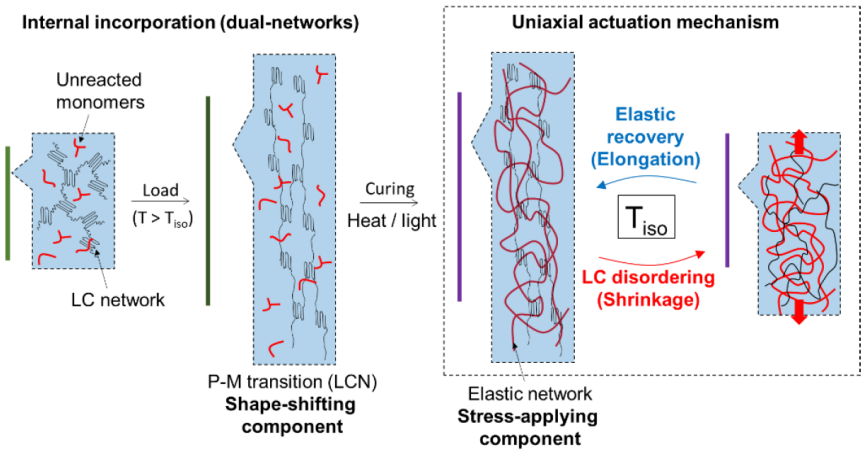

Figure 1.15. Scheme of the free-standing SCE obtained via internal incorporation of a stress-applying component: molecular view and macroscopic mechanism.

The external incorporation (**Figure 1.16**) can be carried out taking advantage of any material able to guarantee an elastic response during the LC transition of the LCN. Glassy

thermosets with a T_g below the LC transition of the LCN or even metallic plates have been proposed as stress-applying component. A sandwich configuration, made of the stretched shape-changing LCN embedded in two layers of elastic component, ensure the mismatch between both, the LCN and the matrix itself, causing the free-standing bidirectional actuation. The first external incorporation was reported by Westbrook et al. [162] who achieved a transversal free-standing bidirectional actuation of about 10% of the initial length of the actuator. The external incorporation of an elastomeric matrix onto a stretched poly(cyclooctene)-based LCN was carried out through direct thermal curing of the matrix over the LCN, thus, strong physical-bonding of the new network onto the LCN surface was achieved. Recently, Belmonte et. al [163] developed a free-standing thermally-triggered "two-way" shape-memory actuators by external incorporation using glassy thermoset (GT) films to "sandwich" a previously programmed LCN film. The GT was obtained via dual-curing, thus enabling the development of complex actuator configurations exploiting the intermediate stage processing window. A compact and resistant design was obtained thanks to the strong adhesion between layers ensured by the final curing stage of the GT. The results showed the capability of these actuators to bend and unbend under various consecutive heating–cooling procedures in a controlled way. The maximum deflection can be modulated through the configuration and the LCN stretching level, showing an excellent fitting with the model predictions. This approach enabled the design of free-standing two-way actuators covering a range of bending actuation from 27 to 98% of the theoretical maximum deflection.

Overall, the internal incorporation depends on the compatibility and interaction between the networks, thus, structural properties at molecular level such as crosslinking density and network mobility influence the actuation performance. Moreover, the actuation process is defined through the molecular design of the network: mechanically asymmetric network architectures are used to produce two- or three-dimensional changes. In contrast, the external incorporation is highly affected by the adhesion and interaction between the faces of the LCN and the elastic component, hence, macroscopic changes such as thermal expansion strongly affects the actuation performance. In this case, two and three- dimensional volume changes are attained by the configuration of the device.

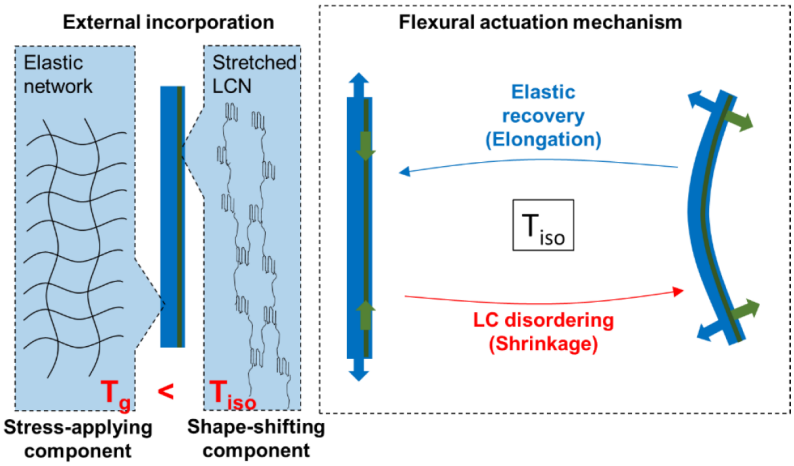

Figure 1.16. Scheme of the free-standing SCE obtained via external incorporation of a stress-applying component: molecular view and macroscopic mechanism.

Another approach to achieve free-standing bidirectional motion consists of semi-crystalline networks with two crystalline domains or confined crystalline domains interacting each other to produce reversible shape-changes. Zharinova et al. [164] reported free-standing bidirectional actuation in water-blown polyurethane foams. The broad crystallization process in these systems permits the separation of the crystalline segments in actuation segments and skeleton segments by fixing the temperature within the transition range. The actuation segments contract upon heating, whereas skeleton segments remain unchanged, thus, interact with the actuation segments and generate the required stress to promote the induced-elongation upon cooling.

In Chapter 8, a similar approach to the one developed by Belmonte et al. [165,166] was proposed to develop a free-standing reversible actuator driven by electric current in. A LC epoxy monomer was synthetized and crosslinked with carboxylic acid in order to obtain a LCN network with a T_{iso}/T_{aniso} compatible with electro-activation.

1.5. Thermosetting adhesives

1.5.1. Adhesive bonding

Adhesive bonding is a method by which materials can be joined to generate assemblies. It represents a valuable alternative to traditional mechanical joining methods, such as nailing, screwing, and riveting. The adhesion phenomenon is defined as the phenomenon by which the adhesive is able to transfer the load from the adherends to the adhesive joint [167]. With respect to mechanical bonding, adhesive joints do not

exhibit high stress concentrations, so the properties of the adherends can be fully utilized. Besides, larger area of contact between the adherends and the adhesive is required to bear the same load of a mechanical fastener. Due to the polymeric nature of the adhesive, adhesive joints provide good damping properties which also enable to have high fatigue strength [168]. Adhesives are widely used in aerospace industry due to the ability of adhesives to not only form a joint but also to seal the assembly in one step. Moreover, corrosion issues are overcome with polymeric adhesion allowing to adhere galvanically dissimilar materials. These advantages resulted in the wide industrial use of adhesive joints. They are widely used in aerospace and automotive industries also thanks their light-weight character. They were extensively used in the wood products industry, although in recent years the research efforts are addressing to replacing synthetic adhesives (formaldehyde-based in particular) with more sustainable solutions. Electronics and microelectronics industry also use adhesives widely for the construction of integrated circuits and the manufacture of electronic devices.

Adhesive bonding is also associated to some disadvantages that leave room for more technological research and development. It is necessary to reduce the peel and cleavage stresses because they concentrate the load in a small area giving poor joint strength. They have limited resistance to extreme temperature and humidity conditions due to the polymeric nature of the adhesive. And, finally, the bonding is usually not instantaneous which requires the use of tools to maintain the substrates in position.

1.5.2. Factors influencing the adhesive performances

The adhesive behaviour is affected by several factors associated to both intrinsic adhesive properties and joint design aspects. Among adhesive material properties the Young modulus of the cured adhesive and the viscosity of the uncured mixture are the most relevant. Although different behaviour is obtained varying the adhesive modulus, an improved behaviour can be obtained for the different values of modulus acting on the joint design [169]. Moreover, mixed modulus joints approach can be used to improve the stress-distribution along the overlapping region and enhance adhesive strength of high modulus adhesives. The stiff, brittle adhesive should be in the middle of the overlap, while the low-modulus adhesive is applied at the edges prone to stress concentrations [170]. The effect of the viscosity of the uncured formulation, instead, is closely related with the wettability concept and the adherend surface roughness. Paz et al. [171] explored this issue for acrylic adhesives and found an optimal value of adhesive viscosity: below this value, poor bond strength due to high shrinkage during curing, which leads to the apparition of residual stresses that weakens the interfacial strength.

A further increase of the viscosity above this value, produced a negative effect on the joint strength as a result of a significant decrease in the wettability. The optimal value is strongly influenced by the surface roughness. The combination of mixture viscosities and the appropriate surface roughness results in stronger joints due to the increase of the actual contact area.

Among the joint design parameters, the effect of bondline thickness was extensively discussed from both theoretical and experimental point of view. Despite classical analytical models predict the opposite, most of the results for typical structural adhesives show that the lap joint strength decreases when thickness increases, highlighting an optimal value of thickness between 0.1 and 0.2 mm for epoxy adhesives [172,173]. Studies were made also on ductile polyurethane adhesives revealing a decrease of adhesive strength with thickness less pronounced with respect to more brittle adhesives [169]. Campilho et al. [174] found an increasing linear trend between fracture toughness and bondline thickness up to 2 mm for largely ductile PU adhesives. The length of the overlapping region has also strong influence on the adhesive performances; in particular da Silva et al. [175] found that the overlapping length was the factor with the biggest impact on the joint strength when ductile adhesive are used.

From the chemical point of view, the chemical composition of the adhesives and the adherends can also play an important role in the joint strength. Most of all the adhesion consists of all the secondary interactions which are formed between adhesive and adherend surfaces and, for this reason, the effective contact area extent is important for the joint design. Nevertheless, stronger chemical bonds can also be formed during the adhesive curing when the appropriate combination adherend/adhesive is chosen or when adherend surface functionalization is carried out.

1.5.3. Epoxy-based adhesives

Thermoset adhesives can be distinguished from hotmelt or thermoplastic adhesives for their high molecular weight polymeric structure formed by heating. When exposed to specific temperatures for a well-specified period of time, the uncured thermoset adhesive formulation undergoes a chemical curing reaction forming the crosslinked network responsible for the physical and chemical properties of thermoset adhesives.

Thermoset adhesives exhibit some extraordinary properties like infusibility, insolubility in various media, high load-bearing ability, and high creep resistance under constant or varying forces. They are compatible with extreme service conditions such as high or low temperatures, exposure to salt water, or radiation. Steel, light metals like aluminium or

magnesium, and a variety of plastic and composite materials can be bonded with high strength to structural, i.e., load-bearing assemblies. Today, engineered variants of thermoset adhesives provide exceptional properties that are directly comparable or even superior to more traditional joining methods like welding, riveting, or clinching. These kinds of structural thermoset adhesives provide stiffness and resistance against dynamic impact loads. Consequently, they are more and more used in lightweight constructions and in many industrial applications. Most common thermoset adhesives are based on acrylic, epoxy, polyurethane, natural or synthetic rubbers (elastomers) and silicone compounds.

Epoxy-based thermoset adhesives constitute one of the main classes of heat-activated reactive compounds. They can be characterized by high strength, excellent adhesion to many metallic and non-metallic substrates, small shrinkage during and after cure, and excellent resistance to chemicals and higher temperatures. Today, the majority of epoxy resin adhesives are based on *diglycidyl ether of bisphenol A* (DGEBA) and the final properties are tailored by proper choice of hardener systems. Low-temperature curing adhesive are commonly obtained by amines or thiols hardeners thanks to their high reactivity with epoxy compound. They are characterized by reduced application times but generally lower joint strength. On the other hand, high-temperature curing epoxy adhesives allow longer open times, higher joint strengths and higher oil absorption rates. Suitable hardeners are based on amides, aromatic amines, polyaminoamides or anhydrides. To obtain higher performance hardeners can be combined with an appropriate catalyst, such as BDMA (*benzyldimethyl amine*) or DMP 30 (*tris-(dimethyl-aminomethyl) phenol*). Together with polyfunctional epoxy resins, the hardener/catalyst system defines the cross-linking density and T_g of the final epoxy adhesive.

Different kind of fillers can be also added to adhesive matrix to enhance thermal and mechanical properties or even to obtain conductive adhesives [176]. Effective improvement of adhesive thermal and mechanical behaviour was demonstrated using Zirconia nanoparticles [177]; adhesive filled with Zirconia showed higher T_g an lap-shear strength. Tutunchi et al. [178] successfully increased the adhesive strength of steel–epoxy composite joints bonded with structural acrylic adhesives by using Silica nanoparticles. Thermally expandable particles (TEPs) were investigated to modify structural adhesives for other new purposes, such as to increase the joint strength by creating an adhesive functionally modified along the overlap of the joint by gradual heating and/or to heal the adhesive in case of damage [179]. Recently, carbon-based nanofillers were also used: CNTs [180], graphene nanosheets [181], graphene oxide nanoplatelets [182]. In case of metallic adherends the use of fillers is also addressed to

reduce the properties mismatch at the interface between polymeric adhesive and metal substrate. The target properties are commonly the Young modulus and the coefficient of thermal expansion (CTE). The reduction of the CTE improve the thermal behaviour of the union by reducing undesired difference in contraction/expansion during the adhesive curing and the working life of the joint.

Although some examples of dual-curable adhesives can be found in the literature, commonly UV/temperature activated [37,183,184], the application and performance of two-stage processing adhesives based on dual-curing adhesives has not been properly investigated yet. In Chapter 6 of the present work, a two-stage dual-curing adhesive (with and without fillers) has been extensively tested in order to highlight the beneficial effects of dual processing in the field of adhesives.

1.6. Epoxy thermosets with thermal conductive fillers

Polymer-based thermally conductive materials are often desired in many applications; besides, they are well-known as good thermal insulator. The absence of free electrons able to transfer the heat, and the lack of an ordered structure in polymeric chains are two of the most important reasons why polymers present this low conductivity. Thus, in amorphous polymers, phonons are the responsible of heat transmission and their scattering needs to be reduced as much as possible to get high thermal conductivity (TC) [185]. Their extreme flexibility and processability makes them suitable for filler incorporation which allows to significantly increase their TC. Typically, heat conductive fillers, such as aluminium oxide, boron nitride, aluminium nitride, silicon nitride, diamond, graphite, metal particles, carbon nanotube, graphene, etc., are introduced into polymers to increase TC. For applications that require both high TC and electrically insulating properties, electrically insulating fillers, such as aluminium oxide, boron nitride, aluminium nitride, etc. can be used, while graphite, metal particles, carbon nanotube, and graphene are often utilized in applications where electrical insulation is not required.

Thermal conductivity is not only affected by the type and content of the fillers. The morphology and the spatial arrangement of the fillers are also crucial, and they can contribute to the formation of a thermal conductive path through the polymer with the shortest quantity of fillers [186]. The formation of a continuous filler network is the key to enable high TC in polymer composite structures. Since high filler loading levels can lead to poor processability and mechanical properties, strategies to obtain the highest TC with the lowest amount of filler has to be employed. The interfacial adhesion

between filler and matrix also affect the TC, improving the interfacial adhesion the TC can be increased [187].

Epoxy thermosets are widely used because of the versatility in their properties. They are used in electrical and electronic applications because of their good compatibility with a large variety of materials, the high electrical insulation and good thermal, corrosion and chemical resistance. However, their low thermal conductivity (0.1-0.3 W/mK) has channelled the research community efforts towards epoxy composites loaded with conductive fillers in order to widespread their applicability. The enhancement of the TC and the coefficient of thermal expansion (CTE) enable the application of epoxy composites as adhesives, coatings and in microelectronics.

Metallic particles or carbon materials, like carbon nanotubes (CNT), graphene and graphite, could be attractive fillers due to their high thermal conductivity, but they can make materials electrically conductive. Although they are useless to encapsulate electronic devices, they are important in aerospace and aeronautics technologies, where high-performance light-weight composites are needed, and electrical conductivity does not represent an issue. In addition, metallic fillers have several disadvantages including high density and they are susceptible to oxidation [188]. For this reason, only selected fillers with high thermal conductivity and acceptable dielectric breakdown strength, such as inorganic ceramic materials, can be used to preserve electrical insulation of composites.

The alumina Al_2O_3 is one of the most used oxide fillers due to its low price and high TC, around 30 W/mK [187]. A thermal conductivity of 13.46 W/mK in an Al_2O_3/epoxy composites at 70% of fillers was reported [189]. Other oxides are Silica (SiO_2)[190], Zinc Oxide [191] and Beryllium oxide.

BN has emerged as one of the best candidates for high thermal conductivity composites and electrical insulating applications. It is a synthetic material with high similarities with carbon, since presents a cubic form as diamond, and hexagonal structure as graphite. BN provides the best combination of properties in terms of high thermal conductivity, low dielectric constant, high electrical resistivity and low thermal expansion coefficient. Moreover, BN presents low density (2.2 g/cm^3), high mechanical strength, high aspect ratio and chemical and thermal stability. The hexagonal form (h-BN) is the most stable with a layered structure, and the TC can vary from 2 to 390 W/mK depending on the direction measured and its purity [192]. Last developments estimate the TC of a single layer of h-BN of around 751 W/mK [193]. During the years, the optimizations of h-BN production processes reduce cost and increase purity [194] and, as consequence,

enhance the thermal conductivity. Besides a huge range of thermal conductivity values can be obtained with BN composites, the best result reported till date are the 32.5 W/mK obtained by Ishida et al. with polybenzoxazine matrix [195]. However, this outstanding result was reached with an extremely high loading of 88 wt. % Usual conductivities of epoxy-BN composite ranges from 0.5 to 10 W/mK [196].

Up to now, there have been only a few publications concerned with combining boron nitride (BN) and CNTs in epoxy matrices, although the synergistic effect of these both systems is demonstrated for other type of matrix. Recently, Isarn et al. [197] prepared epoxy composites with a high TC, keeping the electrical insulation and using various proportions of these particles. The study also aimed to investigate which changes in the matrix and in the fillers affect these characteristics and if there are synergistic effects among them. The addition of CNTs alone led to a marked decrease of the electrical resistivity of the composites. Nevertheless, in the presence of BN, which is an electrically insulating material, it was possible to increase the proportion of pristine CNTs to 0.25 wt% in the formulation without deterioration of the electrical resistivity. A small but significant synergic effect was determined when both fillers were added together. Improvements of about 750% and 400% in thermal conductivity were obtained in comparison to the neat epoxy matrix.

Later in this thesis, BN particles have been used in order to enhance thermal conductivity and the coefficient of thermal expansion (CTE) of dual-cured thiol-acrylate-epoxy thermosets. Loaded sample were used and characterized for adhesive applications (Chapter 6) and electroresponsive SMPC (Chapter 7).

1.7. General objectives

The **primary objective** of this work is to comprehensively design, characterize and explore the applicability of a novel dual-curing process based on the combination of thiol-acrylate Michael addition and thiol-epoxy “click” reaction.

The whole investigation has been arranged as step-by-step process starting from the development and the study of the reaction mechanism through the functional applications of the obtained materials. Intermediate steps comprehend the characterization of the thermal and mechanical final properties and the shape-memory effect while the functional applications studied were as two-stage adhesive and electroresponsive shape memory actuator.

Secondary objectives are organized with respect to the different investigation steps:

1st step) Development and characterization of a dual-curing mechanism based on thiol-acrylate Michael addition and thiol-epoxy "click" reaction:

- Explore the possibility of obtaining a well separated sequential dual-curing system.
- Characterize a dual curing mechanism where both reactions are thermally triggered separated only by their differences in reaction kinetics.
- Qualitative analyse the stability and processability of the intermediate thiol-acrylate network.

2nd step) Rheological and mechanical characterization of dual-curing thiol-acrylate-epoxy thermosets varying the ratio between acrylate and thiol equivalent (r_a):

- Determine the critical ratio of the system by theoretical calculations and experimental rheological analysis.
- Evaluation of the main mechanical properties of the final thermosets covering the entire range of r_a from 0 (thiol-acrylate network) to 1 (thiol-epoxy network).
- Study the thermal and mechanical latency of the second curing step in order to evaluate the stability and the processability of the intermediate materials.

3rd step) Obtention of thiol-acrylate-epoxy dual-curing thermosets with thermomechanical suitable properties for shape-memory applications:

- Effectively modify the network structure in order to developed thiol-acrylate-epoxy thermosets with enhanced thermomechanical properties.
- Comprehensive study of the shape-memory behaviour of final thermosets specially focused on mechanical actuators applications.

4th step) Investigation of the potentiality of dual-curing processing in two-stage adhesives applications:

- Study of the effect of Boron Nitride (BN) fillers dispersed in a thiol-acrylate-epoxy dual-curing matrix in order to enhance the compatibility of these materials for adhesive applications.
- Evaluation of the adhesive strength of single-lap joints prepared with dual-curing process taking advantage of, alternatively, liquid-like and solid-like intermediate materials.
- Evaluation of the adhesive strength of single-lap joints prepared via one-step curing in order to point out detrimental and beneficial effects of the dual processing.

5th step) Development of an electroresponsive shape-memory composites putting together different functional layers exploiting dual-curing thermoresponsive thermosets for faster recovery actuations.

- Increasing the thermal conductivity of a thiol-acrylate-epoxy (3°step) SMP without undermine the SME.
- Comparison of the thermal and electrical activation of, respectively, the thermo-responsive SMP and the electro-responsive composite obtained incorporating a flexible conductive layer between two SMP layers.
- Development of an electro-responsive two-way SMPC by incorporating a shape-changing element.

Observations for the reader

This thesis work is redacted as a compilation of scientific papers, which were published during the PhD period. The investigation line was divided in five standalone research works each one addressed to one of the secondary objectives present in the above section. In particular, the final step of this investigation, that is the development of an electroresponsive two-way SMPC, is still an ongoing work that will be published afterwards. Anyway, the results obtained up to the present day are presented in Chapter 8.

1.8. References

[1] Q. Guo, Thermosets: Structure, Properties, and Applications, 2018. https://books.google.it/books?hl=it&lr=&id=qCxHDgAAQBAJ&oi=fnd&pg=PP1&dq=Guo.+Thermosets:+structure,+properties,+and+applications&ots=60lyUjXgYi&sig=A2-7hCa3MNOuDAhyvL_SFzRr6Gc#v=onepage&q=Guo. Thermosets%3A structure%2C properties%2C and applications&f=f (accessed March 15, 2021).

[2] J.-P. Pascault, H. Sautereau, J. Verdu, R.J.J. Williams, Thermosetting Polymers, Marcel Dekker, Inc., New York, NY, US, 2002. sig=6Jsr2Jt7Eybbqu_mUOAQXKDyvKg#v=onepage&q&f=false (accessed June 18, 2021).

[3] D. Montarnal, M. Capelot, F. Tournilhac, L. Leibler, Silica-like malleable materials from permanent organic networks, Science (80-.). 334 (2011) 965–968. https://doi.org/10.1126/science.1212648.

[4] P. Europe, Plastics – the Facts 2020, PlasticEurope. (2020) 1–64.

[5] L.H. Baekeland, The synthesis, constitution, and uses of Bakelite., Ind. Eng. Chem. (1909).

[6] Global Thermosets Market Is Expected To Reach Above USD 140.8 Million in 2021, (n.d.). http://www.marketresearchstore.com/news/global-thermosets-market-232 (accessed March 16, 2021).

[7] H. Dodiuk, S.H. Goodman, Handbook of Thermoset Plastics, Elsevier Inc., 2013. https://doi.org/10.1016/C2011-0-09694-1.

[8] J.M. Kenny, L. Nicolais, Science and Technology of Polymer Composites, in: Compr. Polym. Sci. Suppl., Elsevier, 1989: pp. 471–525. https://doi.org/10.1016/b978-0-08-096701-1.00236-6.

[9] J.K. Gillham, Characterization of thermosetting materials by torsional braid analysis, Polym. Eng. Sci. 16 (1976) 353–356. https://doi.org/10.1002/pen.760160513.

[10] J. Lange, N. Altmann, C.T. Kelly, P.J. Halley, Understanding vitrification during cure of epoxy resins using dynamic scanning calorimetry and rheological techniques, Polymer (Guildf). 41 (2000) 5949–5955. https://doi.org/10.1016/S0032-3861(99)00758-2.

[11] D. Harran, A. Laudouard, Rheological study of the isothermal reticulation of an epoxy resin, J. Appl. Polym. Sci. 32 (1986) 6043–6062. https://doi.org/10.1002/app.1986.070320732.

[12] Jiping Bai, Advanced Fibre-Reinforced Polymer (FRP) Composites for Structural Applications, 1st editio, Woodhead Publishing, Cambridge, UK, 2013. https://www.elsevier.com/books/advanced-fibre-reinforced-polymer-frp-composites-for-structural-applications/bai/978-0-85709-418-6 (accessed March 16, 2021).

[13] G.A. Ormondroyd, Adhesives for wood composites, in: Wood Compos., Elsevier Inc., 2015: pp. 47–66. https://doi.org/10.1016/B978-1-78242-454-3.00003-2.

[14] P. Penczek, P. Czub, J. Pielichowski, Unsaturated Polyester Resins: Chemistry and Technology, Adv. Polym. Sci. 184 (2005) 1–95. https://doi.org/10.1007/B136243.

[15] C. Decker, Kinetic Study and New Applications of UV Radiation Curing, Macromol. Rapid Commun. 23 (2002) 1067–1093. https://doi.org/10.1002/MARC.200290014.

[16] W.D. Cook, Thermal aspects of the kinetics of dimethacrylate photopolymerization, Polymer (Guildf). 33 (1992) 2152–2161. https://doi.org/10.1016/0032-3861(92)90882-W.

[17] Verfahren zur Herstellung eines härtbaren Kunstharzes., (1938).

[18] E. Petrie, Epoxy Adhesive Formulations, McGraw-Hill, New York, NY, 2015. https://mhebooklibrary.com/doi/book/10.1036/0071455442 (accessed March 16, 2021).

[19] M. Sangermano, N. Razza, J.V. Crivello, Cationic UV-curing: Technology and applications, Macromol. Mater. Eng. 299 (2014) 775–793. https://doi.org/10.1002/mame.201300349.

[20] I.E. Dell'Erba, R.J.J. Williams, Homopolymerization of epoxy monomers initiated by 4-(dimethylamino)pyridine, in: Polym. Eng. Sci., John Wiley & Sons, Ltd, 2006: pp. 351–359. https://doi.org/10.1002/pen.20468.

[21] Q. Guo, Thermosets: Structure, properties, and applications: Second edition, Elsevier, Amsterdam, Netherlands, 2017. https://doi.org/10.1016/C2015-0-06205-0.

[22] L.L. Loleı̈khoun, P. Hubert, Cure Shrinkage Characterization of an Epoxy Resin System by Two in Situ Measurement Methods, Wiley Online Libr. 31 (2010) 1603–1610. https://doi.org/10.1002/pc.20949.

[23] E. Ruiz, F. Trochu, Numerical analysis of cure temperature and internal stresses in thin and thick RTM parts, Compos. Part A Appl. Sci. Manuf. 36 (2005) 806–826. https://doi.org/10.1016/j.compositesa.2004.10.021.

[24] C. Mas, X. Ramis, J.M. Salla, A. Mantecón, A. Serra, Copolymerization of diglycidyl ether of bisphenol A with γ-butyrolactone catalyzed by ytterbium triflate: Shrinkage during curing, J. Polym. Sci. Part A Polym. Chem. 41 (2003) 2794–2808. https://doi.org/10.1002/pola.10826.

[25] S. González, X. Fernández-Francos, J. Maria Salla, A. Serra, A. Mantecón, X. Ramis, New thermosets obtained by cationic copolymerization of DGEBA with γ-caprolactone with improvement in the shrinkage. II. Time–temperature–transformation (TTT) cure diagram, J. Appl. Polym. Sci. 104 (2007) 3406–3416. https://doi.org/10.1002/app.26021.

[26] X. Fernández-Francos, J.M. Salla, A. Cadenato, J.M. Morancho, A. Serra, A. Mantecón, X. Ramis, A new strategy for controlling shrinkage of DGEBA resins cured by cationic copolymerization with hydroxyl-terminated hyperbranched polymers and ytterbium triflate as an initiator, J. Appl. Polym. Sci. 111 (2009) 2822–2929. https://doi.org/10.1002/app.29317.

[27] C.L. Sherman, R.C. Zeigler, N.E. Verghese, M.J. Marks, Structure-property relationships of controlled epoxy networks with quantified levels of excess epoxy etherification, Polymer (Guildf). 49 (2008) 1164–1172. https://doi.org/10.1016/j.polymer.2008.01.037.

[28] X. Fernández-Francos, D. Santiago, F. Ferrando, X. Ramis, J.M. Salla, À. Serra, M. Sangermano, Network structure and thermomechanical properties of hybrid DGEBA networks cured with 1-methylimidazole and hyperbranched poly(ethyleneimine)s, J. Polym. Sci. Part B Polym. Phys. 50 (2012) 1489–1503. https://doi.org/10.1002/polb.23145.

[29] K.L. Van Landuyt, J. Snauwaert, J. De Munck, M. Peumans, Y. Yoshida, A. Poitevin, E. Coutinho, K. Suzuki, P. Lambrechts, B. Van Meerbeek, Systematic review of the chemical composition of contemporary dental adhesives, Biomaterials. 28 (2007) 3757–3785. https://doi.org/10.1016/j.biomaterials.2007.04.044.

[30] K. Studer, C. Decker, E. Beck, R. Schwalm, Thermal and photochemical curing of isocyanate and acrylate functionalized oligomers, Eur. Polym. J. 41 (2005) 157–167. https://doi.org/10.1016/j.eurpolymj.2004.09.004.

[31] P. VAN CAETER, E.J. GOETHALS, Telechelic polymers: new developments, Trends Polym. Sci. (Regular Ed.). 3 (1995).

[32] M.A. Tasdelen, M.U. Kahveci, Y. Yagci, Telechelic polymers by living and controlled/living polymerization methods, Prog. Polym. Sci. 36 (2011) 455–567. https://doi.org/10.1016/j.progpolymsci.2010.10.002.

[33] J. Studer, C. Dransfeld, K. Masania, An analytical model for B-stage joining and co-curing of carbon fibre epoxy composites, Compos. Part A Appl. Sci. Manuf. 87 (2016) 282–289. https://doi.org/10.1016/j.compositesa.2016.05.009.

[34] S.R. White, Y.K. Kim, Staged curing of composite materials, Compos. Part A Appl. Sci. Manuf. 27 (1996) 219–227. https://doi.org/10.1016/1359-835X(95)00023-U.

[35] D.P. Nair, N.B. Cramer, J.C. Gaipa, M.K. McBride, E.M. Matherly, R.R. McLeod, R. Shandas, C.N. Bowman, Two-Stage Reactive Polymer Network Forming Systems, Adv. Funct. Mater. 22 (2012) 1502–1510. https://doi.org/10.1002/adfm.201102742.

[36] X. Fernández-Francos, O. Konuray, X. Ramis, À. Serra, S. De la Flor, Enhancement of 3D-Printable Materials by Dual-Curing Procedures, Materials (Basel). 14 (2020) 107.

https://doi.org/10.3390/ma14010107.

[37] F. Saharil, F. Forsberg, Y. Liu, P. Bettotti, N. Kumar, F. Niklaus, T. Haraldsson, W. Van Der Wijngaart, K.B. Gylfason, Dry adhesive bonding of nanoporous inorganic membranes to microfluidic devices using the OSTE(+) dual-cure polymer, J. Micromechanics Microengineering. 23 (2013) 025021. https://doi.org/10.1088/0960-1317/23/2/025021.

[38] G.P.J.M. Tiemersma-Thoone, B.J.R. Scholtens, K. Dušek, M. Gordon, Theories for network formation in multistage processes, J. Polym. Sci. Part B Polym. Phys. 29 (1991) 463–482. https://doi.org/10.1002/polb.1991.090290409.

[39] X. Fernández-Francos, A.-O. Konuray, A. Belmonte, S. De la Flor, À. Serra, X. Ramis, Sequential curing of off-stoichiometric thiol–epoxy thermosets with a custom-tailored structure, Polym. Chem. 7 (2016) 2280–2290. https://doi.org/10.1039/C6PY00099A.

[40] S. Chatani, D.P. Nair, C.N. Bowman, Relative reactivity and selectivity of vinyl sulfones and acrylates towards the thiol-Michael addition reaction and polymerization, Polym. Chem. 4 (2013) 1048–1055. https://doi.org/10.1039/c2py20826a.

[41] A. Belmonte, X. Fernández-Francos, À. Serra, S. De la Flor, Phenomenological characterization of sequential dual-curing of off-stoichiometric “thiol-epoxy” systems: Towards applicability, Mater. Des. 113 (2017) 116–127. https://doi.org/10.1016/j.matdes.2016.10.009.

[42] A. Belmonte, D. Guzmán, X. Fernández-Francos, S. De la Flor, Effect of the network structure and programming temperature on the shape-memory response of thiol-epoxy “click” systems, Polymers (Basel). 7 (2015) 2146–2164. https://doi.org/10.3390/polym7101505.

[43] K. Dietliker, T. Jung, J. Benkhoff, H. Kura, A. Matsumoto, H. Oka, D. Hristova, G. Gescheidt, G. Rist, New developments in photoinitiators, in: Macromol. Symp., John Wiley and Sons Ltd, 2004: pp. 77–98. https://doi.org/10.1002/masy.200451307.

[44] D. Guzmán, X. Ramis, X. Fernández-Francos, A. Serra, New catalysts for diglycidyl ether of bisphenol A curing based on thiol–epoxy click reaction, Eur. Polym. J. 59 (2014) 377–386. https://doi.org/10.1016/j.eurpolymj.2014.08.001.

[45] C. Decker, F. Masson, R. Schwalm, Dual-curing of waterborne urethane-acrylate coatings by UV and thermal processing, Macromol. Mater. Eng. 288 (2003) 17–28. https://doi.org/10.1002/mame.200290029.

[46] D. Guzmán, X. Ramis, X. Fernández-Francos, A. Serra, Preparation of click thiol-ene/thiol-epoxy thermosets by controlled photo/thermal dual curing sequence, RSC Adv. 5 (2015) 101623–101633. https://doi.org/10.1039/c5ra22055f.

[47] Click Chemistry: Diverse Chemical Function from a Few Good Reactions - Kolb - 2001 - Angewandte Chemie International Edition - Wiley Online Library, (n.d.). https://onlinelibrary.wiley.com/doi/10.1002/1521-3773(20010601)40:11%3C2004::AID-ANIE2004%3E3.0.CO;2-5 (accessed May 27, 2021).

[48] Joerg Lahann, Click Chemistry for Biotechnology and Materials Science - Google Libri, John Wiley & Sons, Ltd, Chirchester, 2009. https://books.google.it/books?hl=it&lr=&id=9eoyUOu4L9IC&oi=fnd&pg=PR7&dq=J.+Lahann,+Click+Chemistry+for+Biotechnology+and+Materials+Science,+John+Wiley+%26+Sons,+Ltd,+2009.&ots=y9vwx1--wa&sig=lJaX05C5wTI2ZWOvPcatP5nc4ok#v=onepage&q=J. Lahann%2C Click Chemistry for Biotechnology and Materials Science%2C John Wiley %26 Sons%2C Ltd%2C 2009.&f=false (accessed May 27, 2021).

[49] A.B. Lowe, C.N. Bowman, Thiol-X Chemistries in Polymer and Materials Science - Google Libri, RSC Publishing , Cambridge, UK, 2012. https://books.google.it/books?hl=it&lr=&id=cYpSUiliYBAC&oi=fnd&pg=PA3&dq=A.+Lowe,+C.+Bowman,+Thiol-X+Chemistries+in+Polymer+and+Materials+Science,+In:+RSC+Polymer+Chemistry+Series,+RSC+Pu

blishing,+2013.&ots=Zwyf2gMWN8&sig=MvA3LLceTAIZC2-o1ykdN30pO6w#v=onepage&q&f=false (accessed May 27, 2021).

[50] U. Tunca, Orthogonal multiple click reactions in synthetic polymer chemistry, J. Polym. Sci. Part A Polym. Chem. 52 (2014) 3147–3165. https://doi.org/10.1002/pola.27379.

[51] M.A. Azagarsamy, K.S. Anseth, Bioorthogonal click chemistry: An indispensable tool to create multifaceted cell culture scaffolds, ACS Macro Lett. 2 (2013) 5–9. https://doi.org/10.1021/mz300585q.

[52] W.H. Binder, R. Sachsenhofer, "Click" chemistry in polymer and materials science, Macromol. Rapid Commun. 28 (2007) 15–54. https://doi.org/10.1002/marc.200600625.

[53] J.E. Moses, A.D. Moorhouse, The growing applications of click chemistry, Chem. Soc. Rev. 36 (2007) 1249–1262. https://doi.org/10.1039/b613014n.

[54] L.S. Higashi, M. Lundeen, K. Seff, Empical Relations between Disulfide Bond Lengths, (N or C)-C-S-S Torsion Angles, and Substituents in Aromatic Disulfides. Crystal and Molecular Structure of 3,3'-Dihydroxydi-2-pyridyl Disulfide, J. Am. Chem. Soc. 100 (1978) 8101–8106. https://doi.org/10.1021/ja00494a013.

[55] S. Chatani, C. Wang, M. Podgórski, C.N. Bowman, Triple shape memory materials incorporating two distinct polymer networks formed by selective thiol-Michael addition reactions, Macromolecules. 47 (2014) 4949–4954. https://doi.org/10.1021/ma501028a.

[56] W. Xi, H. Peng, A. Aguirre-Soto, C.J. Kloxin, J.W. Stansbury, C.N. Bowman, Spatial and temporal control of thiol-michael addition via photocaged superbase in photopatterning and two-stage polymer networks formation, Macromolecules. 47 (2014) 6159–6165. https://doi.org/10.1021/ma501366f.

[57] A.O. Konuray, A. Ruiz, J.M. Morancho, J.M. Salla, X. Fernández-Francos, À. Serra, X. Ramis, Sequential dual curing by selective Michael addition and free radical polymerization of acetoacetate-acrylate-methacrylate mixtures, Eur. Polym. J. 98 (2018) 39–46. https://doi.org/10.1016/j.eurpolymj.2017.11.003.

[58] J.W. Chan, C.E. Hoyle, A.B. Lowe, Sequential phosphine-catalyzed, nucleophilic thiol ene/radical-mediated thiol-yne reactions and the facile orthogonal synthesis of polyfunctional materials, J. Am. Chem. Soc. 131 (2009) 5751–5753. https://doi.org/10.1021/ja8099135.

[59] J.A. Carioscia, J.W. Stansbury, C.N. Bowman, Evaluation and control of thiol-ene/thiol-epoxy hybrid networks, Polymer (Guildf). 48 (2007) 1526–1532. https://doi.org/10.1016/j.polymer.2007.01.044.

[60] C.N. Bowman, C.J. Kloxin, Toward an enhanced understanding and implementation of photopolymerization reactions, AIChE J. 54 (2008) 2775–2795. https://doi.org/10.1002/aic.11678.

[61] D. Guzmán, X. Ramis, X. Fernández-Francos, A. Serra, Preparation of click thiol-ene/thiol-epoxy thermosets by controlled photo/thermal dual curing sequence, RSC Adv. 5 (2015) 101623–101633. https://doi.org/10.1039/C5RA22055F.

[62] J. Shin, H. Matsushima, C.M. Comer, C.N. Bowman, C.E. Hoyle, Thiol-isocyanate-ene ternary networks by sequential and simultaneous thiol click reactions, Chem. Mater. 22 (2010) 2616–2625. https://doi.org/10.1021/cm903856n.

[63] G. González, X. Fernández-Francos, À. Serra, M. Sangermano, X. Ramis, Environmentally-friendly processing of thermosets by two-stage sequential aza-Michael addition and free-radical polymerization of amine–acrylate mixtures, Polym. Chem. 6 (2015) 6987–6997. https://doi.org/10.1039/C5PY00906E.

[64] J. Pavlinec, N. Moszner, Photocured Polymer Networks Based on Multifunctional b-Ketoesters and Acrylates, John Wiley & Sons, Inc, 1997. https://doi.org/10.1002/(SICI)1097-4628(19970705)65:1.

[65] N. Moszner, V. Rheinberger, Reaction behaviour of monomeric β-ketoesters, 4. Polymer network formation by Michael reaction of multifunctional acetoacetates with multifunctional acrylates, Macromol. Rapid Commun. 16 (1995) 135–138. https://doi.org/10.1002/marc.1995.030160207.

[66] M. Uygun, M.A. Tasdelen, Y. Yagci, Influence of type of initiation on thiol-ene “click” Chemistry, Macromol. Chem. Phys. 211 (2010) 103–110. https://doi.org/10.1002/macp.200900442.

[67] N.B. Cramer, C.N. Bowman, Kinetics of thiol-ene and thiol-acrylate photopolymerizations with real-time Fourier transform infrared, J. Polym. Sci. Part A Polym. Chem. 39 (2001) 3311–3319. https://doi.org/10.1002/pola.1314.

[68] A.O. Konuray, X. Fernández-Francos, X. Ramis, Curing kinetics and characterization of dual-curable thiol-acrylate-epoxy thermosets with latent reactivity, React. Funct. Polym. 122 (2018) 60–67. https://doi.org/10.1016/j.reactfunctpolym.2017.11.010.

[69] H. Peng, D.P. Nair, B.A. Kowalski, W. Xi, T. Gong, C. Wang, M. Cole, N.B. Cramer, X. Xie, R.R. McLeod, C.N. Bowman, High performance graded rainbow holograms via two-stage sequential orthogonal thiol-click chemistry, Macromolecules. 47 (2014) 2306–2315. https://doi.org/10.1021/ma500167x.

[70] H. Peng, C. Wang, W. Xi, B.A. Kowalski, T. Gong, X. Xie, W. Wang, D.P. Nair, R.R. McLeod, C.N. Bowman, Facile image patterning via sequential thiol-Michael/thiol-yne click reactions, Chem. Mater. 26 (2014) 6819–6826. https://doi.org/10.1021/cm5034436.

[71] O. Konuray, X. Fernández-Francos, X. Ramis, À. Serra, New allyl-functional catalytic comonomers for sequential thiol-Michael and radical thiol-ene reactions, Polymer (Guildf). 138 (2018) 369–377. https://doi.org/10.1016/j.polymer.2018.01.073.

[72] H. Matsushima, J. Shin, C.N. Bowman, C.E. Hoyle, Thiol-Isocyanate-acrylate ternary networks by selective thiol-click chemistry, J. Polym. Sci. Part A Polym. Chem. 48 (2010) 3255–3264. https://doi.org/10.1002/pola.24102.

[73] D.P. Nair, N.B. Cramer, M.K. McBride, J.C. Gaipa, N.C. Lee, R. Shandas, C.N. Bowman, Fabrication and characterization of novel high modulus, two-stage reactive thiol-acrylate composite polymer systems, Macromol. Symp. 329 (2013) 101–107. https://doi.org/10.1002/masy.201200105.

[74] O. Konuray, X. Fernández-Francos, S. De la Flor, X. Ramis, À. Serra, The use of click-type reactions in the preparation of thermosets, Polymers (Basel). 12 (2020). https://doi.org/10.3390/POLYM12051084.

[75] D. Guzmán, X. Ramis, X. Fernández-Francos, A. Serra, Enhancement in the glass transition temperature in latent thiol-epoxy click cured thermosets, Polymers (Basel). 7 (2015) 680–694. https://doi.org/10.3390/polym7040680.

[76] A. Belmonte, C. Russo, V. Ambrogi, X. Fernández-Francos, S.D.L. Flor, Epoxy-based shape-memory actuators obtained via dual-curing of off-stoichiometric “thiol-epoxy” mixtures, Polymers (Basel). 9 (2017). https://doi.org/10.3390/polym9030113.

[77] R.A. Ortiz, B.A.P. Urbina, L.V.C. Valdez, L.B. Duarte, R.G. Santos, A.E.G. Valdez, M.D. Soucek, Effect of introducing a cationic system into a thiol-ene photopolymerizable formulation, J. Polym. Sci. Part A Polym. Chem. 45 (2007) 4829–4843. https://doi.org/10.1002/pola.22234.

[78] M. Sangermano, M. Cerrone, G. Colucci, I. Roppolo, R.A. Ortiz, Preparation and fcharacterization of hybrid thiol-ene/epoxy UV-thermal dual-cured systems, Polym. Int. 59 (2010) 1046–1051. https://doi.org/10.1002/pi.2822.

[79] M. Flores, A.M. Tomuta, X. Fernández-Francos, X. Ramis, M. Sangermano, A. Serra, A new two-stage curing system: Thiol-ene/epoxy homopolymerization using an allyl terminated hyperbranched polyester as reactive modifier, Polymer (Guildf). 54 (2013) 5473–5481. https://doi.org/10.1016/j.polymer.2013.07.056.

[80] F. Gamardella, V. Sabatini, X. Ramis, À. Serra, Tailor-made thermosets obtained by sequential dual-curing combining isocyanate-thiol and epoxy-thiol click reactions, Polymer (Guildf). 174 (2019) 200–209. https://doi.org/10.1016/j.polymer.2019.04.041.

[81] Y. Jian, Y. He, Y. Sun, H. Yang, W. Yang, J. Nie, Thiol-epoxy/thiol-acrylate hybrid materials synthesized by photopolymerization, J. Mater. Chem. C. 1 (2013) 4481–4489.

https://doi.org/10.1039/c3tc30360h.

[82] K. Jin, N. Wilmot, W.H. Heath, J.M. Torkelson, Phase-Separated Thiol-Epoxy-Acrylate Hybrid Polymer Networks with Controlled Cross-Link Density Synthesized by Simultaneous Thiol-Acrylate and Thiol-Epoxy Click Reactions, Macromolecules. 49 (2016) 4115–4123. https://doi.org/10.1021/acs.macromol.6b00141.

[83] O.D. McNair, D.P. Brent, B.J. Sparks, D.L. Patton, D.A. Savin, Sequential thiol click reactions: Formation of ternary thiourethane/thiol- ene networks with enhanced thermal and mechanical properties, in: ACS Appl. Mater. Interfaces, American Chemical Society, 2014: pp. 6088–6097. https://doi.org/10.1021/am405138e.

[84] M. Podgórski, D.P. Nair, S. Chatani, G. Berg, C.N. Bowman, Programmable mechanically assisted geometric deformations of glassy two-stage reactive polymeric materials, in: ACS Appl. Mater. Interfaces, American Chemical Society, 2014: pp. 6111–6119. https://doi.org/10.1021/am405371r.

[85] G. Malucelli, Hybrid organic/inorganic coatings through dual-cure processes: State of the art and perspectives, Coatings. 6 (2016) 10. https://doi.org/10.3390/coatings6010010.

[86] A.R. Pouladvand, M. Mortezaei, H. Fattahi, I.A. Amraei, A novel custom-tailored epoxy prepreg formulation based on epoxy-amine dual-curable systems, Compos. Part A Appl. Sci. Manuf. 132 (2020) 105852. https://doi.org/10.1016/j.compositesa.2020.105852.

[87] O. Konuray, F. Di Donato, M. Sangermano, J. Bonada, A. Tercjak, X. Fernández-Francos, Serra, X. Ramis, Dual-curable stereolithography resins for superior thermomechanical properties, Express Polym. Lett. 14 (2020) 881–894. https://doi.org/10.3144/expresspolymlett.2020.72.

[88] D.L. Safranski, Introduction to Shape-Memory Polymers, Elsevier Inc., 2017. https://doi.org/10.1016/B978-0-323-37797-3.00001-4.

[89] L.B. Vernon, H.M. Vernon, PROCESS OF MANUFACTURING ARTICLES OF THERMOPLASTIC SYNTHETIC RESINS, 2234993A, 1941.

[90] A. Lendlein, S. Kelch, Shape-Memory Polymers, Angew. Chemie Int. Ed. 41 (2002) 2034. https://doi.org/10.1002/1521-3773(20020617)41:12<2034::AID-ANIE2034>3.0.CO;2-M.

[91] T. Xie, Recent advances in polymer shape memory, Polymer (Guildf). 52 (2011) 4985–5000. https://doi.org/10.1016/j.polymer.2011.08.003.

[92] J. Leng, X. Lan, Y. Liu, S. Du, Shape-memory polymers and their composites: Stimulus methods and applications, Prog. Mater. Sci. 56 (2011) 1077–1135. https://doi.org/10.1016/j.pmatsci.2011.03.001.

[93] M. Anthamatten, K. Cavicchi, G. Li, A. Wang, Cold, warm, and hot programming of shape memory polymers, J. Polym. Sci. Part B Polym. Phys. 54 (2016) 1319–1339. https://doi.org/10.1002/polb.24041.

[94] C.M. Yakacki, S. Willis, C. Luders, K. Gall, Deformation limits in shape-memory polymers, Adv. Eng. Mater. 10 (2008) 112–119. https://doi.org/10.1002/adem.200700184.

[95] I.A. Rousseau, Challenges of shape memory polymers: A review of the progress toward overcoming SMP's limitations, Polym. Eng. Sci. 48 (2008) 2075–2089. https://doi.org/10.1002/pen.21213.

[96] V. Lorenzo, A. Díaz-Lantada, P. Lafont, H. Lorenzo-Yustos, C. Fonseca, J. Acosta, Physical ageing of a PU-based shape memory polymer: Influence on their applicability to the development of medical devices, Mater. Des. 30 (2009) 2431–2434. https://doi.org/10.1016/j.matdes.2008.10.023.

[97] J. Choi, A.M. Ortega, R. Xiao, C.M. Yakacki, T.D. Nguyen, Effect of physical aging on the shape-memory behavior of amorphous networks, Polymer (Guildf). 53 (2012) 2453–2464. https://doi.org/10.1016/j.polymer.2012.03.066.

[98] C.M. Yakacki, R. Shandas, D. Safranski, A.M. Ortega, K. Sassaman, K. Gall, Strong, tailored, biocompatible shape-memory polymer networks, Adv. Funct. Mater. 18 (2008) 2428–2435. https://doi.org/10.1002/adfm.200701049.

[99] D.P. Nair, N.B. Cramer, T.F. Scott, C.N. Bowman, R. Shandas, Photopolymerized thiol-ene systems

as shape memory polymers, Polymer (Guildf). 51 (2010) 4383–4389. https://doi.org/10.1016/j.polymer.2010.07.027.

[100] A. Belmonte, X. Fernández-Francos, S. De la Flor, À. Serra, Network structure dependence on unconstrained isothermal-recovery processes for shape-memory thiol-epoxy "click" systems, Mech. Time-Dependent Mater. 21 (2017) 133–149. https://doi.org/10.1007/s11043-016-9322-z.

[101] D. Santiago, A. Fabregat-Sanjuan, F. Ferrando, S. De La Flor, Recovery stress and work output in hyperbranched poly(ethyleneimine)-modified shape-memory epoxy polymers, J. Polym. Sci. Part B Polym. Phys. 54 (2016) 1002–1013. https://doi.org/10.1002/polb.24004.

[102] C.M. Yakacki, A.M. Ortega, C.P. Frick, N. Lakhera, R. Xiao, T.D. Nguyen, Unique recovery behavior in amorphous shape-memory polymer networks, Macromol. Mater. Eng. 297 (2012) 1160–1166. https://doi.org/10.1002/mame.201200275.

[103] A. Belmonte, C. Russo, V. Ambrogi, X. Fernández-Francos, S.D. la Flor, Epoxy-based shape-memory actuators obtained via dual-curing of off-stoichiometric "thiol-epoxy" mixtures, Polymers (Basel). 9 (2017). https://doi.org/10.3390/polym9030113.

[104] C. Liu, H. Qin, P.T. Mather, Review of progress in shape-memory polymers, J. Mater. Chem. 17 (2007) 1543–1558. https://doi.org/10.1039/b615954k.

[105] D.M. Feldkamp, I.A. Rousseau, Effect of chemical composition on the deformability of shape-memory epoxies, Macromol. Mater. Eng. 296 (2011) 1128–1141. https://doi.org/10.1002/mame.201100066.

[106] M. Fan, H. Yu, X. Li, J. Cheng, J. Zhang, Thermomechanical and shape-memory properties of epoxy-based shape-memory polymer using diglycidyl ether of ethoxylated bisphenol-A, Smart Mater. Struct. 22 (2013) 055034. https://doi.org/10.1088/0964-1726/22/5/055034.

[107] T. Xie, I.A. Rousseau, Facile tailoring of thermal transition temperatures of epoxy shape memory polymers, Polymer (Guildf). 50 (2009) 1852–1856. https://doi.org/10.1016/j.polymer.2009.02.035.

[108] Y. Liu, C. Han, H. Tan, X. Du, Thermal, mechanical and shape memory properties of shape memory epoxy resin, Mater. Sci. Eng. A. 527 (2010) 2510–2514. https://doi.org/10.1016/j.msea.2009.12.014.

[109] G.J.M. Antony, C.S. Jarali, S.T. Aruna, S. Raja, Tailored poly(ethylene) glycol dimethacrylate based shape memory polymer for orthopedic applications, J. Mech. Behav. Biomed. Mater. 65 (2017) 857–865. https://doi.org/10.1016/j.jmbbm.2016.10.011.

[110] M. Ecker, V. Danda, A.J. Shoffstall, S.F. Mahmood, A. Joshi-Imre, C.L. Frewin, T.H. Ware, J.R. Capadona, J.J. Pancrazio, W.E. Voit, Sterilization of Thiol-ene/Acrylate Based Shape Memory Polymers for Biomedical Applications, Macromol. Mater. Eng. 302 (2017) 1600331. https://doi.org/10.1002/mame.201600331.

[111] A. Saralegi, E. Johan Foster, C. Weder, A. Eceiza, M.A. Corcuera, Thermoplastic shape-memory polyurethanes based on natural oils, Smart Mater. Struct. 23 (2014) 025033. https://doi.org/10.1088/0964-1726/23/2/025033.

[112] B. Yan, S. Gu, Y. Zhang, Polylactide-based thermoplastic shape memory polymer nanocomposites, Eur. Polym. J. 49 (2013) 366–378. https://doi.org/10.1016/j.eurpolymj.2012.09.026.

[113] S. Weng, Z. Xia, J. Chen, L. Gong, Shape memory properties of polycaprolactone-based polyurethanes prepared by reactive extrusion, J. Appl. Polym. Sci. 127 (2013) 748–759. https://doi.org/10.1002/app.37768.

[114] X. Jing, H.Y. Mi, X.F. Peng, L.S. Turng, The morphology, properties, and shape memory behavior of polylactic acid/thermoplastic polyurethane blends, Polym. Eng. Sci. 55 (2015) 70–80. https://doi.org/10.1002/pen.23873.

[115] L. Peponi, I. Navarro-Baena, A. Sonseca, E. Gimenez, A. Marcos-Fernandez, J.M. Kenny, Synthesis and characterization of PCL-PLLA polyurethane with shape memory behavior, Eur. Polym. J. 49 (2013) 893–903. https://doi.org/10.1016/j.eurpolymj.2012.11.001.

[116] E. Del Río, G. Lligadas, J.C. Ronda, M. Galià, V. Cádiz, M.A.R. Meier, Shape memory polyurethanes from renewable polyols obtained by ATMET polymerization of glyceryl triundec-10-enoate and 10-undecenol, Macromol. Chem. Phys. 212 (2011) 1392–1399. https://doi.org/10.1002/macp.201100025.

[117] M. Behl, J. Zotzmann, A. Lendlein, Shape-Memory Polymers and Shape-Changing Polymers, in: Adv Polym Sci, Springer, Berlin, Heidelberg, 2009: pp. 1–40. https://doi.org/10.1007/12_2009_26.

[118] K.M. Lee, H. Koerner, R.A. Vaia, T.J. Bunning, T.J. White, Light-activated shape memory of glassy, azobenzene liquid crystalline polymer networks, Soft Matter. 7 (2011) 4318–4324. https://doi.org/10.1039/c1sm00004g.

[119] R. Zentel, Liquid Crystalline Elastomers, Angew. Chemie. 101 (1989) 1437–1445. https://doi.org/10.1002/ange.19891011041.

[120] M. Warner, E.Mi. Terentejev, Liquid Crystal Elastomers - Mark Warner, Eugene Michael Terentjev - Google Libri, Oxford University Press Inc., New York, 2007.

[121] M. Warner, P. Bladon, E.M. Terentjev, "Soft elasticity" — deformation without resistance in liquid crystal elastomers, J. Phys. II. 4 (1994) 93–102. https://doi.org/10.1051/jp2:1994116.

[122] J.K. Whitmer, T.F. Roberts, R. Shekhar, N.L. Abbott, J.J. De Pablo, Modeling the polydomain-monodomain transition of liquid crystal elastomers, Phys. Rev. E - Stat. Nonlinear, Soft Matter Phys. 87 (2013) 020502. https://doi.org/10.1103/PhysRevE.87.020502.

[123] H.J. Sue, J.D. Earls, R.E. Hefner, M.I. Villarreal, E.I. Garcia-Meitin, P.C. Yang, C.M. Cheatham, C.J.G. Plummer, Morphology of liquid crystalline epoxy composite matrices based on the diglycidyl ether of 4,4'-dihydroxy-α-methylstilbene, Polymer (Guildf). 39 (1998) 4707–4714. https://doi.org/10.1016/S0032-3861(98)00053-6.

[124] C. Ohm, M. Brehmer, R. Zentel, Applications of Liquid Crystalline Elastomers, in: Springer, Berlin, Heidelberg, 2012: pp. 49–93. https://doi.org/10.1007/12_2011_164.

[125] V. Ambrogi, M. Giamberini, P. Cerruti, P. Pucci, N. Menna, R. Mascolo, C. Carfagna, Liquid crystalline elastomers based on diglycidyl terminated rigid monomers and aliphatic acids. Part 1. Synthesis and characterization, Polymer (Guildf). 46 (2005) 2105–2121. https://doi.org/10.1016/j.polymer.2005.01.007.

[126] M. Giamberini, P. Cerruti, V. Ambrogi, C. Vestito, F. Covino, C. Carfagna, Liquid crystalline elastomers based on diglycidyl terminated rigid monomers and aliphatic acids. Part 2. Mechanical characterization, Polymer (Guildf). 46 (2005) 9113–9125. https://doi.org/10.1016/j.polymer.2005.04.093.

[127] R. Ishige, K. Osada, H. Tagawa, H. Niwano, M. Tokita, J. Watanabe, Elongation behavior of a main-chain smectic liquid crystalline elastomer, Macromolecules. 41 (2008) 7566–7570. https://doi.org/10.1021/ma801665a.

[128] G.N. Mol, K.D. Harris, C.W.M. Bastiaansen, D.J. Broer, Thermo-mechanical responses of liquid-crystal networks with a splayed molecular organization, Adv. Funct. Mater. 15 (2005) 1155–1159. https://doi.org/10.1002/adfm.200400503.

[129] Y. Li, C. Pruitt, O. Rios, L. Wei, M. Rock, J.K. Keum, A.G. Mcdonald, M.R. Kessler, Controlled shape memory behavior of a smectic main-chain liquid crystalline elastomer, Macromolecules. 48 (2015) 2864–2874. https://doi.org/10.1021/acs.macromol.5b00519.

[130] K.A. Burke, I.A. Rousseau, P.T. Mather, Reversible actuation in main-chain liquid crystalline elastomers with varying crosslink densities, Polymer (Guildf). 55 (2014) 5897–5907. https://doi.org/10.1016/j.polymer.2014.06.088.

[131] A. Lendlein, R. Langer, Biodegradable, elastic shape-memory polymers for potential biomedical applications, Science (80-.). 296 (2002) 1673–1676. https://doi.org/10.1126/science.1066102.

[132] W.M. Huang, C.L. Song, Y.Q. Fu, C.C. Wang, Y. Zhao, H. Purnawali, H.B. Lu, C. Tang, Z. Ding, J.L. Zhang, Shaping tissue with shape memory materials, Adv. Drug Deliv. Rev. 65 (2013) 515–535.

https://doi.org/10.1016/j.addr.2012.06.004.

[133] H. Tamai, K. Igaki, E. Kyo, K. Kosuga, A. Kawashima, S. Matsui, H. Komori, T. Tsuji, S. Motohara, H. Uehata, Initial and 6-month results of biodegradable poly-l-lactic acid coronary stents in humans, Circulation. 102 (2000) 399–404. https://doi.org/10.1161/01.CIR.102.4.399.

[134] L. Sun, W.M. Huang, Mechanisms of the multi-shape memory effect and temperature memory effect in shape memory polymers, Soft Matter. 6 (2010) 4403–4406. https://doi.org/10.1039/c0sm00236d.

[135] V.C. Sonawane, M.P. More, A.P. Pandey, P.O. Patil, P.K. Deshmukh, Fabrication and characterization of shape memory polymers based bioabsorbable biomedical drug eluting stent, Artif. Cells, Nanomedicine Biotechnol. 45 (2017) 1740–1750. https://doi.org/10.1080/21691401.2017.1282867.

[136] C. Wischke, A. Lendlein, Shape-memory polymers as drug carriers-a multifunctional system, Pharm. Res. 27 (2010) 527–529. https://doi.org/10.1007/s11095-010-0062-5.

[137] D.L. Safranski, J.C. Griffis, Applications of Shape-Memory Polymers, Elsevier Inc., 2017. https://doi.org/10.1016/B978-0-323-37797-3.00006-3.

[138] A. Lendlein, M. Behl, B. Hiebl, C. Wischke, Shape-memory polymers as a technology platform for biomedical applications, Expert Rev. Med. Devices. 7 (2010) 357–379. https://doi.org/10.1586/erd.10.8.

[139] L. Santo, F. Quadrini, A. Accettura, W. Villadei, Shape memory composites for self-deployable structures in aerospace applications, in: Procedia Eng., Elsevier Ltd, 2014: pp. 42–47. https://doi.org/10.1016/j.proeng.2014.11.124.

[140] S.C. Arzberger, M.L. Tupper, M.S. Lake, R. Barrett, K. Mallick, C. Hazelton, W. Francis, P.N. Keller, D. Campbell, S. Feucht, D. Codell, J. Wintergerst, L. Adams, J. Mallioux, R. Denis, K. White, M. Long, N.A. Munshi, K. Gall, Elastic memory composites (EMC) for deployable industrial and commercial applications, in: Smart Struct. Mater. 2005 Ind. Commer. Appl. Smart Struct. Technol., SPIE, 2005: p. 35. https://doi.org/10.1117/12.600583.

[141] C. Yuan, D.J. Roach, C.K. Dunn, Q. Mu, X. Kuang, C.M. Yakacki, T.J. Wang, K. Yu, H.J. Qi, 3D printed reversible shape changing soft actuators assisted by liquid crystal elastomers, Soft Matter. 13 (2017) 5558–5568. https://doi.org/10.1039/c7sm00759k.

[142] R. Liu, X. Kuang, J. Deng, Y.C. Wang, A.C. Wang, W. Ding, Y.C. Lai, J. Chen, P. Wang, Z. Lin, H.J. Qi, B. Sun, Z.L. Wang, Shape Memory Polymers for Body Motion Energy Harvesting and Self-Powered Mechanosensing, Adv. Mater. 30 (2018) 1705195. https://doi.org/10.1002/adma.201705195.

[143] W. Li, Y. Liu, J. Leng, Programmable and Shape-Memorizing Information Carriers, ACS Appl. Mater. Interfaces. 9 (2017) 44792–44798. https://doi.org/10.1021/acsami.7b13284.

[144] W. Wang, Y. Liu, J. Leng, Recent developments in shape memory polymer nanocomposites: Actuation methods and mechanisms, Coord. Chem. Rev. 320–321 (2016) 38–52. https://doi.org/10.1016/j.ccr.2016.03.007.

[145] D. Habault, H. Zhang, Y. Zhao, Light-triggered self-healing and shape-memory polymers, Chem. Soc. Rev. 42 (2013) 7244–7256. https://doi.org/10.1039/c3cs35489j.

[146] Z. Bin Wen, D. Liu, X.Y. Li, C.H. Zhu, R.F. Shao, R. Visvanathan, N.A. Clark, K.K. Yang, Y.Z. Wang, Fabrication of Liquid Crystalline Polyurethane Networks with a Pendant Azobenzene Group to Access Thermal/Photoresponsive Shape-Memory Effects, ACS Appl. Mater. Interfaces. 9 (2017) 24947–24954. https://doi.org/10.1021/acsami.7b05280.

[147] C. Wang, B. Kou, Z. Hang, X. Zhao, T. Lu, Z. Wu, J.P. Zhang, Tunable shape recovery progress of thermoplastic polyurethane by solvents, Pigment Resin Technol. 47 (2018) 7–13. https://doi.org/10.1108/PRT-03-2017-0021.

[148] W. Wang, H. Lai, Z. Cheng, H. Kang, Y. Wang, H. Zhang, J. Wang, Y. Liu, Water-induced poly(vinyl alcohol)/carbon quantum dot nanocomposites with tunable shape recovery performance and

fluorescence, J. Mater. Chem. B. 6 (2018) 7444–7450. https://doi.org/10.1039/c8tb02064g.

[149] X. Rui, Q. Yan, M. Skyllas-Kazacos, T.M. Lim, Li3V2(PO4)3 cathode materials for lithium-ion batteries: A review, J. Power Sources. 258 (2014) 19–38. https://doi.org/10.1016/j.jpowsour.2014.01.126.

[150] S. Bai, H. Zou, H. Dietsch, Y.C. Simon, C. Weder, S. Bai, H. Zou, H. Dietsch, Y.C. Simon, C. Weder, Functional Iron Oxide Nanoparticles as Reversible Crosslinks for Magnetically Addressable Shape-Memory Polymers, Wiley Online Libr. 215 (2014) 398–404. https://doi.org/10.1002/macp.201300632.

[151] F. Quadrini, L. Iorio, D. Bellisario, L. Santo, Shape memory polymer composite unit with embedded heater, Smart Mater. Struct. 30 (2021) 075009. https://doi.org/10.1088/1361-665x/ac00cb.

[152] H. Lu, W.M. Huang, J. Leng, Functionally graded and self-assembled carbon nanofiber and boron nitride in nanopaper for electrical actuation of shape memory nanocomposites, Compos. Part B Eng. 62 (2014) 1–4. https://doi.org/10.1016/j.compositesb.2014.02.003.

[153] X. Wang, J. Sparkman, J. Gou, Electrical actuation and shape memory behavior of polyurethane composites incorporated with printed carbon nanotube layers, Compos. Sci. Technol. 141 (2017) 8–15. https://doi.org/10.1016/j.compscitech.2017.01.002.

[154] H. Lu, J. Yin, B. Xu, J. Gou, D. Hui, Y. Fu, Synergistic effects of carboxylic acid-functionalized carbon nanotube and nafion/silica nanofiber on electrical actuation efficiency of shape memory polymer nanocomposite, Compos. Part B Eng. 100 (2016) 146–151. https://doi.org/10.1016/j.compositesb.2016.06.072.

[155] W. Liu, H. Chen, M. Ge, Q.Q. Ni, Q. Gao, Electroactive shape memory composites with TiO2 whiskers for switching an electrical circuit, Mater. Des. 143 (2018) 196–203. https://doi.org/10.1016/j.matdes.2018.02.005.

[156] L. Valentini, M. Cardinali, J. Kenny, Hot press transferring of graphene nanoplatelets on polyurethane block copolymers film for electroactive shape memory devices, J. Polym. Sci. Part B Polym. Phys. 52 (2014) 1100–1106. https://doi.org/10.1002/polb.23539.

[157] R. V. Beblo, J.J. Joo, G.W. Reich, Aligning nickel particles for joule heating in epoxy shape memory polymer using a magnetic field and linear vibration, J. Intell. Mater. Syst. Struct. 27 (2016) 797–807. https://doi.org/10.1177/1045389X15596625.

[158] C.L. Lewis, E.M. Dell, A Review of Shape Memory Polymers Bearing Reversible Binding Groups, J. Polym. Sci., Part B Polym. Phys. 54 (2016) 1340–1364. https://doi.org/10.1002/polb.23994.

[159] J. Zhou, S.S. Sheiko, Reversible Shape-Shifting in Polymeric Materials, J. Polym. Sci., Part B Polym. Phys. 54 (2016) 1365–1380. https://doi.org/10.1002/polb.24014.

[160] Y. Meng, J. Jiang, M. Anthamatten, Shape Actuation via Internal Stress-Induced Crystallization of Dual-Cure Networks, ACS Publ. 53 (2015) 40. https://doi.org/10.1021/mz500773v.

[161] M.O. Saed, A.H. Torbati, C.A. Starr, R. Visvanathan, N.A. Clark, C.M. Yakacki, Thiol-acrylate main-chain liquid-crystalline elastomers with tunable thermomechanical properties and actuation strain, J. Polym. Sci. Part B Polym. Phys. 55 (2017) 157–168. https://doi.org/10.1002/polb.24249.

[162] K. Westbrook, P. Mather, … V.P.-S.M. and, undefined 2011, Two-way reversible shape memory effects in a free-standing polymer composite, Iopscience.Iop.Org. (n.d.). https://iopscience.iop.org/article/10.1088/0964-1726/20/6/065010/meta?casa_token=SUqsV4fh7swAAAAA:FXI-4dhIf8itLg3kLBkt-t8pZ4DFrOhZLHBJ13xMaUsImav_uZ0iPd2q1J7ALJvDkj1vI_c2xwMv (accessed June 6, 2021).

[163] A. Belmonte, G.C. Lama, G. Gentile, P. Cerruti, V. Ambrogi, X. Fernández-Francos, S. De la Flor, Thermally-triggered free-standing shape-memory actuators, Eur. Polym. J. 97 (2017) 241–252. https://doi.org/10.1016/j.eurpolymj.2017.10.006.

[164] E. Zharinova, M. Heuchel, T. Weigel, D. Gerber, K. Kratz, A. Lendlein, Water-Blown Polyurethane Foams Showing a Reversible Shape-Memory Effect, Mdpi.Com. (n.d.).

https://doi.org/10.3390/polym8120412.

[165] A. Belmonte, G.C. Lama, G. Gentile, P. Cerruti, V. Ambrogi, X. Fernández-Francos, S. De la Flor, Thermally-triggered free-standing shape-memory actuators, Eur. Polym. J. 97 (2017) 241–252. https://doi.org/10.1016/j.eurpolymj.2017.10.006.

[166] A. Belmonte, G.C. Lama, P. Cerruti, Motion control in free-standing shape- memory actuators, (2018).

[167] A. V. Pocius, A. V. Pocius, The Relationship of Surface Science and Adhesion Science, Adhes. Adhes. Technol. (2012) 145–179. https://doi.org/10.3139/9783446431775.006.

[168] da S. Lucas F.M:, O. Andreas, A. Robert D., Handbook Of Adhesion Technology, 2nd ed., Springer, Cham, Switzerland, 2018.

[169] M.D. Banea, L.F.M.D.A. Silva, R.D.S.G. Campilho, The Effect of Adhesive Thickness on the Mechanical Behavior of a Structural Polyurethane Adhesive, (2015) 331–346. https://doi.org/10.1080/00218464.2014.903802.

[170] L.F.M. da Silva, M.J.C.Q. Lopes, Joint strength optimization by the mixed-adhesive technique, Int. J. Adhes. Adhes. 29 (2009) 509–514. https://doi.org/10.1016/j.ijadhadh.2008.09.009.

[171] E. Paz, J.J. Narbón, J. Abenojar, M. Cledera, J.C. Real, Influence of Acrylic Adhesive Viscosity and Surface Roughness on the Properties of Adhesive Joint Influence of Acrylic Adhesive Viscosity and Surface Roughness on the Properties of Adhesive Joint, 8464 (2016). https://doi.org/10.1080/00218464.2015.1051221.

[172] L.F.M. Da Silva, T.N.S.S. Rodrigues, M.A. V Figueiredo, M.F.S.F. De, L.F.M. Da, S.T.N.S.S. Rodrigues, M.F.S.F. De Moura, J.A.G. Chousal, Effect of Adhesive Type and Thickness on the Lap Shear Strength, J. Adhes. 82 (2006) 1091–1115. https://doi.org/10.1080/00218460600948511.

[173] R.D. Adams, n. a. Peppiatt, Stress analysis of adhesive-bonded lap joints, J. Strain Anal. Eng. Des. 9 (1974) 185–196. https://doi.org/10.1243/03093247V093185.

[174] R.D.S.G. Campilho, D.C. Moura, M.D. Banea, L.F.M. Silva, International Journal of Adhesion & Adhesives Adhesive thickness effects of a ductile adhesive by optical measurement techniques, Int. J. Adhes. Adhes. 57 (2015) 125–132. https://doi.org/10.1016/j.ijadhadh.2014.12.004.

[175] L.F.M. da Silva, R.J.C. Carbas, G.W. Critchlow, M.A.V. Figueiredo, K. Brown, Effect of material, geometry, surface treatment and environment on the shear strength of single lap joints, Int. J. Adhes. Adhes. 29 (2009) 621–632. https://doi.org/10.1016/j.ijadhadh.2009.02.012.

[176] R. Aradhana, S. Mohanty, S.K. Nayak, A review on epoxy-based electrically conductive adhesives, Int. J. Adhes. Adhes. 99 (2020) 102596. https://doi.org/10.1016/j.ijadhadh.2020.102596.

[177] A. Dorigato, A. Pegoretti, F. Bondioli, M. Messori, Improving epoxy adhesives with zirconia nanoparticles, Compos. Interfaces. 17 (2010) 873–892. https://doi.org/10.1163/092764410X539253.

[178] A. Tutunchi, R. Kamali, A. Kianvash, Adhesive strength of steel-epoxy composite joints bonded with structural acrylic adhesives filled with silica nanoparticles, J. Adhes. Sci. Technol. 29 (2015) 195–206. https://doi.org/10.1080/01694243.2014.981469.

[179] M.D. Banea, Structural Adhesives Modified with Thermally Expandable Particles, (2015). https://doi.org/10.1080/00218464.2014.985785.

[180] P. Sung, T. Chiu, S.C.-C. science and technology, undefined 2014, Microwave curing of carbon nanotube/epoxy adhesives, Elsevier. (n.d.). https://www.sciencedirect.com/science/article/pii/S0266353814003261?casa_token=vSpMG7rNKeQAAAAA:HT4-OTXty10IDtzkjWpLS3vikMKC3gD2dWgQc67RVjRVa98Q82GUcp9drwBbHo2Dm15q6hx-8A (accessed June 7, 2021).

[181] Z. Jia, X. Feng, Y.Z.-C.P.B. Engineering, undefined 2018, Graphene reinforced epoxy adhesive for fracture resistance, Elsevier. (n.d.).

https://www.sciencedirect.com/science/article/pii/S1359836818328002 (accessed June 7, 2021).

[182] R. Aradhana, S. Mohanty, S.K. Nayak, High performance electrically conductive epoxy/reduced graphene oxide adhesives for electronics packaging applications, J. Mater. Sci. Mater. Electron. 30 (2019) 4296–4309. https://doi.org/10.1007/s10854-019-00722-5.

[183] J.G. Lee, G.S. Shim, J.W. Park, H.J. Kim, K.Y. Han, Kinetic and mechanical properties of dual curable adhesives for display bonding process, Int. J. Adhes. Adhes. 70 (2016) 249–259. https://doi.org/10.1016/j.ijadhadh.2016.07.005.

[184] C.H. Park, S.W. Lee, J.W. Park, H.J. Kim, Preparation and characterization of dual curable adhesives containing epoxy and acrylate functionalities, React. Funct. Polym. 73 (2013) 641–646. https://doi.org/10.1016/j.reactfunctpolym.2013.01.012.

[185] J.-H. Lee, C. Yang Koh, J.P. Singer, S.-J. Jeon, M. Maldovan, O. Stein, E.L. Thomas, 25th anniversary article: Ordered polymer structures for the engineering of photons and phonons, Wiley Online Libr. 26 (2013) 532–569. https://doi.org/10.1002/adma.201303456.

[186] H. Chen, V. V. Ginzburg, J. Yang, Y. Yang, W. Liu, Y. Huang, L. Du, B. Chen, Thermal conductivity of polymer-based composites: Fundamentals and applications, Prog. Polym. Sci. 59 (2016) 41–85. https://doi.org/10.1016/j.progpolymsci.2016.03.001.

[187] X. Huang, P. Jiang, T.T.-I.E. Insulation, undefined 2011, A review of dielectric polymer composites with high thermal conductivity, Ieeexplore.Ieee.Org. (n.d.). https://ieeexplore.ieee.org/abstract/document/5954064/?casa_token=Hb-0WTxAAusAAAAA:u5qx7qZGoM8iVwPjYNTKUij4VbHiVUKYksAIVsVqRHwChf2Wtr3KaF474oOw1WUSweR3-cNi (accessed June 8, 2021).

[188] K. Pashayi, H.R. Fard, F. Lai, S. Iruvanti, J. Plawsky, T. Borca-Tasciuc, High thermal conductivity epoxy-silver composites based on self-constructed nanostructured metallic networks, in: J. Appl. Phys., 2012. https://doi.org/10.1063/1.4716179.

[189] Y. Hu, G. Du, N. Chen, A novel approach for Al2O3/epoxy composites with high strength and thermal conductivity, Compos. Sci. Technol. 124 (2016) 36–43. https://doi.org/10.1016/j.compscitech.2016.01.010.

[190] W.S. Lee, J. Yu, Comparative study of thermally conductive fillers in underfill for the electronic components, Diam. Relat. Mater. 14 (2005) 1647–1653. https://doi.org/10.1016/j.diamond.2005.05.008.

[191] L. Guo, Z. Zhang, R. Kang, Y. Chen, X. Hou, Y. Wu, M. Wang, B. Wang, J. Cui, N. Jiang, C. Te Lin, J. Yu, Enhanced thermal conductivity of epoxy composites filled with tetrapod-shaped ZnO, RSC Adv. 8 (2018) 12337–12343. https://doi.org/10.1039/c8ra01470a.

[192] M.T. Alam, M.S. Bresnehan, J.A. Robinson, M.A. Haque, Thermal conductivity of ultra-thin chemical vapor deposited hexagonal boron nitride films, Appl. Phys. Lett. 104 (2014) 013113. https://doi.org/10.1063/1.4861468.

[193] Q. Cai, D. Scullion, W. Gan, A. Falin, S. Zhang, K. Watanabe, T. Taniguchi, Y. Chen, E.J.G. Santos, L.H. Li, High thermal conductivity of high-quality monolayer boron nitride and its thermal expansion, Sci. Adv. 5 (2019) eaav0129. https://doi.org/10.1126/sciadv.aav0129.

[194] Hexagonal boron nitride (hBN): applications from... - Google Scholar, (n.d.). https://scholar.google.it/scholar?hl=it&as_sdt=0%2C5&q=Hexagonal+boron+nitride+%28hBN%29%3A+applications+from+metallurgy+to+cosmetics&btnG= (accessed June 8, 2021).

[195] H. Ishida, S. Rimdusit, Very high thermal conductivity obtained by boron nitride-filled polybenzoxazine, Thermochim. Acta. 320 (1998) 177–186. https://doi.org/10.1016/s0040-6031(98)00463-8.

[196] T. Tanaka, M. Kozako, K. Okamoto, Toward High Thermal Conductivity Nano Micro Epoxy Composites with Sufficient Endurance Voltage, J. Int. Counc. Electr. Eng. 2 (2012) 90–98. https://doi.org/10.5370/jicee.2012.2.1.090.

[197] I. Isarn, L. Bonnaud, L. Massagués, À. Serra, F. Ferrando, Study of the synergistic effect of boron nitride and carbon nanotubes in the improvement of thermal conductivity of epoxy composites, Polym. Int. 69 (2020) 280–290. https://doi.org/10.1002/pi.5949.

Chapter 2.

Materials and experimental procedures

DUAL-CURING THIOL-ACRYLATE-EPOXY
THERMOSETS FOR FUNCTIONAL APPLICATIONS
Claudio Russo

Chapter 2 : MATERIALS AND EXPERIMENTAL PROCEDURES

2.1. Materials

2.1.1. Thiol-acrylate-epoxy dual-cured thermosets

Thiol-acrylate-epoxy dual-curing thermosets were prepared *at Departament de Química Orgànica i Química Analítica* of *Universitat Rovira i Virgili*. The following compounds were used for their preparation:

- A commercial epoxy resin, *Diglycidyl ether of bisphenol A* (DGEBA, EPIKOTE™ Resin 828) with an epoxy equivalent of 187 g/eq, was supplied by Hexion Specialty Chemicals (Columbus, OH, USA). DGEBA was the main resin used in this investigation.
- *Pentaerythritol tetrakis (3-mercaptopropionate)* (S4), with a molecular weight per thiol equivalent unit of 122.17 g/eq (Sigma-Aldrich, St. Louis, MO, USA) was used as crosslinking agent.
- *Tricyclo[5.2.1.02,6]decanedimethanol diacrylate* (TCDDA) with a molecular weight per acrylate equivalent unit of 152.2 g/eq was purchased from Sigma-Aldrich (St. Louis, MO, USA). TCDDA was the main acrylate compound used in this investigation.
- *Pentaerythritol tetraacrylate* (PTTA, 88.0 g/eq) provided by Sigma-Aldrich (St. Louis, MO, USA) was used in section 3.1 as an alternative acrylate compound.
- *Tri(2,3-epoxypropyl)isocyanurate* (ISO), with a molecular weight per epoxy equivalent unit of 99.09 g/eq (Sigma-Aldrich, St. Louis, MO, USA) was used as network modifier (section 4) in different weight proportions: 10, 20 and 50 wt% (i.e., 20:80 wt% ISO:DGEBA).
- *Bisphenol A glycerolate (1 glycerol/phenol) diacrylate* (BAGA, Sigma-Aldrich, 242.3 g/eq) was used as network modifier (section 4) in different weight proportions: 10, 30 and 50 wt% (i.e., 30:70 wt% BAGA:TCDDA).
- *4-(N,N-dimethylamino)pyridine* (DMAP, Fluka, Seelze, Germany) was used as a catalyst in a proportion of 0.025 phr (parts of catalyst per hundred parts of epoxy resin).

- *Boron Nitride* (BN) agglomerates (80 µm average, PCTL5MHF), supplied by Saint-Gobain, USA, were used as inorganic filler to prepare polymer composites with enhanced CTE and TC. Different proportion were used in section 5 and 6.

The DGEBA was previously dried under vacuum at 80 °C overnight and the other reagents were used without further purifications. The chemical structures and proportions are specified in the corresponding chapters. The mixtures were mainly prepared by mechanical stirring the components in a glass vial and then poured in specific moulds or even directly tested when needed (i.e., DSC or FTIR). The curing conditions are specified in each corresponding chapter, together with eventual variation to the preparation procedure.

2.1.2. Epoxy-acid LCNs

In Chapter 8, shape-changing LCNs were prepared in order to develop a free-standing actuator. An LC epoxy monomer was synthetized and then crosslinked by reaction with a carboxylic acid. The LCNs were synthesized and prepared at *Dipartimento di Ingegneria chimica, dei Materiali e della Produzione Industriale*, of *Universitá degli Studi di Napoli "Federico II"*. The compounds used were:

- A commercial compound *4'-hydroxyphenyl,4-hydroxybenzoat*e supplied by Hoechst, (97% purity, 186.21 g/mol), epichlorohydrin (Sigma-Aldrich, 99% purity, 1.183 g/mL, 92.52 g/mol), isopropyl alcohol, and sodium hydroxide were used for the synthesis of the epoxy-based mesogen.
- Dodecanedioic acid (DA, n=10, 230.30 g/mol) supplied by Sigma-Aldrich (St. Louis, MO, USA) was used as crosslinking agent in stoichiometric proportion with the epoxy monomer.
- *Tricaprylyl methylammonium chloride* (TCAC) was used as catalyst for the epoxy-carboxylic reaction (2 phr).

Samples were prepared by mechanical stirring at high temperature and rapidly poured in a specific mould and cured in oven. Precise curing conditions can be found in section 8.2.

2.2. Dual-curing mechanism characterization

2.2.1. Differential scanning calorimetry (DSC)

A vast majority of polymerization processes taking place in the curing of thermosets are exothermic, and many structural transitions or related phenomena in polymeric

materials involve a release or an absorption of heat. In consequence, calorimetric analysis is essential in the analysis of processes and material properties [1]. Differential scanning calorimetry (DSC) is a technique in which the heat flow difference between a sample placed inside a pan and an empty reference pan, both subject to the same temperature programme inside a furnace, is measured. When a thermal event takes place in the sample, the heat released or absorbed produces a temperature difference between the reference and the sample. This temperature difference is recorded and transformed into a heat flow taking into consideration the thermal properties of the furnace.

The breaking and formation of new chemical bonds in a polymerization process leads to a release of heat that is assumed to be proportional to the extent of reaction. In consequence, DSC can be used to monitor curing processes, determine their curing kinetics under different temperature programmes. The curing rate dx/dt and the degree of conversion x can be determined from calorimetric data as

$$\frac{dx}{dt} = \frac{dh/dt}{\Delta h_{total}} \qquad x = \frac{\Delta h_{t/T}}{\Delta h_{total}} \tag{1}$$

where dh/dt is the heat flow (in W/g), Δh_{total} is the total heat evolved in the curing process (in J/g) and $\Delta h_{t/T}$ is the heat released up to a time t (isothermal curing) or temperature T (non-isothermal curing) (**Figure 2.1**). Kinetic modelling of isothermal and non-isothermal data using suitable methods can be used for the optimization and design of suitable curing temperature programmes.

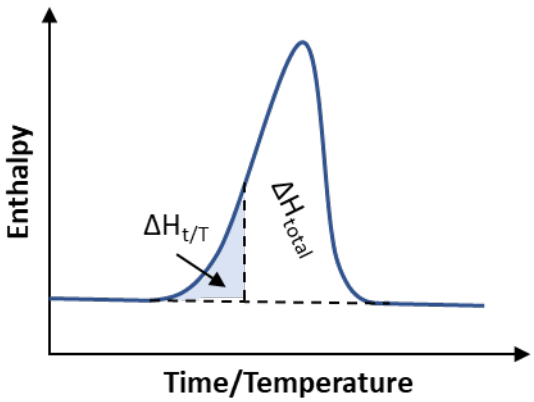

Figure 2.1. DSC analysis of thermosetting polymers: heat released as a function of the temperature or time during curing process.

In the context of sequential dual-curing processes, DSC analysis is an extremely useful tool in order to characterize whether there is significant overlapping of the two reactions involved or else a safe sequential curing schedule can be established, i.e., there is an intermediate state in between curing processes with sufficient stability providing a safe working window from a practical point of view. This is especially important when it is not possible to use selective photoinitiators and/or latent thermal initiators for the activation of the curing process, and the curing process is therefore able to proceed the moment the different components are mixed. In that case, a kinetic control of the curing sequence should be sought for. Preliminary insights on the reaction temperature range of the two separate reactions are obtained by dynamic curing analysis (**Figure 2.2.a**). Then the combined curing of the two networks is analysed always in dynamic conditions.

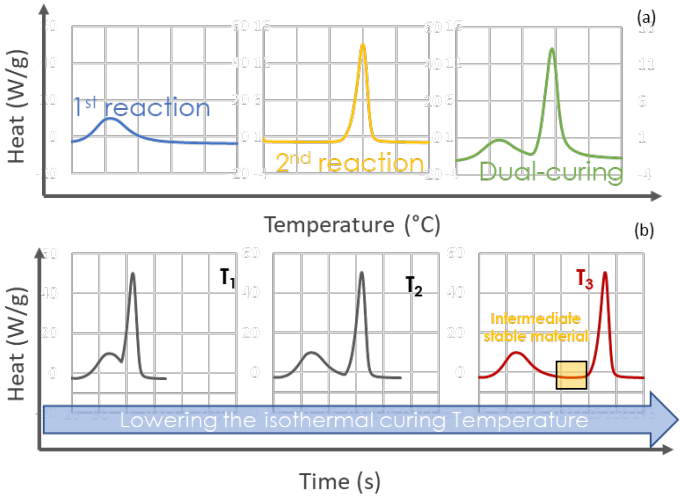

Figure 2.2. Schematical representation of DSC thermograms of dual-curing systems: (a) dynamic analysis of the single isolated reaction and of the two reactions combined in a dual system; (b) Different isothermal curing profiles obtained lowering the isothermal curing temperature.

Kinetic analysis of the individual curing processes will be used to determine the effect of temperature on their curing rate. In the event the temperature dependence of the two reactions are sufficiently different, a kinetic control of the curing sequence may be established. As an example, in **Figure 2.2.b**, it can be seen that lowering the isothermal curing temperature, the peaks corresponding to the two curing process can be gradually separated. Choosing an adequate curing temperature, a stability plateau appears right after the first curing process due to the low reaction kinetic of the second curing process. The second curing rection can be also totally inactivated if the isothermal curing temperature is far lower than its activation temperature.

In this investigation, DSC experiments were carried out at *Departament de Química Orgànica i Química Analítica of Universitat Rovira i Virgili* using a Mettler DSC-821e under N_2 atmosphere.

2.2.2. Fourier-transform infrared spectroscopy (FTIR)

The basic principle of the Fourier transmission infrared spectroscopy (FTIR) is that an IR radiation passes through the sample where it is selectively absorbed, depending on the wavelength absorbed, and obtaining the absorption and transmission spectrum [2]. The curing process can be investigated by identifying the signals corresponding to the reactive groups involved in a curing process and monitoring the corresponding peak area along the curing time.

FTIR isothermal curing analysis can be used as a tool to analyse the chemical process occurring during curing. The evolution of determined peaks, positioned at specific wavelengths, indicates the gradual formation or disappearance of well-defined chemical species (i.e., functional groups, bonds) which can be associated to an ongoing chemical reaction.

FTIR analysis is a fundamental tool for the study of dual-curing systems with controlled curing sequence. The absorption peaks of the different species have first to be identified and the analysis of the evolution of these peaks during the curing process will help to identify which chemical species are reacting and at which rate and order, and therefore determine or verify the curing sequence. The characteristic peaks that provides data related to the thiol-acrylate and thiol-epoxy reactions are:

- Absorbance peak of the acrylate at 810 cm^{-1} gives information on the acrylate group conversion during the thiol-Michael addition (1st stage) [3].
- Absorbance peak at 915 cm^{-1} (epoxy bending) and at 860 cm^{-1} is related to the epoxy-group conversion [4].
- Absorbance peak at 3500 cm^{-1}, related to the formation of OH during the epoxy-thiol reaction, was also used to monitor the thiol-epoxy reaction (2nd reaction).
- Absorbance peak at 2570 cm^{-1} is related to the conversion of the thiol groups due to both reactions.

Normalization of the spectra using a reference band is necessary in order to make up for changes in absorption due to physical processes such as densification due to curing

shrinkage [5] . A common peak used for normalization of spectra is the absorbance peak corresponding to the aromatic ring of DGEBA at 1510 cm^{-1}.

Conversion of functional groups can be determined from the following expressions acrylate functional groups during thiol-acrylate reaction is calculated by Eq. (2):

$$x = 1 - \frac{A'_t}{A'_0} \qquad x = \frac{A'_t - A'_0}{A'_\infty - A'_0} \tag{2}$$

where A'_t, A'_0 and A'_∞ are the normalized absorbances of a given peak at a time t, at the beginning and at the end of the curing process, respectively. The expression to the left can be used for the analysis of chemical species that are disappearing (i.e., thiol, acrylate and epoxy groups), and the expression to the right for the analysis of chemical species that are being formed (i.e., hydroxyl groups). The normalized absorbance is calculated as $A' = A/A_{ref}$, where A is the absorbance of a given peak and A_{ref} is the absorbance of the peak used for normalization.

In this investigation FTIR analysis were performed at *Laboratori de Màquines i Motors Tèrmics* of *Universitat Politècnica de Catalunya* (Barcelona) using an FTIR spectrometer Bruker Vertex 70 with an attenuated total reflection accessory with thermal control and a diamond crystal (Golden Gate Heated Single Reflection Diamond ATR, Specac-Teknokroma).

2.2.3. Isoconversional analysis

The curing kinetics can be analysed using isoconversional methods. Isoconversional or model-free kinetic analysis can produce a set of kinetic parameters at different degrees of conversion without needing to know the underlying mechanism, which can be used for predicting kinetic and for exploring the mechanisms of thermally stimulated processes [6]. This methodology is based on the assumption that the rate dx/dt of a given process can be expressed as separate functions of temperature T and degree of conversion x

$$\frac{dx}{dt} = k(T)f(x) \tag{3}$$

where k(T) is the rate constant, which is usually expressed with an Arrhenius-like temperature dependence, $k(T)=k_0 \cdot \exp(-E/RT)$, where k_0 is the pre-exponential factor and E is the activation energy. f(x) is the kinetic model function representing the underlying reaction mechanism and depends on the extent of conversion x. k_0 , E and f(x) represent the so-called kinetic triplet, which are necessary to completely describe a process. Under

the isoconversional assumptions, the reaction mechanism does not depend on the temperature programme and one can write

$$\frac{dln(dx/dt)}{dT^{-1}} = \frac{dln\big(f(x)\big)}{dT^{-1}} + \frac{dln\big(k(T)\big)}{dT^{-1}} \equiv -\frac{E_x}{R} \tag{4}$$

Where E_x is the apparent activation energy. Linearization of the rate expression leads to the differential isoconversional method of Friedman [6–8] but in the present work we propose to use an integral isoconversional method. The rate expression can be integrated under isothermal conditions [9] as follows:

$$g(x) = \int_0^x \frac{dx}{f(x)} = \int_0^t k_0\, exp\left(\frac{-E}{RT}\right) dt = k_0\, exp\left(\frac{-E}{RT}\right) t \tag{5}$$

where g(x) is the integral form of the kinetic model. Now, taking the natural logarithm of both sides of the equation, we obtain:

$$ln\, t_{x,i} = ln\left[\frac{g(x)}{k_{0,x}}\right] + \frac{E_x}{RT_i} \tag{6}$$

Plotting ln $t_{x,I}$ versus $1/RT_i$ at a fixed conversion x and at different temperature T_is, a line having E_x as slope and ln[g(x)/$k_{0,x}$] as the intercept at the origin, can be obtained.

As illustrated in **Figure 2.3.a,** the starting point in the kinetics analysis is the determination of conversion vs time plots by means of experimental isothermal analysis in this case. The conversion plots at different temperatures can be obtained by monitoring the reaction with DSC or FTIR isothermal experiments. Finally, application of expression (6) to the conversion data at a given degree of conversion leads to linear plot in **Figure 2.3.b**, with a slope equal to the activation energy. In the context of sequential dual-curing processes with kinetic control of the curing sequence such as thiol-acrylate-epoxy systems, a safe curing temperature schedule enabling controlled curing sequence can be established if the activation energy of the two reactions, that is, their temperature dependence, is sufficiently different.

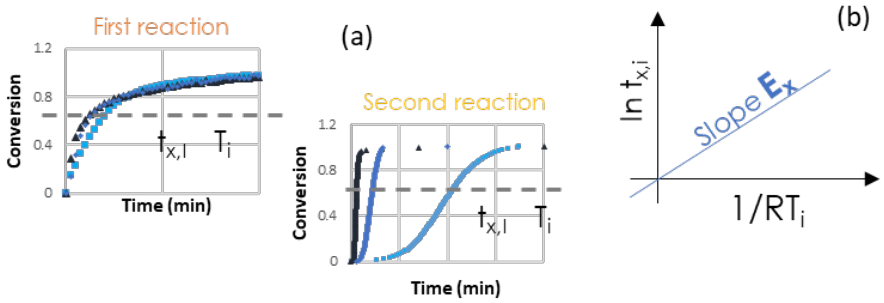

Figure 2.3. Isoconversional analysis: (a) schematical representation of conversion vs time plot obtained for isothermal curing at different isothermal temperature (T_i); (b) Deduction of the activation Energy (E_x) from the graphic expression of the (6).

In Chapter 1, 1st reaction conversion data were obtained by isothermal FTIR analysis at three different temperatures performed at *Laboratori de Màquines i Motors Tèrmics* of *Universitat Politècnica de Catalunya* (Barcelona) using an FTIR spectrometer Bruker Vertex 70. 2nd reaction conversion data were obtained by isothermal DSC analysis instead. DSC analysis were performed at Departament de Química Orgànica i Química Analítica of Universitat Rovira i Virgili using a Mettler DSC-821e under N_2 atmosphere.

2.2.4. Gelation and critical ratio

The curing of thermosets is a complex process, in which crosslinks between polymer chains are formed during the chemical reactions producing an infusible and insoluble polymer network. The gelation (gel point) is defined as the point at which a giant macromolecule percolates the bulk of the sample, and the mass-average molecular weight goes to infinite. This giant macromolecule leads to the incipient insoluble, cross-linked gel fraction. The crosslinking density and the gel fraction increase as the curing process further proceeds, ideally leading to a fully crosslinked network with no soluble fraction [10].

In dual-curing systems the intermediate and final properties depend on the proportion between the different functional groups present in the formulation [11]. In particular, for dual-curing systems based on the excess of one reactant that participates in both reactions, the ratio between the equivalent units of the functional groups involved in the first crosslinking process (r) controls the intermediate and final material properties. The critical ratio (r_c) is defined as the lowest value of r at which the gelation process occurs during the first curing stage. From a practical point of view, it represents a

boundary line between intermediate liquid-like materials and solid-like intermediate and plays a key role on the different application scenarios of dual-curing systems.

Relevant parameters such as the conversion at gelation and the critical ratio r_c can be theoretically predicted by the application of well-known models or determined experimentally by rheological analysis or other methods.

Theoretical analysis

The theoretical prediction of the r_c is based on the Flory-Stockmayer theory [12]. The gel point conversion can be calculated assuming ideal step-growth behaviour using the following expression

$$x_{A,gel} = \sqrt{\frac{1}{r_{AB} \cdot (f_A - 1) \cdot (f_B - 1)}} \tag{7}$$

where $x_{A,gel}$ is the conversion at gelation of monomers with functional group A, and f_A and f_B are the average functionality of the monomers bearing A or B functional groups in the reaction, respectively, and r_{AB} is the ratio of A functional groups with respect to B functional groups (or ratio of equivalents). Assuming that the limiting reactant is A, the critical ratio $r_{AB} = r_c$ can be defined as the limit at which gelation will take place when all reactive A groups are consumed, that is, $x_{A,gel} = 1$. In consequence:

$$r_c = \frac{1}{(f_A - 1) \cdot (f_B - 1)} \tag{8}$$

If $r_{AB} < r_c$, gelation will not occur, therefore leading to a liquid-like material. In contrast, materials will be gelled and therefore will be solid-like if $r_{AB} > r_c$. Non-ideal step-growth will lead to deviations from this predicted behaviour, generally leading to a real critical ratio higher than the theoretical one. In the context of dual-curing processes based on thiol-acrylate-epoxy formulations, this expression will be used nevertheless as a preliminary estimate of the critical ratio of the first curing reaction. It will be seen that the thiol-acrylate reaction takes place before the thiol-epoxy reaction, therefore we will consider only acrylate and thiol groups for the evaluation of r_c. Thiol groups are stoichiometric with respect to the sum of acrylate and epoxy groups, but thiol groups are in excess with respect of acrylate groups, therefore acrylate groups will be the limiting reactant. In consequence, it can be assumed that A refers to acrylate groups and B referes to thiol groups, therefore r_{AB} is the ratio of acrylate equivalents to thiol equivalents, that is, $r_{AB} = r_{system} = r_{acrylate} = eq_{acrylate}/eq_{thiol}$.

Rheological analysis

Rheology is the science of deformation and flow of materials. In fact, all materials can flow, given enough time. In very short processing times, the polymer may behave as a solid, while in long processing times the material may behave as a fluid. This dual nature (fluid-solid) is referred to as viscoelastic behaviour.

Rheology can provide a deep insight on the curing processes of thermosets under oscillatory conditions. If a small oscillatory shear strain is applied to the sample, ϒ(t), this can take the following expression:

$$\gamma = \gamma_0 \sin(\omega t) \tag{9}$$

where Υ_o is the strain amplitude, ω is the angular oscillation frequency and t is the time. The resultant stress, τ(t), has the same frequency but with a phase lag δ:

$$\tau = \tau_0 \sin(\omega t + \delta) \tag{10}$$

Rewriting the shear stress expression as follows:

$$\tau = \tau_0 \sin(\omega t) \cos\delta + \tau_0 \cos(\omega t) \sin\delta \tag{11}$$

The above equation indicate that the shear stress has two components: $\tau_0 \cos\delta$ which is in phase with the strain and $\tau_0 \sin\delta$ which is 90° out of phase with the strain. For small strain amplitudes and time independent polymers (linear viscoelastic regime), the mechanical response of the material can be written in terms of the storage shear modulus (G') and the loss shear modulus (G"):

$$G' = \frac{\tau_0}{\gamma_0}\cos\delta \qquad G'' = \frac{\tau_0}{\gamma_0}\sin\delta \tag{12}$$

The storage modulus G' is the in-phase component and represents the elastic response or the ability of the material to store energy upon deformation, while the loss modulus G'' is the out-of-phase component and represents the viscous response or the ability of the material to dissipate energy. The relation between both moduli determines the damping capabilities of the polymer:

$$\tan\delta = \frac{G''}{G'} \tag{13}$$

The tangent of the phase angle (tan δ) or damping factor provides a measure of how much energy is lost due to the viscous nature of the material.

Monitorization of elastic shear modulus (G'), viscous shear modulus (G'') and phase angle tan δ makes it possible to derive highly useful information about the curing process such as the evolution of viscosity before gelation, conversion at the gel point or crosslinking density at the end of the process.

A thermosetting formulation before gelation behaves like a viscous liquid. In consequence, $G'' > G'$ and G'' increases with increasing degree of conversion due to the increasing molecular weight and therefore increasing viscosity, and the phase angle is high. When the material gels, an incipient network with an elastic mechanical response is formed, with increasing modulus G' as the crosslinking density increases. Given that the gelled material is unable to flow and behaves like a solid, after gelation it is observed that $G' > G''$ and the phase angle tends to 0. Taking this into consideration, gelation can be defined from an operational point of view as the crossover between G' and G''. However, this crossover depends on the oscillation frequency. Given that gelation should only depend on the structure and not on the oscillation frequency of the measurement, a sounder definition of gelation is given by the crossover of tan δ at different frequencies.

In the context of dual-curing processing, rheological analysis can be used to determine whether gelation takes place in the first or the second curing stage, by comparison of oscillatory rheological data (**Figure 2.4**) with curing times or kinetic data. This way, the critical ratio can also be determined.

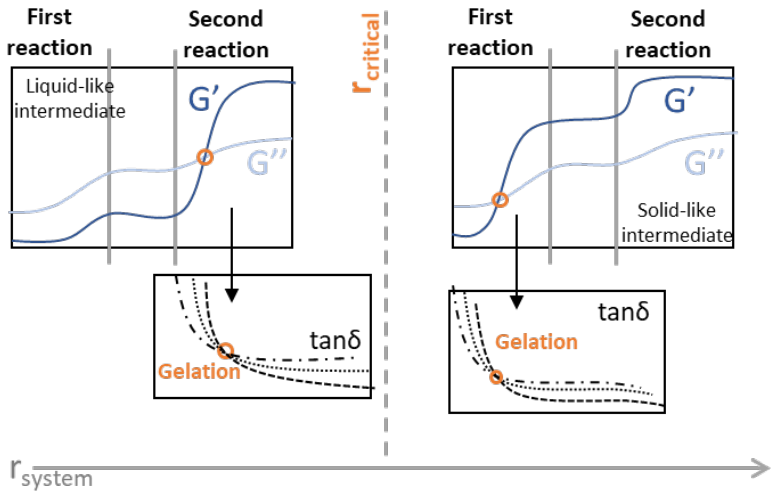

Figure 2.4. Schematical representation of the evolution of G' and tanδ during an isothermal dual-curing rheological analysis.

Rheological measurements were carried out at *Departament de Química Orgànica i Química Analítica* of *Universitat Rovira i Virgili* using a Rheometer AR-G2 (TA Instruments, New Castle, DE) equipped with a parallel plate 25 mm geometry.

2.3. Thermomechanical and Mechanical characterization

2.3.1. Dynamic mechanical analysis (DMA)

Viscoelastic materials, like polymers, exhibit both viscous and elastic behaviour when they undergo deformation. DMA is a powerful and commonly used technique to study the viscoelastic behaviour of polymers. There are three fundamental test methods to characterize the viscoelastic behaviour of polymers: creep, stress relaxation and dynamic mechanical analysis. The most common test is the dynamic mechanical analysis, in which a sinusoidal pulse is applied to the sample and the sample will deform sinusoidally, as showed in **Figure 2.5.a**.

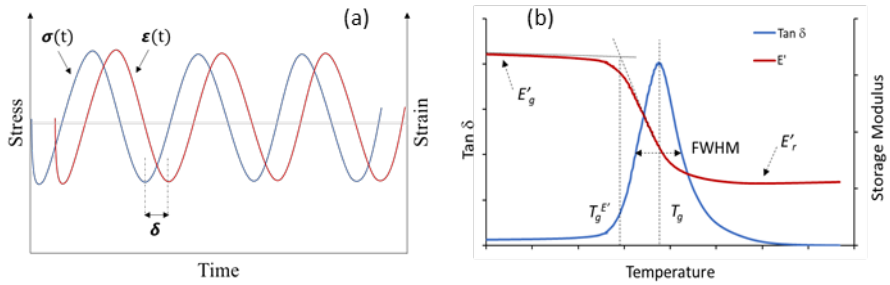

Figure 2.5. (a) Applied strain and related stress as a function of time in DMA; Evolution of the storage modulus and tan δ as a function of the temperature at fixed frequency for a thermoset subjected to an oscillatory stress DMA experiment.

The principles of oscillatory DMA analysis are identical to those of oscillatory rheology, in consequence, we can define storage modulus E', loss modulus E'' and loss factor tan δ in a similar way and the same meaning, setting aside that in DMA flexural modulus is usually measured, instead of shear modulus, hence the change in notation [1]. Moreover, DMA analysis is generally performed on solid samples; however, it can also be used, with some limitations, for the analysis of curing processes in a similar way to rheology.

Analysis of cured materials is usually performed with DMA at a fixed frequency, generally 1 Hz, and a constant heating rate between 2 and 5 °C/min, in order to determine the relevant thermomechanical and structural characteristics of the polymer.

A typical DMA analysis of a crosslinked polymer is showed in **Figure 2.5.b**. The material undergoes a mechanical relaxation which is connected with the devitrification of the material when heated above its glass transition temperature. This relaxation is evidenced by the significant drop in storage modulus E' and the presence of a peak in the tanδ curve. At low temperatures, the material is vitrified so that molecular mobility is highly restricted and therefore the mechanical response is that of a rigid (high E') elastic solid (tanδ → 0). At high temperatures, segmental mobility is high, and the material is relaxed; the mechanical response is that of a soft (low E') elastic solid (tanδ → 0). In between these two solid-like states there is the mechanical relaxation process, which is characterized by the progressive relaxation of the segmental mobility, leading to polymer chain friction and viscous dissipation of mechanical energy, hence the presence of the tanδ peak. The shape of the relaxation curve is indicative of the homogeneity of the material, as the narrower the tanδ peak is, the more homogeneous the network structure. The parameter used to quantify the homogeneity is the "full width at half maximum" (FWHM). The peak of the tanδ curve is normally used to evaluate the glass transition temperature (T_g). The other method used to determine the T_g, which tends to be similar to the T_g defined by pure thermal methods, is to consider the onset temperature of the decrease in the storage modulus, named $T_g^{E'}$. The T_g temperatures determined by the two different methods are not identical. It is important to consider that glass transition occurs in a temperature range and the fact that the results of the DMA analysis depend on the temperature-dependent relaxation time of the material structure and the frequency employed in the DMA analysis (i.e., observation time). Mechanical relaxation occurs when relaxation time decreases below observation time. In consequence, higher frequencies lead to higher temperatures of mechanical relaxation. The criteria for determining the T_g are selected depending on the study and in this thesis the T_g is generally assumed as the temperature of the maximum of the peak of the tanδ curve.

The storage modulus at lower temperatures corresponds to the glassy state of the polymer and the value of E' is comparable to that obtained from stress-strain measurements in the glassy material, as long as the experiment proceeds under linear elasticity conditions. The rubbery modulus, after the glass transition, is related to the crosslinking density of the network. The relation, according to the rubber elasticity theory [13], follows the following expression:

$$E'_r = 3 \cdot R \cdot T \cdot v_f \qquad (14)$$

where R is the universal constant for gases, *T* is the temperature at which the E'_R is determined and ν_F is the density of crosslinks. In this investigation, DMA experiments were carried out at *Departament de Química Orgànica i Química Analítica* of *Universitat Rovira i Virgili* using a DMA Q800 (TA Instruments, New Castle, DE) at oscillatory mode, equipped with 3-point-bending or tension film clamp depending on the sample geometry. Commonly, the oscillation frequency was fixed to 1 Hz and the oscillation strain to 0.1%. A heating rate of 3 °C/min was imposed.

Young modulus measurements

Young Modulus (E) also can be calculated by DMA. Using 3-point bending clamp the Young modulus (or flexural modulus) in a non-destructive flexural test at room temperature can be obtained. The modulus of elasticity (MPa) is calculated using the slope of the load deflection curve in accordance with:

$$E = \frac{L^3 m}{4bt^3} \tag{15}$$

where L is the support span (mm), b and t are the width and the thickness of test sample (mm) and m is the gradient of the slope (N/mm). Flexural experiments were carried out at *Departament de Química Orgànica i Química Analítica* of *Universitat Rovira i Virgili* using a DMA Q800 equipped with a 3-point bending clamp with a spam of 15 mm at 1N/min loading rate.

2.3.2. Tensile tests

Tensile tests consist of applying a controlled uniaxial displacement to a sample until failure occurs. During the analysis, the Force (F) applied by the machine to displace the specimen is registered by a controlling unit. From the data of force vs displacement, the engineering stress and strain are calculated as follow

$$\sigma = \frac{F}{A} = \frac{F}{t \cdot w} \qquad \varepsilon = \frac{L - L_0}{L_0} \cdot 100 \tag{16}$$

where, t is the specimen thickness, w is the specimen width, L_0 is the initial gouge length and L is the gauge length.

The tensile properties of the material depend on the experimental conditions such as: temperature, humidity, and testing rate. A typical stress/strain curve of a thermoset at room temperature is presented in **Figure 2.6**. The stress at break (σ_b) and deformation at break (ε_b) are determined from the failure point. The elastic modulus E is calculated

from the slope of the curve in the initial linear part of the curve. The Strain Energy density can be calculated as the integral of the area under stress/strain curve.

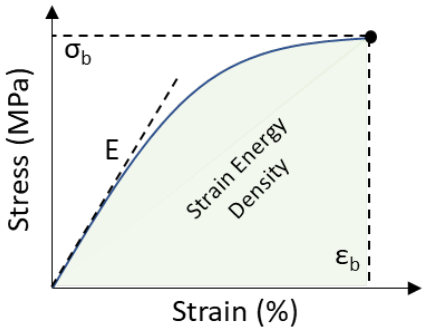

Figure 2.6. Typical stress/strain response of a thermosets at room temperature.

Tensile properties of dog bone shaped samples (80 mm × 25 mm × 1.5 mm) were tested at 10 mm/min speed, according to ASTM D638-14 (ASTM International, West Conshohocken, PA, USA, 2014) standard. In this investigation, uniaxial tensile experiments at room temperature were carried out using a universal testing machine Shimadzu AGS-X (Kyoto, Japan) with a load Cell of 10 kN at *Departament d'Enginyeria Mecànica* of *Universitat Rovira i Virgili.*

2.3.3. Hardness test

Microindentation Vickers hardness

Microhardness testing is used for very brittle materials where only a small indentation may be made for testing purposes. A square-based pyramidal diamond indenter is pressed into the polished surface of the test material with a known force for a specified time. The length of the long diagonal produced by the indentation of a rhomboidal tip can be related with the hardness of the material [14].The pyramidal indenter has a base angle of 136°C and the Vickers hardness is calculated according to the ASTM E384 by the following:

$$HV = 0.0018544 \cdot \frac{L}{d^2} \tag{17}$$

where L is the load applied by the indenter and d is the diagonals average value. HV measurements were performed at *Departament d'Enginyeria Mecànica* of *Universitat Rovira i Virgili* using a Wilson Wolpert 401MAV.

Shore-D hardness

A common way of measuring hardness of plastics is through Shore durometer testing. Shore is a measure of the resistance of the plastic material to indentation. A 'Shore Hardness' gauge has a needle on a spring protruding from one end. The needle is placed against the specimen surface and pressure is applied. Once the gauge is pressed firmly against the material and the needle has penetrated as far as it can go, the measurement needle will indicate the corresponding hardness measurement. Shore A or Shore D scales are used as scales for shore hardness, with Shore A being used for soft material, and Shore D being used for harder material. The Shore A scale is a measure of the Shore A hardness of elastic materials such as rubber or soft plastics, and the Shore D scale is a measure of the Shore D hardness of hard plastics and rubbers. The dimensionless values of the Shore A and D vary between 0 and 100; where 0 represents complete penetration, and 100 represents no penetration. Basically, the higher the number, the higher resistance the material has to indentation.

In this investigation, Shore hardness was measured with an Affri durometer type D (Shore-D hardness) according to ASTM D2240-15 (ASTM International, West Conshohocken, PA, USA, 2015). Ten measurements were done for each sample and the average result is presented. Shore-D measurements were carried out at *Departament d'Enginyeria Mecànica* of *Universitat Rovira i Virgili*.

2.3.4. Lap-shear tests

Lap-shear test on single-lap joints (SLJs) (**Figure 2.7.a**) is one of the most used experimental procedure aimed to produce data on adhesively bonded joints. Variants of this test are described in many standards, for example ISO 4587 and ASTM D 1002. Results from these tests, carried out following these standards are widely quoted in adhesive data sheets. The simplicity and low costs associated with specimen manufacture, testing and data analysis has contributed to the widespread use of this method of quality assurance and to the assessment of chemical or fatigue resistance [15]. Lap-shear testing consists in the application of a tensile load to a SLJ obtained by adhesive bonding of two adherends plates (**Figure 2.7.b**). The analysis assumes the adherends are rigid, and that the adhesive only deforms in shear. End tabs, cut from the same material as the adherend sections, are used to reduce (not eliminate) the eccentricity of the load path which would cause out-of-plane bending moments resulting in high peel stresses and non-uniform shear stresses in the adhesive layer [15]. The long axis of the specimen coincides with the direction of the applied force through the centre line of the grip assembly. The lap-shear strength is given by:

$$\tau = \frac{P}{tL} \tag{18}$$

where P is the maximum load causing the joint failure, t is the joint width and L is the joint length.

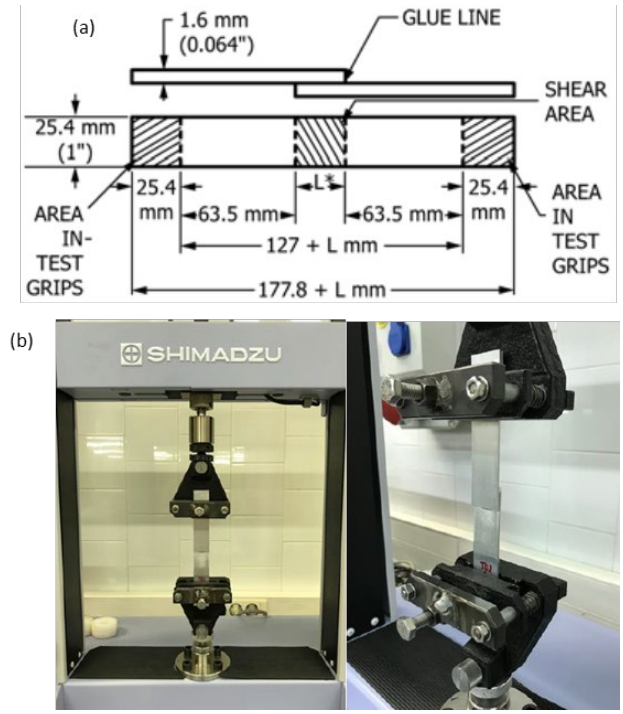

Figure 2.7. (a) Form and dimension of the SLJ has described in ASTM D1002-10; (b) Representation of how the sample is mounted in a universal testing machine.

The procedure for preparation of surfaces prior to application of the adhesive includes the cleaning and drying of metal surfaces and special surface treatments such as sanding and are usually carried out to improve the joint strength. Test specimens shall meet the form and dimensions specified by the ASTM D1002-10 standard while the surface preparation is regulated by the UNE-EN ISO 13887:2004.

In Chapter 6, lap-shear tests were performed in a universal testing machine Shimadzu AGS-X (Kyoto, Japan) equipped with a 10 kN load cell at 1.3 mm/min crosshead speed following the UNE-EN ISO 1465:2009 and ASTM D1002-10 standards for joint design and testing speed. The preparation of the adherend surface was made accordingly to the UNE-EN ISO 13887:2004. All the experiments were conducted at *Departament d'Enginyeria Mecànica* of *Universitat Rovira i Virgili*.

2.4. Shape-memory characterization of glassy thermosets

The characterization of the shape-memory effect (SME) in glassy thermosets is a thermomechanical experiment that consists of several steps. First of all, the stress-strain behaviour at the programming temperature needs to be characterized in order to determine the ultimate stress and strain of the materials and, consequently, determine the achievable programming level. Then, the actual SM experiments is a combination of load application and temperature sweep. They can be carried out in a DMA because is able to control both load and temperature.

Tensile programming processes are the most usual. However, non-standard SMEs, such as bending, compression, torsion or combined tri-dimensional processes can be also programmed through custom-made procedures. Complex tri-dimensional recovery process can be analysed under visual qualitative methodologies due to the complexity of finding devices capable to record their motion. In **Figure 2.8**, an illustration of the typical shape-memory cycle (SMC) for a glassy or semi-crystalline thermoset under free recovery conditions is presented in a 3D plot.

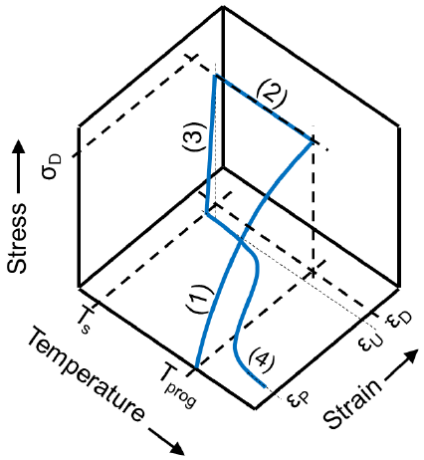

Figure 2.8. 3D illustration of a common SMC of a glassy thermoset under unconstrained conditions.

The SMC 3D plot can be divided in different steps: an initial step (not presented) that consists of heating up the sample to T_{prog}, to further load the sample (1) by applying a stress or strain rate up to the imposed strain (ε_D) or stress (the σ_D). Straightaway (2), the network is frozen by cooling down to T_s, while maintaining the applied stress or strain (this step may lead to creep phenomenon when the process is stress- controlled or stress relaxation if the process is strain-controlled). Afterwards (3), the temporary shape is

fixed by unloading the applied stress, usually at the same loading rate. During the unloading step, shape-losing usually takes place due to the elastic response of the network at low temperature, hence, the programmed strain ε_U is lower than ε_D. Once the temporary shape is fixed, the original shape can be recovered through a heating procedure (4). During the recovery, the original shape is not fully recovered, but a residual or permanent strain remains ($\varepsilon_P > 0$). As explained in section 1.3.1, step 4 can be performed in different loading conditions: unconstrained, partially-constrained and fully constrained conditions.

2.4.1. Tensile SM experiments

The temporary shape can be programmed under stress-controlled or strain-controlled conditions. In stress-controlled procedures, a force ramp is imposed, and the resulting strain is recorded. In contrast, under strain-controlled conditions, the force ramp continuously changes to fit an imposed strain rate.

In this investigation, the tensile programming was carried out using a DMA apparatus equipped with the Tension Film clamp in force-controlled mode. Prismatic rectangular samples of about 20×3.5×0.4 mm^3 were used. The programming process is presented in a "2D" stress-strain plot in **Figure 2.9** extrapolated from the 3D plot of **Figure 2.10**.

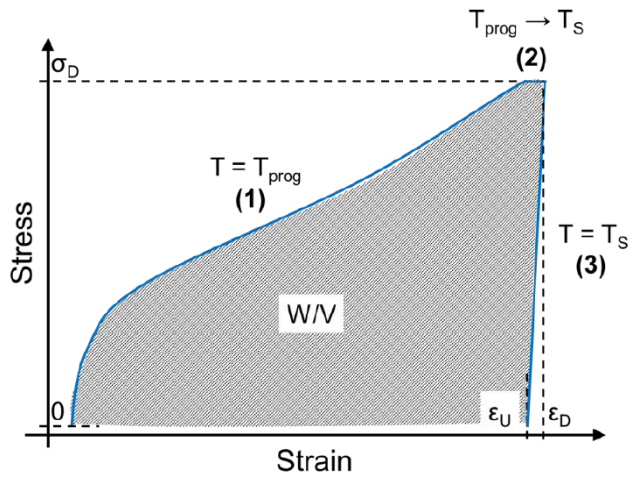

Figure 2.9. Schematic representation of a stress-strain plot of the programming process in a SMP.

The experiments were performed as follows:

Step 1:

- Rapid heating up to T_{prog}.
- Isothermal step for 5 minutes to ensure the thermal stabilization of the sample.
- Force ramp at 1 N/min up to a % of σ_{break} (σ_d)

Step 2:

- Rapid cooling down well below the T_g (T_{low}) while maintaining the force applied.
- Isothermal step for 5 minutes to ensure thermal stabilization of the sample.

Step 3:

- Unload the applied stress at 1 N/min down to zero-stress (ε_U) or to an intermediate value of stress in partially-constrained conditions (**Figure 2.10**).

The programming stress-strain plot gives information about the structural changes and viscoelastic response of the network, and it is related to the elastic energy input necessary to attain the temporary shape. As shown in **Figure 2.9** the process is divided in three steps, (1) loading process, (2) cooling process and (3) unloading process. The fixation of the temporary shape is quantified through the shape-fixation ratio (R_f) which is determined by the following equation:

$$R_f(\%) = \frac{\varepsilon_U}{\varepsilon_D} \cdot 100 \qquad (19)$$

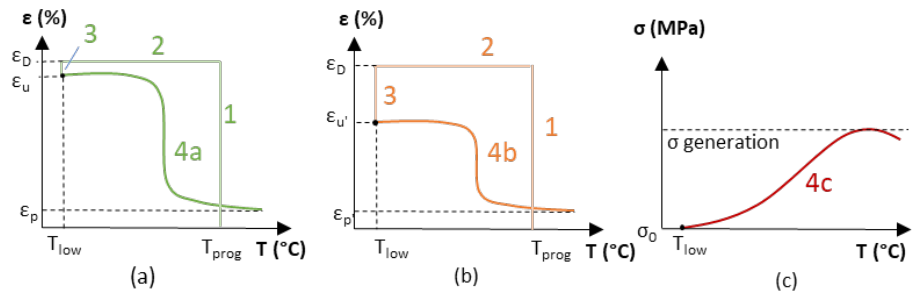

Figure 2.10. (a) free recovery experiment, (b) partially-constrained recovery experiment and (c) constrained recovery experiment. In constrained experiments steps 1,2 and 3 are performed separately.

Unconstrained recovery

The uniaxial unconstrained recovery process (**Figure 2.10.a**) was performed with the Tension Film clamp at a constant heating rate of 3 °C/min from T_{low} up to temperature well above T_g to ensure the completion of process. The recovery step comes right after programming without any break in the experimental procedure. The recovery process is

followed through the variation of the strain during the heating procedure. The strain is calculated as the variation of the length with respect to the initial length of the sample:

$$\varepsilon(t) = \frac{L(t) - L_0}{L_0} \tag{20}$$

Where L(t) is the length at a time t during the SMC and L_0 is the initial length of the sample after the thermal stabilization step at T_{prog}. To analyse and compare the recovery process, ε(t) is usually normalized to (ε_U–ε_P), hence, the shape-recovery (SR) is obtained in % units:

$$SR(t) = \left(1 - \frac{\varepsilon(t) - \varepsilon_P}{\varepsilon_U - \varepsilon_P}\right) \cdot 100 \tag{21}$$

Moreover, the extent of the shape recovery is quantified by the recovery rate (R_r) obtained by:

$$R_r(\%) = \frac{\varepsilon_D - \varepsilon_D}{\varepsilon_D} \cdot 100 \tag{22}$$

The shape-recovery process can be also analysed in terms of shape recovery rate. The instantaneous shape-recovery rate SR_{rate} is calculated by the following

$$SR_{rate}(t) = \frac{dR_r}{dt} \tag{23}$$

The temperature at which the maximum recovery rate is found (T_{peak}), the duration of the process, and the width of the curve at half-height (ΔT_{peak}), can be determined. The velocity of the recovery process (V_r) is calculated as the shape-recovery rate between 15 and 85% of R_r from the following

$$V_r = \frac{\Delta R_{r,15\%-85\%}}{\Delta T_{15\%-85\%}} \cdot \frac{dT}{dt} \tag{24}$$

Partially-constrained recovery

The procedure to perform partially-constrained recovery experiment (**Figure 2.10.b**) differs from the unconstrained one because the programming step do not end in a zero-stress condition. As mentioned before the sample is unloaded to an intermediate value of stress, which is commonly defined as a % of the programming stress. At this point, the recovery process is monitored at a constant heating rate of 3 °C/min from T_{low} up to temperature well above T_g to ensure the completion of process. The value of the constraining stress (σ_{const}) is held constant during the recovery process. The R_r and SR_{rate} can be calculated by (20) and (21), respectively.

In a partially constrained recovery, the SMP recovers a certain amount of deformation against an external stress, thus the material behaves like an actuator and performs a work W_a which can be calculated as [16]:

$$W_a\left(\frac{kJ}{m^3}\right) = \sigma_{const} \cdot (\varepsilon_{U'} - \varepsilon_{P'}) \quad (25)$$

This work output is zero when no constraining stress is applied and for fully constrained conditions. Therefore, a maximum in W_a can always be obtained varying σ_{const}.

Constrained recovery

The procedure for constrained recovery (**Figure 2.10.c**) is performed separately from the programming procedure because it requires a change in DMA working mode. Thus, the sample after programming is unloaded to a zero-stress condition and the DMA apparatus is set into iso-strain mode. The recovery process is carried out heating the sample from T_{low} up to a recovery temperature well above T_g while the deformation ε_U is keeping constant. The evolution of the stress is monitored instead of the strain.

Due to the imposed iso-strain condition, the SMP generates a recovery stress as a consequence of the shape-recovery process. when fully-constrained conditions are applied, the stress generation rate $SG_{rate}(t)$ can be calculated from the stress recovery curve

$$SG_{rate}(t) = \frac{d\sigma_{recovered}}{dt} \quad (26)$$

These experiments were carried out with the DMA Q800 equipped with a film-tension clamp at *Departament de Química Analítica i Química Orgànica* of *Universitat Rovira i Virgili*. Unconstrained and partially constrained shape-memory cycles were performed with a force-controlled mode while, constrained recovery, with an iso-strain mode.

2.4.2. Flexural SM experiments

In this investigation flexural SM experiments were performed starting from a permanent “flat” shape and programming a temporary “bent” shape. The recovery process was performed in the DMA Q800 equipped with a 3-point bending clamp to characterize thermally triggered recovery processes. Electro-activated recovery process was performed using a custom-made electrical controller and by monitoring the recovery with a high-resolution camera.

Flat-to-bent shape programming (isothermal)

As mentioned before, unconventional or alternative shapes can be also employed for SME characterization although custom-made programming procedures have to be developed [13,17]. Prismatic flat samples were programmed into a bent temporary shape following the procedure illustrated in **Figure 2.11**: first, the sample is inserted and held between the two sides of a curved moulding tool. Then, the device is placed inside a preheated oven at T_{prog} (isothermal programming). After 30 minutes, enough to ensure thermal stabilization, the sample is pushed into the curved space of the device (step 1 loading) at a constant force programming force (F_{prog}). The device and the sample are then rapidly cooled down maintaining the force applied. Cooling can be performed by dipping the sample+device in an ice-cold water bath for at least 1 minute. Finally, the sample is removed from the device and the temporary bent shape is obtained.

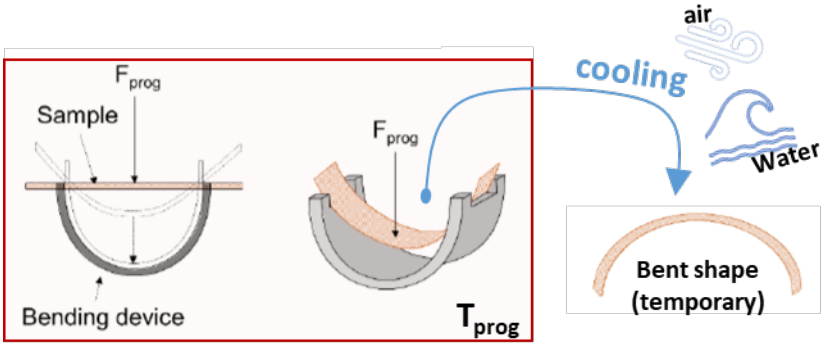

Figure 2.11. Flat-to-bent programming process.

Thermally-activated unconstrained recovery (no-isothermal)

The thermally activated shape recovery experiments were performed from a bent programmed sample using the DMA apparatus to follow the recovery during a heating ramp from room temperature to $T_{recovery} >> T_g$. The sample was placed on the fixed clamp and a minimal force of 0.01 N was applied to ensure the contact between the movable clamp and the sample surface. The experimental setup is illustrated in **Figure 2.12**. First of all, the sample in its permanent shape, prior to programming, is placed on the clamp in order to measure the value p_0 and use it as a reference (**Figure 2.12.a**). The position value of the programmed shape, before the recovery shape (**Figure 2.12.b**), and during the shape recovery process (**Figure 2.12.c**) are indicated as p_{temp} and $p(T)$ respectively. The displacement of the movable clamp $d(T)$ is used to follow the shape recovery, where $d(T)$ is defined as

$$d(T) = p_{temp} - p(T) \tag{27}$$

While the maximum displacement d_{max} associated to a 100% shape recovery is defined as

$$d_{max} = p_{temp} - p_0 \tag{28}$$

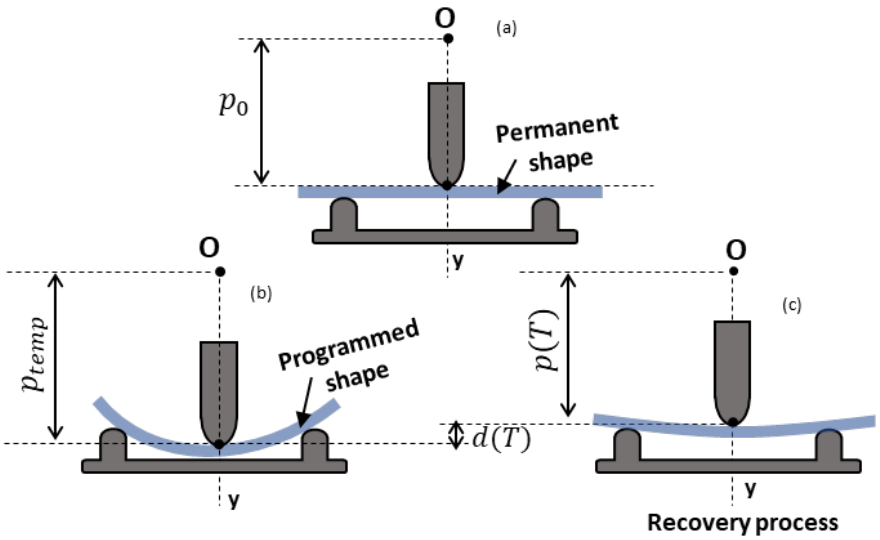

Figure 2.12. Illustration of the DMA testing procedure and analysis methodology at three different moments: (a) before the programming process; (b) right after shape programming; (c) during the recovery process at temperature T.

The displacement of the movable clamp d(T) is used to calculate the SR(%) by the following the equation:

$$SR(\%) = \left(1 - \frac{d(T)}{d_{max}}\right) \cdot 100 \tag{29}$$

The instantaneous shape-recovery speed $SR_{speed}(T)$ is calculated as

$$SR_{speed}(T) = \frac{\partial SR(T)}{\partial T} \tag{30}$$

Using the $SR_{speed}(T)$ curve, the temperature of maximum recovery speed and the duration of the process can be determined, as the peak of the curve (T_{peak}), and as the width of the curve at half-height (ΔT_{peak}), respectively. Both (28) and (29) can be also expressed as a function of time replacing d(T) with d(t), which is the displacement of the movable clamp along the recovery time.

In this investigation thermally-activated unconstrained experiments were carried out with a DMA Q800 with a 3-point bending 15 mm clamp (force controlled mode) at *Departament de Química Analítica i Química Orgànica* of *Universitat Rovira i Virgili*.

Electrically-activated unconstrained recovery

The electro-activation of the recovery process was performed taking advantage of a flexible conductive layer incorporated into the SMP and custom-made thermoelectric-control unit, both developed together with the *Departament d'Enginyeria Electrònica, Elèctrica i Automàtica* of *Universitat Rovira i Virgili.*

The conductive layer consist in a conductive heater made of a conductive silver track, with two electrodes, printed on a thin Kapton® substrate (50µm). Such kind of flexible conductive layer were already employed as substrate in flexible chemo-restive gas sensor manufacturing [18]. The preparation of the conductive layer was conducted as described by Alvarado et al. [18,19]. First of all, the Kapton® substrate is pre-treated by cleaning in acetone and ethanol, rinsing with deionized water and drying at 110°C. For the fabrication of the electrodes, an additional Kapton® layer on which the heating path were cut by CO_2 laser, is used as shadow mask. Silver conductive ink is stencilled with a spatula onto the Kapton®. Then, the ink was dried inside an oven at 130 °C and, afterwards, the shadow mask was peeled-off obtaining the heating path and electrode deposited on the polymeric substrate. In **Figure 2.13** the obtained conductive layer is presented.

In Chapter 7, the conductive layer is incorporated in a thiol-acrylate-epoxy SMP exploiting the dual-curing processing. The incorporation of a conductive layer makes possible to indirectly heating the SMP by means of the Joule heating effect occurring in a conductive heater when a voltage is applied.

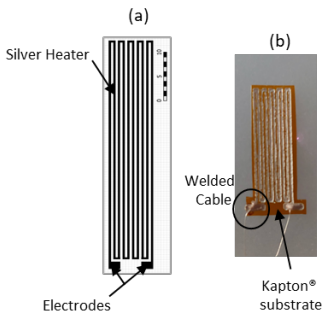

Figure 2.13. Schematic representation of the silver conductive net (a); photo of the conductive layer (b).

The thermoelectric control of the actuator is conducted by a software-controlled development board, equipped with a microprocessor and a load switch. The microprocessor commands the load switch by *pulse-width modulation* (PWM) allowing the regulation of the current supplied to the heater (I_{Heat}) by cyclically powering on and off the current supplied to the heater. The microprocessor regulates the average I_{Heat} as well as the heating complete switch off when the actuator reaches the required temperature. PWM is a way of digitally encoding analog signal levels. Through the use of high resolution counters, the duty cycle of a square wave is modulated to encode a constant analog signal level. The PWM signal is still digital because, at any given instant of time, the power supply is either fully on or fully off. The voltage or current source is supplied to the analog load by means of a repeating series of on and off pulses. The duty cycle (D_{cycle}) indicates the percentage of time the signal is at its high state (on pulse), while the frequency determines how quickly a cycle is completed. As far as the switching time remains much shorter than the system time constant, the load would behave as being driven by a constant magnitude related to the RMS (root mean square) value of the switched supply.

As shown in **Figure 2.14**, the controlling apparatus is made of four main blocks: conditioning unit, switching unit, sensing unit and a computing unit. A conditioning block is placed right after the power supply in order to provide the correct operating voltage to all the circuit components, and consequently allowing the correct regulation of the heating current. The switching block is connected to the output of the conditioning block and relies on the above mentioned load-switch. This block is the one responsible to run the selected heating strategy: it controls the input voltage (V_{IN}) by means of the PWM signal (D_{cycle}) and it provides the V_{IN} defined by the relationship between the R_{Heat} and the I_{Heat} associated with the heating strategy.

PWM is a digital modulation commonly used to control “slow” physical processes. The control signal is periodically switching on and off at a relative “high” frequency, delivering power to the system in a digitally discontinuous mode. But, as long the system time constant is much higher than the switching period, it will be perceived as an average continuous amount of energy. Thus, enabling the direct control of systems with high inertias, without using added electronics to perform the low pass filtering of the digital modulated signal. This is the usual way of controlling electric motors speed or LED lamps glowing intensity. In our case, through the thermal inertia of the involved materials, heat delivered per time unit will be related to t_{on}/t_{PWM} ratio (duty cycle). So, we can control how quick temperature increases just varying this duty cycle (at higher

t_{on}, higher temperature increase ratio) and we are able to obtain different heating strategies (100%, 50% and 25%).

The thermoelectric control relies on the continuous monitoring (or sensing) of the different control parameters such as $V_{Heat,in}$ and $V_{Heat,out}$, to determine R_{Heat}, and the room temperature. These parameters are constantly sent by the sensing unit to the microprocessor to be processed in order to continuously run the apparatus. The R_{Heat} is monitored by a shunt resistor (R_{Sens}) of 10 mΩ. The $V_{Heat,in}$ and $V_{Heat,out}$ are sensed and the R_{Heat} is calculated by the microprocessor following the equation:

$$R_{Heat} = R_{Sens} \cdot \left(V_{Heat,in}/V_{Heat,out} - 1\right) \quad (31)$$

In order to monitor the T_{room} a temperature sensor, which gives an output tension V_{room} proportional to T_{room}, ranging from 0 to 0.35 V (where 1°C corresponds to 10 mV) was used.

Finally, the computing block is based on *Arduino Nano*, a microcontroller development board (open source), based on an Atmel AVR microcontroller. Once the SMP (incorporating the conductive layer) is connected to the apparatus, the software interface requires the insertion of a set-point temperature (T_{set}), which is the target temperature the actuator should reach, and the heating strategy (related to the time spent reaching the target temperature). The heating strategies are defined by a percentage value of the maximum speed at which the setpoint temperature is reached. Once the controlling program is started, the microprocessor collects the T_{room} and $R_{0,Heat}$ data from the sensing block and determines the D_{cycle} corresponding to the selected heating strategy. The heating of the actuators starts when the PWM signal arrives to the load switch, the sensing block starts to continuously sense R_{Heat} by which the computing unit calculates the T_{Heat}. The process stops when the $T_{Heat} = T_{set}$.

Taking advantage of such controlling apparatus, different actuation strategies can be studied by modulating the heating current while maintaining a fixed value of voltage. The electro responsive actuators were heated at T_{set} = 120°C employing three heating strategies, (25%, 50% and 100%) while the power supply is limited at (V_{Batt} = 5 V)

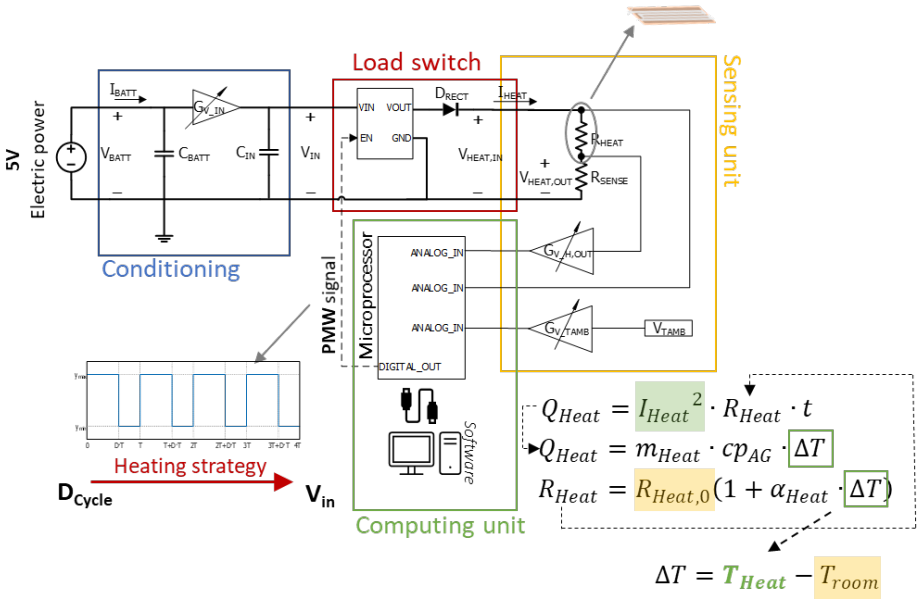

Figure 2.14. Schematic representation of the thermoelectric control for the recovery process.

The recovery process was analysed using a high resolution video-assisted methodology. The bent programmed sample was connected to the controlling unit and was heated thanks to joule-effect to a maximum temperature of 120°C. The recovery process was recorded using a high resolution camera and further analyzed frame by frame, measuring the angles as shown in **Figure 2.15** and applying the (27) on each frame.

$$SR(\%) = \frac{\Delta\theta_t}{180° - \theta_0} \cdot 100 \qquad (32)$$

Where SR(%) is the percentage of shape recovery, θ_0 is the angle at t=0 s and $\Delta\theta_t$ is the difference between the angle at time t (θ_t) and θ_0.

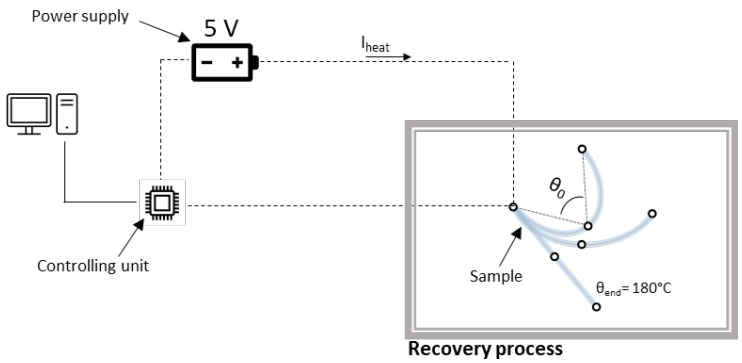

Figure 2.15. Electrically-activated unconstrained recovery experimental setup.

2.5. Liquid crystalline networks characterization

In light of an application as shape-changing element in self-standing electro-responsive actuators a characterization of the essential properties of a LCN material needs to be performed.

2.5.1. Differential scanning calorimetry (DSC)

First order transitions, such as LC transitions, can be measured through the endothermic peak in the heat capacity, ΔC_p, associated to the change in internal volume. Like most of the thermosets, the glass transition is measured through the step variation of ΔC_p associated to the structural reorganization of the network.

To do that DSC were performed in order to measure the T_g and the isotropization temperature (T_{iso}) of the LCN film obtained by an epoxy-acid curing system. The heat released from the isotropization (ΔH_{iso}) can also be measured by the integration of the isotropization peak area and took as a measure of the amount of the LC phase. DSC experiments were carried out at *Dipartimento di Ingegneria chimica, dei Materiali e della Produzione Industriale*, of *Università degli Studi di Napoli "Federico II"* using a TA Instruments DSC Q2000 under N_2 atmosphere.

2.5.2. Dynamo mechanical analysis (DMA)

Thermomechanical properties of the LCN were investigated in order to obtain more information on the P-M transition and the drop in modulus associated. Commonly, DMA oscillatory analysis on LCN thermosets shows two drops in modulus. The first one, right after the glassy plateau, is associated to the glass transition. The extent of the modulus drop is lower than common amorphous thermosets due to the presence of the mesophase (LC domains) which stabilize the properties, resulting in an intermediate plateau. When the T_{iso} is approached, a second modulus drop is produced due to the disordering of the mesophase. Two peaks are present in the tanδ curve, and the second peak temperature can be assumed as the T_{iso} of the LC phase. The extent of both modulus drops is related to the amount of LC phase present in the sample. After the P-M transitions the network is in its rubbery region which is typically characterized by lower E' (around 1 order of magnitude) due to the lightly crosslinked structure of the LCNs.

In this investigation DMA oscillatory analysis were carried out with a DMA Q800 with a tension film clamp (multi-frequency sweep mode) at *Departament de Química Analítica i Química Orgànica* of *Universitat Rovira i Virgili*.

DMA apparatus can be also used to characterize and to evaluate the stress-strain behaviour in the rubbery region. As already mentioned for glassy thermosets, stress-strain analysis at high temperature is performed in order to evaluate the SM programming limit of the LCN. Stress-strain experiments were performed in force controlled mode with a tension film clamp.

2.5.3. Two-way SME characterization

Shape-changing polymers undergo large reversible dimensional changes upon external stimulation through the shape-changing capability (SCC). The characterization of SCC lies on the magnitude and efficiency of the mechanical actuation under thermomechanical cycling processes. In this thesis, the SCE is studied in "epoxy-carboxylic" based LCNs using a DMA apparatus. Uniaxial thermomechanical processes at a constant load level and at different constrained conditions are performed to study the SCE in terms of dimensional change and force generated. The experiments were carried out at *Departament de Química Analítica i Química Orgànica* of *Universitat Rovira I Virgili* using a DMA TA Q800.

Uniaxial experiments at a constant load level were carried out on rectangular-shaped film specimens, using a Tension Film clamp at force controlled mode. In **Figure 2.16.a** the SCC is presented in a "2D" force-strain-temperature plot, while the experimental setup is showed in **Figure 2.16.b**.

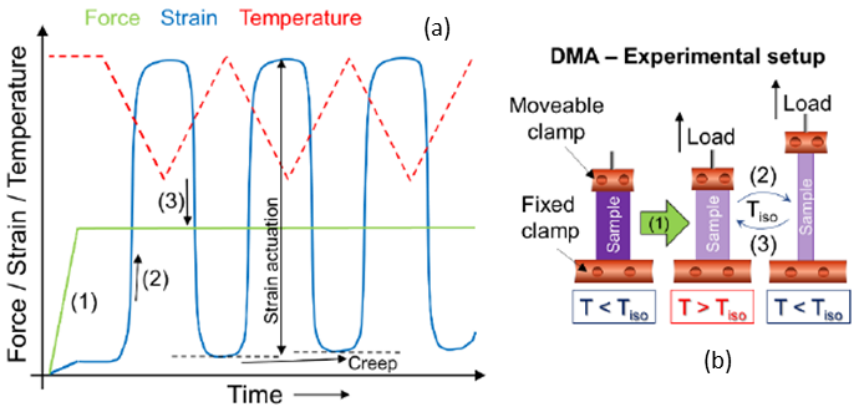

Figure 2.16. Thermomechanical cycling process: (a) strain-force-temperature plot and (b) DMA experimental setup.

The experiments were performed as follows:

Step 1:

- Rapid heating up to T_{iso} + 20 °C.
- Isothermal step for 5 minutes to ensure thermal stabilization of the sample.
- Loading at a force rate of 10 mN/min up to the desired σ_{prog} (commonly choose as a % of σ_b).

Step 2:

- Cooling down to $T < T_{iso}$ at 2 °C/min while maintaining the force applied (induced-elongation).

Step 3:

- Heating up to $T > T_{iso}$ at 2 °C/min while maintaining the force applied (shrinkage).
- Repeat steps 2 and 3 (cycling).

The SCC is analysed through the magnitude and evolution of the strain actuation which is measured as the elongation-shrinkage step in % units for each cycle. The creep or remaining strain after each cycle is determined as a measure of the performance upon cycling processes.

2.6. Other characterization techniques

2.6.1. Environmental Scanning Electron Microscopy (ESEM)

Electron microscopy is a technique based on the irradiation of an electron beam on the surface of a test specimen. The main signals which are generated by the interaction of the primary electrons of the electron beam and the specimen´s bulk are secondary electrons and backscattered electrons and furthermore X-rays. The electrons interact with the atoms that make up the sample producing signals that contain information about the sample's surface. Thanks to a scanner of the emitted beam of electrons it is possible to observe the topography of the surface and obtain an image that we can see through a display.

The surface fracture of thiol-acrylate-epoxy thermosets loaded with BN particles (Chapter 6) were analysed by ESEM in order to investigate the filler dispersion and the possible defects associated to the filler presence. Samples were fractured in liquid N_2 and then coated by gold (Au) particle sputtering. ESEM analysis were performed using a

FEI Quanta 600 Environmental Scanning Electron Microscope (ESEM) equipped with an X-Ray analyser collecting micrographs at 20 kV under high vacuum. ESEM analysis were carried out at *Servei de Recursos Científics i Tècnics* of *Universitat Rovira I Virgili*.

2.6.2. Thermal conductivity measurements

Thermal conductivity can be measured by both steady and transient methods. Steady methods are commonly more accurate than transient ones, but they last a lot longer too. Transient methods measure thermal diffusivity by recording the temperature as function of time following a transient or periodic heat applied to the sample surface. Thermal diffusivity can be calculated from the specimen thickness and the time required for the temperature to reach a percentage of its maximum value. Then, thermal conductivity (TC) can be calculated as

$$TC = \alpha C_p \rho \tag{33}$$

where α is the thermal diffusivity, ρ is the sample density and C_p is the specific heat.

In this investigation, TC was measured by transient pulse heating technique used for thermal conductivity and thermal diffusivity measurements. This technique uses a thin, plane, electrically insulated resistive element, usually in a spiral pattern, as both the temperature sensor and the heat source. Heating element is placed between two test samples of the same material. By recording the increase in resistance as a function of time while heating with an electrical current pulse, the thermal conductivity can be deduced from one single transient recording.

In Chapter 7, the effect of BN fillers on the thermal conductivity of thiol-acrylate-epoxy matrix was investigated. Thermal conductivity was measured using the Transient Hot Bridge method by a THB 100 device from Linseis Messgeräte GmbH. A HTP G 9161 sensor was used with a 3x3 mm^2 of area calibrated with poly (methyl methacrylate) (PMMA), borosilicate crown glass, marble, Ti-Al alloy and titanium. Two equally polished rectangular samples were placed in each one of the faces of the sensor. Due to the small size of sensor, side effects can be neglected. Samples were tested under 10 mA current during 100 s. TC analysis were conducted at *Departament de Màquines i Motors Tèrmics* of *Universitat Politècnica de Catalunya*.

2.6.3. Thermal Mechanical Analysis (TMA)

Polymeric materials suffer dimensional changes, contraction or expansion, during the formation of the network or when are subject to heating/cooling processes.

Thermomechanical analysis (TMA) measures changes in sample length or volume as a function of temperature or time under load at atmospheric pressure. TMA analysis can be used to determinate the coefficient of linear thermal expansion (CTE).

In this investigation, TMA analysis were performed to evaluate the CTE of dual-curing thermosets loaded with BN particles, used in Chapter 6. A Mettler and Toledo TMA SDTA840 were used in static force mode. Cured samples were supported by the clamp and a silica disc to distribute the force uniformly and heated at 5 K/min from 35 °C to needed rubber state temperature. A minimum force of 0.01 N was applied to avoid results distortion. The coefficients of thermal expansion (CTEs) in the glassy state of the material were calculated as follows:

$$CTE = \frac{1}{L_0} \cdot \frac{dL}{dT} = \frac{1}{L_0} \cdot \frac{dL/dt}{dT/dt} \quad (34)$$

Where L is the thickness of the sample, L_0 the initial length and t and T are, respectively, time and temperature. TMA analysis were carried out at *Laboratori de Màquines i Motors Tèrmics* of *Universitat Politècnica de Catalunya.*

2.7. References

[1] Turi, Edith A., Thermal Characterization of Polymeric Materials , Academic Press, Inc., New York, NY, US, 1981.

[2] G. Peter R., de H. James A., Fourier Transform Infrared Spectrometry, second edition, John Wiley & Sons Inc. , Hoboken, New Jersey, USA, 2006.

[3] A.O. Konuray, X. Fernández-Francos, X. Ramis, Curing kinetics and characterization of dual-curable thiol-acrylate-epoxy thermosets with latent reactivity, React. Funct. Polym. 122 (2018) 60–67. https://doi.org/10.1016/j.reactfunctpolym.2017.11.010.

[4] R. Thomas, C. Sinturel, J. Pionteck, H. Puliyalil, S. Thomas, In-situ cure and cure kinetic analysis of a liquid rubber modified epoxy resin, Ind. Eng. Chem. Res. 51 (2012) 12178–12191. https://doi.org/10.1021/ie2029927.

[5] X. Fernàndez-Francos, S.G. Kazarian, X. Ramis, À. Serraa, Simultaneous monitoring of curing shrinkage and degree of cure of thermosets by attenuated total reflection fourier transform infrared (ATR FT-IR) spectroscopy, Appl. Spectrosc. 67 (2013) 1427–1436. https://doi.org/10.1366/13-07169.

[6] S. Vyazovkin, N. Sbirrazzuoli, Isoconversional kinetic analysis of thermally stimulated processes in polymers, Macromol. Rapid Commun. 27 (2006) 1515–1532. https://doi.org/10.1002/marc.200600404.

[7] M.S.-T. acta, undefined 2003, The determination of activation energy from linear heating rate experiments: a comparison of the accuracy of isoconversion methods, Elsevier. (n.d.). https://www.sciencedirect.com/science/article/pii/S0040603103001448?casa_token=Cp66UFsHBv4AAAAA:uf0fuJUDB5JYqt4a-L9Dbuk6q8eBK-zgiJFIVSA6ralAyUNxv3JjRmFed_GP92-HijQ5RqDkuw (accessed June 9, 2021).

[8] X. Fernandez, J.M. Salla, A. Serra, A. Manteco´n, M. Manteco´n, X. Ramis, Cationic Copolymerization of Cycloaliphatic Epoxy Resin with a Spirobislactone with Lanthanum Triflate as Initiator: I. Characterization and Shrinkage, Wiley Online Libr. 43 (2005) 3421–3432. https://doi.org/10.1002/pola.20801.

[9] S. Vyazovkin, N. Sbirrazzuoli, Isoconversional Kinetic Analysis of Thermally Stimulated Processes in Polymers, Wiley Online Libr. 27 (2006) 1515–1532. https://doi.org/10.1002/marc.200600404.

[10] Q. Guo, Thermosets: Structure, properties, and applications: Second edition, Elsevier, Amsterdam, Netherlands, 2017. https://doi.org/10.1016/C2015-0-06205-0.

[11] X. Fernández-Francos, A.-O. Konuray, A. Belmonte, S. De la Flor, À. Serra, X. Ramis, Sequential curing of off-stoichiometric thiol–epoxy thermosets with a custom-tailored structure, Polym. Chem. 7 (2016) 2280–2290. https://doi.org/10.1039/C6PY00099A.

[12] A. Belmonte, X. Fernández-Francos, À. Serra, S. De la Flor, Phenomenological characterization of sequential dual-curing of off-stoichiometric “thiol-epoxy” systems: Towards applicability, Mater. Des. 113 (2017) 116–127. https://doi.org/10.1016/j.matdes.2016.10.009.

[13] A. Belmonte, D. Guzmán, X. Fernández-Francos, S. De la Flor, Effect of the network structure and programming temperature on the shape-memory response of thiol-epoxy “click” systems, Polymers (Basel). 7 (2015) 2146–2164. https://doi.org/10.3390/polym7101505.

[14] R. Brown, Handbook of polymer testing: short-term mechanical tests, (2002). http://www.opengrey.eu/item/display/10068/645284 (accessed June 27, 2021).

[15] B. Duncan, Developments in testing adhesive joints, in: Adv. Struct. Adhes. Bond., Elsevier Inc., 2010: pp. 389–436. https://doi.org/10.1533/9781845698058.3.389.

[16] D. Santiago, A. Fabregat-Sanjuan, F. Ferrando, S. De La Flor, Recovery stress and work output in hyperbranched poly(ethyleneimine)-modified shape-memory epoxy polymers, J. Polym. Sci. Part B Polym. Phys. 54 (2016) 1002–1013. https://doi.org/10.1002/polb.24004.

[17] A. Belmonte, C. Russo, V. Ambrogi, X. Fernández-Francos, S.D.L. Flor, Epoxy-based shape-memory

actuators obtained via dual-curing of off-stoichiometric “thiol-epoxy” mixtures, Polymers (Basel). 9 (2017). https://doi.org/10.3390/polym9030113.

[18] M. Alvarado, È. Navarrete, A. Romero, J. Ramírez, E. Llobet, Flexible Gas Sensors Employing Octahedral Indium Oxide Films, Sensors. 18 (2018) 999. https://doi.org/10.3390/s18040999.

[19] M. Alvarado, S. De La Flor, E. Llobet, A. Romero, J.L. Ramírez, Performance of flexible chemoresistive gas sensors after having undergone automated bending tests, Sensors (Switzerland). 19 (2019). https://doi.org/10.3390/s19235190.

DUAL-CURING THIOL-ACRYLATE-EPOXY
THERMOSETS FOR FUNCTIONAL APPLICATIONS
Claudio Russo

Chapter 3.

Characterization of sequential dual-curing of thiol-acrylate-epoxy systems with controlled thermal properties

European Polymer Journal **2019**,112,376-388

DUAL-CURING THIOL-ACRYLATE-EPOXY
THERMOSETS FOR FUNCTIONAL APPLICATIONS
Claudio Russo

Characterization of sequential dual-curing of thiol-acrylate-epoxy systems with controlled thermal properties

Claudio Russo[1], Àngels Serra[2], Xavier Fernández-Francos[3], Silvia De la Flor[1].

[1]Department of Mechanical Engineering, Universitat Rovira i Virgili, Av. Països Catalans 26, 43007 Tarragona, Spain.
[2]Department of Analytical and Organic Chemistry, Universitat Rovira i Virgili, C/Marcel·lí Domingo s/n, 43007, Tarragona, Spain.
[3]ThermodynamicsLaboratory, ETSEIB, Universitat Politècnica de Catalunya, Av. Diagonal 647, 08028 Barcelona, Spain.

Abstract

In this work, a novel sequential dual-curing system based on thiol-acrylate-epoxy formulations is developed and characterized. Both reaction stages are thermally activated and sequentially relies on difference in the kinetics of the reactions involved. The viability of this system is successfully tested for low curing temperatures and the kinetic of the entire process is completely characterized. Differential scanning calorimetry and Fourier transform infrared spectroscopy analysis revealed an adequate separation between the reactions that leads to a wide interval of time during which the intermediate material can be considered stable. Applicability tests on the resulting thermosets showed the high capability of the intermediate materials to be conformed in complex shapes that can be fixed by means of the second curing stage. This system also shows great potential to be used as adhesive bonding taking advantage of the two-step curing process.

Keywords: Dual-curing; click-chemistry; thiol; acrylate; epoxy; functional material.

---

1. Introduction

Nowadays thermosets cover a broad range of applications thanks to their excellent thermal and mechanical properties (i.e., aviation, automobile, structures or coatings) [1]. Their properties rely on a crosslinked network structure formed during an irreversible curing process that has to be strictly controlled in order to obtain the required shapes and properties. The increasing need to reach complex shape designs [2] to spread the fields of application (i.e., bio-inspired devices or shape-changing materials)

is driving the scientific community to experimenting with new curing techniques, which allows to overcome thermosets limitations in shape [3].

Over the last few years, dual-curing polymer systems have attracted a growing interest because of the enhancement they provide in thermosets processing. A dual-curing process is defined as a combination of two distinct crosslinking reactions taking place simultaneously or sequentially [4]. Combining two sequential curing reactions, we obtain intermediate materials that maintain the ability to react upon application of a second stimulus, achieving fully cured materials with a new set of properties. Sequential dual-curing facilitates ease in processing and handling if the intermediate materials are chemically stable and their properties tailorable. Successful sequential dual-curing procedure requires that (i) both polymerization reactions are selective and compatible in order to avoid undesired reactivity effects and inhibition; (ii) they can be triggered by different external stimuli such as UV light or temperature, or else they can be controlled from a kinetics point of view.

To obtain such system, multiple approaches and a large variety of reactions are possible. “Click chemistry” defines a class of reactions with some characteristics, such as high efficiency, versatility and selectivity [5–7], which represent a valuable tool for sequential dual-curing. Among them, thiol-click reaction has attracted great interest due to their advantages (high conversion, solvent-free, oxygen resistance, etc.) [8–10] which makes them suitable to prepare crosslinked polymers in a fast and efficient way.

Michael-type additions, also included in the group of click reactions, are widely used in dual curing processes, because of the variety of commercially available nucleophiles (Michael donors) and activated double bond compounds (Michael acceptors) that can be used in such processes. Prominent Michael acceptors are acrylates because of a good combination of reactivity, versatility, availability and cost. One of the most common co-reactants for acrylates are thiol (thio-Michael addition). However, thermosetting networks formed by thiol-acrylate reaction generally exhibit flexible structures which limit their applications [11].

A promising way to enhance the mechanical properties is to combine a thiol-acrylate reaction with a thiol-epoxy reaction. Thiol-epoxy thermosets already have different applications such as high-performance coatings, adhesives, composites [5] and shape memory materials [12]. Belmonte et al. have successfully developed shape-memory actuators by taking advantage of the sequential dual-curing of off-stoichiometric thiol-epoxy formulations [13]. Combining these materials with liquid-crystalline networks (LCN) forming films in a sandwich-like configuration, they were able to obtain innovative

free-standing thermally-triggered “two-way” shape-memory actuators which show an actuator behaviour that can be modulated through the configuration and the stretching level of the LCN [14,15]. The dual-cured material is the substrate, strongly adhered to the LCN layer, that is used as the stress-applying component in the above-mentioned actuator. The key to the successful application of the dual-curing scheme lies in the intermediate material properties: (i) enough storage stability in order to handle the materials and produce the actuator and (ii) the presence of unreacted groups in the partially cured material that will ensure good interfacial contact and good adhesion after completion of the second curing process.

Now, the efforts of our group are focused on the development of a similar actuator with a faster and easier activation of the shape memory effect, to reach a greater energy efficiency and make it compatible with an electric control of the temperature. For this purpose, we need to develop custom-tailored thermosets obtained by dual curing procedures with lower transitions temperatures (T_g) and controlled intermediate and final material properties.

A possible way to reduce T_g could be the preparation of thiol-acrylate-epoxy thermosets by a dual-curing process, combining thiol-acrylate Michael addition and thiol-epoxy reaction. The above-mentioned reactions were already used in dual-curing systems. Konuray et al. [16] developed a dual-curing system where the first curing reaction is the thiol-Michael reaction triggered by UV light (a photobase generator was used as catalyst), and the second reaction is a thiol-epoxy reaction between the remaining thiol groups and the epoxides taking place at higher temperature. Jin et al. [17] prepared thiol-epoxy-acrylate hybrid polymer networks combining nucleophilic thiol-acrylate Michael addition and thiol-epoxy reactions in a one-pot simultaneous dual-cure catalysed by *1,8-diazabicyclo[5.4.0]undec-7-ene* (DBU) at 80°C.

Jian et al. [11] obtained hybrid networks by thiol-epoxy/thiol–acrylate polymerization processes in which both reactions are triggered by irradiation with UV light by use of a photobase generator. Even if reactions proceeded sequentially without a clear separation, they found that thiol–acrylate reactions and acrylate homopolymerization were faster and more efficient than the thiol - epoxy reactions, which reduces the control of the curing process. Gonzalez et al. [18] studied the use of the Aza-Michael addition (amine-acrylate) at room-temperature processing of dual-curing formulations and reported much faster kinetics than those commonly observed for amine-epoxy addition [19]. Conversely, the kinetics of Michael reaction are expected to be faster than thiol-epoxy reaction because the nucleophilic addition occurs faster to the acrylate than

to the epoxy, and especially because of the slow activation of the thiol-epoxy reaction caused by its strongly autocatalytic character [10,20].

In the present work, we investigate the viability of a thiol-acrylate-epoxy sequential dual-curing system where both reactions are activated using a single thermal catalyst. This system relies on the faster curing kinetics of the thiol-acrylate Michael addition compared to the thiol-epoxy reaction. We expect the thiol-acrylate reaction to take place first, delaying the onset of the thiol-epoxy until the complete conversion of the acrylate groups. Therefore, we should obtain a stable thiol-acrylate structure, which can be processed at room temperature. After that, thiol-epoxy reaction could finally take place leading to a fully cured thermoset. The extent of the first reaction is regulated by the acrylate/thiol equivalent ratio $r_{acrylate}$, which also controls the intermediate material characteristics.

To this purpose, a ternary reactive system containing an epoxy resin (*diglycidylether of Bisphenol A*, DGEBA), an acrylate monomer (*tricyclo[5.2.1.02,6]decanedimethanol diacrylate*, TCDDA, or *pentaerythritol tetraacrylate*, PTTA) and a thiol crosslinker (*pentaerythritoltetrakis(3-mercaptopropionat*e), S4) is studied. Two different tertiary amines (*1-methylimidazole*, 1MI, and *4-(N,N-dimethylamino)pyridine*, DMAP) are used as basic/nucleophilic catalysts and their effects on the curing process are determined. We have focused on the analysis of how both reactions can be combined during a thermally-activated cure and the possibility to obtain a chemically stable material. A fixed $r_{acrylate}$ was used since our aim is to prove the viability of a thermally activated dual-curing procedure on such systems. The curing process was monitored by means of differential scanning calorimetry (DSC) and Fourier-transform infrared spectroscopy (FTIR). Isoconversional integral analysis were also performed to obtain further information about the curing kinetics of both reactions and to predict the final kinetic behaviour of the dual curing system. Finally, some application tests were made with the materials obtained to understand their potential uses.

2. Experimental part

2.1. Materials

Diglycidyl ether of bisphenol A (DGEBA, EPIKOTE™ Resin 828, with an epoxy equivalent weight of 187 g/eq) was supplied by Hexion Specialty Chemicals. *Pentaerythritol tetrakis(3-mercaptopropionate)* (S4, 122.17 g/eq), *tricyclo[5.2.1.0$_{2,6}$]decanedimethanol diacrylate* (TCDDA, 152.2 g/eq) and *pentaerythritol tetraacrylate* (PTTA, 88.0 g/eq) were provided by Sigma-Aldrich (St. Louis, MO, USA). *1-Methylimidazole* (1MI) was purchased

from Sigma-Aldrich and *4-(N,N-dimethylamino)pyridine* (DMAP) was purchased from Fluka (Switzerland). The epoxy resin was dried under vacuum at 80 °C for 2 h prior to use and all the other components were used as received. The acrylates TCDDA and PTTA were alternatively mixed with S4and DGEBA with a fixed ratio between acrylate groups and thiol groups($r_{acrylate}$ = 0.6). The catalysts 1MI and DMAP were used in a proportion of 0.25 phr (parts of initiator for hundred parts of mixture) or 0.05 phr, respectively. The pure thiol-acrylate ($r_{acrylate}$ = 1) and thiol-epoxy($r_{acrylate}$= 0) formulations were also studied. The samples were pre-pared by manual stirring of all components in a glass vial and analysed immediately after. Components were mixed in a specific order: (i) thiol were premixed with the catalysts; (ii) DGEBA was added, and the mixture was manually stirred; (iii) finally the acrylate was added and the whole mixture was stirred again. The entire preparation was carried out with the vial immersed in a pot with crushed ice to prevent premature activation of the first curing reaction, thus allowing a more precise characterization of the curing kinetics. The composition and notation of the pure formulations under investigation is detailed in **Table 3.1**,whilecomposition and notation of dual formulations with $r_{acrylate}$= 0.6 are presented in **Table 3.2**.

Table 3.1. Composition of the pure formulations of study.

	Formulation	Thiol (wt%)	DGEBA (wt%)	Acrylate (wt%)
Thiol-Epoxy	S4DGEBA.1MI	39.5	60.5	0.0
	S4DGEBA.DMAP			
Thiol-Acrylate	S4TCDDA.1MI	44.5	0.0	55.5
	S4TCDDA.DMAP			
	S4PTTA.1MI	58.1	0.0	41.9
	S4PTTA.DMAP			

Table 3.2. Composition of the dual formulation with a $r_{acrylate}$=0.6.

	Formulation	Thiol (wt%)	DGEBA (wt%)	Acrylate (wt%)
Dual Formulations	S4TCDDA06.1MI	42.4	25.9	31.7
	S4TCDDA06.DMAP			

2.2. Characterization techniques

A differential scanning calorimeter (DSC) Mettler DSC-821e, calibrated using an In standard (heat flow calibration) and an In-Pb-Zn standard (T calibration), was used to study the cure. Samples of approximately 5 mg were tested in aluminium pans with a

pierced lid in N_2 atmosphere with a gas flow of 50 mL/min. Dynamic studies between 0 and 200°C with a heating rate of 10°C/min were performed to characterize the curing process and measure final T_gs. Isothermal curing were also performed at 30, 60, 80 and 100 °C. The calorimetric degree of conversion was determined as $x_{DSC} = \Delta h/\Delta h_{tot}$, where Δh is the reaction heatreleased up to a temperature T or time t and Δh_{tot}, is the totalreaction heat evolved in a dynamic run. The calorimetric rate was determined as $dx_{DSC}/dt = (dh/dt)/\Delta h_{tot}$, where dh/dt is the heat flow. Intermediate T_g were measured with a two-step DSC procedure: (i) isothermal curing at 30°C until the first reaction comes to an end; (ii) dynamic heating from -20 to 100 °C.

A FTIR spectrometer Bruker Vertex 70 with an attenuated total reflection accessory with thermal control and a diamond crystal (Golden Gate Heated Single Reflection Diamond ATR, Specac-Teknokroma) and equipped with a mid-band liquid nitrogen-cooled mercury–cadmium–telluride (MCT) detector was used to monitor thiol, acrylate and epoxy conversions during isothermal curing at temperatures ranging from 30 to 80°C. Real-time spectra were collected in absorbance mode with a resolution of 4 cm^{-1} in the wavelength range from 4000 to 600 cm^{-1} averaging 20 scans for each spectrum. The characteristic absorbance peak of the acrylate at 810 $cm^{-1}$was used to monitor the conversion of the acrylate groups during the thiol-acrylate Michael reaction. The disappearance of the absorbance peak at 915 cm^{-1} (epoxy bending) [21] was used to monitor the reaction of epoxy groups. The absorbance peak at 3500 cm^{-1}, related to the formation of OH during the epoxy-thiol reaction, was also used to monitor the conversion of the epoxy groups only from a qualitative point of view. Absorbances of each scanned sample were normalized with that of the ester group (1720 cm^{-1}). Acrylate conversion of functional groups is calculated by Eq. (1),

$$x_{acrylate} = 1 - \frac{A'_{810}}{A'_{810,0}} \quad (1)$$

Where A'_{810} and $A'_{810,0}$ are the normalized absorbances of the acrylate peak at 810 cm^{-1} at a given reaction time and at the beginning of the curing process, respectively.

Since the direct evaluation of epoxy group conversion could be difficult [22], instead of epoxy conversion, we have calculated the relative intensity of the epoxy band using Eq. (2).

$$a_{epoxy} = \frac{A'_{915}}{A'_{915,0}} \quad (2)$$

Where A'_{915} and $A'_{915,0}$ are the normalized absorbances of the epoxy peak at 915 cm^{-1} at a given reaction time and at the beginning of the curing process, respectively.

3. Theoretical part

3.1. Reaction mechanisms

The curing mechanism of thiol-acrylate Michael addition can be catalysed by bases or nucleophilic initiators [23]. For a weakly basic but nevertheless nucleophilic amine such as 1MI, the thiol-epoxy reaction would take place following the nucleophilic mechanism [5,23], represented in **Scheme 3.1**, involving a number of reaction steps. First, the nucleophilic Michael addition of the 1MI to the acrylate (**Scheme 3.1.a**) results in an enolate anion stabilized by resonance and by the positive charge of the imidazolium cation. Moreover, due to its basic character, the enolate is capable to abstract a hydrogen from the thiol producing the thiolate and a β-imidazolium ester (**Scheme 3.1.b**). The strongly nucleophilic thiolate anion is able to undergo direct conjugate addition to the acrylic C=C bond yielding an enolate intermediate that deprotonates additional thiol generating the reaction product and regenerating the thiolate anion, which continues propagating the reaction (**Scheme 3.1.c**). Thanks to the enolate stabilization in the initiation step, the thiolate formation in (a) could have a lower reaction rate than the recuperation of the thiolate in (**Scheme 3.1.c**). Lastly, as shown in (**Scheme 3.1.d**), there is a possibility of the 1MI regeneration through the nucleophilic displacement, but we assume that this is a minor and slow process.

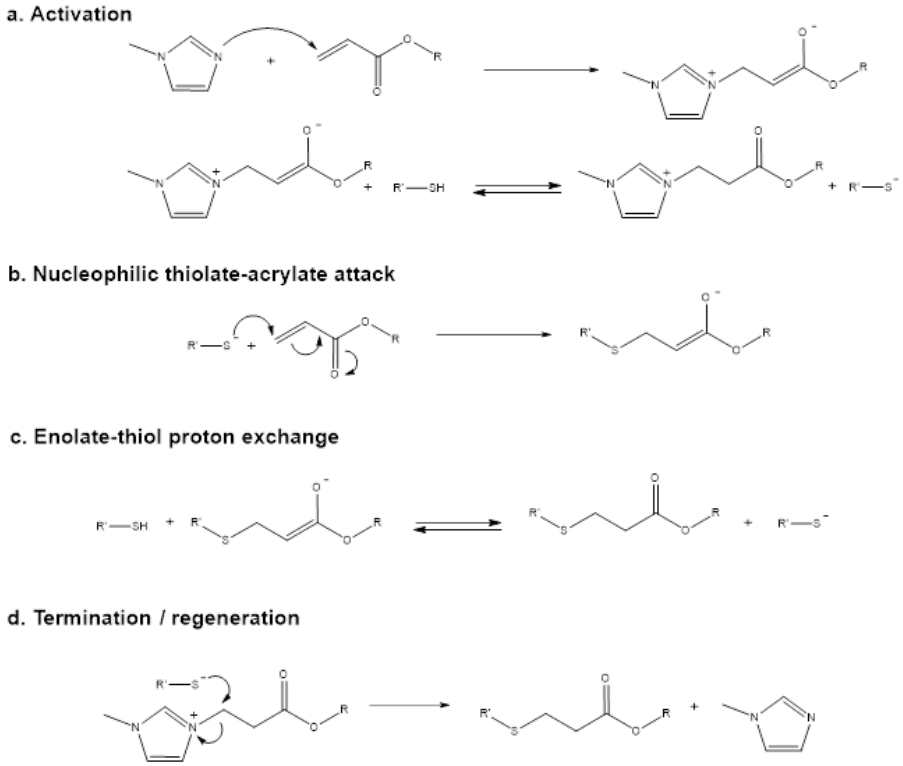

Scheme 3.1. Proposed curing mechanism of thiol-acrylate Michael reaction catalysed by tertiary amines.

Nucleophile-mediated thiol-epoxy reaction follows a similar reaction mechanism, as shown for weakly basic but nucleophilic tertiary amines such as 1MI and BDMA [24]. **Scheme 3.2** shows the proposed mechanism using 1MI as the initiator. The activation step (**Scheme 3.2.a**) starts with the nucleophilic attack of the tertiary amine on the epoxy ring. Then, the proton exchange between the alkoxide, produced in the previous step, and a thiol group yield a thiolate together with a hydroxyammonium compound. The thiolate anion follows the reaction by means of a nucleophilic addition to the epoxy ring, which leaves an alkoxide intermediate (**Scheme 3.2.b**). The thiolate regeneration in (**Scheme 3.2.c**) by proton exchange of the formed alkoxide with another thiol, leads to the thio–ether condensation product with a hydroxyl group (β-hydroxythio-ether). The initiator could be regenerated by a nucleophylic reaction (**Scheme 3.2.d**) which also leads to the reaction product, with a non-negligible contribution to the overall process [20]. Both activation and nucleophilic attack of the thiolate to the epoxide are catalysed by hydroxyl groups, therefore the hydroxyl groups produced in the thiol-epoxy reaction should favour the nucleophilic attacks to the epoxy ring [25,26], hence the reported strong autocatalytic effect [10,20]. Overall, the reaction mechanism is not different from

that of the base-catalysed thiol-epoxy reaction [10,27]. The main differences lie in the activation step (**Scheme 3.2.a**) and the existence of a regeneration (**Scheme 3.2.d**), which may have some consequence in terms of the reaction kinetics [10,20].

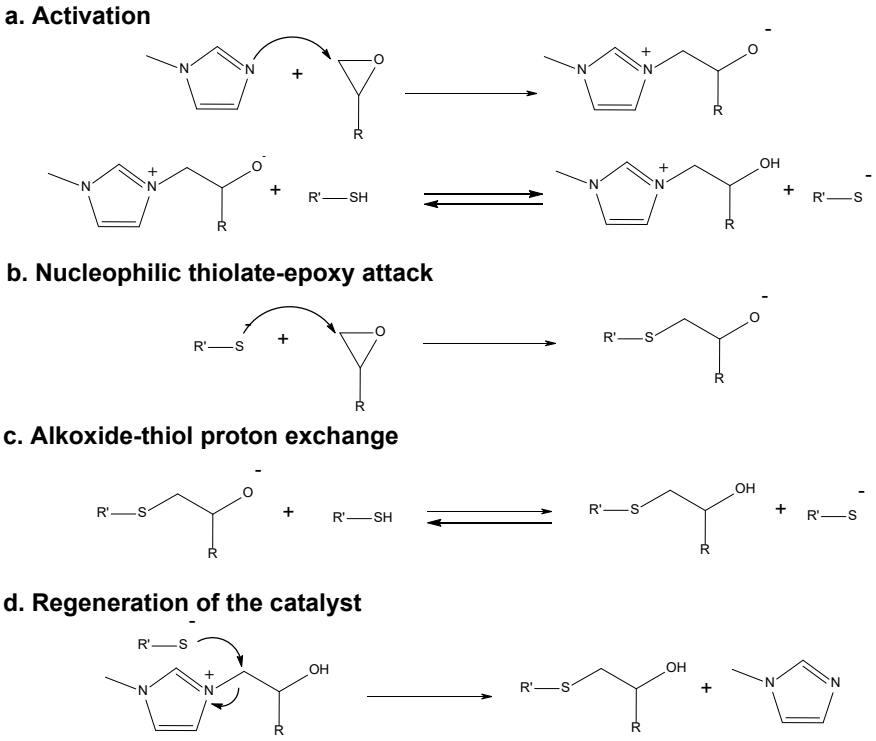

Scheme 3.2. Proposed curing mechanism of thiol - epoxy reaction catalysed by tertiary amines.

3.2. Network Formation

The crosslinking process is illustrated in **Scheme 3.3**. During the first curing stage the reaction between thiol and acrylate groups takes place forming a first network made up of thiol (green) and acrylate(red) in which an excess of thiol groups is left unreacted. Consequently, the second curing stage, consisting in the reaction between unreacted thiol groups and epoxy groups (blue), completes the network build up leading to a fully crosslinked structure without any unreacted ends. Since the thiol-acrylate and thiol-epoxy networks are quite similar, the resulting structure is expected to be homogeneous with a narrow glass transition. The prediction of the crosslinking degree of the intermediate state represents a key factor in dual curing formulation design. In this case itis of interest, therefore, to analyse whether gelation occurs during the thiol-acrylate reaction, in the first stage of the curing process. Although Scheme 1 indicates the presence of different reaction steps (i.e., activation, propagation,...), the cyclic

propagation of the thiol-Michael reaction through the nucleophilic attack of the thiolate to the acrylate, followed by regeneration of the thiolate anion, should take place in a random and step-wise manner as in other reactions such as epoxy-acid [28] or epoxy-phenol [29] processes.

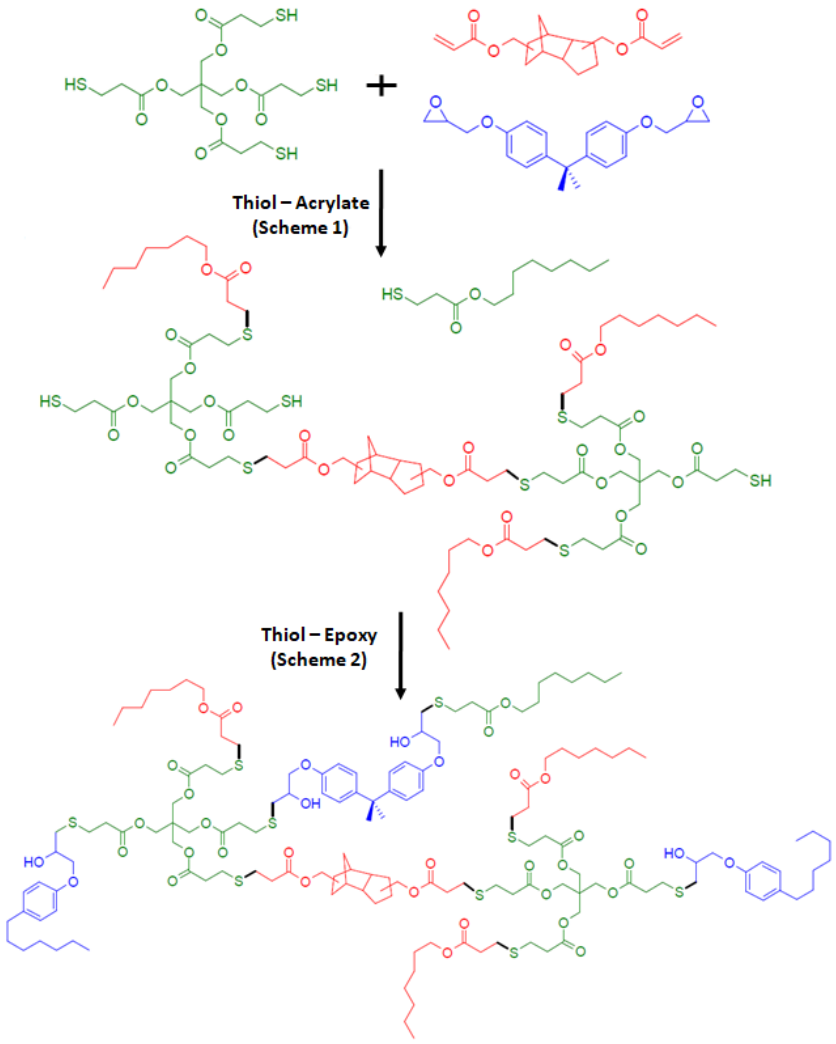

Scheme 3.3. Expected network structure formed by thiol-acrylate-epoxy from DGEBA, TCDDA and S4 formulations.

Neglecting the effect of the initiator-acrylate adducts, the molecular/network structure build-up process can therefore be approximately analysed assuming ideal step-wise

behaviour [1] , and therefore the conversion of acrylate groups at the gel point can be calculated using the well-known Flory-Stockmayer expression:

$$x_{acrylate,gel} = \left[r_{acrylate} \cdot \left(f_{acrylate} - 1\right) \cdot \left(f_{thiol} - 1\right)\right]^{-1/2} \quad (3)$$

where $f_{acrylate}$ and f_{thiol} are the average functionality of epoxy and thiol monomers and $r_{acrylate}$ is defined as the ratio between acrylate and thiol equivalents. This only produces a valid gel point conversion for values of $r_{acrylate}$ higher than r_c, where r_c is the critical gelation ratio (4).

$$r_c = \frac{1}{\left(f_{acrylate} - 1\right) \cdot \left(f_{thiol} - 1\right)} \quad (4)$$

Moreover, using the Fox equation [1], we can estimate the glass transition temperatures of the intermediate material ($T_{g,1}$) and the final thermoset ($T_{g,2}$) for any $r_{acrylate}$. To perform this calculation, T_g of the uncured epoxy-thiol system ($T^0_{g,(e-t)}$) and T_g of the cured epoxy-thiol ($T^\infty_{g,(e-t)}$) and acrylate-thiol systems ($T^\infty_{g,(a-t)}$) are required.

$$\frac{1}{T_{g,1}} = \frac{w_{a-t}}{T^\infty_{g(a-t)}} + \frac{1 - w_{a-t}}{T^0_{g,(e-t)}} \quad (5)$$

$$\frac{1}{T_{g,2}} = \frac{w_{a-t}}{T^\infty_{g(a-t)}} + \frac{1 - w_{a-t}}{T^\infty_{g,(e-t)}} \quad (6)$$

where w_{a-t} is the weight fraction of the acrylate plus the part of thiol which participate to the first curing reaction.

3.3. Isoconversional kinetics analysis

The curing kinetics have been analysed using isoconversional method [30]. This methodology is based on the assumption that the rate dx/dt of a given process can be expressed as separate functions of temperature T and degree of conversion x

$$\frac{dx}{dt} = k(T)f(x) \quad (7)$$

$k(T)$ is the rate constant, which is usually expressed with an Arrhenius-like temperature dependence, $k(T) = k_0 \cdot exp(-E/RT)$, where k_0 is the pre-exponential factor and E is the activation energy. $f(x)$ is the kinetic model function representing the underlying reaction mechanism and depends on the extent of conversion x. k_0, E and $f(x)$ represent the so-called kinetic triplet, which are necessary to completely describe a

process. Under the isoconversional assumptions, the reaction mechanism does not depend on the temperature programme and one can write

$$\frac{dln(dx/dt)}{dT^{-1}} = \frac{dln\big(f(x)\big)}{dT^{-1}} + \frac{dln\big(k(T)\big)}{dT^{-1}} \equiv -\frac{E_x}{R} \tag{8}$$

Where E_x is the apparent activation energy. Linearization of the rate expression leads to the differential isoconversional method of Friedman [30–32], but in the present work we propose to use an integral isoconversional method. The rate expression can be integrated under isothermal conditions [30] as follows:

$$g(x) = \int_0^x \frac{dx}{f(x)} = \int_0^t k_0\, exp\left(\frac{-E}{RT}\right) dt = k_0\, exp\left(\frac{-E}{RT}\right) t \tag{9}$$

Where $g(x)$is the integral form of the kinetic model. Now, taking the natural logarithm of both sides of the equation, we obtain:

$$\ln t_{x,i} = \ln\left[\frac{g(x)}{k_{0,x}}\right] + \frac{E_x}{RT_i} \tag{10}$$

Plotting $\ln t_{x,i}$ versus $1/RT_i$ at fixed conversion x and at different curing temperature T_is we obtain a line with E_x as slope and $\ln\big[g(x)/k_{0,x}\big]$ as the intercept at the origin.

4. Results and discussion

4.1. Studies on pure formulations

First of all, we investigated the curing kinetics of pure thiol-epoxy and pure thiol-acrylate formulations by means of DSC isothermal ana-lysis and isoconversional analysis. The results obtained will allow us to better understand the curing behaviour of the complete thiol-acrylate-epoxy formulations. A heat released of about 60 KJ/eq by thiol-acrylate reaction catalysed by 1MI (0.25 phr), measured by means of DSC dynamic scan at 10 °C/min, was taken as a reference given that no similar data were found in the literature. **Figure 3.1** compares the isothermal curing at 30 °C performed on pure acrylate–S4 formulations with different catalyst. It is shown that in the case of PTTA, the use of 0.05 phr of DMAP leads to a faster activation of the curing reaction and shorter curing time. No significant effects of the catalyst on reaction time were detected using TCDDA. In this case, the use of DMAP seems only to overcome the reaction complexities evidenced by the shape of the curing peeks obtained using 1MI as catalyst. However, the reaction between TCDDA and S4 results in a longer re-action time, with both catalysts, possibly

due to the presence of some poisoning (acidic) impurities in TCDDA, or else some steric hindrance caused by the rigid tricyclic structure.

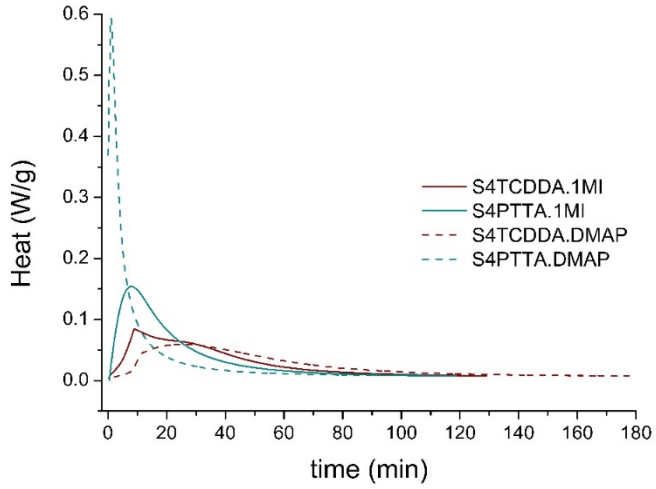

Figure 3.1. Effects of the catalyst and acrylate type on isothermal DSC analysis at 30 °C of thiol-acrylate formulations.

Figure 3.2.a compares the isothermal curing at 30 °C of pure DGEBA-S4and TCDDA-S4 formulations. It is clearly observed that, because of the slower activation and kinetics of the thiol-epoxy reaction, the two re-actions take place in different ranges of time leaving an overlapping region which almost disappears using DMAP as catalyst. Using PTTA as acrylate (**Figure 3.2.b**), the overlapping decreases because of the faster thiol-acrylate reaction. PTTA and DMAP seems to be the best combination in terms of separation but it leads to difficulties in controlling the first reaction.

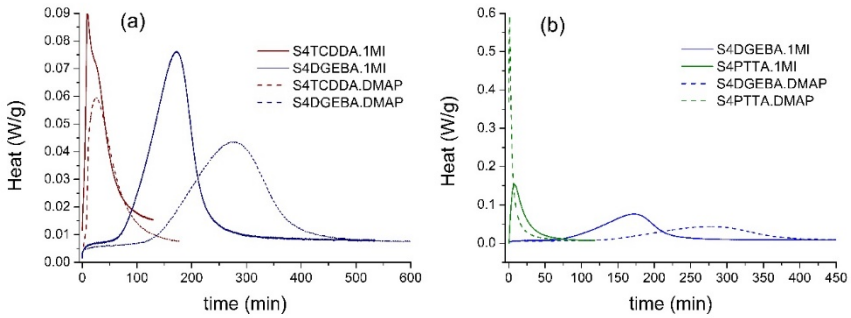

Figure 3.2. Comparison between DSC isothermal analysis of thiol-epoxy and thiol-acrylate (TCDDA in (a) and PTTA in (b)) formulations obtained using 1MI and DMAP as initiators.

Therefore, a good separation between thiol-acrylate and thiol-epoxy systems would be obtained using TCDDA as acrylate and DMAP as initiator, or else using PTTA as acrylate. **Table 3.3** collects some characteristic parameters of the curing process along with glass transition temperatures and heat capacity variation associated with the transition. The heat released during isothermal curing of thiol-acrylate was found to be around 40–50 kJ/eq, but our measurements are affected by experimental error resulting from the fast initial reaction rate and the slow kinetics at the end of the curing process. The reaction heat values for the epoxy-thiol formulations were measured during isothermal curing at 60 °C instead of the 30 °C (too long reaction time and vitrification led to unreliable results at 30 °C), producing values around 130 kJ/eq, similar to those previously reported [24]. In this case, the slow activation of the thiol-epoxy process and the autocatalytic character of the reaction, leading to a faster re-action end, ensured a more reliable detection of the reaction heat. Glass transition temperatures of the obtained thermosets were also measured (**Table 3.3**).

Table 3.3. Calorimetric data: isothermal reaction heat measured after 60°C isothermal for S4DGEBA.1MI and S4DGEBA.DMAP and after 30°C isothermal for S4TCDDA.1MI, S4TCDDA.DMAP, S4PTTA.1MI, S4PTTA.DMAP.

Formulation	ΔH (J/g)	ΔH (kJ/eq)	$T_{g,0}$ (°C)	Δcp_0 (J/gK)	$T_{g,\infty}$ (°C)	Δcp_∞ (J/gK)
S4DGEBA.1MI	408	126	-34	0.393	50	0.25
S4DGEBA.DMAP	439	135				
S4TCDDA.1MI	166	45			13	0.34
S4TCDDA.DMAP	169	46				
S4PTTA.1MI	200	42			15	0.35
S4PTTA.DMAP	199	41				

S4DGEBA.DMAP shows a $T_{g,\infty}$ of 50 °C in accordance with results obtained in other works [13]. Regarding thiol-acrylate formulation, S4TCDDA.DMAP and S4PTTA.DMAP have a $T_{g,\infty}$ of, respectively, 13 °C and 15 °C. Although PTTA has a higher functionality than TCDDA, final thermosets do not show an appreciable difference in terms of $T_{g,\infty}$. This could be ascribed to the highly rigid structure of the linear and lesser-functional TCDDA monomer. Kinetic analysis of pure thiol-epoxy and thiol-acrylate formulations were performed with the purpose of obtaining the apparent activation energy of the thiol-epoxy (E_{th-epo}) and thiol-acrylate (E_{th-acr}) reactions, making use of the isoconversional integral method described in the theoretical section. For the thiol-epoxy reaction, isothermal curing of DGEBA.1MI formulation was carried out in the DSC at 60, 80 and

100 °C. For the thiol-acrylate reaction, the curing of S4TCDDA.1MI was monitored at 40, 60 and 80 °C by FTIR. The choice of different instruments to obtain kinetic data was caused by the difficulty of determining accurately the thiol-acrylate reaction kinetics by DSC (be-because of their very high reaction rate at higher temperatures, leading toa significant loss of data at the beginning of the process), and the precise determination of the epoxy group conversion in thiol-epoxy reactions using FTIR (because of overlapping signals) [5]. However, this change in methodology should produce equally good results if the curing temperature can be controlled in a suitable way. In **Figure 3.3** the conversion-time curves at different temperatures for both systems are represented. **Figure 3.3.a** shows that the thiol-acrylate reaction is very fast, with almost immediate activation after mixing, while **Figure 3.3.b** shows that the thiol-epoxy reaction is slower, with a clear au-to catalytic character with a long induction period before activation. This was expected from the discussion of the reaction mechanisms and the preliminary calorimetric analysis.

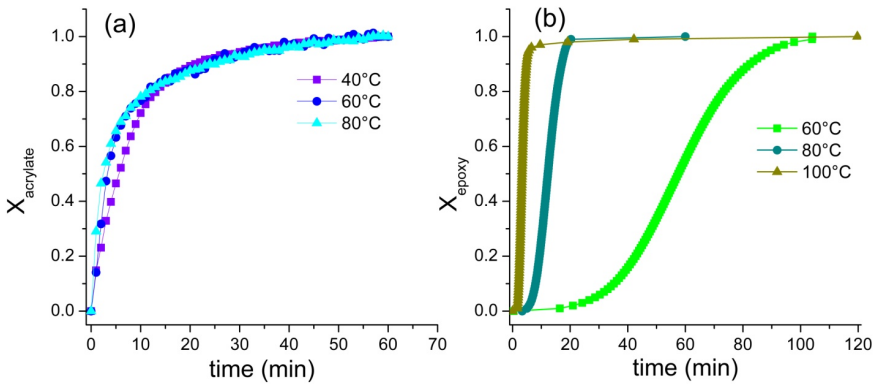

Figure 3.3. (a) FTIR acrylate conversion - time plots of TCDDA.DMAP formulations cured at 40, 60, 80 °C; (b) DSC conversion curves of S4DGEBA.DMAP formulations at 60, 80, 100 °C.

Although the reaction rates are comparable at higher temperatures, the thiol-epoxy reaction is clearly faster at lower temperatures (i.e., below 80–60 °C). Noticeably, the thiol-acrylate reaction has a very weak temperature dependence in contrast with the thiol-epoxy reaction. This is confirmed by the results of the is conversional analysis of both curing processes. In spite of the un-certainty in the analysis of kinetic data and the determination of the kinetic parameters, especially for the thiol-acrylate reaction at higher temperatures, the apparent activation energy of the thiol-acrylate re-action (E_{th-acr}) was found to be around 20 kJ/mol, while that of thethiol-epoxy reaction (E_{th-epo}) is about 70 kJ/mol. The values are ratherconstant, suggesting that the

underlying curing mechanisms do notchange significantly over the curing process. Such a high difference between E_{th-epo} and E_{th-acr} indicates that, in presence of both acrylate and epoxy groups, the reaction between thiol and acrylate is more favourable than thiol- epoxy, which would only take place when acrylate groups are close to the total conversion. In addition, the thiol-epoxy reaction would slow down more significantly than the thiol-acrylate reaction at lower temperatures, i.e., room temperature, in agreement with the preliminary calorimetric results reported in **Figure 3.2**. In consequence, a dual-curing system combining both reactions would show a better separation between the reaction processes and, therefore, a greater selectivity if the first stage were carried out at temperatures as low as room temperature. In the first stage, only the thiol-acrylate reaction would take place, with little overlap between the thiol-acrylate and the thiol-epoxy reaction. If the system were kept at the same temperature, the thiol-epoxy reaction would eventually activate and reach completion, but at a sluggish rate. Therefore, the second stage, where only the thiol-epoxy reaction would occur, should take place at a higher temperature to shorten the curing cycle. Following this procedure, an almost sequential and controllable dual-curing system could be achieved. Lastly, we were able to plot the T_gs of intermediate and final materials as a function of $r_{acrylate}$ by means of a theoretical evaluation based on Fox equation (**Figure 3.4**). The critical ratio $r_{critical}$ was calculated thanks to the Flory-Stockmayer theory, as explained in the theoretical part. As shown in **Figure 3.4**, a range of intermediate and final materials would be obtained using TCDDA and PTTA as acrylates. There is very little influence of the type of acrylate on the intermediate and final T_gs, but the material structure, especially in the intermediate state, would be entirely different. This is caused by the higher functionality of PTTA (f = 4), leading to lower critical ratios than TCDDA (f = 2) (see **Figure 3.4**). Depending on the value of $r_{acrylate}$, one might obtain a liquid or a partially crosslinked material with TCDDA or PTTA, respectively. The use of PTTA enables the preparation of partially crosslinked inter-mediate materials for a wider range of formulations. Taking into ac-count this evaluation, dual-curing formulations with $r_{acrylate}$=0.6 were prepared and characterized. We choose this particular ratio in order to work with an unbalanced proportion between acrylate and epoxy which ensures gelled intermediate materials for both acrylates, and in order to have a more balanced contribution of both thiol-acrylate and thiol-epoxy reactions in terms of reaction heat.

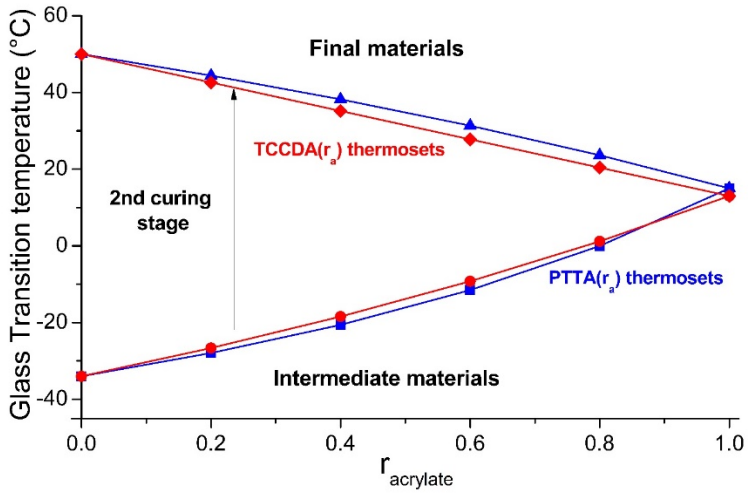

Figure 3.4. Theoretical evaluation of glass transition temperatures along with racrylate for TCDDA-DGEBA and PTTA-DGEBA dual curing formulations.

4.2. Viability of dual-curing of Thiol-Acrylate-Epoxy formulations

The viability of the dual-curing formulations has been analysed using DSC and FTIR. Calorimetric analyses have been carried out using0.05 phr of DMAP on account of the better results, in terms of reactions separation, evidenced in the previous section. However, FTIR analysis has been performed on dual formulations with both 1MI and DMAP. **Figures 3.5** and **3.6** show the isothermal curing at 30 °C of dual-curing formulations and the results of their calorimetric analysis are summarized in **Table 3.4**.

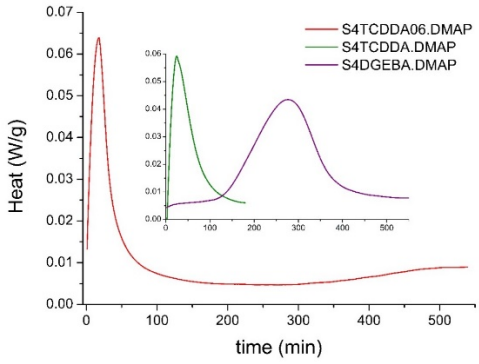

Figure 3.5. DSC thermograms of isothermal curing at 30°C of S4TCDDA06; DSC thermograms of isothermal curing at 30°C of S4DGEBA.DMAP and S4TCDDA.DMAP (inset).

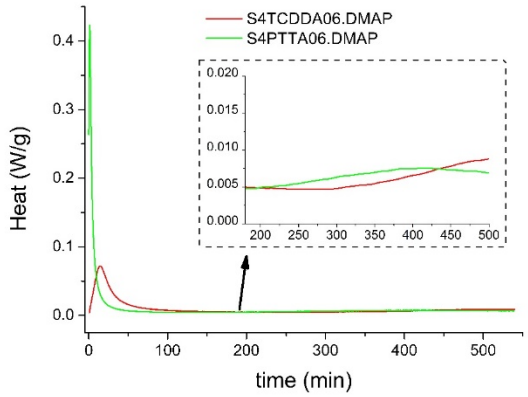

Figure 3.6. DSC isothermal analysis at 30°C of S4TCDDA06.DMAP and S4PTTA.DMAP.

Figure 3.5 shows the curing process of S4TCDDA06.DMAP at 30 °C and compares it with the curing of S4DGEBA.DMAP and S4TCDDA.DMAP at the same temperature. It can be noticed that the dual S4TCDDA06.DMAP shows two well-defined reaction regions which should be associated with the thiol-acrylate and the thiol-epoxy reactions, respectively. The first reaction peak takes place within the same time range as the neat S4TCDDA.DMAP system but, in contrast, the second reaction peak is significantly delayed and slowed down (peak onset at about 300 min) in reference to theS4DGEBA.DMAP system (peak onset at about 100 min). An interval of separation is clearly visible between the two stages proving that the two reactions are sequential. During this interval, even if the second reaction is already beginning it proceeds with a very low rate allowing us to obtain an intermediate material that could be considered as stable at room temperature. In addition, the reaction heat of 58 kJ/eq, released during the first stage (see **Table 3.4**), is quite close to the reference heat released by neat thiol-acrylate systems, confirming that the first process comes to an end. The significant delay and slowing down of the second reaction are mainly caused by the dilution of the thiol-epoxy formulation in the dual system. The dilution of epoxy groups would obviously slowdown the reaction, but it is the dilution of the concentration of catalytic hydroxyl groups coming from the oligomeric DGEBA structure and formed in the thiol-epoxy reaction that produce a further delay in the reaction onset and decrease in the reaction rate. Note that the thiol-acrylate reaction does not produce any species that can contribute to the catalysis of the thiol-epoxy reaction. This observation is in close agreement with our previous analysis of the reaction mechanism of thiol-epoxy systems [20]. In addition, termination, and trapping reaction in the thiol acrylate mechanism together with the partial consumption of the catalyst after the completion

of the first reaction, can lead to the reduction of available catalyst and active species for the second reaction.

Table 3.4. Isothermal reaction heats,ΔH_1 (Stage 1, 200 min at 30°C), ΔH_2 (Stage 2, 120 min at 60 °C); T_{g1} and T_{g2} obtained experimentally (using 0.05 phr of DMAP) measured, respectively after 200 min at 30°C and dynamic curing from 30-180 °C (10°C/min); $T_{g1,th}$ an $T_{g2,th}$ obtained by theoretical prediction.

Formulation	ΔH_1 (J/g)	ΔH_1 (kJ/eq)	ΔH_2 (J/g)	ΔH_2 (KJ/eq)	T_{g1} (°C)	T_{g2} (°C)	$T_{g2,th}$ (°C)	$T_{g2,th}$ (°C)
S4TCDDA06.1MI	55	56	179	129	-5	30	-9	28
S4TCDDA06.DMAP	121	58	168	121				
S4PTTA06.1MI	126	52	182	114	-10	39	-12	31
S4PTTA06.DMAP	140	58	164	102				

The curing process at 30 °C for the S4TCDDA06.DMAP and S4PTTA06.DMAP formulations are compared in **Figure 3.6**. The most visible difference is that PTTA gives a very fast reaction that makes the 1st stage quite difficult to control. The entire curing process is shifted to shorter times and the separation between the curing stages is more or less the same as that obtained with TCDDA. In both cases, the second curing stage is difficult to observe because of the very low reaction rate at which occurs, but the inset in **Figure 3.6** clearly shows the occurrence of the thiol-epoxy reaction. In any case, the results in **Figure 3.5** and **3.6** evidence that curing nearby room temperature delays the starting of the thiol-epoxy and promote the separation between the curing stages.

Table 3.4 shows some important parameters of the dual formulations under investigation. ΔH_1 values measured after the 1st stage at 30 °Care about 10 kJ/eq higher than the one measured for thiol-acrylate pure formulations. One could hypothesize this is caused by the occurrence of thiol-epoxy reaction to some little extent, but such discrepancy is more probably ascribed to the uncertainty associated with the determination of reaction heat from the DSC analysis of the neat thiol-acrylate formulations. Assuming that they are affected by the same experimental error of the pure formulations, these higher values could be ascribed toa fraction of thiol, which starts to react with the epoxy at such low reaction rate that it is not visible in the DSC thermograms. This will be later detected and discussed by FTIR analysis. The intermediate T_{g1}s were very similar to the predicted using the Fox equation, after completion of the thiol-acrylate reaction and before starting the thiol-epoxy reaction. With regards to the final T_{g2}, S4PTTA06 shows a T_{g2}=39°C that is quite higher than 30 °C

reached with the S4TCDDA06. The produced values are higher than those predicted by the Fox equation, but within experimental error. In addition, the Fox equation assumes ideal mixture between the thiol-epoxy and thiol-acrylate networks and is not able to consider other effects such as any structural effects or other secondary interactions between the thiol-acrylate and epoxy networks, as for example, hydrogen bonding.

The influence of the curing temperature was also investigated. **Figure 3.7** compares two curing process performed at 30 °C and 60 °C for S4TCDDA.DMAP. In this case, the second curing stage also comes to an end in a reasonable time. The heat released of 121 J/eq, similar to the value reported for similar epoxy-thiol reaction, is a further proof that confirms the completion of the 2nd stage. Unfortunately, the curing at 60 °C causes an important overlapping of the two reactions which undermines the sequentiality of the process. This could be expected taking into account the previous kinetics analysis of neat thiol-epoxy and thiol-acrylate systems.

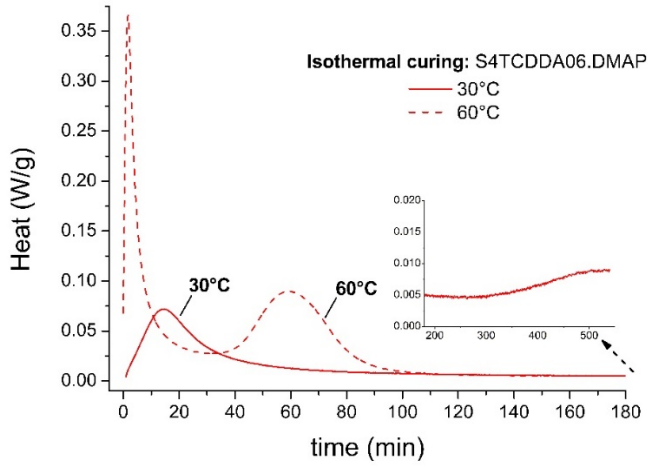

Figure 3.7. Comparison between isothermal curing in DSC at 30°C and 60°C of S4TCDDA06.

DSC results show that the low-temperature curing seems to ensure a sequential curing process with intermediate materials stable enough to manipulate before the second curing stage, which can be performed at higher temperature to accelerate it and ensure complete cure. However, the results of the calorimetric analysis are not precise enough in order to clarify whether the two polymerization processes are strictly sequential or else there is some overlapping between them, and what happens during the stability period between the reaction peaks detected with DSC. For this purpose, the curing

process at 30 °C of S4TCDDA06 formulations with 0.05 phr DMAP and 0.25 phr 1MI were monitored by FTIR.

Figure 3.8 shows the evolution of the FTIR spectra during the curing processes using 1MI as initiator. We have highlighted the evolution of the characteristic peak of acrylate (810, 1410 and 1630 cm^{-1}), thiol (2570 cm^{-1}), hydroxyl (3600 cm^{-1}) and epoxy (860 and 915 cm^{-1})groups. The acrylate conversion (810 cm^{-1}) and the epoxy conversion(860 cm^{-1}) are plotted in **Figure 3.9** for both 1MI and DMAP.

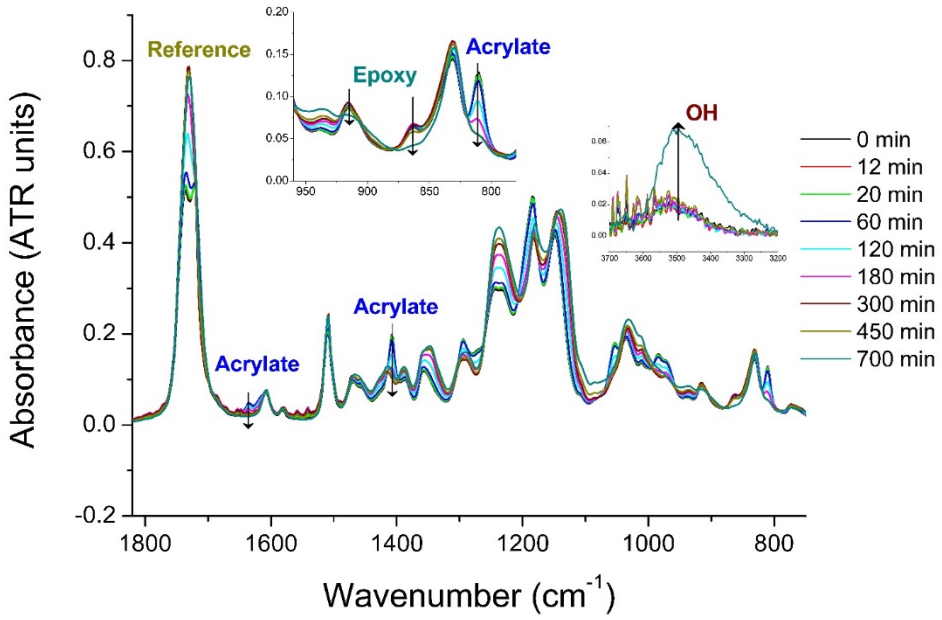

Figure 3.8. Evolution of FTIR spectra at 30°C for S4TCDDA06.1MI monitored during 700min. Insets show the evolution of specific peaks related to OH formation and consumption of acrylate, epoxy and thiol groups.

Figure 3.8 and **Figure 3.9.a** show that the reaction of acrylate groups with 1MI is fast and complete in about 300 min. All the acrylate signals in **Figure 3.8** show a similar evolution. The acrylate conversion profiles in **Figure 3.9** evidence the faster reactivity of S4TCDDA06 with DMAP than with 1MI, in agreement with the calorimetric results. A low rate activation step is visible in the conversion plot of S4TCDDA.1MI. **Figure 3.8** shows that there is some evolution of the 915 cm^{-1} signal, typically used in the analysis of epoxy systems [33], along with the reaction of acrylate groups, suggesting that thiol-epoxy reaction starts together with the thiol-acrylate, although at a very low rate. However, the small size of the peak and the presence of overlapping neighbouring signals make

the analysis of this signal quite uncertain. In addition, the observed changes around 915 cm^{-1} in the first part of the process might be ascribed to the thiol-acrylate reaction instead. We have analysed the evolution of the signal at 915 cm^{-1} (results not shown) and have observed a change in the absorbance at 915 cm^{-1} peak after 400 min for S4TCDDA06.1MI, once the thiol-acrylate reaction is almost complete, indicating the onset of the thiol-epoxy reaction. In order to clarify this, we have analysed other signals that can be associated with the thiol-epoxy reaction. **Figure 3.8** shows that the small peak at 860 cm^{-1} remains virtually unaltered during the thiol-acrylate reaction, showing only appreciable changes at 450 min . The calculation of the conversion of epoxy groups, making use of the peak at 860 cm−1, represented also in **Figure 3.9.a**, confirms that thiol-epoxy reaction is only relevant after400 min. The conversion plots suggest there might be some conversion of epoxy groups during the thiol-acrylate reaction, but this could be an artifact resulting from the small size of the peak, the mathematical deconvolution procedure needed to separate the contribution of the different peaks in that region of the spectrum (see inset in **Figure 3.8**) and the changes taking place in neighbouring signals because of the thiol-acrylate reaction (i.e., disappearance of the peak at 810 cm−1).

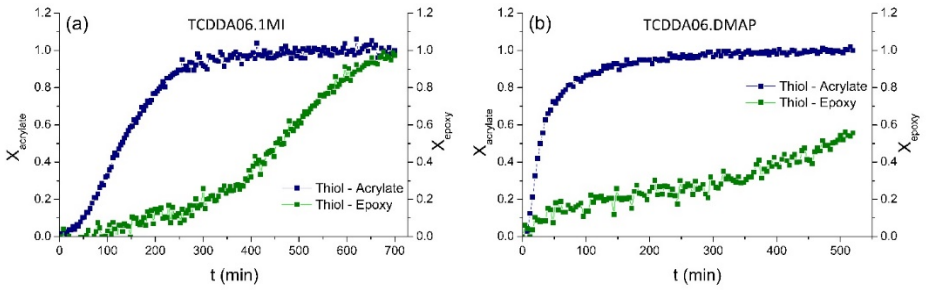

Figure 3.9. FTIR acrylate conversion - time plot and FTIR epoxy conversion – time plot for S4TCDDA06.1MI (a) and S4TCDDA06.DMAP (b).

Moreover, **Figure 3.8** shows that, setting aside baseline noise, no relevant changes take place in the OH peak at 3600 cm^{-1} during the thiol-acrylate re-action, indicating that the concentration of OH groups remains almost constant and therefore the thiol-epoxy reaction is not taking place. Relevant changes in the OH band at 3600 cm^{-1}, caused by the thiol-epoxy reaction, are only detected after 400 min for the formulation with 1MI. The evolution of thiol group peak at 2570 cm^{-1} was also investigated (**Figure 3.10**). Despite the experimental uncertainty caused by the small size of the peak and experimental noise, thiol conversion along time shows a certain stability step between 200 and 400 min, confirming that thiol-acrylate and thiol-epoxy reactions take place in

an almost sequential way. **Figure 3.9.b** shows that there is some apparent conversion of epoxy groups during the thiol-acrylate reaction forS4TCDDA06.DMAP but is probably an artifact coming from the mathematical procedure to determine the individual area of the signal at 860 cm^{-1} and therefore the conversion. The thiol-epoxy reaction was not observed to take place quantitatively because the FTIR analysis was not extended long enough.

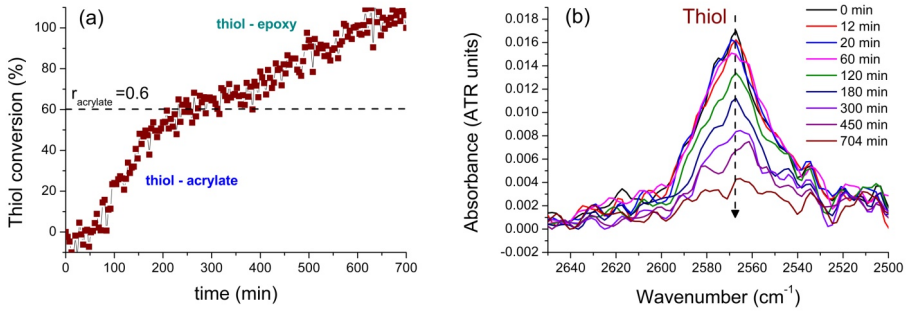

Figure 3.10. FTIR thiol conversion along time (a); FTIR spectra of the thiol peek at 2600 cm-1 (b).

These findings are in line with the results obtained by DSC con-firming that, even if the system is not exactly sequential, the low re-action rate of the second stage shall ensure that the process can be accepted as sequential. In the case of the dual system with 1MI, it is confirmed that one can find an extended period of time (250–400 min)in which the acrylate reaction is almost complete, and the thiol-epoxy reaction is not yet started or taking place at a very slow rate, during which the properties should not change appreciably. This should allow for some manipulation of this intermediate material at room temperature before quantitative activation of the second curing reaction and completion of the crosslinking process.

4.3. Potential applications of the developed materials

In this last section, the potential application of these materials is discussed. First of all, a curing procedure of the selected formulation in the oven has to be optimized. In the previous section, we have explained that a curing temperature close to T_{room} lead to a good separation between the two reactions. The problem is that at this temperature the thiol-epoxy is very slow and, according to the values of T_g reported in **Table 3.4**, vitrification might take place, leading to in-complete cure. Taking in consideration these results we decided to divide the process in two temperature steps (**Figure 3.11**): the first curing step at 30 °C to promote the thiol-acrylate and, after that, raising the temperature to 60 °C to allow the complete curing of thiol-epoxy in a reasonable time. As already

discussed, the inhibition of the second reaction at room temperature will give us enough time to manipulate the intermediate materials out of the oven to get the desired shape or to adhere to other materials.

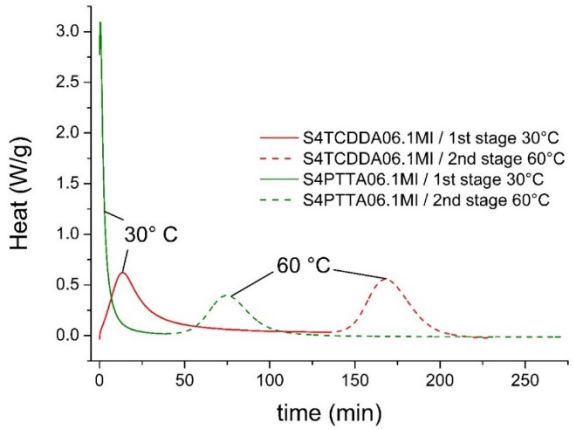

Figure 3.11. DSC two-isothermal-step curing of S4TCDDA06 and S4PTTA06 with 0.25 phr of 1MI: First stage at 30°C (solid line); second stage at 60°C (dot-dot line).

We performed some curing tests in the oven to identify the time required for each stage. After some tests, the adequate procedure was set as follow: 2 h at 30 °C for (1st stage); 3 h at 60 °C (2nd stage) followed by 1 h at 80 °C to ensure completion of the curing process. The second stage could be replaced with 1–2 h at 80 °C to shorten the duration of the process. In **Figure 3.12** some examples of conformation and processing of complex shapes are shown using S4TCDDA06.1MI formulations. As expected, the $r_{acrylate}$= 0.6 gives gelled and conformable intermediate materials. Starting from the intermediate shape, obtained with standard open moulds, we were able to transform the specimen into complex shapes that were finally fixed through the second curing stage. We were also able to obtain a rod-like specimen using a silicon tube as moulding part. After the first curing stage the rod-shaped specimen was extracted, and it was rolled up around a teflonated cylinder to achieve a spring-like shape. After the second curing step the final spring was obtained. Dog-bone specimens were also obtained by die-cutting of intermediate materials sheets. Intermediate materials samples can also be cut in complex shape simply using cutters or scissors. Damaged samples also demonstrate self-repairing properties during the second curing stage. All these examples prove the high versatility of this material processing which makes them potentially suitable for numerous applications.

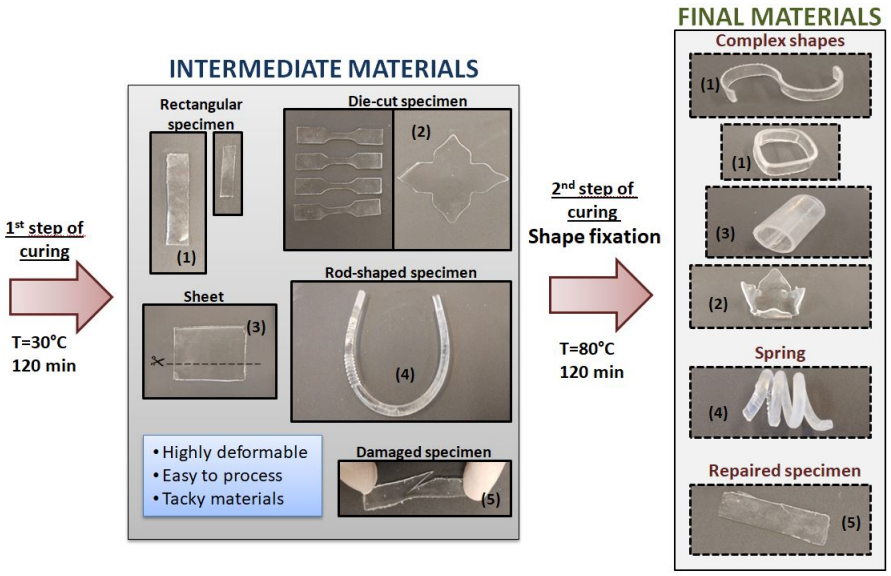

Figure 3.12. Examples of complex shapes obtained by intermediate material processing followed by fixation of the final material shapes through second curing stage.

Finally, the intermediate materials were tested as adhesive bonding (**Figure 3.13**). We tested two different configurations: external joining configuration suitable to connect pipes and internal joining that can be used for solid rods. First, the uncured formulation was poured into a mould and cured at 30° for 90 min. We decided to reduce the curing time to obtain intermediate materials with enhanced adhesive proper-ties. Once an intermediate sheet was obtained, an especially designed die cutting mould was used to obtain a strip (**Figure 3.13.a**), while a circular shape (**Figure 3.13.b**) was cut from another sheet. The circular sample was placed between two metal rods. An unspecified weight was placed on the top, to ensure the adhesion between metal and polymeric surfaces, and the assembly was put in the oven for the second curing stage. The strip was used to join two pipe pieces. Thanks to the high deformability, the material was wrapped around the pipes and an adhesive Teflon strip was rolled onto it to maintain contact during the second curing stage. When the curing process is over, almost perfect adhesion was achieved in both configurations, the two pieces had adhered to each other perfectly and they could not be separated by any hand manipulation. Since promising results was obtained with this visual evaluation, we propose to go ahead with a more precise characterization of this behaviour. The effect of $r_{acrylate}$ and 1st stage curing time on the resistance of the junction will be evaluated in future works.

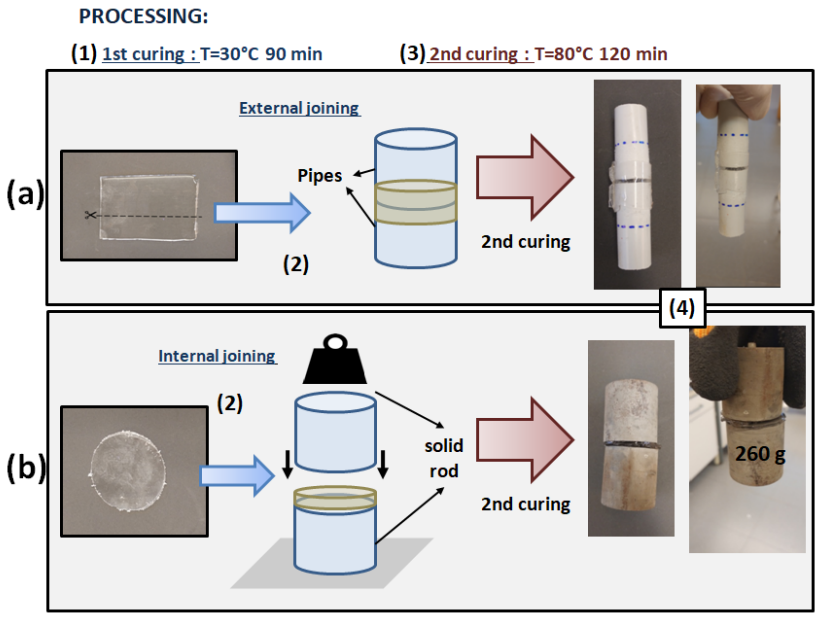

Figure 3.13. Illustration of the adhesive bonding tests: (a) Intermediate material strip used as external bonding of two pipe pieces; (b) circular shaped specimen used to bond two metal rods (all the surfaces in contact with the adhesive were pre-treated with abrasive paper to improve the adhesion).

5. Conclusions

In this work, we have studied the sequential character of dual-curing systems based on the combination of thiol-acrylate and thiol-epoxy formulations, using basic/nucleophilic tertiary amines as thermal catalysts. The curing process of the pure acrylate-thiol and epoxy-thiol formulations and dual systems has been studied using differential scanning calorimetry and infrared spectroscopy.

The analysis of the curing kinetics of pure thiol-acrylate and thiol-epoxy systems revealed completely different kinetic behaviour due to: (1) the faster kinetics of the nucleophile-mediated thio-Michael addition to acrylates, (2) the autocatalytic character of the thiol-epoxy re-action, with a long induction period due to slow initiation kinetics and (3) the weak temperature dependence of the thiol-acrylate reaction in comparison with the thiol-epoxy reaction. All these factors pointed out at the possibility of defining dual-curing formulations with an almost sequential character. The preliminary analysis also allowed us to identify PTTA and DMAP as the best combination of acrylate and catalyst to enhance the separation between the thiol-acrylate and thiol-epoxy reactions.

Calorimetric results demonstrated that the curing process takes place in well-defined curing stages with enough stability of the inter-mediate materials at room temperature to enable safe handling and manipulation before the final application and triggering of the second curing stage. The dilution of the epoxy monomer in the dual-curing formulation enhanced the separation between curing stages due to the further slowing down of the thiol-epoxy reaction. The evolution of the characteristic signals of acrylate, epoxy, thiol and hydroxyl groups, in the mid-infrared spectrum, confirmed the almost sequential character of the dual-curing system, with little or no overlapping at all between the thiol-acrylate and thiol-epoxy reactions. Safe curing schedules, ensuring a sequential curing process, could thus be defined: 2 h at 30 °C for the first curing stage, followed by 2 h at a higher temperature of 60–80 °C.

The dual-curing systems based on ternary acrylate-epoxy-thiol formulations can produce a range of intermediate and final materials with highly tailorable properties depending on the monomer structure and feed ratio. We were able to easily process the intermediate materials, which were conformed or die-cut into complex shapes. The obtained shapes were transformed and fixed by the second curing stage and different rigid shapes were finally obtained. Furthermore, the viability of intermediate materials to act as adhesive bonding were successfully tested. Two different bonding configurations were tested: an external joining of pipes and an internal joining of metal rods. Optimum results were obtained with both configurations proving the high potentiality of these materials in this field of application.

Acknowledgements

The authors would like to thank MINECO (MAT2017-82849-C2-1-Rand 2-R) and GENCAT (2017-SGR-77 and Serra Húnter programme) for the financial support.

References

[1] J.-P. Pascault, H. Sautereau, J. Verdu, R.J.J. Williams, Thermosetting Polymers, Marcel Dekker, Inc., New York, NY, US, 2002. sig=6Jsr2Jt7Eybbqu_mUOAQXKDyvKg#v=onepage&q&f=false (accessed June 18, 2021).

[2] A. Lendlein, Progress in actively moving polymers, J. Mater. Chem. 20 (2010) 3332–3334. https://doi.org/10.1039/c004361n.

[3] B. Mather, K. Viswanathan, … K.M.-P. in P., undefined 2006, Michael addition reactions in macromolecular design for emerging technologies, Elsevier. (n.d.). https://www.sciencedirect.com/science/article/pii/S0079670006000335?casa_token=o0tLBP-qj6AAAAAA:gnJD4re_FTPhROu_MJjXouBWqRaJMizVTy97tQiuZ6TyY9rAF0qDYNcn5OvUtmye3jLjjG-emA (accessed June 19, 2021).

[4] X. Ramis, X. Fernández-Francos, S.D.L.F.- Thermosets, undefined 2018, Click-based dual-curing thermosets and their applications, Elsevier. (n.d.). https://www.sciencedirect.com/science/article/pii/B9780081010211000162 (accessed June 19, 2021).

[5] C.E. Hoyle, A.B. Lowe, C.N. Bowman, Thiol-click chemistry: A multifaceted toolbox for small molecule and polymer synthesis, Chem. Soc. Rev. 39 (2010) 1355–1387. https://doi.org/10.1039/b901979k.

[6] J.E. Moses, A.D. Moorhouse, The growing applications of click chemistry, Chem. Soc. Rev. 36 (2007) 1249–1262. https://doi.org/10.1039/b613014n.

[7] W.H. Binder, R. Sachsenhofer, "Click" chemistry in polymer and materials science, Macromol. Rapid Commun. 28 (2007) 15–54. https://doi.org/10.1002/marc.200600625.

[8] S. De, A. Khan, Efficient synthesis of multifunctional polymers via thiol-epoxy "lick" chemistry, Chem. Commun. 48 (2012) 3130–3132. https://doi.org/10.1039/c2cc30434a.

[9] A.B. Lowe, C.E. Hoyle, C.N. Bowman, Thiol-yne click chemistry: A powerful and versatile methodology for materials synthesis, J. Mater. Chem. 20 (2010) 4745–4750. https://doi.org/10.1039/b917102a.

[10] K. Jin, W.H. Heath, J.M. Torkelson, Kinetics of multifunctional thiol-epoxy click reactions studied by differential scanning calorimetry: Effects of catalysis and functionality, Polymer (Guildf). 81 (2015) 70–78. https://doi.org/10.1016/j.polymer.2015.10.068.

[11] Y. Jian, Y. He, Y. Sun, H. Yang, W. Yang, J. Nie, Thiol-epoxy/thiol-acrylate hybrid materials synthesized by photopolymerization, J. Mater. Chem. C. 1 (2013) 4481–4489. https://doi.org/10.1039/c3tc30360h.

[12] A. Belmonte, D. Guzmán, X. Fernández-Francos, S. De la Flor, Effect of the network structure and programming temperature on the shape-memory response of thiol-epoxy "click" systems, Polymers (Basel). 7 (2015) 2146–2164. https://doi.org/10.3390/polym7101505.

[13] A. Belmonte, C. Russo, V. Ambrogi, X. Fernández-Francos, S. De la Flor, Epoxy-Based Shape-Memory Actuators Obtained via Dual-Curing of Off-Stoichiometric "Thiol–Epoxy" Mixtures, Polymers (Basel). 9 (2017) 113. https://doi.org/10.3390/polym9030113.

[14] A. Belmonte, G.C. Lama, G. Gentile, P. Cerruti, V. Ambrogi, X. Fernández-Francos, S. De la Flor, Thermally-triggered free-standing shape-memory actuators, Eur. Polym. J. 97 (2017) 241–252. https://doi.org/10.1016/j.eurpolymj.2017.10.006.

[15] A. Belmonte, G.C. Lama, G. Gentile, X. Fernández-Francos, S. De La Flor, P. Cerruti, V. Ambrogi, Synthesis and Characterization of Liquid-Crystalline Networks: Toward Autonomous Shape-Memory Actuation, J. Phys. Chem. C. 121 (2017) 22403–22414. https://doi.org/10.1021/acs.jpcc.7b04610.

[16] A.O. Konuray, X. Fernández-Francos, X. Ramis, Curing kinetics and characterization of dual-curable thiol-acrylate-epoxy thermosets with latent reactivity, React. Funct. Polym. 122 (2018) 60–67. https://doi.org/10.1016/j.reactfunctpolym.2017.11.010.

[17] K. Jin, N. Wilmot, W.H. Heath, J.M. Torkelson, Phase-Separated Thiol-Epoxy-Acrylate Hybrid Polymer Networks with Controlled Cross-Link Density Synthesized by Simultaneous Thiol-Acrylate and Thiol-Epoxy Click Reactions, Macromolecules. 49 (2016) 4115–4123. https://doi.org/10.1021/acs.macromol.6b00141.

[18] G. González, X. Fernández-Francos, À. Serra, M. Sangermano, X. Ramis, Environmentally-friendly processing of thermosets by two-stage sequential aza-Michael addition and free-radical polymerization of amine–acrylate mixtures, Polym. Chem. 6 (2015) 6987–6997. https://doi.org/10.1039/C5PY00906E.

[19] S. Paz-Abuin, A. Lopez-Quintela, M.V.- Polymer, undefined 1997, Method for determination of the ratio of rate constants, secondary to primary amine, in epoxy-amine systems, Elsevier. (n.d.). https://www.sciencedirect.com/science/article/pii/S0032386196010932 (accessed June 19, 2021).

[20] A.O. Konuray, X. Fernández-Francos, X. Ramis, Analysis of the reaction mechanism of the thiol-epoxy addition initiated by nucleophilic tertiary amines, Polym. Chem. 8 (2017) 5934–5947. https://doi.org/10.1039/c7py01263b.

[21] R. Thomas, C. Sinturel, J. Pionteck, H. Puliyalil, S. Thomas, In-situ cure and cure kinetic analysis of a liquid rubber modified epoxy resin, Ind. Eng. Chem. Res. 51 (2012) 12178–12191. https://doi.org/10.1021/ie2029927.

[22] X. Fernández-Francos, A.-O. Konuray, A. Belmonte, S. De la Flor, À. Serra, X. Ramis, Sequential curing of off-stoichiometric thiol–epoxy thermosets with a custom-tailored structure, Polym. Chem. 7 (2016) 2280–2290. https://doi.org/10.1039/C6PY00099A.

[23] J.W. Chan, C.E. Hoyle, A.B. Lowe, M. Bowman, Nucleophile-initiated thiol-michael reactions: Effect of organocatalyst, thiol, and Ene, Macromolecules. 43 (2010) 6381–6388. https://doi.org/10.1021/ma101069c.

[24] D. Guzmán, X. Ramis, X. Fernández-Francos, A. Serra, New catalysts for diglycidyl ether of bisphenol A curing based on thiol–epoxy click reaction, Eur. Polym. J. 59 (2014) 377–386. https://doi.org/10.1016/j.eurpolymj.2014.08.001.

[25] B.A. Rozenberg, KINETICS, THERMODYNAMICS AND MECHANISM OF REACTIONS OF EPOXY OLIGOMERS WITH AMINES., Adv. Polym. Sci. 75 (1986) 113–165. https://doi.org/10.1007/bfb0017916.

[26] X. Fernàndez-Francos, Theoretical modeling of the effect of proton donors and regeneration reactions in the network build-up of epoxy thermosets using tertiary amines as initiators, Eur. Polym. J. 55 (2014) 35–47. https://doi.org/10.1016/j.eurpolymj.2014.03.022.

[27] J.A. Carioscia, J.W. Stansbury, C.N. Bowman, Evaluation and control of thiol-ene/thiol-epoxy hybrid networks, Polymer (Guildf). 48 (2007) 1526–1532. https://doi.org/10.1016/j.polymer.2007.01.044.

[28] L. Matějka, S. Pokorný, K. Dušek, Acid curing of epoxy resins. A comparison between the polymerization of diepoxide-diacid and monoepoxide-cyclic anhydride systems, Die Makromol. Chemie. 186 (1985) 2025–2036. https://doi.org/10.1002/macp.1985.021861006.

[29] M.S. Heise, G.C. Martin, J.T. Gotro, Characterization of imidazole-cured epoxy–phenol resins, J. Appl. Polym. Sci. 42 (1991) 1557–1566. https://doi.org/10.1002/app.1991.070420609.

[30] S. Vyazovkin, N. Sbirrazzuoli, Isoconversional kinetic analysis of thermally stimulated processes in polymers, Macromol. Rapid Commun. 27 (2006) 1515–1532. https://doi.org/10.1002/marc.200600404.

[31] M.J. Starink, The determination of activation energy from linear heating rate experiments: A comparison of the accuracy of isoconversion methods, Thermochim. Acta. 404 (2003) 163–176. https://doi.org/10.1016/S0040-6031(03)00144-8.

[32] X. Fernandez, J.M. Salla, A. Serra, A. Manteco´n, M. Manteco´n, X. Ramis, Cationic Copolymerization of Cycloaliphatic Epoxy Resin with a Spirobislactone with Lanthanum Triflate as Initiator: I. Characterization and Shrinkage, Wiley Online Libr. 43 (2005) 3421–3432.

https://doi.org/10.1002/pola.20801.

[33] X. Fernández-Francos, W.D. Cook, À. Serra, X. Ramis, G.G. Liang, J.M. Salla, Crosslinking of mixtures of DGEBA with 1,6-dioxaspiro[4,4]nonan-2,7-dione initiated by tertiary amines. Part IV. Effect of hydroxyl groups on initiation and curing kinetics, Polymer (Guildf). 51 (2010) 26–34. https://doi.org/10.1016/j.polymer.2009.11.013.

Chapter 4.

Rheological and Mechanical Characterization of Dual-Curing Thiol-Acrylate-Epoxy Thermosets for Advanced Applications

Polymers **2019**,11(6), 997

DUAL-CURING THIOL-ACRYLATE-EPOXY
THERMOSETS FOR FUNCTIONAL APPLICATIONS
Claudio Russo

Rheological and Mechanical Characterization of Dual-Curing Thiol-Acrylate-Epoxy Thermosets for Advanced Applications

Claudio Russo[1], Xavier Fernández-Francos[2], Silvia De la Flor[1].

[1]Department of Mechanical Engineering, Universitat Rovira i Virgili, Av. Països Catalans 26, 43007 Tarragona, Spain.

[2]ThermodynamicsLaboratory, ETSEIB, Universitat Politècnica de Catalunya, Av. Diagonal 647, 08028 Barcelona, Spain.

Abstract

Mechanical and rheological properties of novel dual-curing system based on sequential thiol-acrylate and thiol-epoxy reactions are studied with the aim of addressing the obtained materials to suitable advanced applications. The crosslinking process is studied by rheological analysis in order to determine conversion at gelation and the critical ratio. These parameters are used to discuss the intermediate material structure for each acrylate proportion and their possible application in the context of dual-curing and multi-step processing scenarios. Results from dynamo-mechanical analysis and mechanical testing demonstrate the high versatility materials under investigation and revealed a wide range of achievable final properties by simply varying the proportion between acrylate and thiol group. The intermediate stability between curing stages has been analysed in terms of their thermal and mechanical properties, showing that these materials can be stored at different temperatures for a relevant amount of time without experiencing significant effects on the processability. Experimental tests were made to visually demonstrate the versatility of these materials. Qualitative tests on the obtained materials confirm the possibility of obtaining complex shaped samples and highlight interesting shape-memory and adhesive properties.

Keywords: epoxy; thiol; acrylate; dual-curing; shape-memory polymer; adhesive.

---

1. Introduction

Crosslinked polymeric materials are used in many application fields because of their excellent thermal and mechanical properties (i.e., aviation, automobile, structures or coatings) [1]. The formation of crosslinked thermosetting network is a non-reversible process involving drastic changes in polymer and network structures which leads to relevant restrictions in shape designs. Recently, the increasing need to reach complex

shape designs to cater for the high demand of complex shaped smart materials (i.e., bio-inspired devices or shape-changing materials [2]), is focusing the attention on alternative curing techniques which allow to overcome thermosets limitations in shape. In this context, dual-curing polymer systems have attracted a growing interest as they represent a versatile approach for better controlling network formation and properties during processing [3,4].

Dual-curing processing is a promising methodology to develop thermosetting polymers taking advantage of two compatible and well-controlled crosslinking reactions [5]. These reactions can be simultaneously or sequentially triggered by different stimuli as well as difference in reaction kinetics. Sequential dual-curing allows to obtain materials with two different sets of properties after the first curing reaction (intermediate material) and second curing reaction (final material). This kind of processing is becoming attractive due to the possibility to attain complex three-dimensional structures by means of the accurate control of the materials properties in the intermediate state (i.e., low T_g, low crosslinking density and high deformability).

Successful sequential dual-curing processing requires that: (i) both polymerization reactions are selective and compatible so that no undesired inhibition or reactivity effects take place; (ii) they can be triggered using different stimulus such as UV light [6] or temperature [7], or else they have sufficiently different reaction rates so that they can be controlled from a kinetics point of view; (iii) the properties of the final and intermediate stages can be custom-tailored changing the composition of the formulation.

Thermosetting dual-curing materials have been obtained from the combination of a large variety of reactions, but “Click” reactions represent one of the most effective tools to obtain such systems. “Click chemistry” defines a class of reactions that are highly efficient, orthogonal and selective [8]. Moreover, they reach high yields, they can react in mild, or solvent-less conditions and they can be applied to broad range of compounds [9–11]. For those reasons, “click” reactions are widely used in thermosets preparation and are fit for combination in dual-curing procedures. In particular, thiol-click reactions have attracted great interest due to their advantages (high conversion, solvent-free, oxygen resistance, etc.) [11–14] which makes them suitable to prepare crosslinked polymers in a fast and efficient way.

Michael-type addition reactions are currently used in dual-curing processing because of the variety of commercially available nucleophiles (Michael donors) and activated double bond compounds (Michael acceptors) that can be used in such processes. One

of the most common and clickable Michael donors are thiols. Although thiol-acrylate addiction has a good combination of reactivity, versatility and cost, the final thermosetting structures exhibit week mechanical and thermal properties which makes them unable to fit the standards required for advanced applications [15]. On the other hand, thiol-epoxy "click" reaction, which is also used in dual-curing systems, leads to soft functional materials with enhanced mechanical properties such as high deformability, resistance at break, high impact resistance and adhesion. All these properties make them suitable for advanced applications as coatings [16], adhesives [17] and shape-memory actuators [18]. The combination of these reactions in dual-curing procedure is already reported in the literature: Konuray et al. [6] presented a novel photolatent dual-cure thiol-acrylate-epoxy system where the first curing reaction is the thiol-Michael reaction triggered by UV light (a photobase generator was used as catalyst), and the second reaction is a thiol-epoxy activated at higher temperature. Jin et al. [7] prepared thiol-epoxy-acrylate hybrid polymer networks combining nucleophilic thiol-acrylate Michael addition and thiol-epoxy reactions in a one-pot simultaneous dual-cure catalysed by *1,8-diazabicyclo[5.4.0]undec-7-ene* (DBU) at 80 °C. In our previous work [19] a new thiol-acrylate-epoxy sequential dual-curing system, where both reactions are activated using a single thermal catalyst, was developed. Although thiol-acrylate Michael addition and thiol-epoxy "click" reaction are both thermally-activated within a similar temperature range, the former's faster reaction kinetic ensures the sequentiality of the process.

Suitable choice of monomer feed ratio, structure and functionality makes it possible to obtain an intermediate thiol-acrylate conformable network after the first curing step. This network could be processed in complex shape designs and then, thanks to the presence of unreacted thiol and epoxy groups, a second crosslinking reaction could be triggered leading to the final materials. Therefore, complex-shaped thermosets can be achieved thanks to the two-step processing. Since thermosetting networks formed by thiol-acrylate reaction generally exhibit flexible structures, the addition of a further thiol-epoxy crosslinking process could enhance the final properties of the thermosets. Thermal and mechanical properties of intermediate and final thermosets can be easily tailored controlling the ratio between acrylate and thiol groups (r_a). Therefore, it is possible to obtain intermediate materials with properties ranging from liquid-like to gelled solid-like covering a wide range of possible applications. The critical ratio (r_c), defined as the lower r_a at which gelation occurs within the first crosslinking process, sets a boundary line between liquid and solid-like intermediate materials. Therefore, this parameter must be accurately evaluated to address each resulting material to the

adequate application. Further analysis of the chemorheological behaviour of these dual formulations, taking into consideration the complex effect of temperature and curing progress on the viscosity during processing [20,21], would also be highly valuable in the simulation and optimization of other processing scenarios [22].

Such design capabilities can be exploited to produce multi-layer assemblies with controlled layer thickness and complex shape, with the purpose of creating complex-shape mechanical actuators [18], making use of the good wetting properties of intermediate lightly crosslinked or nearly gelled materials and the good adhesion obtained after the thiol-epoxy reaction.

The aim of this work is to characterize the mechanical, thermal, and rheological properties of a novel thiol-acrylate-epoxy dual-curing system. Mixtures at various thiol-acrylate ratios, covering the entire range between 0 and 1, were prepared and final thermosets properties were studied. The evolution of rheological properties during the curing process were monitored to determine the actual critical ratio for this system. After that, the main mechanical properties (hardness, flexural and tensile modulus, tensile strength, and deformation at break), of the totally cured materials (final thermosets) were evaluated in order to highlight the high versatility of the applications of the dual-curing system developed. To characterize the storage time of the intermediate materials, the evaluation of the latency of the second curing reaction was carried out on two different formulations, one with a $r_a > r_c$ and one with $r_a < r_c$. The progression of the thiol-epoxy was evaluated in terms of residual heat (DSC), complex viscosity η^* (rheometer) and tensile module E_t. Lastly, qualitative, and visual demonstrations of different applications are presented to show the possibility of this systems to be exploited for two-stage adhesive technologies and for the preparation of complex-shaped shape-memory actuators.

2. Materials and Methods

2.1. Materials

Diglycidyl ether of bisphenol A (DGEBA, EPIKOTE™ Resin 828, with an epoxy equivalent weight of 187 g/eq) was supplied by Hexion Specialty Chemicals (Columbus, OH, USA), and dried under vacuum at 80 °C before use. *Pentaerythritol tetrakis(3-mercaptopropionate)* (S4, 122.17 g/eq) and *tricyclo[5.2.1.02,6]decanedimethanol diacrylate* (TCDDA, 152.2 g/eq) were purchased from Sigma-Aldrich (St. Louis, MO, USA) and used as received. *4-(N,N-dimethylamino)pyridine* (DMAP) was purchased from Fluka (Seelze, Germany)and used at 0.05 phr to act as catalyst for both curing reactions.

Different formulations have been prepared varying the ratio between acrylate groups and thiol groups (r_a). All samples were cured at 40 °C for 2 h (1st step), 80 °C for 3 h (2nd step) and 100 °C for 1 h (post curing).

Formulations have been coded as TCDDAxx where xx is the r_a (00 and 10 correspond to respectively thiol-epoxy and thiol-acrylate pure formulations). The compositions of the investigated formulations are listed in **Table 4.1**.

Table 4.1. Compositions of the different formulation of study.

Formulation	r_a	Thiol (wt%)	DGEBA (wt%)	Acrylate (wt%)
TCDDA00	0	40	60	0
TCDDA02	0.2	40	49	10
TCDDA04	0.4	41	38	21
TCDDA045	0.45	42	35	23
TCDDA05	0.5	42	32	26
TCDDA06	0.6	42	26	32
TCDDA08	0.8	43	13	43
TCDDA10	1	45	00	55

2.2. Characterization techniques

2.2.1. Rheological Characterization of the Gel Point and r_c

The dual-curing process was monitored using a rheometer AR-G2 TA Instruments, (New Castle, DE, USA), equipped with an electrical heated plate device (EHP) and 20 mm parallel plate geometry. The evolution of the storage (G') and loss modulus (G") was monitored through dynamo-mechanical experiment at 30 °C for 8 h. The oscillation amplitude was set at 0.2% and the frequencies at 0.5, 1.75 and 3 Hz. Gel point was determined as the tanδ crossover at the three different frequencies and the first gelled formulation (r_c) was defined as the formulation with the lower r_a that shows a gel point within the first curing process. Gelation during dual-curing procedure was also tested step-wise as follows: first curing stage 3 h at 30 °C with an amplitude of 3%; after that a temperature ramp from 30 to 60 °C at 2 °C/min (with the same oscillation amplitude) and finally second curing stage 2 h at 60 °C with an amplitude of 0.2%. Three different frequencies of 0.5, 1.75, 3 Hz were continuously measured during the whole procedure. The experimental r_c was compared with the theoretical value obtained for ideal step-wise processes using the Flory-Stockmayer theory, as follows:

$$r_c = \frac{1}{(f_{acrylate} - 1) \cdot (f_{thiol} - 1)} \quad (1)$$

where $f_{acrylate}$ and f_{thiol} are the average functionality of acrylate and thiol monomers.

Complex viscosity (η*) of the intermediate materials were recorded as function of angular frequency ω (rad/s) at constant deformation in the range of linear viscoelasticity, obtained from constant shear elastic modulus (G') in a strain sweep experiment at 1 Hz, always at 25 °C.

2.2.2. Mechanical properties

Final thermosets were analysed with a TA Instruments DMA Q800 (New Castle, DE, USA) equipped with 3-point bending clamp (15 mm) to characterize the relaxation process. Prismatic rectangular samples (15 × 6 × 2.5 mm^3) were analysed in oscillation mode at 1 Hz, 0.1% of strain amplitude and imposing a temperature ramp of 3 °C/min from −20 to 120 °C. The T_g was determined as the tanδ peak temperature, glassy (E_g) and rubbery (E_r) moduli were determined at 0 and 100 °C, respectively.

Mechanical properties were tested at room temperature to investigate the processability of final materials at normal or usual operating temperatures.

The Flexural modulus (E) of final materials was determined with the same apparatus by means of a force ramp at a constant rate of 1 N/min in controlled-force mode. The slope (m) within the linear zone of force-displacement curve was obtained. E was calculated in accordance with the following equation:

$$E = \frac{L^3 m}{4wt^3} \quad (2)$$

where L is the support span and w and t are the width and the thickness of test sample respectively.

Tensile properties of dog bone shaped samples (80 mm × 25 mm × 1.5 mm) were obtained by tensile test on a Shimadzu AGS-X 10 kN (Kyoto, Japan) testing machine at 10 mm/min speed, according to ASTM D638-14 (ASTM International, West Conshohocken, PA, USA, 2014) standard. Shore hardness was measured with an Affri durometer type D (Shore-D hardness) according to ASTM D2240-15 (ASTM International, West Conshohocken, PA, USA, 2015) in samples of 4 mm thickness. Ten measurements were done in each sample and the average result is presented.

2.2.3. Latency Test on Intermediate Materials

Latency tests were performed for TCDDA02 and TCDDA06 intermediate thermosets at two different storage conditions (5 and 22 °C). Samples at different storage times were tested using a differential scanning calorimeter (DSC) Mettler DSC-821e (Mettler-Toledo, Greifensee, Switzerland), calibrated using an In standard (heat flow calibration) and an In-Pb-Zn standard (T calibration). Samples of approximately 10 mg were placed in aluminium pans with pierced lids and cured in the oven. After the first curing stage, samples were stored in a climatic chamber at 5 and 22 °C and were periodically tested by DSC dynamic analysis from −20 to 200 °C with a heating rate of 10 °C/min under N_2 atmosphere. The residual heat of the second curing step has been used as measure of the curing degree reached by the samples during the storage.

The evolution of the intermediate materials properties, during a representative storage time interval, were monitored by measuring at T_{room} the tensile modulus for sample TCDDA06 and the viscosity for sample TCDDA02, since the latter leads to a liquid-like intermediate.

3. Results

3.1. Rheological Analysis

Rheological analysis is accepted as a reliable tool to determine the gelation of thermosetting systems. The critical ratio of our system was determined to be $r_c = 0.33$ using Equation (1). In light of the approximations made and taking into account previous experience [23], we expected the real critical ratio to be higher than the theoretical one, so we started the rheological analysis from $r_a = 0.4$. The curing process was monitored at an isothermal temperature of 30 °C according to the results obtained in our previous work [19]. **Figure 4.1** shows the rheological monitoring of the isothermal curing process of three formulations with r_a values above the theoretical r_c, TCDDA04, TCDDA045 and TCDDA05. As shown in these figures, the network formation during the polymerization process results in a drastic increase of both storage (G') and loss (G') moduli. Two polymerization processes are visible in all three figures since the increase in moduli shows a two-step trend.

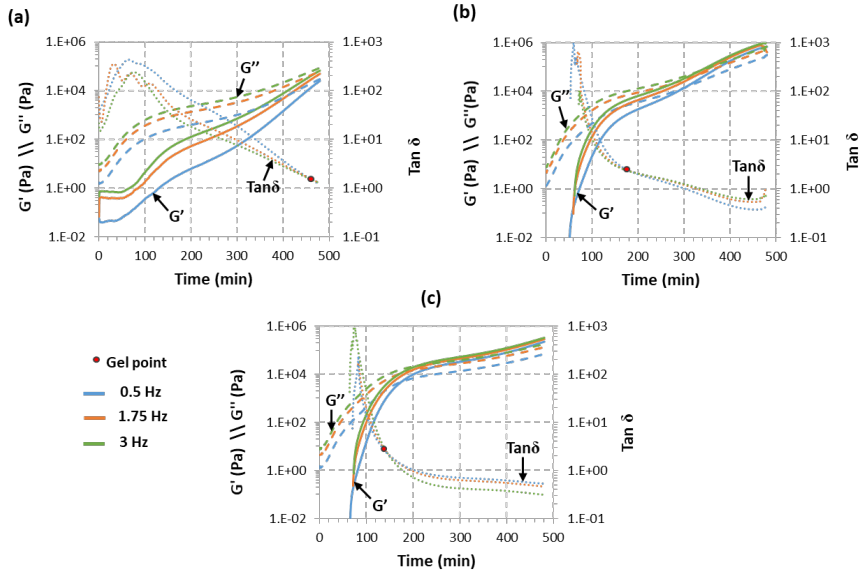

Figure 4.1. Evolution of storage modulus (G'), loss modulus (G") and tanδ with time at 30 °C for samples: TCDDA04 (a); TCDDA045 (b) and TCDDA05 (c).

For all three samples thiol-acrylate reaction occurs within the first 180 min (as verified with DSC, results similar to those reported previously [19], not shown) leaves a reaction tale overlapped with the thiol-epoxy which proceed at a low rate because of the low curing temperature. Along the process, the material goes through a substantial transformation: at the beginning the material has liquid-like behaviour and G" is higher than G'. As the reaction takes place, structure starts to develop leading to molecular weight increase, resulting in an increase of G" and also G'. When gelation takes place, a network develops, and the material start to behave as solid (G' > G"). **Figure 4.1.a** shows that no gelation is detected in the first three hours of curing of formulation TCDDA04, and the gel point is clearly visible only after the second crosslinking process is started. Gelation occurs right before the end of the analysis and G" remains higher than G'. Raising the r_a to 0.45, gelation occurs after 194 min (**Figure 4.1.b**) and it seems to take place right after the first curing reaction ends. Finally, as shown in **Figure 4.1.c**, TCDDA05 formulation has the gel point within the first curing process and during the first 3 h of curing. As a result, the r_a of 0.45–0.5 can be established as the actual r_c. As already reported for other dual-curing systems [23], the effective critical ratio (r_c = 0.45–0.5) is higher than the one obtained theoretically from the Flory-Stockmayer relationship. Deviation from the ideal step-wise behaviour could be explained by the action of intramolecular cyclization which would lead to a delay in gelation phenomenon [24,25]. The presence of impurities in the S4 (reported by Sigma-Aldrich to be lower than 5%)

could reduce the actual functionality of the curing agents resulting in higher conversion at gelation.

The rheological behaviour for samples TCDD04 and TCDDA05 was also monitored during a dual-curing procedure divided as follows: a first isothermal step at 30 °C for 180 min a temperature ramp at 2 °C/min from 30 to 60 °C and, finally, a second isothermal step at 60 °C until G' and G" reach a plateau. The results can be observed in **Figure 4.2** (TCDD04) and **Figure 4.3** (TCDDA05).

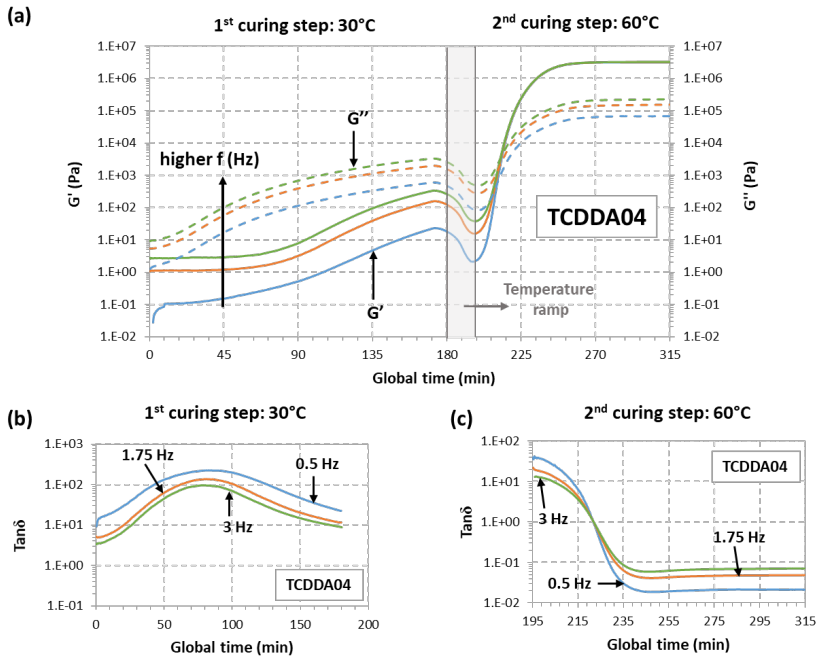

Figure 4.2. Rheological analysis of TCDDA04 dual-curing procedure: (a) Storage modulus (G') and loss modulus (G") evolution with time during the whole dual-curing process; (b) evolution of tanδ with time during the 1st curing stage and (c) evolution of tanδ during the 2nd curing stage.

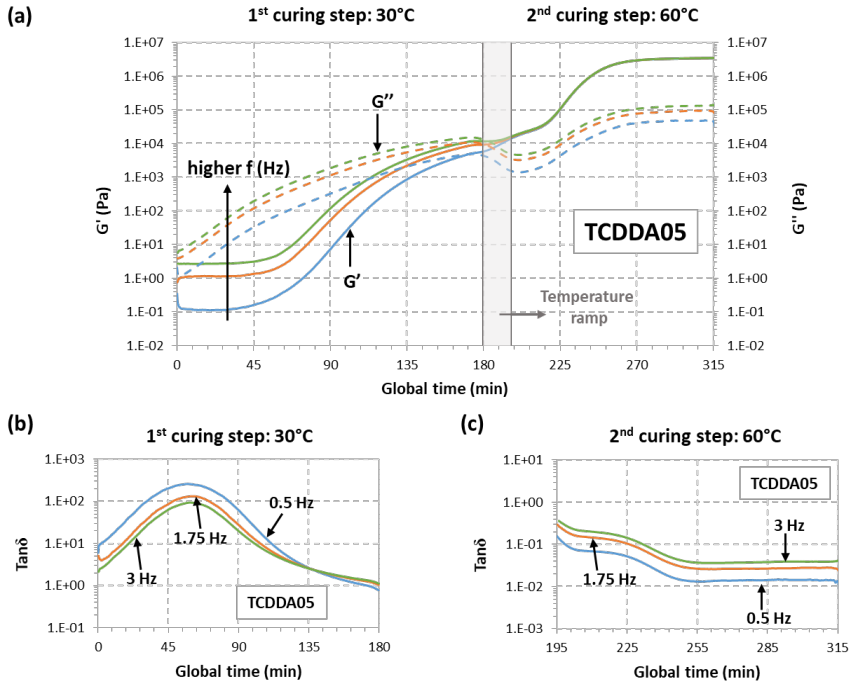

Figure 4.3. Rheological analysis of TCDDA05 dual-curing procedure: (a) Storage modulus (G') and loss modulus (G") evolution with time during the whole dual-curing process; (b) evolution of tanδ with time during the 1st curing stage and (c) evolution of tanδ during the 2nd curing stage.

Starting with TCDDA04, **Figure 4.2.a** shows that, G" remains higher than G' along the first curing stage thus, the material is still acting as liquid since the network is not already formed. G" decreases during the heating ramp due to the decrease in viscosity with temperature, and so does G'. Crossover of G' and G" is clearly visible in the second stage, within the thiol-epoxy crosslinking process. The evolution of tanδ during the first and the second stage of curing is presented, respectively, in **Figure 4.2.b,c**. As expected, tanδ crossover is only visible about 30 min after the second stage has started. In the case of formulation TCDDA05, **Figure 4.3.a** shows that, for crossover of G' and G" takes place at the very end of the first curing stage, but the tanδ crossover is clearly observed in the first curing step (**Figure 4.3.b**), therefore confirming that an intermediate gelled material could be obtained with a proportion of 0.5. It can also be observed in **Figure 4.3.a** a slight decrease in G" during the heating ramp from 30 to 60 °C, while G' remains fairly constant and even increases due to the existence of an incipient network that is developing.

3.2. Mechanical and Thermomechanical Analysis

In this section, thermomechanical properties and the mechanical behaviour of the final thermosets are discussed. The aim of this characterization is to evaluate the properties which determine the final use of the material in real applications. **Figure 4.4** presents the evolution of storage modulus E' and tanδ with temperature during the network relaxation of the different materials, obtained by a DMA temperature sweep analysis. **Table 4.2** summarizes some relevant parameters associated with the network relaxation. As expected, raising the proportion between thiol and acrylate results in lower T_gs for the final materials because of the softening effect of the thiol-acrylate network. The shape of the tanδ peak during the material relaxation can be correlated with its network structure: the higher and narrower the peak of tanδ, the more homogeneous and mobile the network structure [26]. Similar values of FWHM around 11 °C were obtained with both thiol-epoxy and thiol-acrylate pure formulation since these networks were built with the same crosslinking functionality. Dual formulations present broader tanδ transition paths due to the higher heterogeneity of the network, which is made up of two different crosslinking reactions. Belmonte at al. [27] reported a strong relationship between the sharpness of the relaxation process and the rate of the shape-recovery process. Materials with higher FWHM values are unfavourable for shape-memory applications because broader relaxation profile leads to a slowdown of the recovering process. In general, broad transitions lead to an undesired anticipation of the softening of the materials with respect to the expected T_g. It can also be observed that the relaxed modulus E'_r decreases with increasing acrylate ratio, as a consequence of the higher mobility of the TCDDA network in contrast with the DGEBA network, rather than a difference in crosslinking density. In contrast, the glassy modulus E'_g increased with increasing acrylate ratio, suggesting that a better chain packing, and stronger intermolecular interactions take place in acrylate rich formulations. Tentatively, this can be rationalized in terms of the higher mobility of the TCDDA monomer in comparison with DGEBA, and the higher presence of polar carbonyl groups. Flexural Modulus (E) for all the samples was calculated from 3-point-bending test by means of Equation (2). As can be observed in **Table 4.2**, some samples present a very low value of E because their relaxation processes lie around room temperature (see **Figure 4.4**). Although these results are not representative values of Young Moduli in glassy state for these samples, they provide an effective measure of the material behaviour at the temperature of usage. Low flexural moduli result in high conformability at room temperature making these materials suitable for advanced applications based on soft materials (i.e., soft robotics).

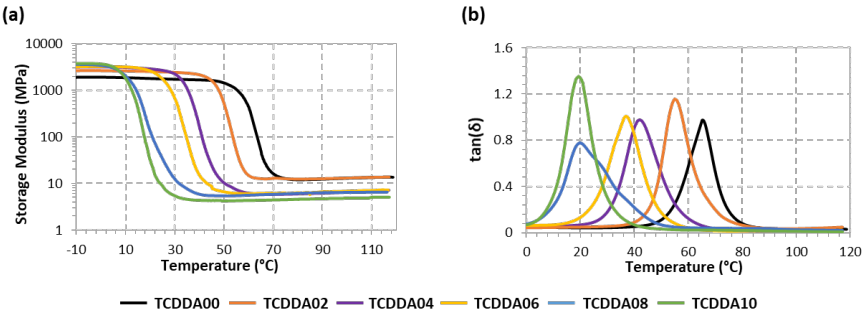

Figure 4.4. Storage Modulus (a) and tanδ (b) versus temperature during dynamic mechanical analysis.

Table 4.2. Thermomechanical data collected from DMA (dynamic mechanical analysis). Coefficients of variation less than 2% for thermomechanical data and 5% for Flexural Modulus.

Sample	T_g (°C)	E'_g (MPa)	E'_r (MPa)	FWHM (°C)	E (MPa)[(a)]
TCDDA10	19.2	3679	4.85	11.3	5.23
TCDDA08	20.6	3422	6.43	18.3	5.76
TCDDA06	37.1	3230	5.82	13.6	21.83
TCDDA04	42.4	3181	6.50	14.3	39.82
TCDDA02	55.7	2648	13.06	11.4	1358
TCDDA00	65.5	1911	13.03	11.0	1028

[(a)] calculated using eq. (2)

Tensile behaviour of final materials was also evaluated from tensile test in a universal testing machine. Tests were made at room temperature and the data obtained is presented in **Table 4.3**. Significant differences in terms of tensile modulus are observed between the thermosets above and below the r_c. This trend is due to the shift of the glass transition towards T_{room} when increasing the acrylate proportion, with the consequent softening of the materials. The effect of the acrylate proportion is clearly visible in the stress-strain curves in **Figure 4.5** . When $r_a = 0$ (sample TCDDA00), a sudden fracture appears right after the yielding point and almost no plastic deformation is observed. When the acrylate ratio r_a is raised, a gradual increase in network deformability is observed in samples TCDDA02 and TCDDA04 (**Figure 4.5.a**). A drastic change in tensile behaviour at T_{room} is observed in samples with $r_a > r_c$ (**Figure 4.5.b**). For TCDDA06 (r_a = 0.6), $T_g \approx T_{room}$ and network relaxation occurs during the strain-stress experiment. Network relaxation allows a higher dissipation of stress by viscous friction of polymer chains, reaching higher deformability and a relative high strength value at break with strain hardening at the end, as commonly observed in the programming of shape-memory thermosets at temperatures close to their relaxation temperature.

However, when $r_a > 0.6$ (samples TCDDA08 and TCDDA10), it is observed that $T_g < T_{room}$. In consequence, this stress-absorbing network relaxation mechanism is no longer operative, and therefore it is the relaxed network structure the main responsible for the mechanical response. A low elastic modulus is measured and given the limited stretching ability of the polymer chains, a low stress at break σ_{max} is obtained. Consequently, increasing the epoxy-thiol content in the final network, higher strength at break can be obtained. The same effect is also visible in terms of strain energy density as it can be appreciated in **Table 4.3**. The differences in network relaxation state at T_{room} results in an increase of the material capability to absorb energy during deformation which achieves the highest value for TCDDA06 and then drastically decrease for TCDDA08 and TCDDA10. A similar trend is observed in hardness measurements; hence the same conclusions are applicable to this property. From the analysis of the data reported in **Table 4.3** and **Figure 4.5**, it can be observed that the behaviour of TCDDA02 and TCDDA08 is very close to that of TCDDA00 and TCDDA10, respectively, suggesting that small deviations from the pure networks produce minor effects on final thermosets properties.

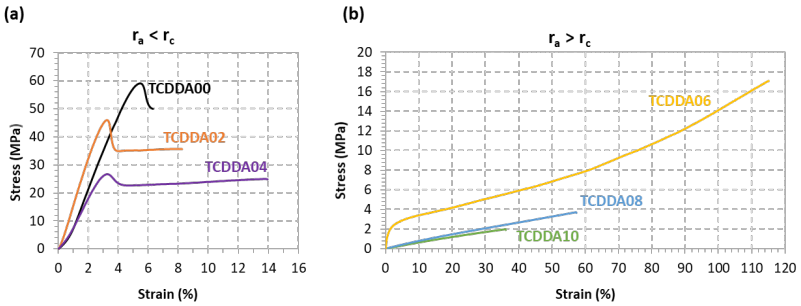

Figure 4.5. Stress-strain curves from tensile tests on final materials: (a) $r_a < r_c$; (b) $r_a > r_c$.

Table 4.3. Characteristic mechanical parameters obtained from tensile test and hardness measurements. Coefficients of variation less than 10% for stress, strain, and tensile modulus, and less than 5% for Shore-D hardness.

	Formulations	E_t (MPa)	σ_{max} (MPa)	ε_{max} (%)	σ_{break} (MPa)	ε_{break} (%)	Strain energy density (KJ/m3)	Hardness (Shore-D)
$r_a < r_c$	TCDDA00	1580.8	41.7	3.66	34.1	6.88	1861.7	72.5
	TCDDA02	1580.0	39.4	2.79	23.6	6.57	2299.5	73.1
	TCDDA04	1418.6	20.5	9.56	17.0	23.68	3531.9	65.3
$r_a > r_c$	TCDDA06	372.8	17.0	108.94	17.0	109.04	9534.2	43.7
	TCDDA08	8.0	2.8	44.39	2.8	44.65	725.3	28.1
	TCDDA10	6.6	1.6	28.46	1.6	29.57	271.2	27.3

This analysis confirms that a wide range of final properties can be obtained by varying the composition of the formulation: the thiol-acrylate proportion in the network has been proved to have a softening effect on the final network, resulting in lower T_g and higher capability of absorbing energy during application deformation process. An interesting combination of these two reactions is present in the 0.6 proportion between acrylate and thiol: a highly deformable final material is be obtained together with an intermediate gelled network that make it suitable for application in which two-step processing is required (with a highly conformable manufacturing step in the intermediate one). On the other hand, acrylate proportions between 0.2 and 0.4 lead to a decrease in T_g with respect to the characteristic thiol-epoxy T_g, without a major loss in terms of mechanical properties (final strength, E_t, hardness). In this case, these materials could be exploited for two-stage application in which a viscous intermediate is required, such as adhesives or coatings.

3.3. Latency and Storage Time

The evaluation of latency of the second reaction represents a crucial analysis in dual-curing procedure. The storage time of the intermediate materials is strictly related to the amount of time required to activate the second reaction at T_{room} (or at different storage temperature), without significant alteration of the intermediate material properties. For that purpose, we chose to analyse the storage stability of TCDDA02 and TCDDA06 formulations.

To begin with, the first curing stage was carried out in the oven at 40 °C for 2 h. After that, they were stored at 22 and 5 °C in a controlled climatic chamber. The samples were analysed by DSC at determined storage times in order to monitor the evolution of residual heat with storage. As shown in **Figure 4.6.a**, intermediate TCDDA06 material experiences no significant changes in residual heat during 10 hours of storage at 22 °C. After that, a drastic decrease in residual heat is observed and the samples take six days (144 h) to react completely curing at storage conditions. On the contrary, TCDDA02 shows a rapid decrease in residual heat during the first six hours of storage, and it reaches a plateau after 24 h. In this case, even if the thiol-epoxy reaction proceeds faster thus considerably reducing the storage time, it never reaches the complete curing because vitrification takes place during storage. Main differences between TCDDA02 and TCDDA06 can be explained by the higher epoxy content of TCDDA02, which enhances the reactivity of the epoxy-thiol reaction [28] and is therefore less stable. In fact, premature activation of the epoxy-thiol reaction might also take place during the first curing step. A practical consequence of this is that controlled curing sequences are

more easily achieved in dual formulations with a moderate or low epoxy content. In addition, the fully cured TCDDA02 material has a higher T_g, clearly above storage temperature (see **Table 4.2**), therefore explaining vitrification during storage. In contrast, the lower of T_g of TCDDA06 (see **Table 4.2**, calorimetric T_g is even lower [19]) makes it possible to react completely under storage conditions.

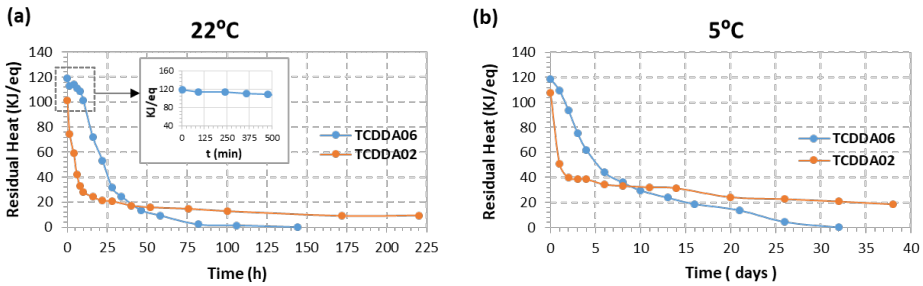

Figure 4.6. Results of latency evaluation at two different storage temperature for TCDDA02 and TCDDA06 formulations.

The same effects are observed when the samples are stored at 5 °C (**Figure 4.6.b**): after 1–2 days of stability, TCDDA06 shows a gradual progression of the second reaction until no residual heat is registered, while TCDDA02 reach the final plateau after only 2 days of storage.

Furthermore, we studied the effect of storage on the intermediate mechanical in order to assess how the workability during the intermediate step is affected by storage time and conditions. Since TCDDA02 has a liquid-like intermediate stage, the increase of complex viscosity during storage was used to evaluate latency. During 4 hours at 25 °C (**Figure 4.7.a**) a significant increase from 50 Pa·s to value of about 300 kPa·s (both measured at 1 Hz and at 25 °C) can be observed. When the samples were stored at 5 °C, an increase up to 3–4 kPa·s (measured at 1 Hz and at 25 °C) is observed (**Figure 4.7.c**), two orders of magnitude less with respect the storage at 25 °C. Although this increase in complex viscosity could affect the processing ability of these materials, there is enough time to process the material in the intermediate state for two-stage applications. Tensile tests were performed on intermediate TCDDA06 materials in order to evaluate the increase of the tensile modulus during the storage process. As shown in **Figure 4.7.b**, the initial modulus E_t has a value of 28 kPa, and it increases gradually up to 1 MPa after eight hours of storage at 25 °C. However, storage at 5 °C delays significantly the evolution of the modulus, producing the same increase up to 1.1 MPa in about four days (**Figure 4.7.d**) confirming that these intermediate materials can be stored for an appreciable time without affecting the processability in the intermediate stage.

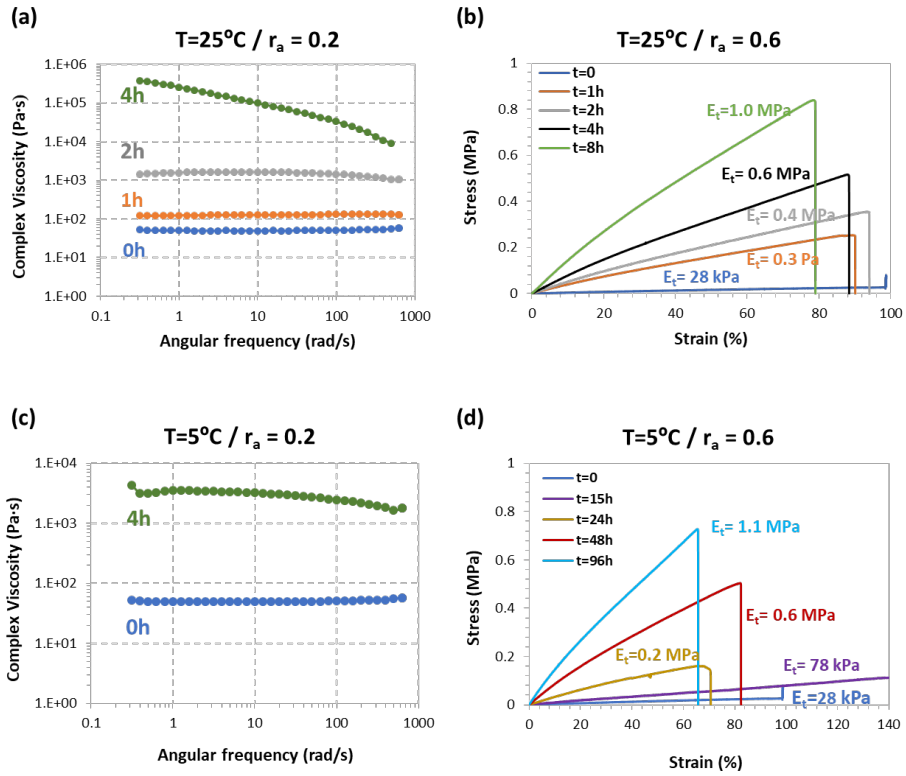

Figure 4.7. Results of the mechanical evaluation of the second reaction latency: (a) changes in complex viscosity of TCDDA02 during 25 °C storage; (b) evolution of the tensile modulus of TCDDA06 intermediate at 25 °C storage temperature; (c) changes in complex viscosity of TCDDA02 during 5 °C storage and (d) evolution of the tensile modulus of TCDDA06 intermediate at 5 °C storage temperature.

3.4. Stage Processing application

3.4.1. Adhesive Bonding

The characteristic two-stage manufacturing process achievable with dual-curing system can be exploited for applications such as dry bonding adhesives [29]. Intermediate materials with $r_a = 0.2$ can be suitable to be used as viscous adhesive which can be easily spread on the adhesion surface. After the application, the second curing stage can be performed resulting in an extremely good final adhesion of the surfaces (**Figure 4.8**). The curing temperature (and time) can be adjusted to the thermomechanical properties of the materials that we want to adhere. In this case, we can take advantage of the dual-curing procedure to reduce the shrinkage, but difficulties in final thickness control arise with thicker adhesive layers because of the viscosity in the intermediate stage. Using

TCDDA06 formulation, intermediate solid materials sheets with different thickness can be obtained and used as solid-like adhesives that can be easily adjusted to the shape of the adhesion surface. As shown in **Figure 4.8.b**, a precise control of the final thickness is thus achieved thanks to the gelled network formed during the first curing stage. The final thickness of the layer remains close to the designed thickness (the thickness of the mould used to prepare each sheet). The effective strength of the bonding and the relation between strength and adhesive layer thickness will be analysed in depth in a future work.

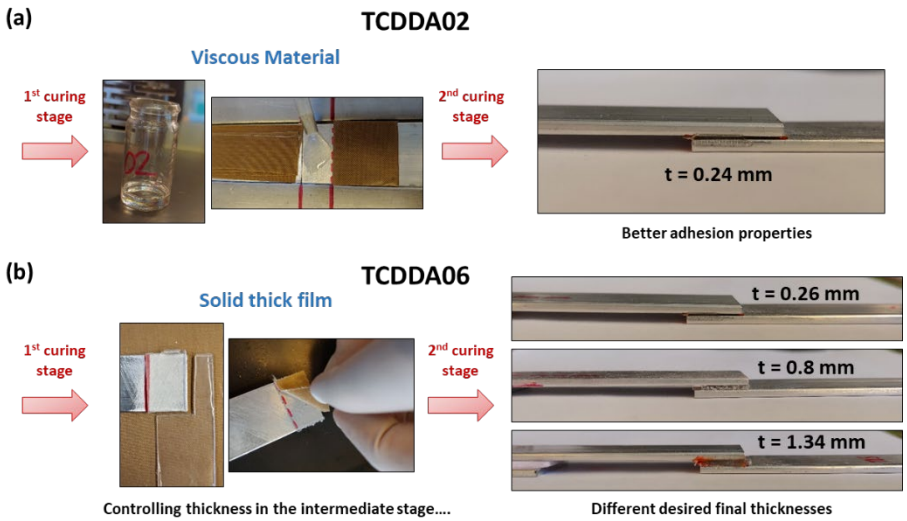

Figure 4.8. Processing of the adhesive bonding: (a) adhesive bonding with the viscous intermediate TCDDA02 material; (b) adhesive bonding with the solid intermediate film of TCDDA06.

The high conformability of the intermediate material with $r_a = 0.6$ can also be exploited for different kind of adhesion joint such as external joining of tubes or pipes [19]. The precise control of the thickness also results in the possibility of stick together different shapes, adjusting the thickness to the complexity of the shapes. In **Figure 4.9**, different thickness intermediate films of TCDDA06 were placed in-between two ABS pieces in order to stick them together in a one-piece-sample.

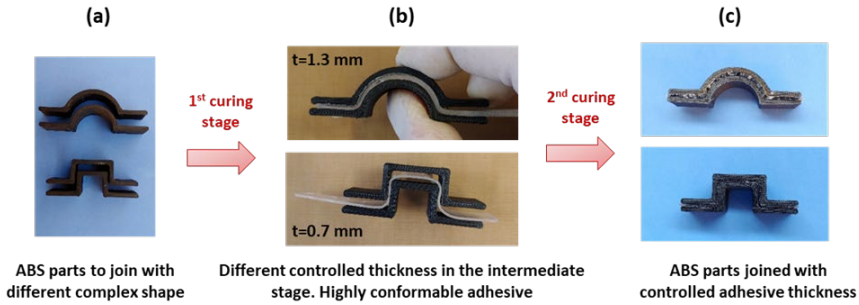

Figure 4.9. (a) Complex ABS (Acrylonitrile Butadiene Styrene) samples to join; (b) positioning the intermediate TCDDA06 film in-between the ABS samples to adhere and (c) result for the two different parts adhered.

3.4.2. Shape-Memory Devices

Finally, the shape-memory behaviour of these materials has been qualitatively investigated taking advantage of the ease of processing of the intermediate material into complex shapes. Final spring-shaped samples were obtained with a two-step curing process of TCDDA06. The uncured formulation was poured into a thin silicon tube with the aid of a syringe (**Figure 4.10.a**), and both ends of the tube were sealed. Afterwards it was cured through the first curing stage, with the tube acting as a mould, and intermediate materials in the form of wires were obtained after removing the silicon tube. The wires were wrapped around a cylindrical rod (**Figure 4.10.b**) and cured for the second stage. As shown in **Figure 4.10.c**, finished springs of controlled dimensions (perfect circular cross-section) were obtained with this procedure highlighting the capability of this material of being processed in complex shapes in the intermediate state. TCDDA02 wires were prepared removing the material from the silicon tube after the second curing step. Here again, excellent surface finish is obtained, with a constant cross-section in the wire along its whole length, as seen in **Figure 4.10.d**.

The shape-memory properties of the spring and the wire shapes obtained were qualitatively tested. Springs prepared with TCDDA06 formulations were programmed at T_g+20 °C in a compressed spring (**Figure 4.11.a**). Conversely, TCDDA02 wire was programmed in the shape of spring rolling up the heated sample around a cylindrical rod (**Figure 4.11.b**).

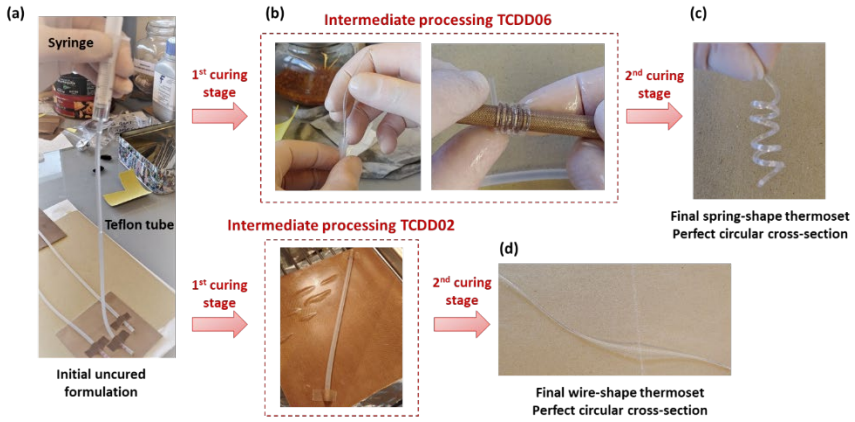

Figure 4.10. Preparation of a spring-shaped (c) and wire-shaped (d) samples from, respectively, TCDDA06 and TCDDA02 formulations (a,b).

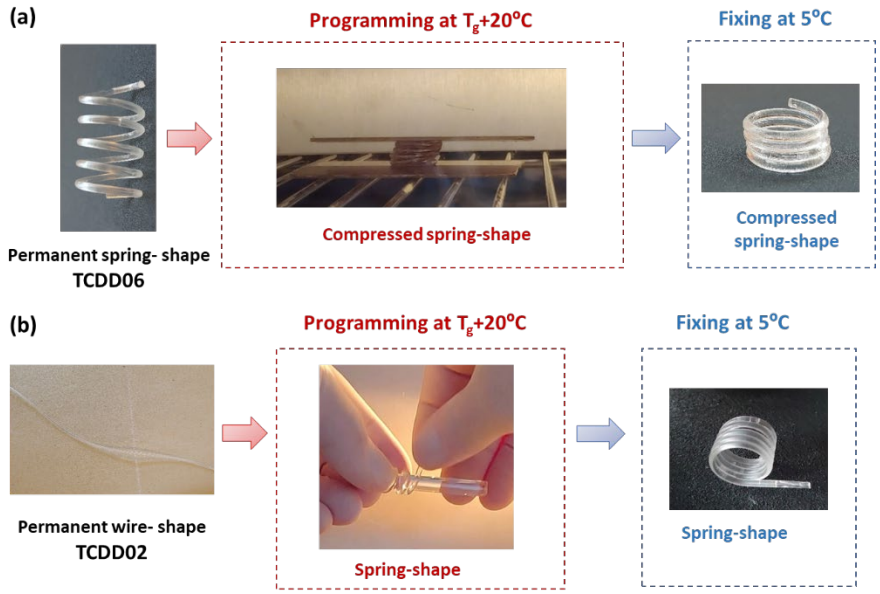

Figure 4.11. Programming of TCDDA06 and TCDDA02 samples: (a) TCDDA06 with a permanent spring shape is programmed in the form of a compressed spring. (b) TCDDA02 with a permanent shape of wire is rolled up around a cylindrical rod and a temporary spring shape is obtained.

Shape fixation was obtained in both situations cooling the deformed samples down to 5 °C. The permanent shape can be recovered in the oven by heating to 75 °C for TCDDA02 and 60 °C for TCDDA06 (T_g+20 °C) as shown in **Figure 4.12**, leading to a complete recovering of the initial shape. As can be seen in **Figure 4.12.a** the compressed spring perfectly recovered the initial length and the actuation seemed perfect to be exploited

for a shape-memory actuator. However, the capability to give a work-output during the recovery process is somehow limited by the low stiffness of the final material. Some partially constrained recovery tests were done but the compressed spring sample was only able to recover is initial shape if a light weight was applied. This problem could be overcome by increasing the functionality of the epoxy resin thus obtaining final materials with tailorable stiffness and without affecting the high deformability of the intermediate state. This problem will be object of further studies.

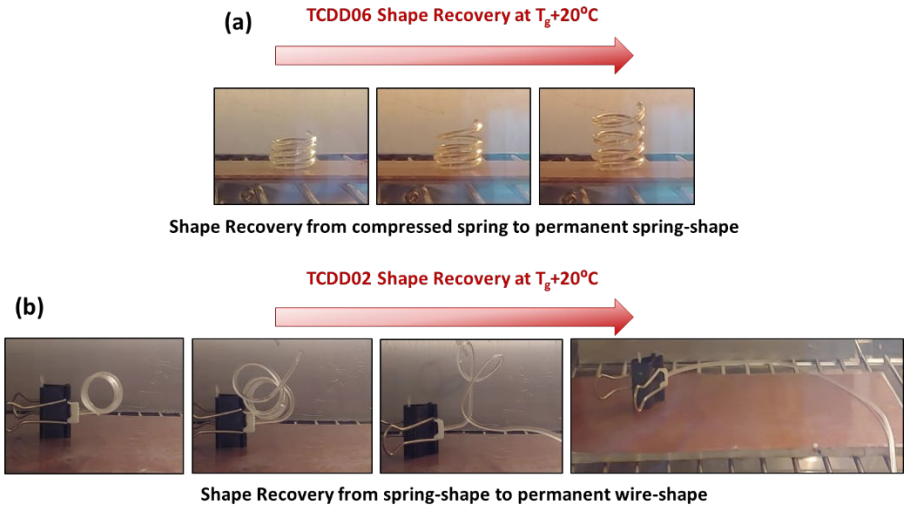

Figure 4.12. (a) TCDDA06 shape-recovery process to permanent spring shape (b) TCDDA02 shape-recovery process to permanent wire-shape.

4. Conclusions

In this work dual-curing thiol-acrylate-epoxy system was rheological and mechanically characterized and potential applications of the obtained materials were proposed. Rheological analysis was performed to determine the actual critical ratio for this system which defines the material behaviour in the intermediate stage. Mechanical and thermomechanical characterization of the materials resulting from the complete curing was performed by means of dynamo-mechanical analysis, Flexural 3-point-bending, tensile test and Shore-D hardness. Stability of the intermediate materials during storage were also evaluated by monitoring the advancement of the reaction in terms of thermal and mechanical properties.

Rheological analysis of the curing process showed that gelation takes place within the first curing stage when the acrylate-thiol ratio is $r_a > 0.45–0.5$. A wide range of both solid-

like and liquid-like intermediate materials can be obtained varying the r_a respectively above and below the r_c. Thermomechanical characterization shows a network softening effect (decrease in flexural and E'_r moduli) together with a toughening effect in the glassy state (E'_g) with the increase of r_a.

Characterization of final thermoset mechanical behaviour at room temperature reveals that a wide range of properties can be obtained varying the proportion between acrylate and thiols group. An interesting combination of the properties of the two network is obtained with 0.6 proportion: final materials with high deformation at break with a gelled intermediate state is obtained. Moreover, slight variation from the pure thiol-epoxy mechanical properties were observed when a small thiol-acrylate proportion is added to the network, meaning that a two-stage curing procedure can be obtained without significant worsening the final materials properties. These evidenced features make this system suitable to be exploited for a large variety of advanced application such as shape-memory actuator and two-stage adhesives.

Storage stability of the intermediate material, between the first and second curing stage, was investigated at storage temperatures of 25 and 5 °C and analysed with DSC and mechanical or rheological characterization. Differences in storage stability were found to be strictly related to the acrylate/epoxy proportion in the mixture. Formulations with a lower acrylate content have lower intermediate stability because the higher content of epoxy groups enhances the reactivity of the second stage thiol-epoxy reaction. Anyway, a relevant amount of time, in which processability of the materials was not affected, is observed for both formulations.

Visual qualitative examples have been presented to demonstrate the possibility to obtain complex shapes for shape-memory actuators and two-stage adhesives with controlled adhesive layer thickness and excellent adhesion.

Author Contributions

X.F.-F. and S.D.l.F. conceived and designed the experiments, which were performed and analysed by C.R. C.R. prepared and characterized the samples under investigation. C.R. wrote the paper. S.D.l.F. and X.F.-F. revised the paper.

Funding

This research was funded by MCIU (Ministerio de Ciencia, Innovación y Universidades), FEDER (Fondo Europeo de Desarrollo Regional) grant number MAT2017-82849-C2-1-R

and MAT2017-82849-C2-2-R, and Generalitat de Catalunya (grant number 2017-SGR-77 and Serra Húnter programme).

Conflicts of Interest

The authors declare no conflicts of interest.

References

[1] J.-P. Pascault, H. Sautereau, J. Verdu, R.J.J. Williams, Thermosetting Polymers, Marcel Dekker, Inc., New York, NY, US, 2002. sig=6Jsr2Jt7Eybbqu_mUOAQXKDyvKg#v=onepage&q&f=false (accessed June 18, 2021).

[2] A. Lendlein, Progress in actively moving polymers, J. Mater. Chem. 20 (2010) 3332–3334. https://doi.org/10.1039/c004361n.

[3] D.P. Nair, N.B. Cramer, J.C. Gaipa, M.K. McBride, E.M. Matherly, R.R. McLeod, R. Shandas, C.N. Bowman, Two-Stage Reactive Polymer Network Forming Systems, Adv. Funct. Mater. 22 (2012) 1502–1510. https://doi.org/10.1002/adfm.201102742.

[4] S. Simić, B. Dunjić, S. Tasić, B. Božić, D. Jovanović, I. Popović, Synthesis and characterization of interpenetrating polymer networks with hyperbranched polymers through thermal-UV dual curing, Prog. Org. Coatings. 63 (2008) 43–48. https://doi.org/10.1016/j.porgcoat.2008.04.006.

[5] Q. Guo, Thermosets: Structure, Properties, and Applications, 2018. https://books.google.it/books?hl=it&lr=&id=qCxHDgAAQBAJ&oi=fnd&pg=PP1&dq=Guo.+Thermosets:+structure,+properties,+and+applications&ots=60lyUjXgYi&sig=A2-7hCa3MNOuDAhyvL_SFzRr6Gc#v=onepage&q=Guo. Thermosets%3A structure%2C properties%2C and applications&f=f (accessed March 15, 2021).

[6] A.O. Konuray, X. Fernández-Francos, X. Ramis, Curing kinetics and characterization of dual-curable thiol-acrylate-epoxy thermosets with latent reactivity, React. Funct. Polym. 122 (2018) 60–67. https://doi.org/10.1016/j.reactfunctpolym.2017.11.010.

[7] K. Jin, N. Wilmot, W.H. Heath, J.M. Torkelson, Phase-Separated Thiol-Epoxy-Acrylate Hybrid Polymer Networks with Controlled Cross-Link Density Synthesized by Simultaneous Thiol-Acrylate and Thiol-Epoxy Click Reactions, Macromolecules. 49 (2016) 4115–4123. https://doi.org/10.1021/acs.macromol.6b00141.

[8] Click Chemistry: Diverse Chemical Function from a Few Good Reactions - Kolb - 2001 - Angewandte Chemie International Edition - Wiley Online Library, (n.d.). https://onlinelibrary.wiley.com/doi/10.1002/1521-3773(20010601)40:11%3C2004::AID-ANIE2004%3E3.0.CO;2-5 (accessed May 27, 2021).

[9] W.H. Binder, R. Sachsenhofer, "Click" chemistry in polymer and material science: An Update, Macromol. Rapid Commun. 29 (2008) 952–981. https://doi.org/10.1002/marc.200800089.

[10] Joerg Lahann, Click Chemistry for Biotechnology and Materials Science - Google Libri, John Wiley & Sons, Ltd, Chirchester, 2009. https://books.google.it/books?hl=it&lr=&id=9eoyUOu4L9IC&oi=fnd&pg=PR7&dq=J.+Lahann,+Click+Chemistry+for+Biotechnology+and+Materials+Science,+John+Wiley+%26+Sons,+Ltd,+2009.&ots=y9vwx1--wa&sig=lJaX05C5wTI2ZWOvPcatP5nc4ok#v=onepage&q=J. Lahann%2C Click Chemistry for Biotechnology and Materials Science%2C John Wiley %26 Sons%2C Ltd%2C 2009.&f=false (accessed May 27, 2021).

[11] A.B. Lowe, C.N. Bowman, Thiol-X Chemistries in Polymer and Materials Science - Google Libri, RSC Publishing , Cambridge, UK, 2012. https://books.google.it/books?hl=it&lr=&id=cYpSUiliYBAC&oi=fnd&pg=PA3&dq=A.+Lowe,+C.+Bowman,+Thiol-X+Chemistries+in+Polymer+and+Materials+Science,+In:+RSC+Polymer+Chemistry+Series,+RSC+Publishing,+2013.&ots=Zwyf2gMWN8&sig=MvA3LLceTAIZC2-o1ykdN30pO6w#v=onepage&q&f=false (accessed May 27, 2021).

[12] S. De, A. Khan, Efficient synthesis of multifunctional polymers via thiol-epoxy "lick" chemistry, Chem. Commun. 48 (2012) 3130–3132. https://doi.org/10.1039/c2cc30434a.

[13] A.B. Lowe, C.E. Hoyle, C.N. Bowman, Thiol-yne click chemistry: A powerful and versatile

methodology for materials synthesis, J. Mater. Chem. 20 (2010) 4745–4750. https://doi.org/10.1039/b917102a.

[14] K. Jin, W.H. Heath, J.M. Torkelson, Kinetics of multifunctional thiol-epoxy click reactions studied by differential scanning calorimetry: Effects of catalysis and functionality, Polymer (Guildf). 81 (2015) 70–78. https://doi.org/10.1016/j.polymer.2015.10.068.

[15] Y. Jian, Y. He, Y. Sun, H. Yang, W. Yang, J. Nie, Thiol-epoxy/thiol-acrylate hybrid materials synthesized by photopolymerization, J. Mater. Chem. C. 1 (2013) 4481–4489. https://doi.org/10.1039/c3tc30360h.

[16] C.E. Hoyle, A.B. Lowe, C.N. Bowman, Thiol-click chemistry: A multifaceted toolbox for small molecule and polymer synthesis, Chem. Soc. Rev. 39 (2010) 1355–1387. https://doi.org/10.1039/b901979k.

[17] F. Lapique, K. Redford, Curing effects on viscosity and mechanical properties of a commercial epoxy resin adhesive, Int. J. Adhes. Adhes. 22 (2002) 337–346. https://doi.org/10.1016/S0143-7496(02)00013-1.

[18] A. Belmonte, G.C. Lama, G. Gentile, P. Cerruti, V. Ambrogi, X. Fernández-Francos, S. De la Flor, Thermally-triggered free-standing shape-memory actuators, Eur. Polym. J. 97 (2017) 241–252. https://doi.org/10.1016/j.eurpolymj.2017.10.006.

[19] C. Russo, À. Serra, X. Fernández-Francos, S. De la Flor, Characterization of sequential dual-curing of thiol-acrylate-epoxy systems with controlled thermal properties, Eur. Polym. J. 112 (2019). https://doi.org/10.1016/j.eurpolymj.2018.12.048.

[20] R. Geissberger, J. Maldonado, N. Bahamonde, A. Keller, C. Dransfeld, K. Masania, Rheological modelling of thermoset composite processing, Compos. Part B Eng. 124 (2017) 182–189. https://doi.org/10.1016/j.compositesb.2017.05.040.

[21] F. Dimier, N. Sbirrazzuoli, B. Vergnes, M. Vincent, Curing kinetics and chemorheological analysis of Polyurethane formation, Polym. Eng. Sci. 44 (2004) 518–527. https://doi.org/10.1002/pen.20046.

[22] A. Keller, C. Dransfeld, K. Masania, Flow and heat transfer during compression resin transfer moulding of highly reactive epoxies, Compos. Part B Eng. 153 (2018) 167–175. https://doi.org/10.1016/j.compositesb.2018.07.041.

[23] A. Belmonte, X. Fernández-Francos, À. Serra, S. De la Flor, Phenomenological characterization of sequential dual-curing of off-stoichiometric “thiol-epoxy” systems: Towards applicability, Mater. Des. 113 (2017) 116–127. https://doi.org/10.1016/j.matdes.2016.10.009.

[24] Y. Tanaka, J.L. Stanford, R. Stepto, Interpretation of gel points of an epoxy-amine system including ring formation and unequal reactivity: Measurements of gel points and analyses on ring structures, Macromolecules. 45 (2012) 7197–7205. https://doi.org/10.1021/ma3009838.

[25] Y. Tanaka, J.L. Stanford, R. Stepto, Interpretation of gel points of an epoxy-amine system including ring formation and unequal reactivity: Reaction scheme and gel-point prediction., Macromolecules. 45 (2012) 7186–7196. https://doi.org/10.1021/ma300984u.

[26] X.L. Wu, S.F. Kang, X.J. Xu, F. Xiao, X.L. Ge, Effect of the crosslinking density and programming temperature on the shape fixity and shape recovery in epoxy-anhydride shape-memory polymers, J. Appl. Polym. Sci. 131 (2014). https://doi.org/10.1002/app.40559.

[27] A. Belmonte, D. Guzmán, X. Fernández-Francos, S. De la Flor, Effect of the network structure and programming temperature on the shape-memory response of thiol-epoxy “click” systems, Polymers (Basel). 7 (2015) 2146–2164. https://doi.org/10.3390/polym7101505.

[28] A.O. Konuray, X. Fernández-Francos, X. Ramis, Analysis of the reaction mechanism of the thiol-epoxy addition initiated by nucleophilic tertiary amines, Polym. Chem. 8 (2017) 5934–5947. https://doi.org/10.1039/c7py01263b.

[29] F. Saharil, F. Forsberg, Y. Liu, P. Bettotti, N. Kumar, F. Niklaus, T. Haraldsson, W. Van Der Wijngaart, K.B. Gylfason, Dry adhesive bonding of nanoporous inorganic membranes to microfluidic devices using the OSTE(+) dual-cure polymer, J. Micromechanics Microengineering. 23 (2013) 025021.

DUAL-CURING THIOL-ACRYLATE-EPOXY
THERMOSETS FOR FUNCTIONAL APPLICATIONS
Claudio Russo

https://doi.org/10.1088/0960-1317/23/2/025021.

DUAL-CURING THIOL-ACRYLATE-EPOXY
THERMOSETS FOR FUNCTIONAL APPLICATIONS
Claudio Russo

Chapter 5

Shape-memory actuators based on dual-curing thiol-acrylate-epoxy thermosets

Express Polymer Letters **2021**,15(1), 58-71

DUAL-CURING THIOL-ACRYLATE-EPOXY
THERMOSETS FOR FUNCTIONAL APPLICATIONS
Claudio Russo

Shape-memory actuators based on dual-curing thiol-acrylate-epoxy thermosets

Claudio Russo[1], Xavier Fernández-Francos[2], Silvia De la Flor[1].

[1]Department of Mechanical Engineering, Universitat Rovira i Virgili, Av. Països Catalans 26, 43007 Tarragona, Spain.

[2]ThermodynamicsLaboratory, ETSEIB, Universitat Politècnica de Catalunya, Av. Diagonal 647, 08028 Barcelona, Spain.

Abstract

In this work, new shape-memory thermosets have been developed using a thiol-acrylate-epoxy dual-curing system. A previously studied system has been successfully modified introducing different amounts of tri(2,3-epoxypropyl)isocyanurate (ISO) and bisphenol A glycerolate (1 glycerol/phenol) diacrylate (BAGA) in order to enhance the thermomechanical properties and the glass transition temperature of the final materials. Preliminary studies on the curing process proved that the curing process is not affected, and the critical ratio remains unchanged. Glass transition temperatures and thermomechanical properties were successfully improved, extending the applicability of these thermosets to the field of soft-actuator. Shape-memory behaviour was comprehensively investigated in unconstrained, fully and partially constrained conditions. Unconstrained experiments results showed excellent shape fixation and recovery coupled with fast recovery process. On the other hand, fully and partially constrained recovery experiments evidenced optimal performances obtained by the combination of both high crosslinking density and high deformability in the programming stage. Considerably high values of recovery stress (up to 7 MPa) and work output (up to 1300 kJ/m3) were found confirming the high potentiality of this dual-cured thermosets in the field of soft-actuation.

Keywords: thermosetting resins, dual-curing, actuator, shape-memory, recovery stress.

---

1. Introduction

Shape-memory polymers (SMPs) are a class of smart materials capable of storing a temporarily deformed shape and subsequentially recover their original permanent shape under the application of an external stimulus [1]. They represent one of the most extensively investigated mechanical active materials due to their potential applications

in a large variety of fields such as aerospace industry, soft-robotics, bio-medicine, and sensors [2–5]. The shape-memory effect (SME) is usually thermally activated because itis easier to operate, but it can also be induced by light, magnetic field, or an electrical current [6–8].Recently, many studies have focused on crosslinked thermosets reporting excellent shape-memory properties enabling the use of SMPs in highly mechanical demanding applications [9–11]. Among them, epoxy-based shape-memory polymers have been widely used thanks to their optimal mechanical, thermal, electrical, and optical properties. On the other hand, their rigid structure and brittle behaviour with small elongation at break have always represented important drawbacks that have limited their uses. Nowadays, a lot of different strategies to overcome this issue are available in the literature, relying on both the design of the material [12,13] and the optimization of programming conditions [14,15]. The combination of these two strategies allowed improving both the deformability and ultimate strength of SMPs, as demonstrated by the results obtained by Belmonte and co-workers [16,17]. More flexible materials with lower glass transition temperature T_g can be obtained using acrylate monomers. Acrylate based shape-memory thermosets were also deeply investigated during years, efforts being directed at the understanding of the effect of the network design on their thermal, mechanical, and shape memory properties [18–20]. One example can be found in Dhulst et al. [21], who combined both thiol-epoxy and thiol-acrylate network in phase-separated networks with good mechanical properties and interesting shape-memory properties. Another interesting way to combine acrylate and epoxy is a dual-curing procedure in which a combi-nation of two distinct crosslinking reactions, taking place simultaneously or sequentially, form the final network [22]. The combination of two sequential curing reactions makes it possible to obtain intermediate materials that maintain the ability to react upon application of a second stimulus, leading to fully cured materials with a new set of properties. In previous works, a promising epoxy-acrylate dual-curing system, based on the combination of thiol-acrylate Michael addition (first curing reaction) and thiol-epoxy addition (second curing reaction), was developed and characterized [23,24]. It was found that the curing process was almost sequential, with very little overlapping of both reactions at room temperature and remarkable intermediate stability. Mechanical and thermo-mechanical characterization of final thermosets revealed that a wide range of properties could be obtained upon variation of the ratio between acrylate and thiols group (r_a). An interesting combination of the properties of the two networks was obtained with r_a= 0.6, resulting in final materials with high deformation at break, with a gelled intermediate state. Moreover, qualitative tests showed promising shape-memory properties in terms of recovery and fixation ratio together with high material

processability in the intermediate stage and during the programming step. However, the generally low T_g of the final thermosets and the poor thermo-mechanical properties in the rubbery state strongly limited their use as SMPs for mechanical actuators. An interesting application of sequential dual-curing systems is the preparation of multi-layered assemblies incorporating liquid crystal elastomers (LCE), which can act as free-standing thermally reversible actuators [25]. Thermal actuation of such devices can be triggered by the isotropization temperature of the LCE component, and it is affected by the thermomechanical properties and relaxation dynamics of the thermosetting component. In this work, we explore the possibility of improving thermomechanical properties of sequential dual-curing materials based on thiol-acrylate and thiol-epoxy chemistry by modification of both the acrylate and epoxy components. Thermosets were prepared at the critical acrylate:thiol ratio $r_a = r_c = 0.5$ in order to produce a gelled material at the very end of the first curing stage and a final material with a T_g as high as possible [24]. The effect of the new components on the dual-curing kinetic was evaluated by differential scanning calorimetry (DSC) in order to prove that the sequential character of the system is preserved. The first curing stage was also monitored through rheological analysis in order to confirm that no alteration of critical ratio was caused by the incorporation of the new components. Dynamic mechanical analysis (DMA) was performed in order to evaluate the effect of the new compositions on the network relaxation and thermomechanical properties. Best materials were selected, and their shape-memory behaviour was tested in three different recovery situations (unconstrained, partially-constrained and fully-constrained) in order to evaluate their capability to generate work or stress during the recovery process.

2. Materials and Methods

2.1. Materials

Different mixtures of *tricyclo[5.2.1.02,6]decanedi -methanol diacrylate* (TCDDA, Sigma-Aldrich, St.Louis, USA, 152.2 g/eq) and *bisphenol A glycero-late (1 glycerol/phenol) diacrylate* (BAGA, Sigma-Aldrich, 242.3 g/eq) were prepared using 10, 30 and50 wt% of BAGA (i.e., 20:80 wt% BAGA:TCDDA).A commercial epoxy resin, *diglycidyl ether of bisphenol A* (DGEBA, EPIKOTE™ Resin 828, Hexion specialty chemicals, Columbus, USA) with an epoxy equivalent weight of 187 g/eq was used as the main epoxy resin. In addition, a *tri(2,3-epoxypropyl)isocyanurate* (ISO, Sigma-Aldrich) with an epoxy equivalent weight of 99.09 g/eq was used as modifier in different proportions: 10, 30 and 50 wt% (i.e., 20:80 wt% ISO:DGEBA). *Pentaerythritol tetrakis(3-mercapto-propionate*) (S4, Sigma-Aldrich), with a molecular weight per thiol equivalent unit of

122.17 g/e, was used as thiol crosslinker maintaining the ratio between acrylate and thiol groups fixed at 0.5 (r_a=0.5). *4-(N,N-dimethylamino)pyridine* (DMAP, Fluka,Seelze, Germany) used at 0.05 phr to catalyse both curing reactions. **Figure 5.1** shows the structure of the different reagents employed in this work.

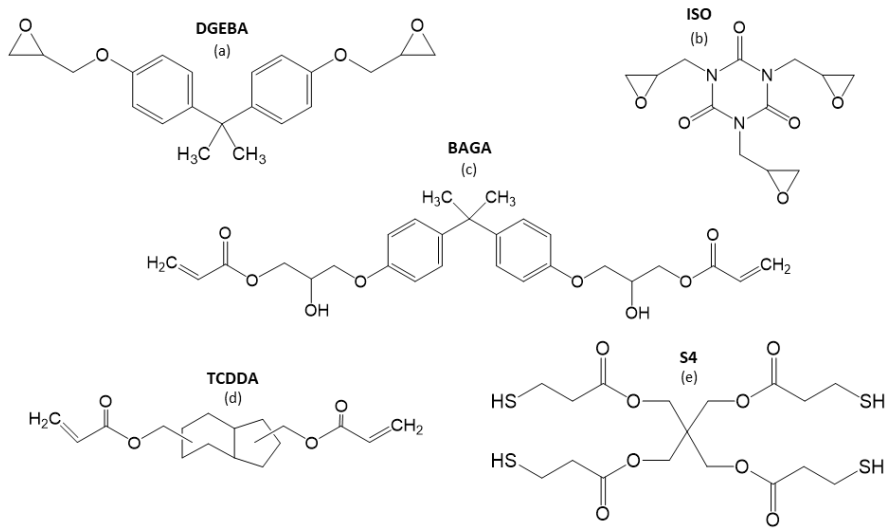

Figure 5.1. Schematic representation of the system components: (a) diglycidyl ether of bisphenol A(DGEBA); (b) tri(2,3-epoxypropyl)isocyanurate(ISO); (c) bisphenol A glycerolate (1 glycerol/phenol) diacrylate(BAGA); (d) tricy-clo[5.2.1.02,6]decanedimethanol diacrylate(TCDDA); (e) Pentaerythritol tetrakis(3-mercaptopropionate)(S4).

First of all, epoxy and acrylate mixtures were pre-pared separately, homogenizing the components, respectively, at 150 and 70°C under magnetic stirring. After that, selected quantities of both mixtures were mixed with S4 and catalyst and manually stirred at room temperature. All samples were cured at 40°Cfor 2 h (1st step), 80°C for 3 h (2nd step), and 100°Cfor 1 h (post-curing). Samples in **Table 5.1** were coded with two number indicating, respectively, the per-centage of ISO and the percentage of BAGA (i.e., 2050 indicates the 20:50 mixture of DGEBA and ISO together with the 50:50 mixture of BAGA and TCDDA while 5050 indicates the 50:50 mixture of DGEBA and ISO together with the 50:50 mixture of BAGA and TCDDA). Formulation with no percent-age of BAGA and ISO was coded NN, where N stands for the use only TCDDA or DGEBA.

Table 5.1. Composition of the formulation under investigation.

Formulation	TCDDA (eq%)	BAGA (eq%)	DGEBA (eq%)	ISO (eq%)	S4 (eq%)
NN	25.00	-	25.00	-	50.00
N10	23.72	1.66	24.88	-	49.75
N30	20.37	5.48	24.70	-	49.45
N50	15.98	10.04	24.68	-	49.30
10N	24.91	-	20.90	4.38	49.81
20N	24.83	-	17.33	8.17	49.67
50N	24.78	-	8.89	16.77	49.56
2050	15.88	9.97	17.10	8.07	48.98
5050	15.84	9.95	8.77	16.55	48.88

2.2. Characterization techniques

2.2.1. Curing process characterization

The effect of different proportions of BAGA and ISO on the dual-curing process was evaluated by differential scanning calorimetry (DSC) in a Mettler Toledo (Greifensee, Switzerland) DSC-3+ apparatus, calibrated using an In standard (heat flow calibration) and an In-Pb-Zn standard (T calibration). Dynamic studies between 0 and 200°C with a heating rate of 10°C/min were performed to characterize the curing process. The dual-curing process was monitored using a rheometer AR-G2 TA Instruments, (New Castle, USA),equipped with an electrically heated plate device(EHP) and 20 mm parallel plate geometry. The evolution of the storage (G') and loss modulus (G'') was monitored through dynamo-mechanical experiments at 40°C for 3 h. The oscillation amplitude was set at0.2% and the frequencies at 0.5, 1.75, and 3 Hz. Gel point was determined as the tanδ crossover at the three different frequencies.

2.2.2. Thermomechanical characterization

A DMA Q800 (TA Instruments New Castle, USA)equipped with a 3-point-bending clamp (with a span of 15 mm) was used. The experiments were per-formed at 3°C/min heating rate, from 0 to 120°C, at1 Hz and 0.1% of strain. Prismatic rectangular samples were thoroughly polished until homogeneous dimensions of about 30×5.5×2.5 mm^3 were obtained. The glass transition temperature T_g and the full wid that half maximum (FWHM) were determined from the tanδ curve peak. The values of storage modulus E'

below and above glass transition were evaluated. The $T_g^{E'}$ was calculated as the onset point of the drop in storage modulus upon mechanical relaxation of the network. A peak in the deformability is obtained at this temperature coinciding with the onset of the mechanical relaxation [14,15]. The flexural modulus (E) of final materials was determined with the same apparatus by means of a force ramp at a constant rate of 1 N/min in controlled-force mode. The slope (m) within the linear zone of the force-displacement curve was obtained. E was calculated in accordance with Equation (1):

$$E = \frac{L^3 m}{4wt^3} \quad (1)$$

where L is the support span, and w and t are the widths and the thickness of the test sample, respectively.

2.2.3. Mechanical characterization

The mechanical properties in tension at $T_g^{E'}$ were measured using a DMA Q800 (TA Instruments, New Castle, USA) equipped with a film-tension clamp in force-controlled mode. Prismatic rectangular samples of about 20×3.5×0.4 mm3were tested until break at $T_g^{E'}$ with a force rate of 1 N/min. Stress and deformation at break were evaluated together with the values of tensile modulus (E_t) for all samples. In addition, the strain energy density (SED) was calculated as the area under the stress-strain curve.

2.2.4. Shape-memory characterization

The shape-memory properties of prismatic rectangular samples of about 20×3.5×0.4 mm^3 were measured using a DMA Q800 (TA Instruments, New Castle, USA) with a film-tension clamp in force-controlled mode. Three different shape-memory experiments were performed: free-recovery test (**Figure 5.2.b**), fully-constrained recovery test (**Figure 5.2.c**), and partially-constrained recovery test (Figure 2d). Each test was carried out following customized methods consisting of various steps, as described in **Figure 5.2**.

In all cases, there is a programming of the sample (path 1-2-3 in **Figure 5.2.a**) prior to the shape-memory analysis. Samples were heated to the programming temperature (T_{prog}) at which the sample was de-formed, applying a prescribed value of maximum stress σ_{max}, reaching a value of maximum deformation ε_{max} (path 1-2). Afterward, sample deformation was fixed by rapidly cooled down to a fixation temperature (T_{low}) well below its T_g(path 2-3).For the free-recovery test, the stress was released (σ_0= 0) after cooling down, and the deformation was stabilized at an ultimate deformation ε_u, slightly lower than ε_{max}. The permanent shape was recovered by heating the programmed

sample at 3°C/min to a temperature above T_g ($T_{recovery}$) (path 4a). The recovery process ended with a deformation value of ε_p, which represents the amount of deformation that the sample is not able to recover.

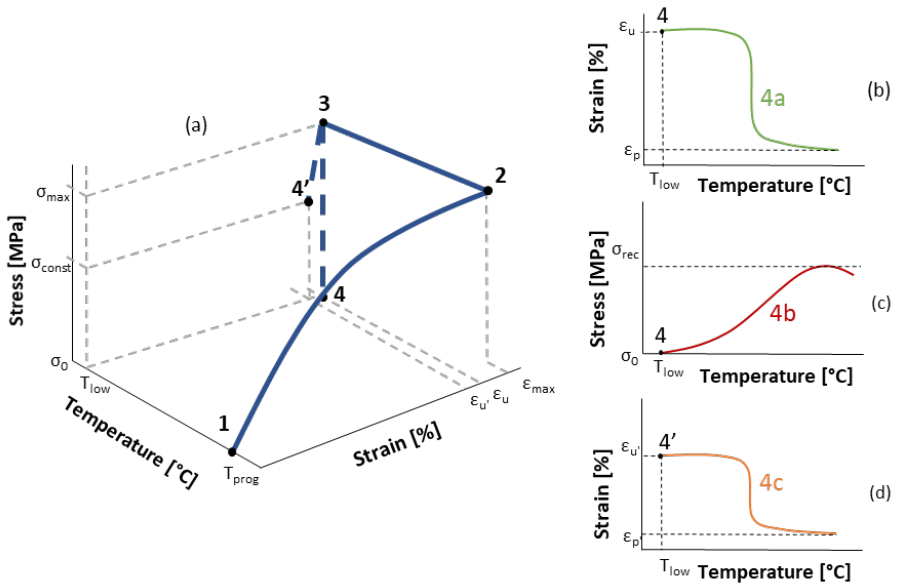

Figure 5.2. Schematic representation of the shape-memory tests: (a) thermomechanical programming, (b) free recovery experiment, (c) constrained recovery experiment, (d) partially-constrained recovery experiment.

At this point a new cycle began by adjusting the temperature again to T_{prog}. Three consecutive cycles were performed foreach sample. In order to quantify the shape-memory properties of our materials, shape-recovery ratio (R_r) and shape-fixation ratio (R_f) were calculated using Equation (2) and (3):

$$R_r[\%] = \frac{\varepsilon_{max} - \varepsilon_p}{\varepsilon_{max}} \cdot 100 \quad (2)$$

$$R_f[\%] = \frac{\varepsilon_u}{\varepsilon_{max}} \cdot 100 \quad (3)$$

These two parameters quantify the ability of the material, respectively, to recover its original shape and to fix a temporary one. Both values were calculated as the average of all the obtained values after each cycle. The maximum stress applied during the path1-2 was 75% of the stress at break (σ_{max}= 0.75·σ_{break})in order to perform a comparative study with the same load level for each sample. Samples were programmed at $T_g^{E'}$ since it is widely reported as the most effective programming condition [14–16]. To ensure a

complete recovery process, samples were heated to $T_{recovery}$= T_g+ 20°C, while T_{low}= 10°C was chosen as fixation temperature as a result of the fixation tests presented in the previous section. Loading and unloading force ramp were carried out at 1 N/min.

Fully-constrained recovery is aimed to compute the recovery stress that our materials are able to generate. To do that, samples were heated while the deformation after the unloading ε_u was kept constant (path 4b). As a result, the stress increased as the temperature increased, reaching a maximum value σ_{rec}. All samples were programmed at the same level of stress (σ_{max}= 8 MPa) selected within the failure limit of all samples.

The work released during the recovery process in partially-constrained recovery experiments was calculated. In this case, samples were unloaded to a value of stress σ_{const} after cooling down. The temperature was increased to $T_{recovery}$, holding constant σ_{const} (path 4c) while the strain recovered under con-straining stress $\varepsilon_{u'}$– $\varepsilon_{p'}$ was measured. The work out-put per volume unit [kJ/m^3] was calculated as follows from Equation (4):

$$W_a(kJ/m^3) = \sigma_{const} \cdot \left(\varepsilon_{u'} - \varepsilon_{p'}\right) \quad (4)$$

The work output is zero when no constraining stress is applied and for fully constrained conditions. Therefore, a maximum in W_a is always present varying σ_{const} [26]. Partially-constrained recovery experiments were carried out, maintaining a 20, 40, and 60% of σ_{max} (σ_{max}= 0.75·σ_{break}) applied during the temperature ramp.

3. Results

3.1. Curing process

The effect of the 50% of BAGA (N50 formulation)and 50% of ISO (50N formulation) on the curing process was studied in order to ensure that the new components did not affect the dual curing kinetics. Rheological properties evolution during the curing process was also monitored to confirm that the presence of 50% of BAGA did not move gelation to the second curing stage. Since gelation is a frequency-independent phenomenon, the gel point was deter-mined as the crossover point of the tanδ at three different frequencies [24]. These analyses were limited to the formulation with the highest amount of BAGA and ISO. We assumed that the most significant effects would be visible in these cases. In consequence, if no effect was detected, it was assumed that lower percentages would clearly not affect the curing. **Figure 5.3** shows the evolution of tanδ during the first curing stage at 40°C. The crossover of the tanδ curves at different

frequencies fall within the first 120 min of the process, proving that gelation will occur during the first curing stage with the curing procedure established (40°C for 2 hours). The curing kinetics were also analysed with a dynamic DSC scan to evaluate the effect of the new components on the dual kinetic.

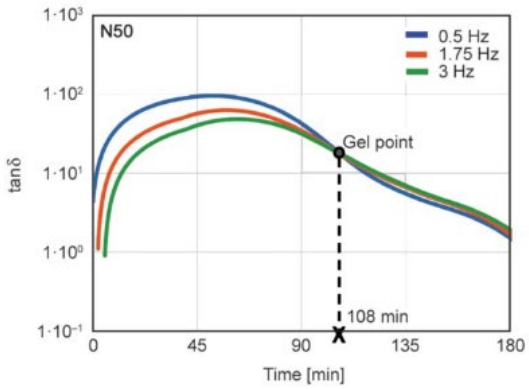

Figure 5.3. Evolution of tanδ with time obtained from the rheological analysis of N50 during the 1stcuring stage at 40°C.

The curing kinetics of a dual-curing system were fully characterized in previous publications [23,24] using TCDDA and DGEBA, so the aim of the present analysis is to confirm that no significant changes in the curing time are produced in the first curing step by the addition of BAGA. First of all, the effect of BAGA on the kinetics of the thiol-acrylate reaction was evaluated comparing the dynamic curing of pure thiol-acrylate samples pre-pared with TCDDA and TCDDA mixed with BAGA (50:50). **Figure 5.4.a** shows no significant changes in the curing kinetics associated with the presence of BAGA. The disappearance of the shoulder visible for NN sample (0% of both BAGA and ISO) only produces a minor change in the shape of the long TCDDA-S4 reaction tale, with no practical effect on the isothermal curing time. The curing behaviour of dual formulations with, alternatively, 50% of BAGA(N50) and 50% of ISO (50N) was compared with the NN formulation curing behaviour (**Figure 5.4.b**).

The first curing reaction, the thiol-acrylate Michael addition, seems to be not affected, while some differences are visible for the second curing reaction, the thiol-epoxy addition. In particular, the separation between the re-actions is not clearly affected, even if a slight shift in the curing process is visible. The long reaction tale characteristic of the reaction between TCDDA and S4 is the reason of the slight overlapping between the two reactions involved. Although this system seems to be not perfectly sequential, in previous works [23,24], we demonstrated that a strong de-crease in the overlapping

region is achieved by controlling the first stage curing temperature, obtaining an intermediate material whose properties are quite stable for a significant amount of time at room temperature.

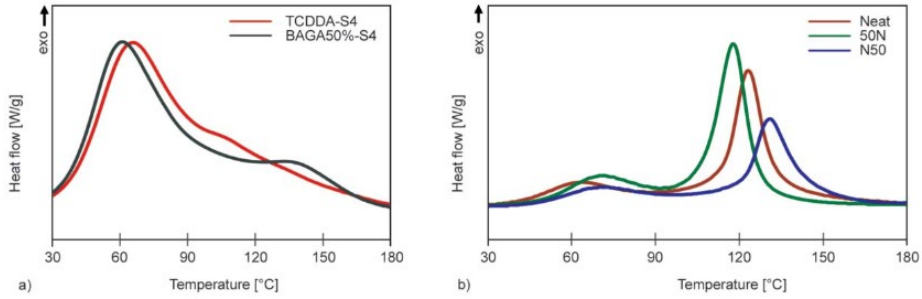

Figure 5.4. (a) DSC dynamic curing scan of pure thiol-acrylate formulations; (b) DSC dynamic curing scans of 50N and N50 formulations compared with the neat formulation.

3.2. Thermomechanical properties

First, the effect of the addition of ISO and BAGA on thermomechanical properties was investigated separately. Data collected, adding an increasing percentage of ISO are summarized in **Table 5.2**. The addition of a different percentage of ISO (**Figure 5.5.a**) results in a slight increase of the T_g without any improvements in terms of FWHM. Introducing ISO in the mixture implies the introduction of new crosslinking points in the final network, which leads to a more restricted molecular mobility, thus increasing T_g. Transitions remain as wide as the one of the neat samples, with a further broadening in the case of 50N caused by the appearance of a shoulder, as already reported by Belmonte et al. [16]. The increase in crosslinking density is confirmed by the increase in E'_r, which is considered to be roughly proportional to the crosslinking density. The values of the flexural modulus E at 25°C are quite low in comparison with the values of the storage modulus at 10°C E'_g because network relaxation is already active at 25°C, as deduced from the relaxation curves in Figure 5a. However, it slightly improves with increasing ISO because of the shifting of the network relaxation to higher temperatures.

A similar effect on the glass transition temperature has been detected, adding different proportions of BAGA to the formulation (**Figure 5.5.b** and **Table 5.3**). Some authors have described a positive effect of the presence of hydroxyl groups on T_g due to the presence of hydrogen-bonds [19] interaction, which affects the network mobility delaying the glass transition. However, Xie and Rousseau [27] reported a decrease in T_g in a series of epoxy-amine based SMPs in spite of the increase of crosslinking density and, consequently, hydroxyl groups.

Table 5.2. Summary of thermomechanical properties of the materials obtained adding ISO.

Formulation	E'_g (MPa)[a]	E'_r (MPa)[b]	T_g (°C)	$T_g^{E'}$ (°C)[c]	FWHM (°C)	E (MPa)[d]
NN	3190	5.2	41.1	26	14	111
10N	2726	12.4	42.8	29	11	304
20N	2848	14.1	43.3	24	13	347
50N	3199	16.7	46.5	27	16	458

[a] Calculated at 10°C; [b] Calculated at 100°C; [c] Onset temperature of the relaxation process; [d] calculated by eq. (1) at 25°C.

Table 5.3. Summary of thermomechanical properties of the materials obtained adding BAGA.

Formulation	E'_g (MPa)	E'_r (MPa)	T_g (°C)	$T_g^{E'}$ (°C)	FWHM (°C)	E (MPa)
NN	3190	5.2	41	26	14	111
N10	2810	10.9	42	27	11	207
N30	2629	10.7	44	30	9	414
N50	2576	14.7	47	33	9	892

It is acknowledged that hydroxyl groups mainly have an influence on the cohesive properties of the material and on the glassy modulus [28]. In contrast, the glass transition temperature, which is more related to network mobility, is generally connected with the rigidity of the network strands and the crosslinking density [28]. The effect observed in this work may be analogous to the one described by Xie and Rousseau [27]. The addition of BAGA reduces the crosslinking density of the material due to the larger size of the BAGA monomer in comparison with TCDDA, but the inherent rigidity of the bisphenol A structure in the BAGA monomer makes up for it and even produces an increase in T_g. Moreover, the FWHM is significantly reduced, adding a percentage of BAGA to the formulation leading to more homogeneous network structure with sharp transitions that better fit the shape-memory requirements. Consequently, the increase in T_g, along with the decrease in FWHM explains the higher value of E at T_{room} (**Table 5.3**). In **Figure 5.5.c** and **Table 5.4** are shown the results obtained for the 2050 (20% of ISO and 50% of BAGA)and 5050 (50% of ISO and 50% of BAGA) formulations, which combine both components, in comparison with the N50 formulation. A slight increase in T_g is visible using 20% of ISO, while a significant increase is detected using 50%. Moreover, the addition of ISO produces only a discrete increase in FWHM, which remains around 10°C. The evolution of the loss modulus (E'') against temperature for these formulations shows that the E'' peak is shifted to temperatures higher than T_{room}, thereby increasing the glassy state stability (**Figure 5.5.d**). Accordingly, we can also

appreciate the positive effect of ISO on the flexural modulus (**Table 5.4**) caused by the shift of T_g to higher temperatures, as discussed previously. A significant difference in storage modulus between the glassy and rubbery states is a crucial requirement for shape-memory polymers [29]. In order to have good control of the recovery process, the onset of the relaxation process has to be a bit higher than the room temperature in order to avoid unintended recovery of the shape when samples are stored at Troom. Furthermore, the value of FWHM is important because of its influence on the shape recovery speed.

Table 5.4. Summary of thermomechanical properties obtained adding both BAGA and ISO.

Formulation	E'_g (MPa)	E'_r (MPa)	T_g (°C)	$T_g^{E'}$ (°C)	FWHM (°C)	E (MPa)
N50	2576	14.7	47	33	9	892
2050	2739	14.7	48	33	11	1188
5050	3067	16.3	56	41	10	1298

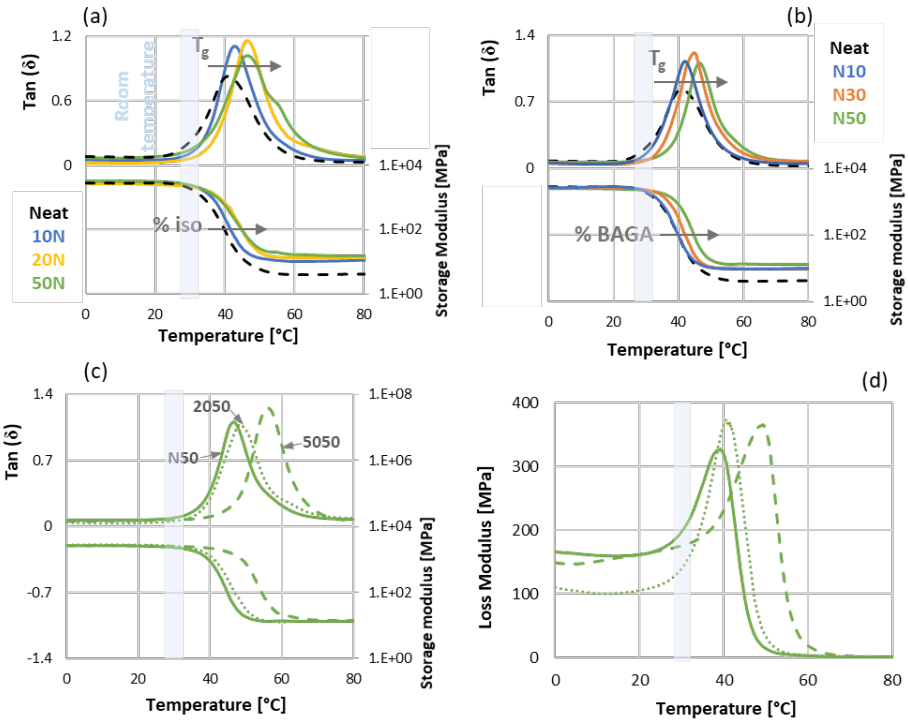

Figure 5.5. Evolution of storage modulus and tanδ along temperature during dynamic mechanical analysis: effect of the addition of (a) ISO, (b) BAGA and (c) both compounds. (d) Loss modulus evolution with temperature for N50, 2050 and5050 formulations.

Considering that all investigated materials meet the requirement in terms of E'_g/E'_r, samples for shape-memory characterization were chosen to look at the characteristic parameters of the relaxation process (T_g, $T_g^{E'}$, FWHM). To this end N50, 2050 and 5050 appears to be the best candidates since they present suitable T_gs for our purpose together with narrow tanδ peaks and $T_g^{E'}$ higher than 30°C. In spite of having a $T_g^{E'}$ lower than 30°C, we chose to study also the behaviour of 20N and 50N in order to isolate the effect of the ISO percentage in samples that present the advantage of being programmable at room temperature, without any additional heat.

3.3. Shape-memory behaviour

3.3.1. Mechanical properties

Tensile test at $T_g^{E'}$ were made to evaluate the limit of these materials during the programming process. The values of stress at break (σ_b) and strain at break (ε_b), are of paramount importance in shape-memory performance because they estimate the network capability to store strain for successive recovery. The strain energy density (SED), calculated as the area under the stress-strain diagram, is the energy required for the programming of the material as it is deformed. It should not correspond to the energy stored because of the large dissipation of the energy produced by the network relaxation during deformation at $T_g^{E'}$, but it gives a qualitative idea in comparative terms. In fact, it is observed that ε_b and SED are fairly proportional, given that the network relaxation behaviour and relaxed modulus of the different systems are not that different. Tensile modulus in **Table 5.5** correlates well with the trend found for E'_r values since the relaxation time at $T_g^{E'}$ is comparable with the tensile test time-scale. N50 exhibits a high level of deformation at break and, due to a strain-hardening effect, values of σ_{break} close to the one obtained using the ISO compound (50N and 20N). Both formulations with ISO show a behaviour dictated from their higher level of cross -linking, which leads to the same level of stress butat a lower level of deformation at break. The behaviour of the mixtures of both ISO and BAGA (2050 and 5050) seems to be improved in terms of ductility by the presence of BAGA, but the increase in crosslinking density limits the strain-hardening effect causing a decrease in the final strength of 2050 and 5050.

Table 5.5. Tensile data at $T_g^{E'}$ obtained by DMA.

Formulation	σ_{break} (MPa)	ε_{break} (%)	E_t (MPa)	SED (kJ/m^3)	$T_g^{E'}$ (°C)
N50	13.6	107.1	199	7040	33
20N	12.5	55.2	298	4842	24
50N	13.2	35.0	357	3746	26.7
2050	9.3	74.5	595	5351	33.2
5050	10.2	48.7	696	4020	40.7

The high deformation at break reached with N50 results also in the highest SED. If one compares the values obtained for 2050 and 5050 with the one obtained for 20N and 50N, it can be clearly observed the increase in ductility caused by the presence of BAGA, thereby leading to higher values of SED. On the other hand, the presence of ISO reduces ductility and inconsequence, SED. There is a close relation between SED and the work generation during partially-constrained recovery, as it will be demonstrated in the following section. We would expect that the Work out-put in materials with of 50% of BAGA is higher due to their capability to store higher energy during de-formation.

3.3.2. Free recovery tests

Taking into consideration the relaxation curves obtained from DMA analysis (section 3.2), the fixation temperature T_{low} was set to 10°C. This temperature is located within the E' plateau in the glassy region and far enough from the modulus drop for all the samples tested. Results obtained in free recovery conditions are shown in **Figure 5.6**. Fixation rates close to 100% were obtained for all analysed samples meaning that at 10°C all samples have low network mobility, regardless of the crosslinking density. Excellent results were also obtained in terms of Recovery ratio, which is about 95–97%. The lowest R_r value was found in N50 sample (100% of DGEBA and 50% of BAGA) due to the damage produced by the excessive programming strain [17], which was selected, taking into account the large strain at break related with the strain-hardening phenomenon mentioned before. Plasticization related to this effect, caused by the production of irreversible damage to the network structure, leads to the presence of a higher portion of unrecoverable deformation after the programming step for N50. As shown in **Figure 5.6.b**, the onset of the recovery process has a good correlation with the T_g of the samples. Besides the optimal results in terms of R_r and R_f obtained, samples of N50, 20N and 50N start to recover too close to T_{room} undermining their application. On the contrary, the higher T_g of 2050 and 5050 shifts the recovery process to higher

temperatures, therefore, avoiding premature recovery. Therefore, it can be concluded that we have at our disposal a high-quality SME activated at different temperatures.

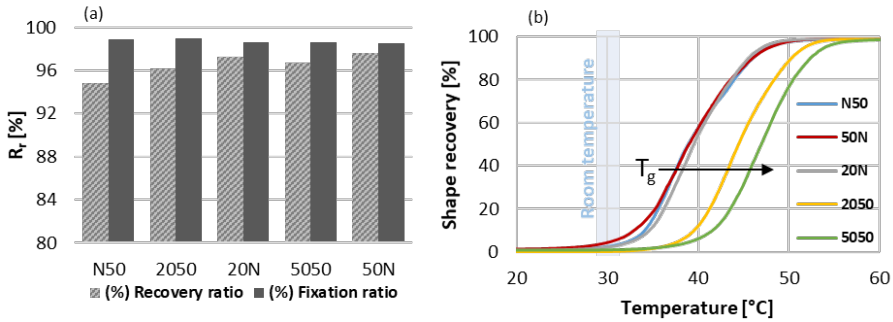

Figure 5.6. (a) Average values of recovery (R_r) and fixation (R_f) rate values from three consecutive free-recovery SMCs; (b) Shape-recovery [%] along temperature during the recovery step of the third cycle

3.3.3. Fully-constrained recovery tests

The recovery stress generation was measured with a fully constrained shape-recovery test at 8 MPa, a stress value within the failure limits of each formulation. **Figure 5.7.a** shows the recovery stress generation of sample programmed at 8 MPa. During the recovery process, the recovery stress progressively in-creases with temperature until a maximum is reached at $T_{recovery}$ marked in **Figure 5.7.a**. In general, two competitive thermomechanical processes are involved in the recovery stress generation: a constrained thermal expansion that generates a compression plateau at lower temperature and the shape-memory effect, which produces a shift towards positive stress values when activated at higher temperature [26,30]. In this case, no compression plateau is visible because of the relatively low transition temperatures of these materials. As shown in **Figure 5.7.b**, 2050 and 5050 generate the highest values of recovery stress while20N and 50N exhibit the lowest ones. Some studies in the literature have shown that more crosslinked networks exercise higher driving recovery forces making the crosslinking density the key factor in recovery stress generation [18,30]. In our case, there seems to be some correlation between SED or as discussed above, the deformability of the material, and the maximum recovered stress. Still, the effect is complex, given that it might also depend on the apparent crosslinking density or relaxed modulus and, especially, the underlying thermal expansion during network relaxation, which in the current experimental setup would have an opposite effect. To the best of our knowledge, the values obtained are positioned between the highest values found in the literature. Arrieta et al. [31] reported recovery stress of around 6 MPa in an acrylic

based shape-memory polymer pre-strained to 55%. Ortega et al. [32] reported recovery stress of almost 4 MPa in (meth)acrylated based shape-memory polymers. Hashmi et al. [33] enhanced the recovery stress of polyurethanes to 6.95 MPa by means of MWCNTs. Although Santiago et al. [26] reported that hyper-branched amine-epoxy SMPs reached values of 7 MPa of stress generated, the stress used to program the samples was 10 MPa. Li et al. obtained higher values of around 17 MPa using UV-cured thermosets and around 14 MPa after recycling the same thermosets [34,35]. In the former cases, samples were programmed in compression, reaching values of de-formation that cannot be easily obtained in tension.

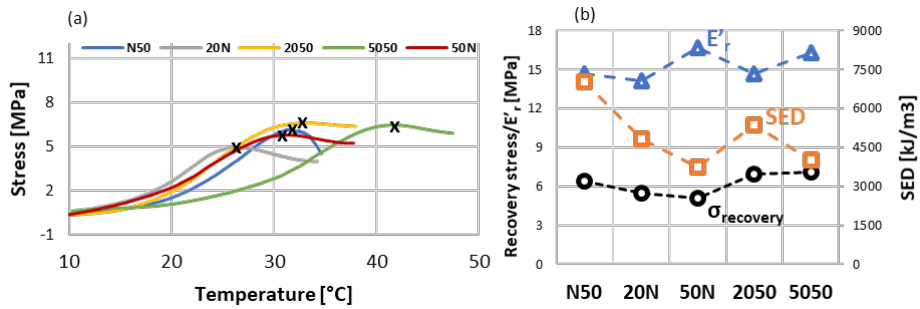

Figure 5.7. (a) Recovery stress generation as function of temperature during a recovery stage of samples programmed at 8 MPa of maximum stress; (b) Values of the maximum stress generated during the recovery stage (**o**) compared with the values of strain energy density (□) and storage modulus in the rubbery state (Δ).

3.3.4. Partially-constrained recovery tests

The level of work output given by the materials during partially-constrained recovery tests was measured under a constrain percentage of 20, 40 and 60% of σ_{max}, and the results are presented in **Figure 5.8**. The best results were obtained with N50, which was able to generate a significantly higher work under any constraining level (**Figure 5.8.a**), reaching a maximum value of about 1300 kJ/m^3 when a 40% of the σ_{max} was maintained during the recovery. Work output, calculated by Equation (4), strongly depends on the deformation obtained after the programming step $\varepsilon_{u'}$ which is directly related to ε_{break} of the material and the SED used during programming. As shown in a previous section, N50 exhibit the highest value of strain at break and, consequently, the highest value of SED, which constitutes the main reasons behind its ability to produce a higher work output. **Figure 5.8.b** presents the work output values obtained for all the percentages of constrain and compares them with the SED, showing a good correlation. Materials with more crosslinked networks have a lower work output during recovery due to their

lower ductility at $T_g^{E'}$. This indicates that deformability plays a fundamental role in work output rather than crosslinking density.

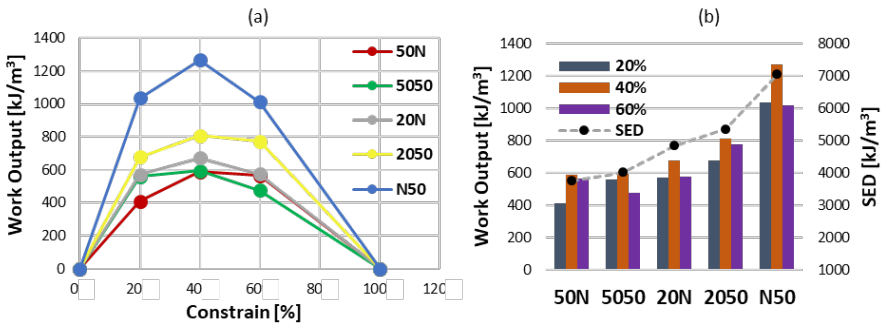

Figure 5.8. (a) Variation of Work output with the constraining percentage; (b) values of Work output at 20, 40 and 60% of constrain compared with strain energy density (SED).

However, the values obtained are considerably higher than values reported in the literature: Santiago et al. [26] obtained a maximum value of 750 kJ/m^3 with hyperbranched epoxy polymers Lakhera et al. [29] reached values of around 300 kJ/m^3 in acrylate-based thermosets programmed in compression; Rapp and Baier [30] reported a maximum of 280 kJ/m^3 in poly-styrene-based Veriflex® [30]. These thiol-acrylate-epoxy thermosets showed are able to perform remarkable work output from 400 to almost 1300 kJ/m^3, confirming the high potentiality of these materials.

The shape-recovery process was also analysed in terms of shape recovery rate. The instantaneous shape-recovery rate $SR_{rate}(t)$ was calculated using Equation (5):

$$SR_{rate}(t) = \frac{dR_r}{dt} \tag{5}$$

Instead, when fully-constrained conditions are applied, the stress generation rate $SG_{rate}(t)$ was calculated from the stress recovery curve by means of Equation (6):

$$SG_{rate}(t) = \frac{d\sigma_{recovery}}{dt} \tag{6}$$

The temperature at which the maximum recovery rate is found (T_{peak}), and the duration of the process as the width of the curve at half-height (ΔT_{peak}) were determined. The velocity of the recovery process (V_r) was calculated as the shape-recovery rate between 15 and 85% of R_r from Equation (7):

$$V_r = \frac{\Delta R_{r,15\%-85\%}}{\Delta T_{15\%-45\%}} \cdot \frac{dT}{dt} \tag{7}$$

Results collected in **Table 5.6** shows that formulations with a higher crosslinking degree present higher values of V_r and a narrower shape-recovery rate peak (lower ΔT_{peak}). As reported by Belmonte et al. [36], the width of the relaxation process deduced from FWHM values is closely related to the shape-recovery rate in glassy materials, which should exhibit a faster recovery when narrower transitions are obtained. In our case, results obtained for the recovery speed for N50 do not correlate with the results obtained for FWHM in **Table 5.3**.

Table 6. Parameters obtained from the shape-memory analysis (unconstrained, fully-constrained, partially constrained) of the different materials under investigation.

	Fully-constrained			**Partially-constrained (40%)**			**Unconstrained**			
	ΔT_{peak} (°C)	**T_{peak} (°C)**	**$\sigma_{recovery}$ (MPa)**	**ΔT_{peak} (°C)**	**T_{peak} (°C)**	**W_a (kJ/m³)**	**ΔT_{peak} (°C)**	**T_{peak} (°C)**	**V_r (%/min)**	**R_r (%)**
N50	11	32	6.4	12	42	1268	12	39	21.0	95.21
20N	8	26	5.5	11	42	672	11	40	24.2	97.24
50N	7	27	5.1	11	44	590	11	40	21.5	97.65
2050	12	33	6.9	10	49	809	10	44	25.4	96.20
5050	14	42	7.1	10	45	593	9	49	26.2	96.74

The explanation can be found in the shape of the SR_{rate} curves (**Figure 5.9.a**). As shown in **Figure 5.9.a** inset, a shoulder in the N50 recovery rate curve is present. This indicates that the recovery process is slowed down due to damages caused to the network at the high level of strain at which the material is programmed. Materials obtained only with the ISO have a slower V_r than 2050 and 5050 as one would expect from their high FWHM values. As it can be seen for any material, values of T_{peak} are slightly below the T_g and vary materials T_g (**Tables 5.2–4**). The effect of the % of constraint on the evolution of the recovery rate along time during a partially-con-strained recovery test was studied, as shown in **Figure 5.9.b** for N50. The recovery process necessitates as lightly higher temperature to starts when constraining stress is applied, but the effect is very small. This is confirmed by the values of T_{peak}, which are slightly shifted to higher values with respect to the unconstrained recovery. It is noteworthy that the values of T_{peak} almost match the loss modulus peak temperature which is the most accredited criterion to determine the T_g from DMA analysis. In contrast, T_{peak} in fully-constrained recovery experiment is significantly reduced compared to the other recovery conditions. The stress generation, in contrast with the recovery of the shape in free and partially-constrained experiments, starts earlier, and T_{peak} turns out to be close to $T_g^{E'}$. This can

be rationalized in terms of the kinetics of network relaxation. It is well known that creep phenomena are retarded with respect to stress relaxation due to the nature of viscoelastic relaxation processes. Consequently, free or partially constrained shape recovery processes should always be delayed with respect to stress build-up in fully constrained processes.

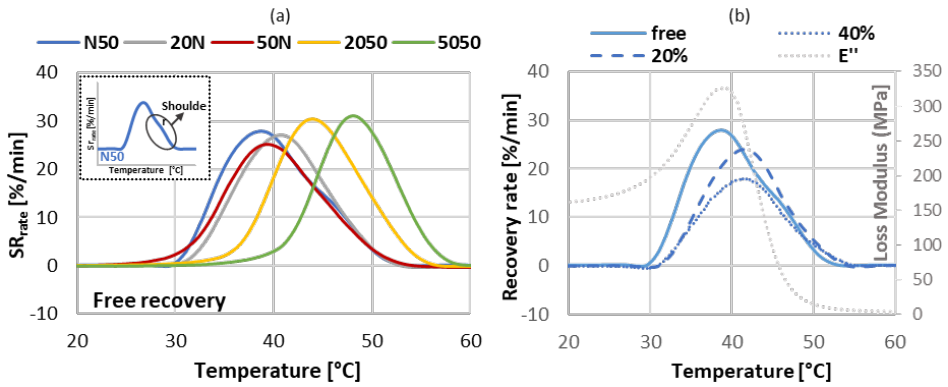

Figure 5.9. (a) Recovery rate variation with temperature during the free-recovery process; (b) effect of the constraining per-centage on the recovery rate curve of N50 samples.

4. Conclusions

In this work, we modified the network structure of thiol-epoxy–acrylate thermosets introducing different percentages of ISO and BAGA in order to obtain final properties suitable for soft actuation. DSC dynamic analysis revealed no significant effects on the dual-curing kinetics, curing reactions maintain an acceptable separation. The evolution of the rheological properties during the first curing stage at 40°C confirmed that gelation still occurs during the first curing step, even if 50% of BAGA was used. The thermomechanical properties of the final mate-rials were successfully enhanced by the modification of the network structure introduced by the new com-ponents. Increasing the percentage of ISO led to an increase in crosslinking density, which is reflected by flexural modulus and glass transition temperatures increase. BAGA has similar effects in terms of T_g together with a strong reduction in FWHM parameter. The relaxation process is steeper and is moved to higher temperatures causing a significant enhancement of material stiffness at room temperature. Materials obtained with the combination of 20and 50% of ISO with the 50% results to be the best one thanks to a simultaneous enhance in terms of T_g and network rigidity. Free-recovery experiments showed an efficient recovery process for all studied materials. The fully-constrained recovery experiments showed an excel-lent capability of these materials to generate stress(up to

7 MPa) on heating above T_g due to the com-bination of high ductility and more crosslinked structure. Finally, partially-constrained recovery experiments demonstrated the capability of these materials to produce a high work output (up to 1300 kJ/m3)during recovery thanks to the high energy stored during programming process. In general, N50, 2050, and 5050 showed excellent shape-memory performances in all recovery scenarios proving they could be suitable to be used as actuator in mechanical demanding applications.

Acknowledgements

The authors would like to thank MCIU (Ministerio de Cien-cia, Innovación y Universidades) and FEDER (Fondo Europeo de Desarrollo Regional) (MAT2017-82849-C2-1-Rand MAT2017-82849-C2-2-R) and Generalitat de Catalunya (2017-SGR-77 and Serra Húnter programme) for the financial support.

5. References

[1] A. Lendlein, S. Kelch, Shape-Memory Polymers, Angew. Chemie Int. Ed. 41 (2002) 2034. https://doi.org/10.1002/1521-3773(20020617)41:12<2034::AID-ANIE2034>3.0.CO;2-M.

[2] Y. Liu, H. Du, L. Liu, J. Leng, Shape memory polymers and their composites in aerospace applications: A review, Smart Mater. Struct. 23 (2014) 023001. https://doi.org/10.1088/0964-1726/23/2/023001.

[3] L. Fang, T. Fang, X. Liu, S. Chen, … C.L.-M., undefined 2016, Near-Infrared Light Triggered Soft Actuators in Aqueous Media Prepared from Shape-Memory Polymer Composites, Wiley Online Libr. 301 (2016) 1111–1120. https://doi.org/10.1002/mame.201600139.

[4] M. Behl, K. Kratz, U. Noechel, T. Sauter, A. Lendlein, Temperature-memory polymer actuators, Proc. Natl. Acad. Sci. U. S. A. 110 (2013) 12555–12559. https://doi.org/10.1073/pnas.1301895110.

[5] J. Reeder, M. Kaltenbrunner, T. Ware, D. Arreaga-Salas, A. Avendano-Bolivar, T. Yokota, Y. Inoue, M. Sekino, W. Voit, T. Sekitani, T. Someya, Mechanically Adaptive Organic Transistors for Implantable Electronics, Wiley Online Libr. 26 (2014) 4967–4973. https://doi.org/10.1002/adma.201400420.

[6] S. Chen, S. Yang, Z. Li, S. Xu, H. Yuan, S. Chen, Z. Ge, Electroactive two-way shape memory polymer laminates, Polym. Compos. 36 (2015) 439–444. https://doi.org/10.1002/pc.22958.

[7] D. Yang, W. Huang, X. He, M. Xie, Electromagnetic activation of a shape memory copolymer matrix incorporating ferromagnetic nanoparticles, Polym. Int. 61 (2012) 38–42. https://doi.org/10.1002/pi.3188.

[8] A. Lendlein, H. Jiang, O. Jünger, R. Langer, Light-induced shape-memory polymers, Nature. 434 (2005) 879–882. https://doi.org/10.1038/nature03496.

[9] D. Santiago, A. Fabregat-Sanjuan, F. Ferrando, S. De la Flor, Hyperbranched-modified epoxy thermosets: Enhancement of thermomechanical and shape-memory performances, J. Appl. Polym. Sci. 134 (2017) 44623. https://doi.org/10.1002/app.44623.

[10] G.J. Berg, M.K. McBride, C. Wang, C.N. Bowman, New directions in the chemistry of shape memory polymers, Polymer (Guildf). 55 (2014) 5849–5872. https://doi.org/10.1016/j.polymer.2014.07.052.

[11] S. Parker, R. Reit, H. Abitz, G. Ellson, K. Yang, B. Lund, W.E. Voit, High-Tg Thiol-Click Thermoset Networks via the Thiol-Maleimide Michael Addition, Macromol. Rapid Commun. 37 (2016) 1027–1032. https://doi.org/10.1002/marc.201600033.

[12] D.M. Feldkamp, I.A. Rousseau, Effect of chemical composition on the deformability of shape-memory epoxies, Macromol. Mater. Eng. 296 (2011) 1128–1141. https://doi.org/10.1002/mame.201100066.

[13] A.B. Leonardi, L.A. Fasce, I.A. Zucchi, C.E. Hoppe, E.R. Soulé, C.J. Pérez, R.J.J. Williams, Shape memory epoxies based on networks with chemical and physical crosslinks, Eur. Polym. J. 47 (2011) 362–369. https://doi.org/10.1016/j.eurpolymj.2010.12.009.

[14] C.M. Yakacki, S. Willis, C. Luders, K. Gall, Deformation limits in shape-memory polymers, Adv. Eng. Mater. 10 (2008) 112–119. https://doi.org/10.1002/adem.200700184.

[15] D.M. Feldkamp, I.A. Rousseau, Effect of the deformation temperature on the shape-memory behavior of epoxy networks, Macromol. Mater. Eng. 295 (2010) 726–734. https://doi.org/10.1002/mame.201000035.

[16] A. Belmonte, D. Guzmán, X. Fernández-Francos, S. De la Flor, Effect of the network structure and programming temperature on the shape-memory response of thiol-epoxy “click” systems, Polymers (Basel). 7 (2015) 2146–2164. https://doi.org/10.3390/polym7101505.

[17] A. Belmonte, X. Fernández-Francos, S. De la Flor, New understanding of the shape-memory response in thiol-epoxy click systems: towards controlling the recovery process, J. Mater. Sci. 52 (2017) 1625–1638. https://doi.org/10.1007/s10853-016-0456-9.

[18] C.M. Yakacki, R. Shandas, D. Safranski, A.M. Ortega, K. Sassaman, K. Gall, Strong, tailored, biocompatible shape-memory polymer networks, Adv. Funct. Mater. 18 (2008) 2428–2435.

https://doi.org/10.1002/adfm.200701049.

[19] G.J.M. Antony, S.T. Aruna, R. Samikkannu, C.S. Jarali, Effect of Cross-Linking Agent on the Thermo-Mechanical Properties of Acrylate Shape Memory Polymer Network, Front. Mater. Process. Appl. Res. Technol. (2018) 359–364. https://doi.org/10.1007/978-981-10-4819-7_31.

[20] D. Santiago, S. De La Flor, F. Ferrando, X. Ramis, M. Sangermano, Thermomechanical Properties and Shape-Memory Behavior of Bisphenol A Diacrylate-Based Shape-Memory Polymers, Macromol. Chem. Phys. 217 (2016) 39–50. https://doi.org/10.1002/macp.201500261.

[21] E.A. Dhulst, W.H. Heath, J.M. Torkelson, Hybrid thiol-acrylate-epoxy polymer networks: Comparison of one-pot synthesis with sequential reactions and shape memory properties, Polym. (United Kingdom). 96 (2016) 198–204. https://doi.org/10.1016/j.polymer.2016.04.032.

[22] Q. Guo, Thermosets: Structure, Properties, and Applications, 2018. https://books.google.it/books?hl=it&lr=&id=qCxHDgAAQBAJ&oi=fnd&pg=PP1&dq=Guo.+Thermosets:+structure,+properties,+and+applications&ots=60lyUjXgYi&sig=A2-7hCa3MNOuDAhyvL_SFzRr6Gc#v=onepage&q=Guo. Thermosets%3A structure%2C properties%2C and applications&f=f (accessed March 15, 2021).

[23] C. Russo, À. Serra, X. Fernández-Francos, S. De la Flor, Characterization of sequential dual-curing of thiol-acrylate-epoxy systems with controlled thermal properties, Eur. Polym. J. 112 (2019). https://doi.org/10.1016/j.eurpolymj.2018.12.048.

[24] C. Russo, X. Fernández-Francos, S. De la Flor, Rheological and mechanical characterization of dual-curing thiol-acrylate-epoxy thermosets for advanced applications, Polymers (Basel). 11 (2019). https://doi.org/10.3390/polym11060997.

[25] A. Belmonte, G.C. Lama, G. Gentile, P. Cerruti, V. Ambrogi, X. Fernández-Francos, S. De la Flor, Thermally-triggered free-standing shape-memory actuators, Eur. Polym. J. 97 (2017) 241–252. https://doi.org/10.1016/j.eurpolymj.2017.10.006.

[26] D. Santiago, A. Fabregat-Sanjuan, F. Ferrando, S. De La Flor, Recovery stress and work output in hyperbranched poly(ethyleneimine)-modified shape-memory epoxy polymers, J. Polym. Sci. Part B Polym. Phys. 54 (2016) 1002–1013. https://doi.org/10.1002/polb.24004.

[27] T. Xie, I.A. Rousseau, Facile tailoring of thermal transition temperatures of epoxy shape memory polymers, Polymer (Guildf). 50 (2009) 1852–1856. https://doi.org/10.1016/j.polymer.2009.02.035.

[28] J.-P. Pascault, H. Sautereau, J. Verdu, R.J.J. Williams, Thermosetting Polymers, Marcel Dekker, Inc., New York, NY, US, 2002. sig=6Jsr2Jt7Eybbqu_mUOAQXKDyvKg#v=onepage&q&f=false (accessed June 18, 2021).

[29] N. Lakhera, C.M. Yakacki, T.D. Nguyen, C.P. Frick, Partially constrained recovery of (meth)acrylate shape-memory polymer networks, J. Appl. Polym. Sci. 126 (2012) 72–82. https://doi.org/10.1002/app.36612.

[30] S. Rapp, H.B.-S. materials and structures, undefined 2010, Determination of recovery energy densities of shape memory polymers via closed-loop, force-controlled recovery cycling, Iopscience.Iop.Org. (n.d.). https://iopscience.iop.org/article/10.1088/0964-1726/19/4/045018/meta?casa_token=TA0dzw_VVlUAAAAA:7-xaP7piSERNQCQ3h2Hj4plJ-4_eymIBfz1-evGgoWmnpuE3hIksiRHSYRge6zhE9FFT_9Gri5sJ (accessed June 19, 2021).

[31] J.S. Arrieta, J. Diani, P. Gilormini, Cyclic and monotonic testing of free and constrained recovery properties of a chemically crosslinked acrylate, J. Appl. Polym. Sci. 131 (2014) 39813. https://doi.org/10.1002/app.39813.

[32] A.M. Ortega, C.M. Yakacki, S.A. Dixon, R. Likos, A.R. Greenberg, K. Gall, Effect of crosslinking and long-term storage on the shape-memory behavior of (meth)acrylate-based shape-memory polymers, Soft Matter. 8 (2012) 7381–7392. https://doi.org/10.1039/c2sm25298h.

[33] S.A.R. Hashmi, H.C. Prasad, R. Abishera, H.N. Bhargaw, A. Naik, Improved recovery stress in multi-walled-carbon-nanotubes reinforced polyurethane, Mater. Des. 67 (2015) 492–500.

https://doi.org/10.1016/j.matdes.2014.10.062.

[34] J. Fan, G. Li, High enthalpy storage thermoset network with giant stress and energy output in rubbery state, Nat. Commun. 9 (2018) 1–8. https://doi.org/10.1038/s41467-018-03094-2.

[35] A. Li, J. Fan, G. Li, Recyclable thermoset shape memory polymers with high stress and energy output: Via facile UV-curing, J. Mater. Chem. A. 6 (2018) 11479–11487. https://doi.org/10.1039/c8ta02644k.

[36] A. Belmonte, C. Russo, V. Ambrogi, X. Fernández-Francos, S. De la Flor, Epoxy-Based Shape-Memory Actuators Obtained via Dual-Curing of Off-Stoichiometric "Thiol–Epoxy" Mixtures, Polymers (Basel). 9 (2017) 113. https://doi.org/10.3390/polym9030113.

DUAL-CURING THIOL-ACRYLATE-EPOXY
THERMOSETS FOR FUNCTIONAL APPLICATIONS
Claudio Russo

Chapter 6.

Adhesive properties of thiol-acrylate-epoxy composites obtained by dual-curing procedures

International Journal of Adhesion and Adhesives **2021**, (Accepted)

DUAL-CURING THIOL-ACRYLATE-EPOXY
THERMOSETS FOR FUNCTIONAL APPLICATIONS
Claudio Russo

Adhesive properties of thiol-acrylate-epoxy composites obtained by dual-curing procedures

Claudio Russo[1], Francesc Bustamante[1], Xavier Fernández-Francos[2], Silvia De la Flor[1].

[1]Department of Mechanical Engineering, Universitat Rovira i Virgili, Av. Països Catalans 26, 43007 Tarragona, Spain.
[2]ThermodynamicsLaboratory, ETSEIB, Universitat Politècnica de Catalunya, Av. Diagonal 647, 08028 Barcelona, Spain.

Abstract

Composite materials were prepared using a thiol-acrylate-epoxy dual-curing system filled with Boron Nitride (BN) agglomerates. The adhesive properties obtained with two different acrylate ratios (r_a) were tested to characterize differences and applicability of final thermosets. The effect of bondline thickness, BN wt% and curing procedure on the adhesive strength was evaluated for both acrylate ratios r_a by means of lap-shear tests. Materials with viscous intermediate (r_a=0.2) results were observed to have the best performance reaching a maximum of almost 5 kN with 20 wt% of BN. On the other hand, materials with an intermediate gelled network (r_a=0.5) showed a high accuracy in dimension control but lower values of adhesive strength were obtained. A decrease of adhesive strength with the increase of thickness was found for both r_a, while the increase of BN wt% lead to higher adhesive strength. The beneficial effect of dual-curing processing on the adhesive properties of liquid intermediate materials was also experimentally demonstrated.

Keywords: Dual-cure; BN fillers; Film thickness; Mechanical properties of adhesives.

---

1. Introduction

Dual-curing processing is a novel methodology to develop dual network thermosets via two independent but compatible reaction processes [1]. These reactions can be simultaneously activated or sequentially triggered by combination of different stimuli, such as, UV-light and heat, or different reaction kinetics. Sequential dual-curing processing is more attractive due to the possibility of achieving a wide range of material properties in two stages that allows their application in flexible processing scenarios. In previous works a promising epoxy-acrylate dual-curing system, based on the

combination of thiol-acrylate Michael addition and thiol-epoxy “click” reaction, was developed and characterized [2,3]. Thermal and mechanical properties of intermediate and final thermosets can be easily tailored controlling the ratio between acrylate and thiol groups (r_a). Therefore, it is possible to obtain intermediate materials with properties ranging from liquid-like to gelled solid-like, covering a wide range of possible applications. The critical ratio (r_c), defined as the lower ratio at which gelation occurs within the first crosslinking process, sets a boundary line between liquid and solid-like intermediate materials.

Such design capabilities can be exploited to produce multi-layer assemblies with controlled layer thickness and complex shape making use of the good wetting properties of intermediate lightly crosslinked or nearly gelled materials and the good adhesion obtained after the thiol-epoxy reaction. In our previous work, qualitative testing of the adhesive properties of the intermediate materials revealed promising bonding capability and an interesting processing flexibility originated by the dual-curing procedure [3]. Intermediate gelled materials showed interesting characteristics such as high flexibility, capacity to be precisely die-cut and a good stickiness due to the unreacted groups in the network.

Adhesive bonding is a method by which materials can be joined to generate assemblies [4]. Nowadays, due to the increasing use of adhesive bonding in the industry, a lot of efforts are addressed to satisfy the growing demand of new adhesive materials than can be used as valuable alternatives to mechanical joints. Adhesive bonding has found application in various sectors such as aeronautics, electronics, automotive and even for structural purposes [5–9]. Automotive and aerospace industry are pushing for the development of advanced engineered adhesive in order to replace mechanical fastening technology, such as welding and riveting, and considerably reduce the weight. Moreover, adhesive bonds present interesting advantages: a more uniform stress distribution [10], high noise and vibrations reduction [11], good fatigue resistance [12] or protection of the joint against moisture and debris [10].

Over the years, numerous studies were conducted on the relationship between final strength of the adhesive bonding and the adhesive layer thickness. It was found no generalized trend between these parameters because the behaviour of the joint depends on several factors such as the type of loading, adherend nature, adhesives mechanical behaviour (ductile or brittle) and the geometry of the joint [13]. Consequently, depending on the characteristic of the joint, a maximum value of strength can be achieved working with a specific adhesive thickness. In this view, the possibility

of obtaining a constant bondline thickness is of paramount importance during the joint design and fabrication. Properties and quality of the adhesive layer can also be affected by the bondline thickness: a thicker bondline can result in higher adhesive porosity, while a thinner adhesive layer can suffer from resin depletion and debonding. The influence of the adherend surface treatment on adhesive strength cannot be disregarded either.

Dual-curable adhesives are supposed to be able to take advantage of the presence of the network structure formed during the first curing stage, enabling an accurate control of the thickness, and minimizing shrinkage during second curing step. Moreover, thanks to the high deformability of the intermediate materials, it is possible to adapt the adhesive layer to complex adhesion surfaces making possible to obtain complex-shaped joints. On the other hand, intermediate liquid-like materials, which are characterized by higher final strength and glass transition temperatures, could also be exploited as adhesives. Although intermediate liquid-like materials are expected to produce a loss in thickness accuracy, a significant gain in terms of joint strength could be achieved thanks to higher toughness of the final materials and the higher presence of unreacted groups that could be results in a higher number of bonds between the adhesive and the adherends. Compared to the common liquid adhesives an important reduction of the shrinkage during the curing could lead to a higher durability of the joint.

For all these reasons, we found interesting to investigate deeper the potentiality of dual-curing thermosets to be used as adhesives, by means of quantitative testing of the adhesive properties of both liquid-like and solid-like intermediate materials.

A common drawback of epoxy-based adhesives is their generally high coefficient of thermal expansion (CTE) compared to the ones of the adherends. The mismatch in the CTE between adherends and adhesives is one of the main reasons for the failure of adhesive joints. Therefore, the adhesive layer requires reinforcing materials which can reduce the CTE and, at the same time, improve mechanical strength [14]. The addition of microparticles in epoxy thermosets formulation is proven to sufficiently contain thermal expansion without excessively worsen the deformation at break. Among them, the effect of Boron Nitride (BN) microparticles on the properties of epoxy-thiol thermosets has been deeply investigated in our research group [15].

In this paper, the adhesive properties of thiol-acrylate-epoxy thermosets were investigated by means of lap shear test. We decided to characterize the adhesive behaviour of a gelled intermediate obtained with $r_a = r_c = 0.5$ (critical ratio at gelation, [3]) compared with the behaviour of a liquid like intermediate obtained with a $r_a = 0.2$. In both

cases, we added to the formulation, alternatively a 15 wt% and 20 wt% of BN particles with the purpose of reducing the CTE and increasing the toughness at once. BN particles were employed because the high compatibility with epoxy thermosets and their proven capability to reduce CTE as found in previous works by our group [15]. Preliminary characterization of the obtained final materials was carried out through thermomechanical and mechanical testing to assess the final materials properties and investigate the effect of BN particles on the final properties. CTEs were measured by thermo-mechanical analysis (TMA). Finally, single-lap joint samples were prepared in order to evaluate their mechanical behaviour. The effect of the percentage of BN and the adhesive layer thickness on the lap-shear strength was evaluated and the results were compared to commercial adhesives to evaluate the reliability of these thermosets as adhesive. Joint samples were also prepared using the uncured formulations as adhesive and performing a single step curing procedure in order to assess the effect of the curing process on the final strength of the joints.

2. Materials and Methods

2.1. Materials

Diglycidyl ether of bisphenol A (DGEBA, EPIKOTE™ Resin 828, with an epoxy equivalent weight of 187 g/ee) was supplied by Hexion Specialty Chemicals, and dried under vacuum at 80 °C before use. *Pentaerythritol tetrakis(3-mercaptopropionate)* (S4, 122.17 g/eq) and *tricyclo[5.2.1.02,6]decanedimethanol diacrylate* (TCDDA, 152.2 g/eq) were purchased from Sigma-Aldrich and used as received. *4-(N,N-dimethylamino)pyridine* (DMAP) was purchased from Fluka and used at 0.05 phr to act as catalyst for both curing reactions. Two different r_a were employed for this study. Formulation with a viscous intermediate material were prepared fixing the ratio between acrylate groups and thiol groups (r_a) at 0.2. Solid-like intermediate materials were prepared using a r_a=0.5. For loaded samples, 15 wt% or 20 wt% of BN agglomerate (80 µm average, PCTL5MHF, supplied by Saint-Gobain, USA) was added to the previous formulation. The samples were mechanically stirred until homogeneous mixture was obtained. All samples were cured at 40°C for 2 h (1st curing step), 80°C for 3 h (2nd curing step) and 100°C for 1 h (post curing). Single step curing samples were prepared by curing at 100°C for 5 hours in oven. The reaction mechanism of the thiol-acrylate-epoxy system was thoroughly investigated in a previous work [2]. In **Scheme 6.1** the formation of the network is presented:

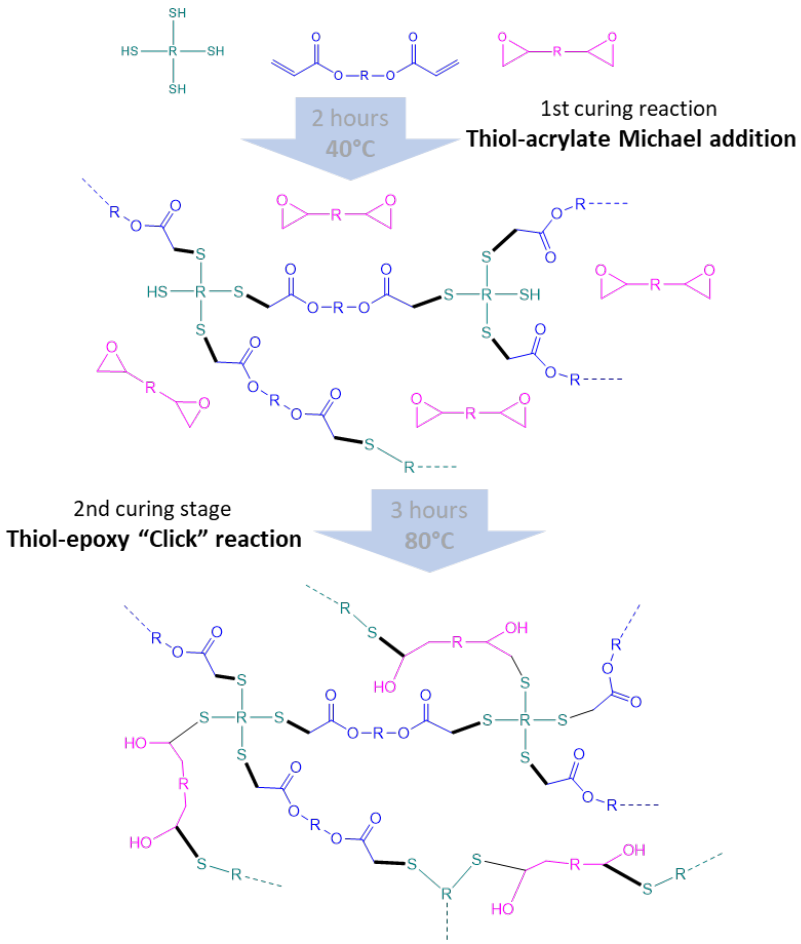

Scheme 6.1. Illustration of network formation mechanism made of two sequential reactions.

Curing at low temperatures the thiol-acrylate Michael addition is favoured respect to thiol-epoxy reaction because of its lower activation energy. Therefore, thiols groups react first with acrylates monomers until no unreacted acrylate groups remains in the mixture. At this point, a first network made up of thiol (green) and acrylate (blue) with unreacted thiol ends is obtained: depending on the r_a of the mixture, a still viscous material ($r_a<r_c$) or a gelled network ($r_a>r_c$) is formed. At room temperature, the thiol-epoxy reaction was found to proceed at such a low rate that a processing window, in which materials properties remains almost stable, is present. Consequently, a second curing stage (at higher temperature) consisting in the reaction between unreacted thiol groups and epoxy (pink) groups, is performed to complete the network build up. The composition of all the samples prepared are shown in **Table 6.1**.

Table 6.1. Composition of the formulation under investigation.

Formulation	r_a	TCDDA (eq%)	DGEBA (eq%)	S4 (eq%)	BN (wt%)
Vis	0.2	10.00	40.00	50.00	0
Vis-15%					15
Vis-20%					20
Gel	0.5	25.00	25.00	50.00	0
Gel-15%					15
Gel-20%					20

2.2. Single-lap joint preparation

Aluminum sheets of 100 x 25 mm2 with a thickness of 1.5 mm, according to the standard UNE-EN ISO 1465:2009 [16] and (ASTM D1002-10) [17], were used as adherends. The manufacturing of the joints presents some differences related to the intermediate materials nature. Adhesives with a viscous intermediate material (Vis-) were prepared by carrying out the first curing stage of r_a=0.2 formulations directly in the glass vial. Then, the intermediate viscous material was poured on the adhesion surface, the upper aluminum sheet was placed, and the joint was cured in the oven (2° curing step). Three different bondline thickness (0.2, 0.7 and 1.5 mm) were obtained by means of Teflon spacers. On the other hand, gelled intermediate adhesives (Gel-) strips of specific thickness (0.2, 0.7 and 1.5 mm) were cut from larger sheet obtained by first curing r_a=0.5 formulations in a Teflon mold. The adhesive layer was positioned covering the adhesion surface before the upper substrate was placed, and the second curing stage was performed in the oven. Teflon spacers of different thickness were used to maintain the distance between the adherends in order to preserve the correct alignment of the aluminum sheets and to control the thickness when viscous adhesive is employed. The overlapping length of 12.5 mm was used in compliance with the UNE-EN ISO 1465:2009 standard

The adhesion surfaces of the aluminium substrates were prepared following the UNE-EN ISO 13887:2004 [18] standard in order to get a strong and durable joint. Overlapping regions were polished and degreased with acetone to remove any greasy impurity. Mechanical abrasion by P360 sandpaper was performed to roughening the bond area. Surfaces were again degreased with acetone in order to remove any abrasion residue. In addition, a constant pressure of 6.27 kPa was applied on the joints during curing in order to ensure good contact between adherends and adhesive.

2.3. Dynamic mechanical analysis

Thermomechanical properties of the different final thermosets were studied by Dynamic mechanical analysis (DMA) employing a TA Instruments DMA Q800 device (TA Instruments, New Castle, DE, USA) equipped with a 3-point bending clamp (15 mm). Prismatic rectangular samples of 3 x 6 x 20 mm^3 were tested ramping the temperature from -10 to 120 °C with a heating rate of 3 °C/min following the UNE-EN ISO 6721-11:2012 [19] standard. Samples were analyzed at a frequency oscillation of 1 Hz and an oscillation strain of 0.1%. The T_g was determined as the tanδ peak temperature, glassy (E_g) and rubbery (E_r) moduli were determined at 10 and 100 °C, respectively. Those temperature were selected in order to ensure the sample to be in the glassy or rubbery region. Full width at half maximum (FWHM) of the tanδ peak was also evaluated as a measure of network heterogeneity.

The Flexural modulus (E) of each sample was determined with the same apparatus in 3-point bending mode at 25 °C by using a force ramp at a constant rate of 1 N/min. E was calculated from the slope of the load deflection curve according to the following equation:

$$E = \frac{L^3 m}{4wt^3} \quad (1)$$

where E is the Flexural modulus of the sample (MPa), L is the support span (mm), w and t are the width and the thickness, respectively, of the sample tested (mm) and m is the gradient of the slope in the linear region (N/mm). The values of E thus determined were aimed to compare the effect of BN wt.% on the mechanical response.

DMA samples were also analyzed by Quanta 600 Environmental SEM instrument (FEI Company, Hillsboro, OR, USA) to investigate fillers dispersions within the matrix. Samples were fractured in liquid nitrogen and then fracture surfaces were coated with gold particles (sputtering). Micrographs were collected at 20 kV and high vacuum. Fracture surface was also analyzed by Field emission scanning electron microscopy (FESEM, Scios 2,Thermo Fisher Scientific, Waltham, MA, US) equipped with an energy-dispersive spectroscopy (EDS) tool. EDS analyses were performed in order to assess the element distribution and, consequently, to confirm that a homogeneous particle distribution was obtained.

2.4. Tensile tests

Tensile properties of dog bone shaped samples of final thermosets (80 mm × 25 mm × 1.5 mm) were obtained by tensile test on a Shimadzu AGS-X (Kyoto, Japan) testing machine equipped with a 10 kN load cell at crosshead speed of 10 mm/min, according to ASTM D638-14 [20] standard. At least five samples were tested for each material. Strain was computed by monitoring the crosshead displacement. However, as the evaluation of tensile properties is used for comparative purposes, by using the same dimensions and testing conditions we can assume that the error introduced by the clamps affects equally all the samples.

The stress at break (σ_b) and deformation at break (ε_b) are determined from the failure point. The elastic modulus E is calculated from the slope of the curve in the initial linear part of the curve. The Strain Energy density can be calculated as the integral of the area under the stress/strain curve.

2.5. Hardness test

Shore hardness of final thermosets was measured with an Affri durometer type D (Shore-D hardness) according to ASTM D2240-15 [21] (ASTM International, West Conshohocken, PA, USA, 2015) in samples of 4 mm thickness. Ten measurements were done in each sample and the average result is presented. Final thermosets obtained with a r_a=0.2 were also analyzed by Vickers microhardness measurements.

2.6. Coefficient of thermal expansion (CTE)

The Coefficient of thermal expansion of final thermosets was measured by means of Thermomechanical analyses (TMA) carried out on a Mettler TMA40 thermomechanical analyzer. Square cured samples (5 × 5 × 2 mm^3) were supported by the clamp and a silica disc to distribute the force uniformly and heated at 5 °C/min from 30 to 90 °C A minimum force of 0.01 N was applied to avoid results distortion. The coefficients of thermal expansion (CTEs) in the glassy state and, where possible, in the rubbery state of the final thermosets were calculated as follows:

$$CTE = \frac{1}{L_0} \cdot \frac{dL}{dT} = \frac{1}{L_0} \cdot \frac{dL/dt}{dT/dt} \quad (2)$$

where L is the thickness of sample, L_0 the initial length, t the time, T the temperature and dT/dt the heating rate.

2.7. Lap-shear test

Final strength of the single-lap joint prepared (and explained in section 2.2) with different materials was evaluated by tensile lap shear tests according to the standard ASTM D1002-10. The geometry of the lap-shear joint specimens used is shown in **Figure 6.1**. An accurate selection was made and only joints within a range of ± 0.03 mm around the desired thickness were tested. The tests were performed in a universal testing machine Shimadzu AGS-X (Kyoto, Japan) equipped with a 10 kN load cell at 1.3 mm/min crosshead speed.

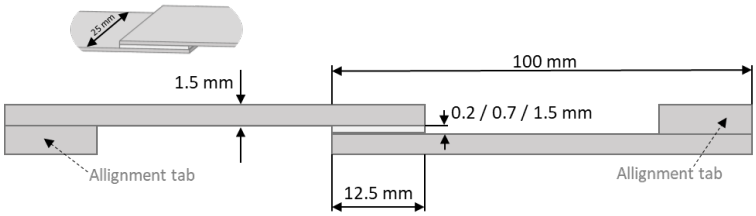

Figure 6.1. Single Lap Joint sample dimensions.

3. Results

3.1. Dynamic mechanical analysis (DMA)

DMA analysis were performed on final thermosets obtained after the complete cure in the oven. The effect of the increasing BN percentage on the thermomechanical properties was investigated. In agreement with the results obtained by Isarn et al. [15], an overall improvement of the thermomechanical behaviour was found for both r_a (**Table 6.2**). In **Figure 6.2** the evolution of the storage modulus and tanδ with temperature are presented. Similar effects were detected for both r_a under investigation. Storage modulus was significantly increased evidencing the reinforcement effect of the BN, particularly, in the rubbery state when the polymer matrix is relaxed. The mechanical effect of the BN particles in the relaxation process results in a glass transition temperature increase of about 4°C. This effect is closely related to the hindrance of the chain motions together with possible interaction between matrix and the filler particles [15]. The increase of T_g is already obtained with 15 wt% of BN without any further increase when the percentage is raised to 20 wt%.

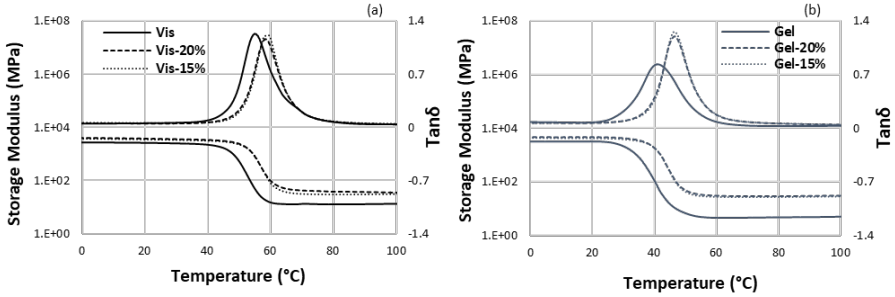

Figure 6.2. Evolution of storage modulus and tanδ with temperature during dynamic mechanical analysis: (a) Vis thermosets; (b) Gel thermosets.

The presence of BN did not alter the shape of the mechanical relaxations, as evidenced from the unimodal shape of the tanδ peaks in **Figure 6.2**, indicating that a homogeneous material is formed even if a significant wt% of BN is used. The shift of the mechanical relaxation to higher temperatures upon addition of BN produces a highly beneficial effect in the case of Gel sample (r_a=0.5), making it possible to obtain a glassy material at room temperature. For that same reason, the flexural modulus E (measured at room temperature) is generally improved for both the Vis and Gel materials upon addition of BN (see **Table 6.2**), therefore reducing its difference with respect to the glassy modulus E_g measured at 10 °C. It can also be seen that just a 15 wt% of BN produces a significant effect, with only a marginal improvement if the filler content is increased to 20 wt%. The increase of T_g indicates there is an interaction between filler and matrix which also affect the crosslinking density distribution as confirmed by the lower FWHM obtained for loaded samples.

Table 6.2. Summary of thermomechanical properties of all investigated materials. Coefficients of variation less than 2% for Tg and FWHM and less tanh 5% for storage and flexural moduli data.

Sample	T_g (°C)	FWHM (°C)	E'_g (MPa)[a]	E'_r (MPa)[b]	E (MPa)[c]
Vis	54.9	10.4	2648	13	1468
Vis-15%	59.6	8.9	3719	31	2226
Vis-20%	58.3	9.5	4065	35	2332
Gel	41.1	14	3194	5	96
Gel-15%	46.7	9.2	4338	28	351
Gel-20%	46.6	9.8	4650	30	520

[a] Calculated at 10°C; [b] Calculated at 100°C; [c] calculated by eq. (1) at 25°C.

Filler dispersion was examined by ESEM microscopy. From the ESEM micrograph presented in **Figure 6.3** it can be clearly observed that all samples present a quite homogeneous dispersion of the filler. Although the BN agglomerates remain intact and

well dispersed within the matrix, some isolated BN particles can be also found. No significant differences were observed between Gel and Vis matrix.

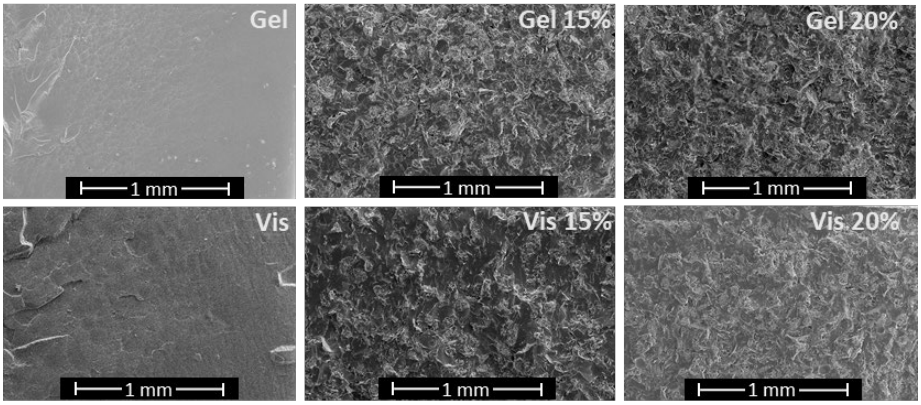

Figure 6.3. ESEM micrographs for the fracture surfaces of the materials prepared on varying the BN content at 100 magnifications.

EDS mapping analyses were performed on the fracture surfaces for a better evaluation of the distribution of BN particles. In **Figure 6.4** the N-mapping and B-mapping on a region obtained at 300 magnifications are presented. For both Vis and Gel adhesive with 20 wt% of fillers, the homogeneity of the N and B elements dispersion throughout the fracture surface was confirmed.

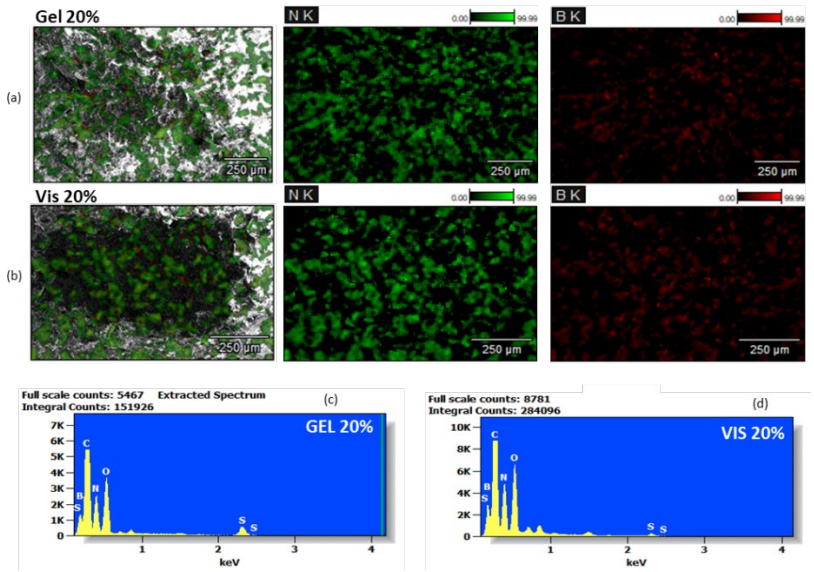

Figure 6.4. FESEM-EDS analysis on the fracture surface: (a) N and B elemental mapping on Gel 20% fracture surface; (b) N and B elemental mapping on Vis 20% fracture surface; (c) EDS spectra for Gel 20%; (d) EDS spectra for Vis 20%.

3.2. Thermomechanical analysis (TMA)

CTE defines the dimensional stability upon temperature changes. It is a crucial parameter in application fields, such as adhesive, when a polymeric material is assembled with low CTE materials such as metallic substrates. To determine the CTE of our materials, TMA analysis were performed on final thermosets and the results obtained were shown in **Table 6.3**. As expected, the introduction of the BN agglomerate results in a decrease of the CTE. This means that, due to the lower CTE mismatch of the components, lower internal stresses will be produced at the organic-inorganic interface in case of working temperature changes. The combination of higher E modulus with lower CTE with increasing BN content will be beneficial in terms of adhesion because the properties of adhesive and substrate become closer.

Table 6.3. Coefficients of thermal expansion (CTE) obtained by TMA analysis.

Sample	$CTE_{rubbery}$ (10^{-6} K^{-1}) [(a)]	$CTE_{rubbery}$ (10^{-6} K^{-1}) [(b)]
Vis	218	125
Vis-15%	207	111
Vis-20%	185	99
Gel	223	146
Gel-15%	194	139
Gel-20%	163	122

[(a)] $CTE_{rubbery}$ is determined at $T>T_g$. [(b)] CTE_{glassy} is determined at $T<T_g$.

3.3. Mechanical properties

Tensile properties of thermosets obtained varying the r_a has been already investigated in our previous work [3] and thus is out of the scope of this work. In order to figure out the effect of BN wt%, dog-bone specimens of final cured samples were tested at room temperature and the data obtained are shown in **Table 6.4**. Tensile tests were performed at room temperature in order to evaluate the values of stress at break (σ_{break}), strain at break (ε_{break}), the tensile modulus (E_t) and the Absorbed Energy during deformation, calculated as the area under the stress-strain diagram.

Table 6.4. Characteristic mechanical parameters obtained from tensile test and hardness measurements.

Sample	E_t (MPa)	Absorbed Energy (kJ/m^3)	σ_{break} (MPa)	ε_{break} (%)	Hardness (Shore-D)	Hardness (HV)
Vis	1580 ± 51.7	2935 ± 121	46 ± 0.4	9.10 ± 0.11	73.1 ± 1.2	10.5 ± 0.5
Vis-15%	1886 ± 80	293 ± 32	25 ± 0.6	1.93 ± 0.34	72.8 ± 0.5	12.0 ± 0.2
Vis-20%	2294 ± 72	355 ± 55	32 ± 1.1	1.94 ± 0.13	73.0 ± 0.4	12.2 ± 0.3
Gel	1347 ± 61	9774 ± 178	24 ± 3.7	59.97 ± 0.82	52.4 ± 1.7	-
Gel-15%	1683 ± 102	179 ± 21	16 ± 1.2	1.77 ± 0.11	68.4 ± 0.3	-
Gel-20%	1946 ± 59	153 ± 27	17 ± 1.9	1.47 ± 0.17	68.7 ± 0.3	-

Significant differences are observed between the neat thermosets (without BN) due to the lower T_g obtained with higher acrylate proportion and the consequent softening of the materials. When r_a=0.5 (**Figure 6.5.b**), a large plastic deformation region appears after the yielding point due to the high network deformability which characterizes this thermoset. In contrast, when r_a=0.2 (**Figure 6.5.a**), the network structure is mostly based on the thiol-epoxy network, which is characterized by higher tensile strength and tensile modulus but a lower deformability due to the lower chain mobility.

Thermosets loaded with BN microparticles are more brittle than neat thermosets, showing a decrease in σ_{break} and a high decrease in ε_{break}. The loss in terms of σ_{break} is more pronounced for Vis thermosets (r_a=0.2) due to the higher inherent brittleness of the neat Vis material. Wattanakul et al. [22] showed the beneficial effects of BN filler on the flexural properties, therefore the worsening of mechanical properties observed in the present work could be ascribed to the particle loading method, leading to a non-uniform dispersion of the filler particles and the presence of defects such as agglomerates and voids. When this kind of composites are submitted to a tensile stress, the mechanical response is provided by the matrix and the filler only act as a defect.

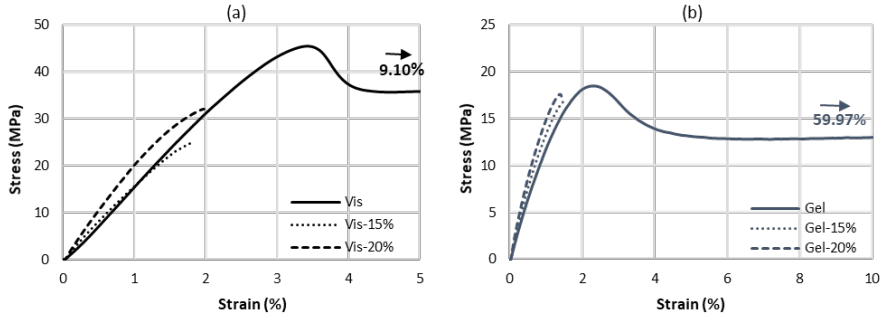

Figure 6.5. Stress-strain curves from tensile tests on final materials: (a) Vis thermosets (r_a=0.2); (b) Gel thermosets (r_a=0.5).

In addition, few isolated voids in loaded samples were detected by ESEM fracture surface analysis (**Figure 6.6**). Those voids could have been originated by the manufacturing process due to the incorporation of air during the formulation stirring. Consequently, few air bubbles can be trapped due to high viscosities of the formulations resulting in a detrimental effect on the tensile properties.

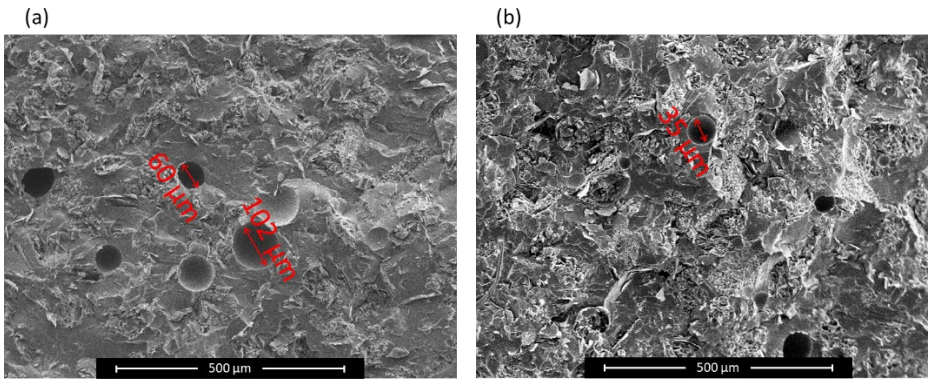

Figure 6.6. ESEM micrographs for the fracture surfaces at 100 magnifications: (a) Gel 20%; (b) Vis 20%.

Shore-D hardness results show slight differences between the final thermosets. As expected, Gel materials are less hard than Vis ones and a slight increase can be observed when loaded with 20 wt% and 15 wt% of BN. However, there are no appreciable differences in Shore-D hardness between neat and loaded samples for Vis thermosets. More precise hardness measurements were made by Vickers durometer which showed a slight increase of HV when thermosets are loaded with BN filler. In any case, no appreciable differences were found between 15 wt% and 20 wt% of BN.

3.4. Lap-shear tests

3.4.1. Effects of BN wt%

It is well known that particles increase the matrix viscosity, which can be detrimental for adhesion applications because of the decrease in the wettability. However, their effect on the adhesive strength could be beneficial. **Figure 6.7.a** shows the average adhesive strength obtained from the lap-shear test on 0.2 mm thick samples. The presence of BN particles leads to a general increase of the failure load for both Gel (r_a=0.5) and Vis (r_a=0.2) thermosets. While neat materials present a similar value of load, the increase of BN wt% results to be more effective for Vis materials which reaches significantly higher adhesive strength values. Increasing the BN wt% to 20 wt% did not lead to a significant change in failure behavior and just a slight increase of adhesive strength was found. **Figure 6.7.b** shows that the failure mode of Vis samples changes from adhesive to cohesive when BN particles are loaded. In contrast, **Figure 6.7.c** shows that Gel specimens have an adhesive failure mode regardless of the presence of BN.

The explanation of this behavior relies on the different structure of the two adhesives when they are applied on the adherend surface. In this phase the viscosity of the materials plays a key role in the development of a durable adhesion. Low viscosities were found to have a detrimental effect on the bond strength due to the residual stress originated from the high shrinkage produced during curing [23]. On the other hand, a high viscosity reduces the capability to replicate the adherend surface morphology leading to a reduced wettability. Paz et al. [24] showed that an optimal viscosity value can be found, and it is closely related to the surface roughness. In our case, the significant increase of the adhesive strength and failure mode change of Vis materials filled with BN particles can be ascribed to the increase of the intermediate material viscosity and the reduction in the global shrinkage caused by the 2nd curing stage, therefore limiting the residual stress between the adhesive and the substrate while maintaining the wetting capabilities of the adhesive.

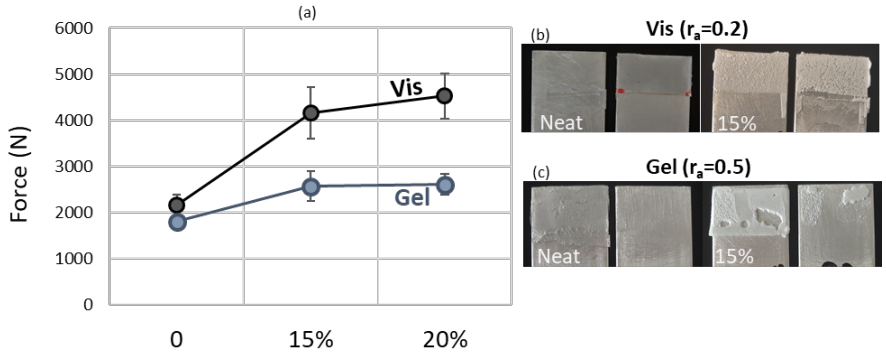

Figure 6.7. (a) Average lap-shear strength as function of BN% for 0.2±0.03 mm joints; (b) fracture surface of Vis and Vis-15% samples; (c) fracture surface of Gel and Gel-15% samples.

When the intermediate adhesive is gelled (Gel materials), only a small increase of adhesive strength was found with 15 wt% and no further decrease was detected increasing BN to 20 wt%. In this case, since the adhesive has a gelled network structure, the presence of the filler cannot produce any viscosity change, and the increase of bond strength can only result from the increase of the rigidity of the cured adhesive. As shown in **Figure 6.7.c**, we were not able to obtain a cohesive failure not even with BN particles. We assume that the poor interfacial strength is caused by the low number of contact point formed at the interface due to total absence of the wetting process. Since the adhesive has solid-like behaviour it can only deform to adapt to the surface, and it prevents the effective penetration of the adhesive into the pores and topographical features of the adherend surface. The aim of this study is to evaluate and compare adhesive properties of materials that have not been tested as adhesive yet, therefore, we decide to always maintain the same condition of preparation and testing even if parameters such as surface roughness strongly influence the joint performance. Actually, surface treatment which produces a higher level of roughness may overcome the absence of wettability resulting in stronger bonding.

3.4.2. Effect of bondline thickness

The average lap-shear strength as function of the bondline thickness is presented in **Figure 6.8**. In general, the increase of the adhesive thickness leads to a reduction of the joint failure load In accordance with the results found in literature [25–27]. There is one exception with Vis adhesive **(Figure 6.8.a)** where a slight increase of the adhesive strength was found from 0.2 to 0.7 mm and then a significant decrease was found from 0.7 to 1.5 mm. Despite classical analytical analysis [28] predict a joint strength improvement for thicker bondlines, there are a lot of experimental data evidencing the

lower performance of thicker bondlines. Adams and Peppiatt [29] attribute the premature failure to higher presence of defects (voids, microcracks...) in a thick bondline. Crocombe et al. [30] showed that thicker joints have a lower strength by considering the plasticity of the adhesive. On the other hand, Banea et al. [31] suggested that ductile adhesives might perform better when a moderately thicker layer is employed. Thickness increases allows to better exploit the adhesive ductility because it increases the volume of material within which energy is dissipated. Grant et al. [32] proposed an interesting explanation to the decrease of adhesive strength with bondline thickness based on the stress distribution inside the adhesive layer. They demonstrated that single lap joints under tension are submitted to a longitudinal stress caused by the direct load and by an additional bending stress produced by the load offset. As the bondline thickness increase, there is an increase in the bending stress due to the load offset leading to a decrease of the joint strength. This stress-state can create plastic strains when the adherend becomes plastic causing failure in the adhesive. In the case of Vis adhesives, a stronger adhesion is obtained with 0.7 mm but not stronger enough to reach the desirable cohesive failure. It can be seen that the failure load is strongly reduced for 1.5 mm joints due to the increasing interface stresses arising from the increased thickness [33], which further undermine the interface adhesion. According to Grant et al. [32], as the lap joint under tension is very sensitive to adhesive thickness, the effect of the plasticity of the adherend is significant with bondline thickness higher than 1 mm. Therefore, the local yielding of the adherend could be the reason behind the lower failure load of 1.5 mm joints.

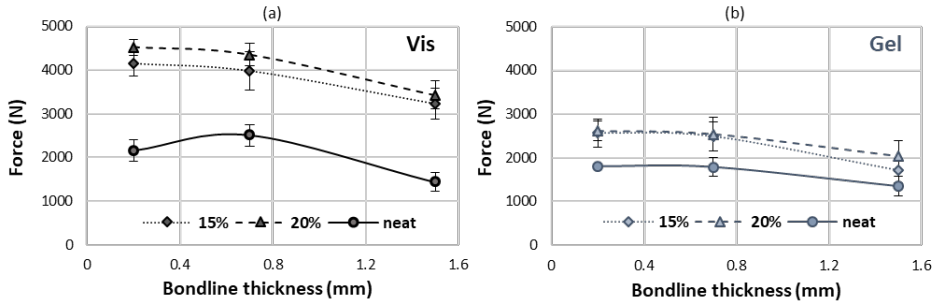

Figure 6.8. Average lap-shear strength as function of adhesive thickness (bondline thickness within a range of ± 0.03 mm were considered): Vis materials (a); Gel materials (b).

Vis adhesives filled with BN particles showed gradual decrease of adhesive strength when increasing thickness in line with the results found in literature for brittle adhesives [32][32]. This behaviour could be also related to higher presence of defects and, especially, voids originated in the manufacturing process as shown in section 3.3. For

brittle adhesive the joints failure is dominated by the stress concentration and might arise from a maximum stress concentration zone, as described by Banea et al. [31].

Analysis of the fracture surface confirms this scenario (**Figure 6.9.a).** In this Figure it is clearly visible the crack propagation for 0.7 and 1.5 mm thick joints (black dotted line). Moreover, fracture surfaces of Vis-15% joints show also that failure moves closer to the interface as the joint thickness is increased. The Increase of BN wt% lead to an increase of failure load as already discussed in the previous section.

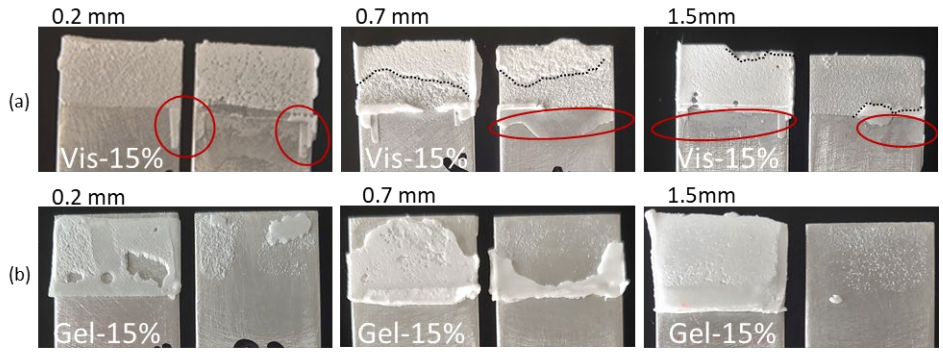

Figure 6.9. (a) Fracture surface of Vis-15% joints of three different thickness: (b) Fracture surface of Gel-15% joints of three different thickness. The dotted black lines in (a) represent the crack propagation line. The red ellipses in (a) highlight the liquid leakage produced upon application of pressure in the preparation of the lap-shear specimens.

Figure 6.8.b shows the average adhesive strength of Gel materials for 0.2, 0.7 and 1.5 mm joints. Increasing the thickness from 0.2 to 0.7 mm produces a loss in adhesive strength of around 3%. The joints undergo to an adhesive failure and as expected, increasing the thickness can only weaken the interface bonding. Fracture surfaces for 0.2 and 0.7 mm joints evidence small spots of cohesive failure which totally disappear for 1.5 mm joint (**Figure 6.9.b**). The lower adhesion of for Gel materials (r_a=0.5) with respect to Vis materials (r_a=0.2) regardless of the bondline thickness was to be expected, in agreement with the results of the previous section, because we decided to characterize the adhesive strength of all sample fixing the joints assembly parameters (i.e., surface treatment, overlapping length) with the aim of comparing the results obtained.

However, Gel adhesives have a significant advantage in comparison with Vis in terms of the control of the bondline thickness and leakages. For that purpose, we decided to analyze the joint thickness distribution for each target thickness (0.2, 0.7 and

1.5 mm) and considered all the prepared specimens. It should be noted that, for the lap-shear tests shown before only samples with a controlled bondline thickness within a range of ± 0.03 mm was considered. Results plotted in **Figure 6.10** clearly highlights the higher precision obtained with Gel adhesives which are characterized by significantly narrower thickness distribution with respect to the Vis ones. The gelled network allows an easy joint thickness control only by controlling the thickness of adhesive sheet placed between the substrates. Indeed, no significant shrinkage is produced during second curing and the network can bear the weight without squeezing. Moreover, liquid formulation leakage, such the ones evidenced in **Figure 6.9.a,** can alter the final thickness of Vis-15% joints while it is avoided for employing gel materials.

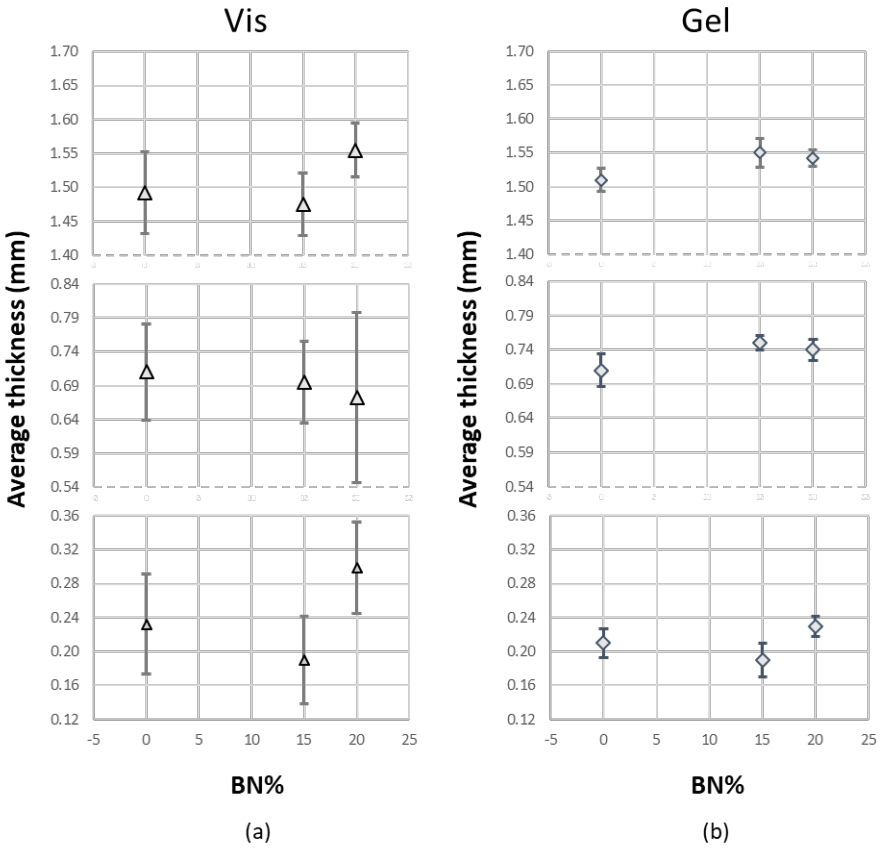

Figure 6.10. Representation of the thickness distribution (confidence interval of 95%) at each BN% percentage for: (a) Vis material joints; (b) Gel materials joints.

3.4.3. Effects of the curing process

In order to highlight the advantages and disadvantages of the dual-curing procedure, 0.7 mm single-lap joints were prepared by a one-step curing procedure at 100 °C and compared to the same sample prepared in a dual-cure process. A high curing temperature was chosen in order to maximize the differences between the two ratios: for r_a=0.2 thiol-acrylate first reaction happens very quickly leaving an intermediate viscous material with an extremely low viscosity at 100°C. On the other hand, for r_a=0.5 the thiol-acrylate reaction leads to a network which is able to withstand high temperature while the thiol-epoxy reaction takes place. It is important to clarify that direct curing strategy is not expected to produce changes on network chemical structure since there are no effect on monomers reactivity, but just reactions sequentiality is prejudicated. The main properties of the final thermosets (T_g, E) are not affected because they depend on the amount of the two reaction which is controlled by the r_a.

As shown in **Figure 6.11.a**, the dual-curing procedure increases the failure load in Vis materials joints. The higher increase was found for Vis-15% and Vis-20% joints because, together with the beneficial effects of BN particles, the higher viscosity of the adhesives ensures lower shrinkage during second curing. In addition, one-step curing produces flow of the adhesive out from the overlapping region due to the low viscosity of the adhesive (**Figure 6.12.a**), leading to irregular adhesion surfaces and making it hard to control the joint thickness. Therefore, dual-curing procedure is extremely favorable in case of liquid-like intermediate materials.

On the contrary, gel materials submitted to a one step curing seems to produce stronger joints at any percentage of BN (**Figure 6.11.b**). The reason has to be found in the lower capability of a solid adhesive to build a strong bonding interface with the substrates due to the absence of the wetting process. The liquid formulation used for one step curing joints is able to properly wet the adhesion surface penetrating the topographical features. This allows the adhesive to take advantage of the surface roughness increasing greatly the contact area and, consequently, the interfacial strength. The major drawback is the significant material contraction during curing which is clearly evidenced in **Figure 6.12.b**. In summary, the one step curing procedure appears to provide better adhesive performance in case of solid-like intermediate materials.

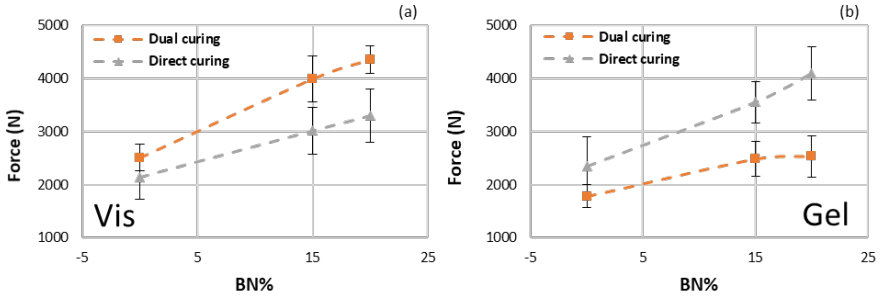

Figure 6.11. Comparison between the average lap-shear strength as function of BN% obtained with a dual-curing a direct curing procedure: (a) Vis materials; (b) Gel Materials.

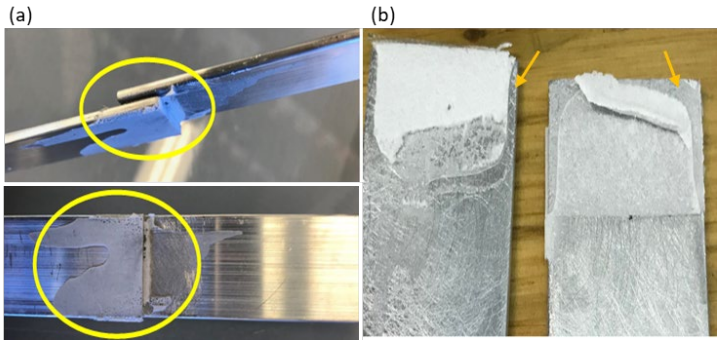

Figure 6.12. (a) Adhesive filtration outside the overlapping region in Vis-20% joint prepared with one step curing procedure; (b) Heavy contraction of the adhesive in Gel-15% joint obtained by one step curing.

Qualitative testing of different configurations was made to prove the extreme flexibility of solid-like intermediate adhesives and their potential use. Some pictures are presented in **Figure 6.13**. Gel-10% sheets of different thickness were used for various purpose. Controlling the sheets thickness, it is possible to perfectly adhere complex shaped substrates without leaving undesirable voids. Moreover, using a 0.2 mm thick sheets we were able to obtain a perfect external pipe joint (**Figure 6.13.a**), while die-cut disc of 0.4 mm was used to obtain a rod-joints (**Figure 6.13.b**). Joints with complex geometrical shapes and good control of joint thickness could be easily prepared from Gel-15% sheets (**Figure 6.13.c**).

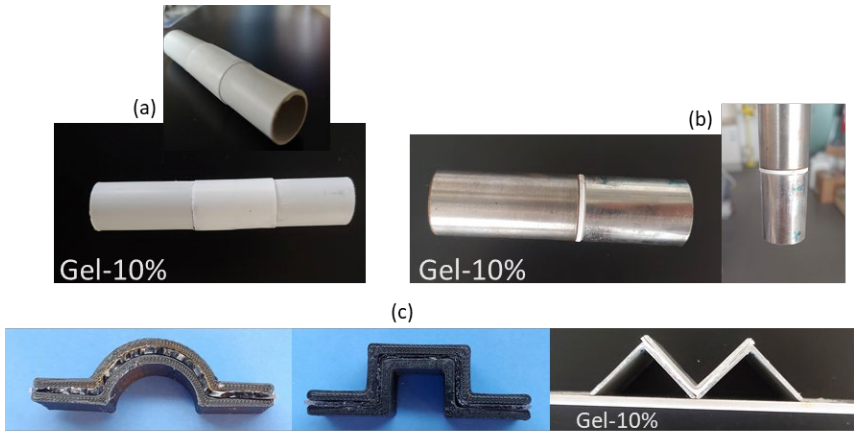

Figure 6.13. (a) External pipe joint using 0.2 mm Gel-10% sheets; (b) Rod-joint using a 0.4 mm disc of Gel-10%; (c) complex shaped substrates adhesion using different thickness sheets of Gel-15%.

4. Conclusions

In general, a significant reinforcement effect caused by the presence of BN particles was detected from the storage modulus curves, in particular, when the polymer matrix is in the rubbery state. Loaded samples also showed a slight increase of T_g compared to neat samples. In the case of Gel samples (r_a=0.5), the increase in T_g also produced beneficial effect on the flexural modulus. Moreover, TMA analysis confirmed that the increase in BN% led to a decrease of CTE contributing to reduce the difference of properties between the adhesive and the substrates. On the other hand, the presence of BN particles strongly affects the tensile behavior of the thermosets leading to a decrease in deformability with respect to the neat samples while, only a slight increase of Shore-D hardness was found.

Single-lap joints with three different bondline thickness were prepared and tested in order to characterize the adhesive properties of all materials under investigation. First, the effect of BN wt% was evaluated comparing joints with a fixed bondline thickness of 0.2 mm. The adhesive strength of Vis materials was significantly increased with 15 wt% of BN while, the adhesive strength increase found for Gel materials was only moderate due to the different structure of the intermediate adhesive. Further increase of the BN content did not produce a relevant effect in adhesive strength. The increase of adhesive bondline thickness produced a decrease of the adhesive strength except for Vis neat materials which showed an increase of adhesive strength from 0.2 to 0.7 mm and then a decrease from 0.7 to 1.5 mm. Control of bondline thickness was much more accurate with Gel adhesive in comparison with the Vis adhesive, due to the

lightly crosslinked structure of the intermediate Gel material, preventing undesired adhesive leakage after application of the intermediate adhesive and subsequent curing. Finally, we evaluated the difference of adhesive strength obtained by one-step curing and a dual-curing procedure. It was seen that intermediate liquid-like materials benefited greatly from dual-curing procedures and enhanced adhesive performance, while Gel materials produced significantly lower shrinkage but weaker joints.

In conclusion, we were able to obtain good level of adhesion and consistently low variation in bondline thickness with, respectively, Vis and Gel materials. In addition, two-stage processing resulted also in reduced shrinkage and leakage in comparison with single-stage processing. Therefore, dual-curing procedures appears to be promising for adhesive applications: further studies aimed to enhance the adhesive strength can be performed combining the advantages of intermediate liquid-like and solid-like materials. The influence of other factors such as overlapping length and surface roughness on adhesive strength could be also tested.

Declaration of Competing Interest

The authors declare that they have no known competing financial interests or personal relationships that could have appeared to influence the work reported in this paper.

Acknowledgements

The authors would like to thank MCIU (Ministerio de Ciencia, Innovación y Universidades) and FEDER (Fondo Europeo de Desarrollo Regional) (MAT2017-82849-C2-1-R and MAT2017-82849-C2-2-R) and Generalitat de Catalunya (2017-SGR-77 and Serra Húnter programme) for the financial support.

5. References

[1] X. Ramis, X. Fernández-Francos, S.D.L.F.- Thermosets, undefined 2018, Click-based dual-curing thermosets and their applications, Elsevier. (n.d.). https://www.sciencedirect.com/science/article/pii/B9780081010211000162 (accessed June 19, 2021).

[2] C. Russo, À. Serra, X. Fernández-Francos, S. De la Flor, Characterization of sequential dual-curing of thiol-acrylate-epoxy systems with controlled thermal properties, Eur. Polym. J. 112 (2019). https://doi.org/10.1016/j.eurpolymj.2018.12.048.

[3] C. Russo, X. Fernández-Francos, S. De la Flor, Rheological and mechanical characterization of dual-curing thiol-acrylate-epoxy thermosets for advanced applications, Polymers (Basel). 11 (2019). https://doi.org/10.3390/polym11060997.

[4] A. V. Pocius, A. V. Pocius, Adhesion and Adhesives Technology, Third Edit, Carl Hanser Verlag GmbH & Co. KG, 2012. https://doi.org/10.3139/9783446431775.fm.

[5] L. Vertuccio, L. Guadagno, G. Spinelli, S. Russo, G. Iannuzzo, Effect of carbon nanotube and functionalized liquid rubber on mechanical and electrical properties of epoxy adhesives for aircraft structures, 129 (2017). https://doi.org/10.1016/j.compositesb.2017.07.021.

[6] O. Ozdemir, N. Oztoprak, An investigation into the effects of fabric reinforcements in the bonding surface on failure response and transverse impact behavior of adhesively bonded dissimilar joints, Compos. Part B Eng. 126 (2017) 72–80. https://doi.org/10.1016/j.compositesb.2017.06.005.

[7] I. Akpinar, K. Gültekin, S. Akpinar, … H.A.-C.P.B., undefined 2017, Research on strength of nanocomposite adhesively bonded composite joints, Elsevier. (n.d.). https://www.sciencedirect.com/science/article/pii/S1359836817312532 (accessed June 20, 2021).

[8] F.M.F. Ribeiro, R.D.S.G. Campilho, R.J.C. Carbas, L.F.M. da Silva, Strength and damage growth in composite bonded joints with defects, Compos. Part B Eng. 100 (2016) 91–100. https://doi.org/10.1016/j.compositesb.2016.06.060.

[9] S.G. Prolongo, M.R. Gude, J. Sanchez, A. Ureña, Nanoreinforced epoxy adhesives for aerospace industry, in: J. Adhes., 2009: pp. 180–199. https://doi.org/10.1080/00218460902881766.

[10] F. Ascione, M. Lamberti, A.G. Razaqpur, S. Spadea, Strength and stiffness of adhesively bonded GFRP beam-column moment resisting connections, Compos. Struct. 160 (2017) 1248–1257. https://doi.org/10.1016/j.compstruct.2016.11.021.

[11] J.R. Vinson, Adhesive bonding of polymer composites, Polym. Eng. Sci. 29 (1989) 1325–1331. https://doi.org/10.1002/pen.760291904.

[12] da S. Lucas F.M:, O. Andreas, A. Robert D., Handbook Of Adhesion Technology, 2nd ed., Springer, Cham, Switzerland, 2018.

[13] S. Budhe, M.D. Banea, S. de Barros, L.F.M. da Silva, An updated review of adhesively bonded joints in composite materials, Int. J. Adhes. Adhes. 72 (2017) 30–42. https://doi.org/10.1016/j.ijadhadh.2016.10.010.

[14] S.Y. On, M.S. Kim, S.S. Kim, Effects of post-treatment of meta-aramid nanofiber mats on the adhesion strength of epoxy adhesive joints, Compos. Struct. 159 (2017) 636–645. https://doi.org/10.1016/j.compstruct.2016.10.016.

[15] I. Isarn, L. Massagués, X. Ramis, À. Serra, F. Ferrando, New BN-epoxy composites obtained by thermal latent cationic curing with enhanced thermal conductivity, Compos. Part A Appl. Sci. Manuf. 103 (2017) 35–47. https://doi.org/10.1016/j.compositesa.2017.09.007.

[16] UNE-EN 1465:2009 Adhesivos. Determinación de la resistencia a ..., (n.d.). https://www.une.org/encuentra-tu-norma/busca-tu-norma/norma?c=N0043309 (accessed June 20, 2021).

[17] ASTM D1002 - 10 Standard Test Method for Apparent Shear Strength of Single-Lap-Joint Adhesively

Bonded Metal Specimens by Tension Loading (Metal-to-Metal), (n.d.). https://www.astm.org/DATABASE.CART/HISTORICAL/D1002-10.htm (accessed June 20, 2021).

[18] UNE-EN 13887:2004 Adhesivos estructurales. Guía para la prepar..., (n.d.). https://www.une.org/encuentra-tu-norma/busca-tu-norma/norma?c=N0030499 (accessed June 20, 2021).

[19] UNE-EN ISO 6721-1:2012 Plásticos. Determinación de las propied..., (n.d.). https://www.une.org/encuentra-tu-norma/busca-tu-norma/norma?c=N0049059 (accessed June 20, 2021).

[20] ASTM D638 - 14 Standard Test Method for Tensile Properties of Plastics, (n.d.). https://www.astm.org/Standards/D638 (accessed June 20, 2021).

[21] ASTM D2240 - 15 Standard Test Method for Rubber Property—Durometer Hardness, (n.d.). https://www.astm.org/DATABASE.CART/HISTORICAL/D2240-15.htm (accessed June 20, 2021).

[22] K. Wattanakul, H. Manuspiya, Thermal conductivity and mechanical properties of BN-filled epoxy composite : effects of filler content , mixing conditions , and BN agglomerate size, (2010). https://doi.org/10.1177/0021998310393297.

[23] P.C. Briggs, G.L. Jialanella, Advances in acrylic structural adhesives, in: Adv. Struct. Adhes. Bond., Elsevier Inc., 2010: pp. 132–150. https://doi.org/10.1533/9781845698058.1.132.

[24] E. Paz, J.J. Narbón, J. Abenojar, M. Cledera, J.C. Real, Influence of Acrylic Adhesive Viscosity and Surface Roughness on the Properties of Adhesive Joint Influence of Acrylic Adhesive Viscosity and Surface Roughness on the Properties of Adhesive Joint, 8464 (2016). https://doi.org/10.1080/00218464.2015.1051221.

[25] R. Kahraman, M. Sunar, B. Yilbas, Influence of adhesive thickness and filler content on the mechanical performance of aluminum single-lap joints bonded with aluminum powder filled epoxy adhesive, J. Mater. Process. Technol. 205 (2008) 183–189. https://doi.org/10.1016/j.jmatprotec.2007.11.121.

[26] L.F.M. Da Silva, T.N.S.S. Rodrigues, M.A. V Figueiredo, M.F.S.F. De, L.F.M. Da, S.T.N.S.S. Rodrigues, M.F.S.F. De Moura, J.A.G. Chousal, Effect of Adhesive Type and Thickness on the Lap Shear Strength, J. Adhes. 82 (2006) 1091–1115. https://doi.org/10.1080/00218460600948511.

[27] M.D. Banea, L.F.M.D.A. Silva, R.D.S.G. Campilho, The Effect of Adhesive Thickness on the Mechanical Behavior of a Structural Polyurethane Adhesive, (2015) 331–346. https://doi.org/10.1080/00218464.2014.903802.

[28] M. Goland, E. Reissner, The Stresses in Cemented Joints, J. Appl. Mech. 11 (1944) A17–A27. https://doi.org/10.1115/1.4009336.

[29] R.D. Adams, n. a. Peppiatt, Stress analysis of adhesive-bonded lap joints, J. Strain Anal. Eng. Des. 9 (1974) 185–196. https://doi.org/10.1243/03093247V093185.

[30] A.C.-I.J. of A. and Adhesives, undefined 1989, Global yielding as a failure criterion for bonded joints, Elsevier. (n.d.). https://www.sciencedirect.com/science/article/pii/0143749689901103 (accessed June 20, 2021).

[31] M.D. Banea, L.F.M. da Silva, Mechanical characterization of flexible adhesives, in: J. Adhes., 2009: pp. 261–285. https://doi.org/10.1080/00218460902881808.

[32] L.D.R. Grant, R.D. Adams, L.F.M. da Silva, Experimental and numerical analysis of single-lap joints for the automotive industry, Int. J. Adhes. Adhes. 29 (2009) 405–413. https://doi.org/10.1016/j.ijadhadh.2008.09.001.

[33] D.M. Gleich, M.J.L. Van Tooren, A. Beukers, Analysis and evaluation of bondline thickness effects on failure load in adhesively bonded structures, J. Adhes. Sci. Technol. 15 (2001) 1091–1101. https://doi.org/10.1163/156856101317035503.

DUAL-CURING THIOL-ACRYLATE-EPOXY
THERMOSETS FOR FUNCTIONAL APPLICATIONS
Claudio Russo

Chapter 7.

Electro responsive shape-memory composites obtained via dual-curing processing

Smart Materials and Structure **2021**, (Under review)

DUAL-CURING THIOL-ACRYLATE-EPOXY
THERMOSETS FOR FUNCTIONAL APPLICATIONS
Claudio Russo

Electro responsive shape-memory composites obtained via dual-curing processing

Claudio Russo[1], José Luis Ramírez[2], Xavier Fernández-Francos[3], Silvia De la Flor[1].

[1]Department of Mechanical Engineering, Universitat Rovira i Virgili, Av. Països Catalans 26, 43007 Tarragona, Spain.

[2]Department of Electrical Electronic Engineering and Automation, ETSE, Universitat Rovira i Virgili, Av. Països Catalans 26, 43007 Tarragona, Spain.

[3]Thermodynamics Laboratory, ETSEIB, Universitat Politècnica de Catalunya, Av. Diagonal 647, 08028 Barcelona, Spain.

Abstract

In this work, electro responsive shape-memory actuators were developed by incorporating a conductive heater in a dual-curing thiol-acrylate-epoxy shape-memory polymer (SMP). A conductive heater, consisting of an electrically conductive silver-ink track printed on Kapton® substrate, was assembled to the SMP taking advantage of the dual-curing processing. The shape-memory effect (SME) was activated by the heat dissipated by Joule effect in the conductive track. Boron Nitride agglomerates were dispersed in the thiol-acrylate-epoxy layers in order to increase the thermal conductivity and achieve faster shape-recovery. A thermoelectric control unit was developed in order to control the shape recovery of the electro responsive actuators and provide different activation strategies. The electrically activated SME was investigated and compared to a traditional SME based on an external heating source given by DMA apparatus. Electro responsive actuators were found extremely faster than the conventional SMPs based on external heating. The fastest recovery was obtained by the 15% BN actuator which recovered the 100% of the original shape in only 8 s. The thermoelectric controlling device provided an optimal control of the shape recovery speed based on the pulse width modulation (PWM) of the heating current under the application of a low voltage (5 V).

Keywords: Dual-curing, shape-memory polymers, electro-responsive actuators, conductive heater.

---

1. Introduction

Shape-memory polymers (SMPs) are a class of stimuli responsive materials that are able to change shape in response to an external stimulus [1,2]. The shape memory effect

(SME) consists in the recovery of a permanent shape, triggered by external stimuli such as heating, electromagnetic field, light or vapor. SMPs found a wide range of applications which is ever wider thanks to the progress and design of more advanced polymeric materials: from biomedical applications [3–5], through self-morphing and self-deploying structures in aviation [6], to smart open-closing mechanisms in industrial applications [7], the SMPs have gained a crucial role in fulfilling the increasing demand of materials suitable for smart applications.

The movement associated to the SME made them extensively used for the fabrication of actuators, which are mechanical devices able to change their shape with respect to the environmental conditions [8]. An external heating source is usually used to stimulate the material response which is triggered by thermal phase transition of the polymeric network [9–13]. In the last few years, several studies were conducted on shape-memory composites taking advantage of alternative actuation mechanisms such as chemo-responsive [14,15], light activated [16], electro-responsive [17] and microwave heated SMPs composites.

In particular, the growing demand to get rid of external heating source and the increase interest in self-standing actuators has channeled research efforts towards electro responsive composites. In this respect, electro responsive composites have been developed combining thermo responsive SMPs with an electrically conductive component. External heating is replaced by a DC voltage applied to the material, which is able to activate the SME thanks to the heat dissipation produced by Joule effect [18,19]. An electrically conductive component is necessary owing to the poor electrical conductivity of polymers. However, the presence of such component should provide adequate electrical conductivity without undermining shape-memory properties. One way to obtain conductive sample is a dispersion of discrete conductive fillers (i.e., CNTs, graphene-oxide or metallic particles). In this case the actuation capability of the composite strongly depends on the formation of a percolating conductive network and on the homogeneous filler dispersion, making it hard to achieve high-speed actuations. For example, Liu et al. reported a non-uniform temperature distribution during the recovery process caused by an inhomogeneous dispersion of fillers, leading to differences in resistivity along the PU/TiO_2 composite [20]. Furthermore, the high amount of filler needed to obtain enough high electrical conductivity is usually accompanied by high processing viscosities, which may prevent efficient transfer of properties from filler to matrix [17]. On the other hand, Luo et al. achieved a significantly high recovery speed using a pre-defined network of non-woven carbon nanofibers (CNFs) incorporated into an epoxy-amine matrix. The highly interconnected CNFs

network guaranteed high electrical conductivity and heat transfer efficiency resulting in recovery times within 2 and 18 s [17].

Another successful strategy is to employ conductive layers coated onto SMP surface: Lu et al. developed an electrically conductive composites by coating the surface of an epoxy-based SMP with a self-assembled CNFs and Boron Nitride (BN) nanopaper [21]. The use of BN significantly enhances the thermal coupling of the layers leading to a recovery speed increase. However, the mismatch of electrical and thermal properties at the bonding interface produced interface dislocations leading to incomplete recovery and low-speed recovery. Considerable enhancement in recovery speed was obtained coupling the epoxy based SMP with layers of self-assembled carboxylic acid-functionalized CNTs and nafion/silica nanofiber [22].

Dual-curing procedure represents a valuable tool to prepare shape-memory thermosets and complex shaped actuators. In particular, we demonstrated that thiol-acrylate-epoxy thermosets with relatively low T_g and high quality SME can be obtained via dual-curing [23,24]. Our research group also used a dual-curing process to develop a self-standing thermally triggered actuator incorporating a pre-programmed liquid-crystal elastomer layer (LCE, shape shifting component) between two layers of glassy thermoset (GT, stress applying component) based on off-stoichiometric thiol-epoxy chemistry [25,26]. Successful assembly of the LCE and GT layers was achieved thanks to the dual-curing processing, leading to a very strong adhesion after completion of the second curing stage, as reported by Belmonte et al. [27]. In a similar way, dual-curing processing could be exploited to incorporate a conductive/heating layer sandwiched between two SMP layers, producing a compact and mechanically consistent piece. The resulting electro responsive actuator can be programmed in a temporary shape and the joule heating produced in the conductive layer can trigger the thermal-activated recovery when needed. The optimal adhesion between layers achieved would produce, in consequence, a compact and durable multi-layered structure with efficient heat transfer between layers and therefore efficient actuation upon electrical activation.

In this work, we studied a novel electro responsive actuation mechanism based on a flexible hater placed between two layers of a recently developed shape-memory thermoset [24]. The heater component consists of a metallic track printed on a thin Kapton® substrate, which has been already employed as substrate material for the fabrication of flexible chemo-resistive gas sensors [28]. Two main reasons can be found behind this choice: (i) the combination of Kapton® and the conductive layer would reach a thickness lower than 0.1 mm, so the global stiffness of the SMP actuator should not

be significantly affected; (ii) since the heater component is originally designed for wearable sensors, its electrical resistance remains almost constant even during cyclic bending tests [28]. A dual-curing thiol-acrylate-epoxy thermoset [24] was used as SMP, using a suitable ratio between acrylate and thiol groups (r_a) in order to obtain gelled material after the first curing stage. In order to enhance the thermal conductivity of the thermosets and therefore enable a rapid heating throughout the material, BN particles were dispersed in the thermoset matrix. The electrical activation of the SME was tested by means of a thermoelectric controlling apparatus enabling the pulse width modulation (PWM) of the electrical current and, consequently, the control of the heating rate. Therefore, the variation of the actuation speed was investigated by varying the average current applied, instead of the voltage as commonly found in literature. This allows us to increase/decrease the actuation speed always maintaining a low voltage value of 5 V. A comprehensive comparison between the traditional thermal-activated shape recovery experiments and electrically-activated shape recovery was also carried out. The effects of multiple parameters, such as BN%, SMP layer thickness and heating strategies, were evaluated in order to point out the beneficial effects of the electrical activation with respect to the traditional one.

2. Experimental section

2.1. Materials

2.1.1. Shape-memory polymer layer (SMP)

A thermoset based on a thiol-acrylate-epoxy sequential dual-curing system was used as SMP component. The acrylate monomers employed are a 50:50 (%wt) mixture of tricyclo[5.2.1.02,6]decanedimethanol diacrylate (TCDDA, Sigma-Aldrich, St. Louis, USA, 152.2 g/eq) and bisphenol A glycero-late (1 glycerol/phenol) diacrylate (BAGA, Sigma-Aldrich, 242.3 g/eq). A commercial epoxy resin, diglycidyl ether of bisphenol A (DGEBA, EPIKOTE™ Resin 828, Hexion specialty chemicals, Columbus, USA) with an epoxy equivalent weight of 187 g/eq was used as the main epoxy resin. In addition, a tri(2,3-epoxypropyl)isocyanurate (ISO, Sigma-Aldrich) with an epoxy equivalent weight of 99.09 g/eq was used as modifier. The proportion between BAGA and DGEBA is fixed at 50:50 (%wt). Pentaerythritol tetrakis(3-mercapto-propionate) (S4, Sigma-Aldrich), with a molecular weight per thiol equivalent unit of 122.17 g/e, was used as thiol crosslinker maintaining the ratio between acrylate and thiol groups fixed at 0.5 (r_a=0.5). 4-(N,N-dimethylamino)pyridine (DMAP, Fluka, Seelze, Germany) was used as catalyst for both reactions. 0.05 phr of DMAP were used in all formulations.

BN-loaded thermoset layers containing 10 %wt and 15 %wt of BN agglomerate (80 μm average, PCTL5MHF, supplied by Saint-Gobain, USA) were prepared by adding BN to the previous formulations.

2.1.2. Conductive heater

The conductive heater is shown in **Figure 7.1.a.** The electrode and heater patterns are made of a DuPont® 5064H silver ink (DuPont Inc., Wilmington, USA) with a solid content between 63 and 66 %, a viscosity of 10-20 Pa·s and a resistivity ≤ 6 mΩ/sq/25μm. The polymer substrate is a 50 μm Kapton® film supplied by DuPont Inc. (Wilmington, USA). Substrate material and silver ink specifics are summarized in **Table 7.1**. Firstly, substrates were cleaned in an acetone bath for 5 min, followed by an ethanol bath for 5 min and, at last, rinsed with deionized water and dried at 110 °C for 10 min. Once substrates were cleaned, the stencil technique used in [29] was employed to deposit the electrode and heater onto the substrate. The heater pattern showed in **Figure 7.1.b** was designed to meet four major requirements: (i) low energy consumption; (ii) rapid activation intended as short time needed to reach the required activation temperature; (iii) homogeneous temperature distribution throughout the sample surface and (iv) a design easy to print. As it can be seen in **Figure 7.1.c**, different heating profile can be obtained controlling the current passing through the heater: increasing the current the target temperature can be achieved in a shorter time.

Table 7.1. Kapton® HPP-ST and Silver ink 5064H specifics.

	Kapton®	**Silver ink**
Resistivity at 20°C (Ω·m)	$1.5 \cdot 10^{15}$	$1.6 \cdot 10^{-8}$
Thermal linear expansion coefficient (K^{-1})	0.000020	0.002209
Thermal conductivity ($W \cdot m^{-1} \cdot K^{-1}$)	0.12	429
Density ($kg \cdot m^{-3}$)	1420	10490
Heat capacity ($J \cdot Kg^{-1} \cdot K$)	1090	232

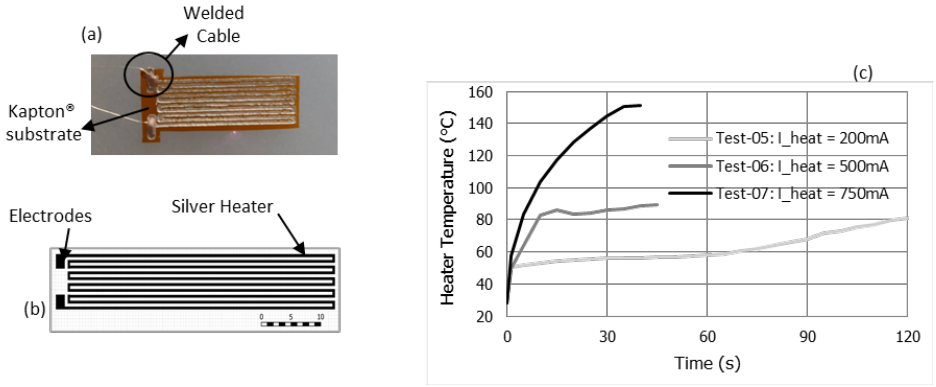

Figure 7.1. Schematic representation of the printed silver net (a); FEM simulation of a heating to T=80°C assuming a heater initial resistance $R_{Heat,0}$= 4.5 Ω and a heating current I_{Heat}=500 mA (b). Preliminary measurements performed with a thiol-epoxy thermoset films of 0.4 mm used for testing purpose: heating profiles obtained varying the heating current intensity (c); Actual photo of the conductive layer (d).

2.1.3. Preparation of thermo-responsive SMPs

Neat samples were prepared following the procedure described in [24] and using suitable moulds and a curing schedule consisting of a first curing stage of 2h at 40 °C followed by a second curing stage of 4h at 80 °C. Loaded samples were prepared by adding 10 and 15 wt% of BN agglomerate to the formulation. The formulations were mechanically stirred until homogeneous mixture was obtained and then cured following the same curing schedule of neat sample. From this point on SMPs thus obtained, when thermally activated, will be referred as thermo-responsive actuators (TRA).

2.1.4. Preparation of electro-responsive actuator

First of all, intermediate cured SMP material sheets were obtained after the first curing stage of 2 hours at 40°C. Large sheets of 30x30 mm^2 with three different thickness of 0.4, 0.8 and 1.4 mm were prepared. The heater (9x23 mm^2) is placed on a SMP sheet (**Figure 2.a**) and a second SMP layer with the same thickness is placed on top in order to obtain the sandwich design (**Figure 2.b**). The SMP excess is cut away from the sandwich leaving an exceeding width of 1 mm on both sides (**Figure 2.c**). The actuator was designed with an excess of SMP on both edges in order to ensure a good contact between the two layers of SMP and, consequently, to achieve a perfect fit of the conductive component within the SMP. The assembly is then confined using Teflon spacers and lightly fastened between Teflon-coated glass plates (**Figure 2.d**). Finally, the second curing stage of the SMP material is performed (4h at 80°C) leading to the desired

actuator configuration. The multilayered actuators obtained, activated by the electrical stimulus, will be referred as electro-responsive actuators (ERA).

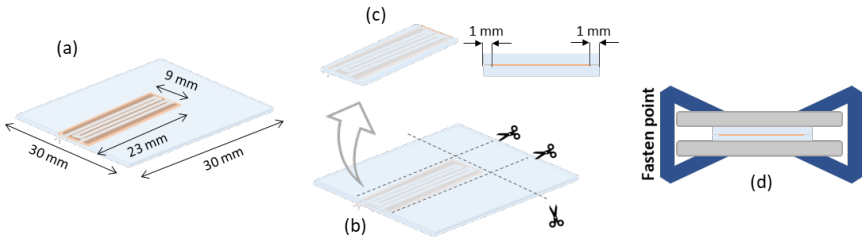

Figure 7.2. Schematical representation of actuator assembling: (a) assembling of the first GT layer and the heater; (b) assembling of the second GT layer; (c) cutting to final dimensions; (d) Second curing stage of the assembled actuator.

2.2. Thermoelectric control apparatus (controlling unit)

The thermoelectric control of the actuator is conducted by an electronic board equipped with a microcontroller, a load switch, a current sensor and a temperature sensor. The microcontroller commands the load switch by *pulse-width modulation* (PWM), allowing the regulation of the average current supplied to the heater (**Scheme 7.1**). Additionally, the microcontroller also drives the heater switch off when the actuator reaches the required temperature.

PWM is a digital modulation commonly used to control “slow” physical processes. The control signal is periodically switching on and off at a relative “high” frequency, delivering power to the system in a digitally discontinuous mode. However, as long as the system time constant is sufficiently higher than the switching period, it will be perceived as an average continuous amount of energy, thereby enabling the direct control of systems with high inertias without using added electronics to perform the low pass filtering of the digital modulated signal. This is the usual way of controlling electric motors speed or LED lamps glowing intensity. In our case, heat released per time unit will be related to the t_{on}/t_{PWM} ratio (duty cycle), where t_{on} is the time during which the signal is “on” and t_{PWM} is the PWM signal period. In this way, we can control how quick temperature increases just varying this duty cycle (at higher t_{on}, faster temperature increase is obtained).

Additionally, the temperature of the heater (T_{Heat}) can be indirectly measured at any time. Taking advantage of the quasi-linear behavior of the metallic resistances at varying temperatures the resistance of the heater (R_{Heat}) can be computed as:

$$R_{Heat} = R_{Heat,0} \cdot \left(1 + \alpha_{Heat} \cdot \left(T_{Heat} - T_{Heat,0}\right)\right) \quad (1)$$

where $R_{Heat,0}$ is the initial value of the heater resistance, α_{Heat} is the temperature coefficient of resistance of the heater and $T_{Heat,0}$ is the initial temperature of the heater. By means of an ambient temperature sensor together with the $V_{Heat,in}$ (the input voltage of the heater) sensing, $T_{Heat,0}$ and $R_{Heat,0}$ can be easily measured at the beginning of every experiment. In order to measure R_{Heat}, a shunt resistance R_{sens}=10 mΩ (precisely calibrated and with a very low value which is not heated and remains constant) was added. The value of R_{Heat} can be deducted from the circuit analysis (sensing unit in **Scheme 7.1**) as follows:

$$R_{Heat} = R_{sens}\left(\frac{V_{Heat,in}}{V_{Heat,out}} - 1\right) \quad (2)$$

where the heater output voltage ($V_{Heat,out}$) is measured by the microcontroller sensing unit, and it is also employed to calculate I_{Heat} from $V_{Heat,out} = I_{Heat} \cdot R_{sens}$. In this way, combining the (1) and (2) the microcontroller can easily calculate the T_{Heat} during every experiment, for any device, at any room temperature and any supplied voltage (V_{batt}).

The microcontroller also performs some user interface tasks. Once the actuator is connected to the apparatus, the software interface requires the insertion of a set-point temperature (T_{set}), which is the target temperature the actuator should reach, and the heating strategy (related to the time spent in reaching the target temperature). The heating strategies are named after the percentage value of the maximum speed at which the setpoint temperature is reached. In this paper, the electro-responsive actuators (ERAs) were heated at T_{set} = 120°C employing three heating strategies, (25%, 50% and 100% heating speed) while the power supply was limited at V_{Batt} = 5 V. Using this controlling board, many different actuation strategies can be studied by modulating the heating current while maintaining the supply voltage constant and with a very low value (in the working range of a USB charger)

All this procedure (user interface, measures, calculus, and control loop) is conducted by software running on *Arduino Nano*, open source microcontroller development board mounting an Atmel AVR microcontroller.

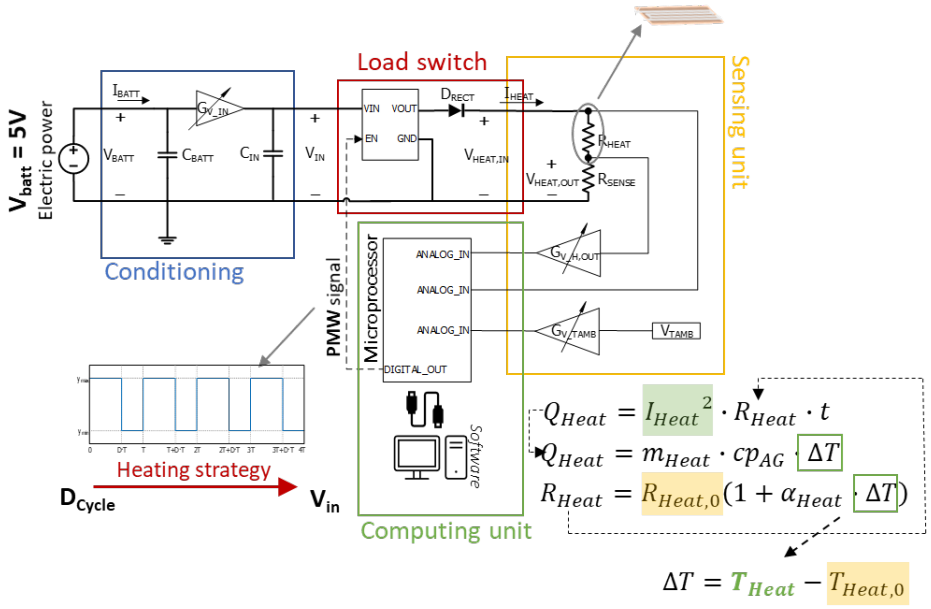

Scheme 7.1. Schematic representation of the thermoelectric control of the actuation.

2.3. Characterization of thermo-responsive actuators (TRAs)

Dynamic mechanical analysis was performed in order to characterize the effect of BN% on the thermomechanical properties of the SMP in use. TA Instruments DMA Q800 (New Castle, DE, USA) equipped with a 3-point bending clamp (15 mm) was used to characterize the relaxation process. Prismatic rectangular samples (15x6x2.5 mm^3) were analyzed in oscillation mode at 1 Hz, 0.1% of strain amplitude and at a heating rate of 3 °C/min from 20 to 150 °C. The T_g was determined as the tanδ peak temperature and glassy (E_g) and rubbery (E_r) moduli were determined at 0 and 100 °C, respectively.
The flexural modulus (E_{SMP}) of final SMPs was determined with the same apparatus by means of a force ramp at a constant rate of 1 N/min in controlled force mode. The slope (m) within the linear zone of the force-displacement curve was obtained and E_{SMP} was calculated in accordance with Equation (3):

$$E_{SMP} = \frac{L^3 m}{4wt^3} \quad (3)$$

where L is the support span, and w and t are the width and the thickness of the test sample, respectively.

Thermal conductivity of the SMP was measured using the *Transient Hot Bridge method* (THB) by means of a THB 100 device from Linseis Messgeräte GmbH (Selb, Germany). A

HTP G 9161 sensor was used with a 3×3 mm^2 of area calibrated with polymethylmethacrylate (PMMA), borosilicate crown glass, marble, Ti-Al alloy, and titanium. Two equal polished circular SMP samples (10 mm in diameter and 2.3 mm of thickness) were placed in each face of the sensor. Due to the small size of sensor, side effect can be neglected. A measuring time of 100 seconds with a current of 10 mA was applied to the five measures done for each different formulation.

The thermally activated shape recovery of all the TRAs was recorded by means of free recovery experiments carried out using the DMA equipment in force-controlled mode, equipped with a 3-point bending clamp (15 mm). Rectangular flat samples (11x25x0.8 mm^3) were previously programmed in a curved shape following the next steps: (i) the sample was heated up in an oven to the programming temperature (T_g+20°C), and then deformed to a curved-shape using a bending guide a shown in **Figure 7.3.a**; (ii) the bending guide and the sample were rapidly cooled down with ice water while maintaining the force applied; (iii) finally samples were unloaded. The programmed samples were placed on the DMA clamp as shown in **Figure 7.3.b** left and the shape-recovery process was monitored under constant heating rates of 3, 5 and 10 °C/min until the final shape is recovered (**Figure 7.3.b** right). A small preload force of 0.1 N was used in order to ensure good contact with the sample during the monitoring of the shape recovery process. **Figure 7.3.c** shows a schematic representation of the experimental setup. The displacement of the movable clamp d(T) was used to calculate the SR(%) following Equation (4):

$$SR(\%) = \left(1 - \frac{d(T)}{d_{max}}\right) \cdot 100 \quad (4)$$

where d_{max} is the displacement obtained by the original shape prior to sample programming. The instantaneous shape-recovery speed $SR_{speed}(T)$ was calculated by Equation (5):

$$SR_{speed}(T) = \frac{\partial SR(T)}{\partial T} \quad (5)$$

using the $SR_{speed}(T)$ curve, the temperature of maximum recovery speed and the duration of the process were determined as the peak of the curve (T_{peak}) and as the width of the curve at half-height (ΔT_{peak}), respectively.

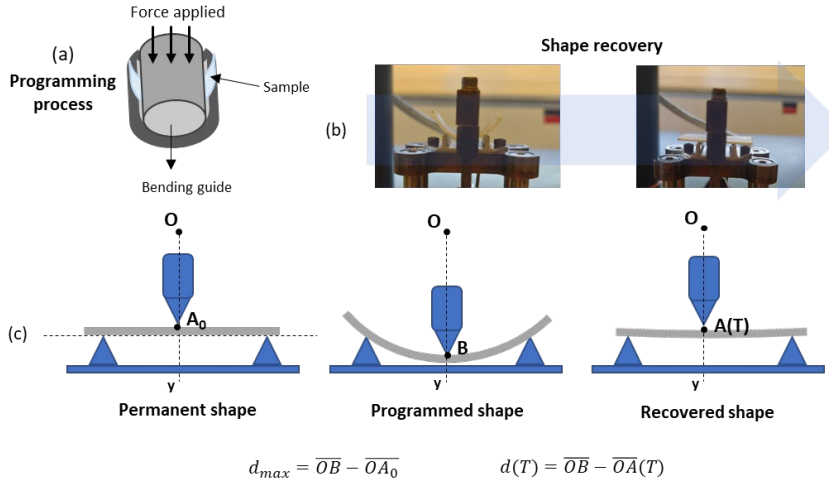

Figure 7.3. DMA recovery experiments: (a) programming process; (b) sample leaned on the DMA clamp before and after the recovery process; (c) Illustration of the DMA testing procedure.

2.4. Characterization of electro-responsive actuator (ERAs)

The flexural modulus of the electro-responsive actuator (E_{ERA}) was determined by a DMA force controlled analysis as detailed in the above section. DMA oscillatory analysis on the assembled actuator were also performed in order to determine the effect of the layered structure on the thermomechanical properties. TA Instruments DMA Q800 equipped with a 3-point bending clamp (15 mm) was used. Assembled ERAs were tested at 1 Hz, 0.1% of strain amplitude and 3°C/min of heating rate.

The electrically activated shape recovery of the actuator was analyzed as follows. The programming process was performed with the same methodology described in section 2.3 (**Figure 7.3.a**). After removing the force applied, the sample was perfectly dried and connected to the controlling unit to activate and monitor the shape recovery. The electro-responsive actuators were heated at T_{set} = 120 °C employing three heating strategies, 25%, 50% and 100% while the power supply is limited at 5V (V_{Batt} = 5 V). The recovery strategies were referred as *fast*, *medium* and *slow* indicating respectively the 100%, 50% and 25% strategy. The recovery process was recorded using a high resolution camera and further analyzed frame by frame, measuring the angles as shown in **Figure 7.4** and applying Equation (6) on each frame.

$$SR(\%) = \frac{\theta_t - \theta_0}{180° - \theta_0} \cdot 100 \qquad (6)$$

where SR(%) is the percentage of shape recovery, θ_0 is the angle at t=0 s and θ_t is the angle at time t. A frame interval of 1 s was used for 50% and 25% strategies, while a frame interval of 0.25 s was used for 100% strategy.

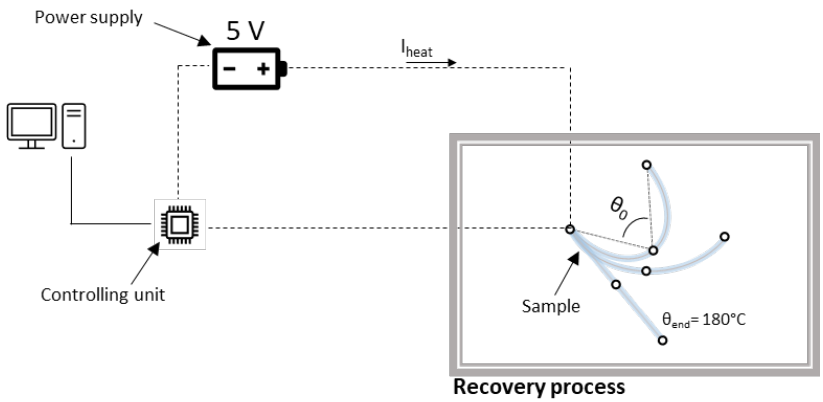

Figure 7.4. Schematic representation of shape-recovery scenario.

3. Results

3.1. Characterization of thermo-responsive actuators (TRAs)

Thermomechanical properties of fully cured SMPs were investigated in order to assess the effect of the BN particles, which are expected to increase the material toughness without altering the T_g [30]. Moreover, BN particles are proven to not increase electrical conductivity of epoxy-based thermosets keeping their electrical insulations [30,31]. In **Figure 7.5** the evolution of storage modulus and tanδ with respect to temperature are presented. As expected, the incorporation of 10 %wt BN filler leads to a noticeable increase of the storage modulus (**Figure 7.5.a**), while only a slight increase was found when increasing BN filler content from 10 %wt to 15 %wt. On the other hand, it can be observed that the glass transition is not significantly affected by the filler (**Figure 7.5.b**). DMA results are resumed in **Table 7.2** together with the measured value of E_{TRA}. BN loaded samples showed a similar value of T_g while the FWHM slightly increase probably due to the increase in sample heterogeneity. It is noteworthy that only a small broadening of tanδ is present, otherwise, shape-memory properties would have been adversely affected in terms of recovery speed [32]. Furthermore, the increase of BN %wt lead to an enhancement of the rubbery modulus E_r. which also has beneficial effect on shape-memory properties, particularly in constrained recovery processes. Flexural

moduli measured at 25 °C increase about 50% when 10 %wt of BN is used and almost a 70% in case of 15 %wt of BN, as a direct consequence of the presence of filler.

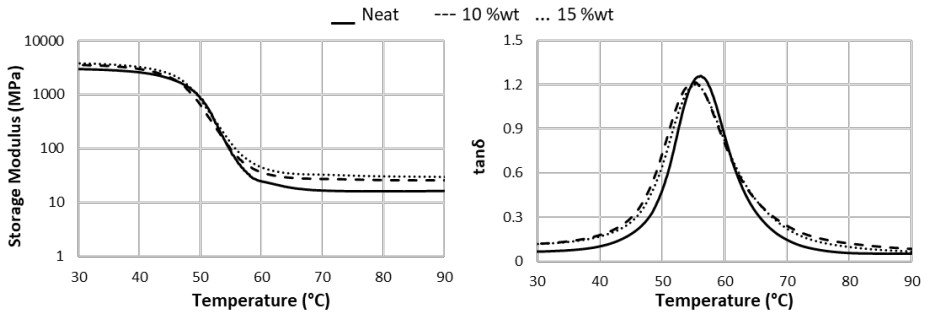

Figure 7.5. Evolution of storage modulus and tanδ with temperature during DMA analysis on the SMPs tested.

Table 7.2. Summary of thermomechanical properties of all investigated materials.

	E'_g (Mpa)[a]	E'_r (MPa)[b]	T_g (°C)	T_g+30°C (°C)	FWHM (°C)	E_{SMP} (GPa)[c]
Neat	3067	16.3	56	86	10.1	1.30
10 %wt	3637	25.7	55	85	11.8	2.00
15 %wt	3881	29.6	55	85	11.6	2.18

[a] Calculated at 20 °C; [b] Calculated at 100°C; [c] calculated by eq. (1) at 25°C.

The effect of increasing %wt of BN on thermal conductivity was also investigated and results are presented in **Figure 7.6**. The thermal conductivity of these thermoset is significantly enhanced by the incorporation of BN fillers: 15 wt% sample reaches a thermal conductivity of 0.587 W/mK, which is almost three times higher than the value reached by the neat sample (0.206 W/mK). Such increase in thermal conductivity would be crucial during the joule heating process allowing faster and more homogenous heating through whole sample.

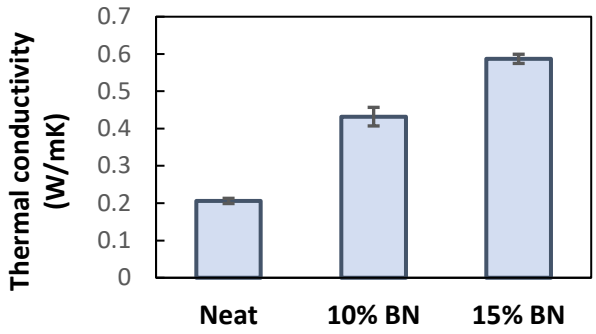

Figure 7.6. Thermal conductivity of the SMP materials prepared varying the proportion of BN.

Shape-memory behavior of these materials was investigated by means of free-recovery experiments in DMA apparatus as explained in Section 2.3. Samples were programmed in an oven and then the recovery process was monitored by DMA at different heating rates. When analyzing the recovery process at 3 °C/min, it can be observed that the presence of BN filler slightly affects the shape recovery (**Figure 7.7**). At this heating rate, the presence of BN slightly retards the recovery process with respect to the neat sample. The maximum effect was found for 15 %wt sample which shows a higher T_{peak} (about 1°C higher) and ΔT_{peak}, leading to an increase of $t_{5\%-95\%}$ from 4.05 to 8.01 min (**Table 7.3**). The observed delay can be ascribed to the broader tanδ peak obtained for 10% and 15% samples. Moreover, the recovery of 15 %wt seems to slowdown in the final stages (**Figure 7.7**) probably due to presence of the filler hindering the network elastic response.

The effect of the heating rate on the recovery process was also investigated in order to explore a way to control the speed at which the actuation is triggered. As expected, the activation of the shape-recovery is significantly anticipated in time because the sample merely takes less time to reach the activation temperature, therefore $t_{5\%-95\%}$ (calculated as the amount of time between 5 and 95 $R_r(\%)$) is significantly reduced to about 1.5 min. Although the recovery process is faster, **Figure 7.7.a** clearly shows that the T_{peak} increases with the heating rate. This effect can be due to either to viscoelastic or heat transmission issues: when the sample is rapidly heated, the material does not have the necessary time to relax its structure leading to a delay in the recovery of the shape. On the other hand, samples in oven are heated by convection which can produce small temperature gradient from the surface to the sample core. Increasing the heating rate, a greater gradient is produced contributing to shift the recovery process to higher temperature. In this scenario, the difference in T_{peak} between Neat and BN loaded

samples is slightly reduced and, at 10°C/min, samples with BN slightly anticipates the neat sample recovery. The higher thermal conductivity obtained with BN particles enhance the heat transmission within the sample leading to a reduction of the temperature gradient and therefore a lower T_{peak}. A clear trend in Recovery rate (R_r) is not visible (**Table 7.3**) and all samples recover about 97-98% at all heating conditions.

Table 3. Parameters obtained from unconstrained shape-memory analysis at different heating rates.

	BN wt%	T_{peak} (°C)	ΔT_{peak} (°C)	R_r (%)	$t_{5\%-95\%}$ (min)
3°C/min	0	53.4	5.1	97.7	4.05
	10	54.6	5.2	99.7	4.08
	15	54.9	5.4	97.3	8.01
5°C/min	0	60.5	5.9	99.2	2.85
	10	61.4	5.9	98.5	2.77
	15	61	6.4	97.3	4.89
10°C/min	0	75.9	6.9	98.0	1.30
	10	75.7	7	98.7	1.50
	15	74.8	7.1	98.1	1.48

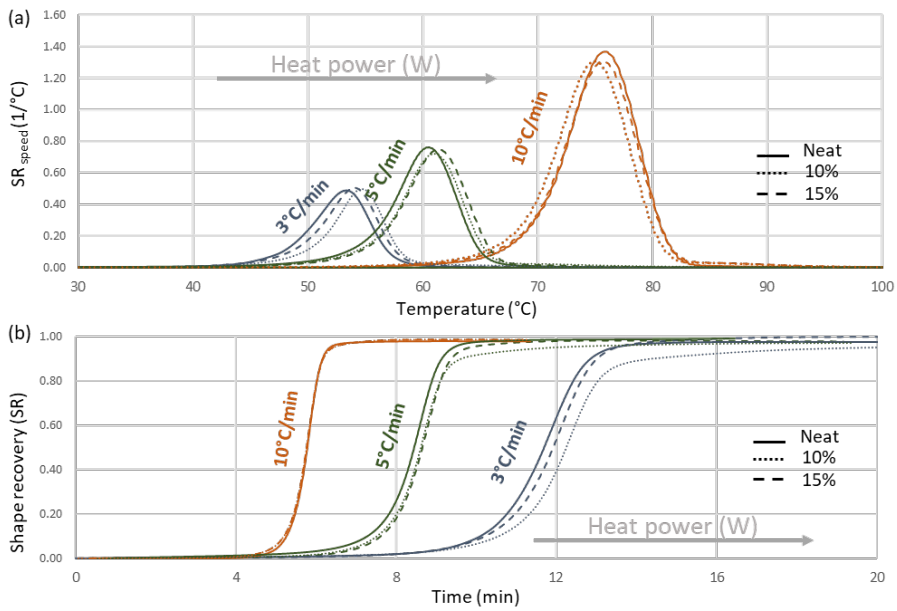

Figure 7.7. Free recovery experiments at three different heating rates: (a) instantaneous recovery speed evolution with temperature; (b) Shape-recovery evolution along time.

3.2. Electro-responsive actuators characterization

First of all, thermomechanical properties of the composite assembly with the heating layer were tested together with the resulting flexural modulus. As shown in **Figure 7.8** for the 15 %wt BN actuator, the presence of the heater positioned at the mid-plane does not significantly affect the thermomechanical behavior. The most visible effect is on the shape of the tanδ peak. As expected, a broader peak is obtained for the actuator due to the heterogeneity of the sample resulting from the assembly of the different layers. Although the SMP layers have identical properties and T_g, the Kapton® substrate of the heating layer has a T_g between 360 and 410°C, therefore it remains in the glassy state while the other layers relax. Nonetheless, even in the rubbery region, where the glassy Kapton® response could be dominant, only a slight increase of E'_r is detected.

The flexural modulus of the assembled actuator at 25 °C was also measured and the results are presented in **Table 7.4**. The modulus of the actuator shows a slight increase with the respect to E_{TRA} in all %wt of BN probably owing to the incorporation of more rigid layer. In light of this findings, we assume that the presence of the intermediate layer would not result in appreciable effects on the SME.

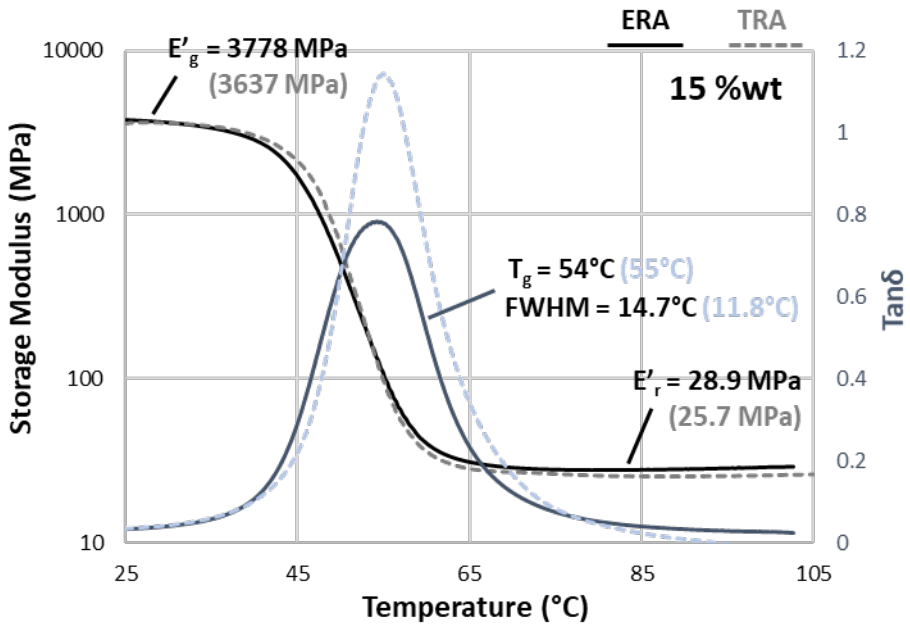

Figure 7.8. . DMA analysis of 10 %wt BN ERA (both SMP layers thickness is 0.4 mm) compared with the 10 %wt BN TRA (0.8 mm thickness): characteristic thermomechanical data are also indicated (values obtained for the 10 %wt SMP in brackets).

Table 7.4. Flexural Modulus values of the actuators and SMPs under investigation.

BN (wt%)	E_{SMP} (GPa)[a]	$E_{Kapton®}$(GPa)[b]	E_A (GPa)[c]
0	1.30	2.8	1.38
10	2.00		2.10
15	2.18		2.34

[a] 0.8 mm thickness; [b] Tensile Modulus; [c] 0.4 mm SMP layers thickness.

The recovery process of the electro-responsive actuators was tested in unconstrained conditions under 5V of applied voltage. Preprogrammed ERAs were connected to the controlling unit which is able to modulate the current passing through the heater at three different levels of average current, corresponding to three heating strategies: *fast*, *medium* and *slow*. In order to minimize any eventual external friction, samples were hanged midair with a gripper. The shape-recovery process over time is reported in **Figure 7.9**. In contrast with classical thermal triggering, the higher thermal conductivity obtained with BN fillers clearly results in faster activation of the recovery and reduced recovery time (**Table 7.5**). In this configuration the sample got heated up from the inner layer and therefore, thermal conductivity plays a crucial role in the acceleration of the heat transmission outwards. Loaded samples took less time to recover the initial shape in all three activation conditions.

Table 7.5. Characteristic values of the electrically triggered recovery process at three different actuation strategies.

		fast - 701 mA		medium - 361 mA		slow - 168 m A	
	t_{layer} (mm)	$t_{recovey}$ (s)	$v_{recovery}$ (%/s)	$t_{recovey}$ (s)	$v_{recovery}$ (%/s)	$t_{recovey}$ (s)	$v_{recovery}$ (%/s)
Neat	0.4	11.25	15.9	26.0	6.1	68.0	1.6
10 wt%	0.4	9.0	19.8	21.0	7.9	58.0	1.9
15 wt%	0.4	8.0	22.3	21.0	9.1	57.0	2.0

*t_{layer} is the thickness of both SMP layers

The best results are obtained by the 15 %wt ERA which was able to recover almost the 100% of the original shape in just 8 s with the *fast* heating strategy (**Figure 7.9.a**). In particular, loaded samples were able to recover the 80% of the original shape in only 4 s, then the recovery process slightly slows down probably due to a network structural effect. Recovery time and velocity can be controlled by the intensity of the current

responsible for the joule heating. Reducing the heating current, we obtained gradually slower recovery processes as shown in **Figure 7.9.b** and **Figure 7.9.c**. The highest recovery ratios between 99-100% are obtained with *fast* and *medium* strategies while slightly lower recovery ratios (around 97%) are obtained with *slow* heating strategy.

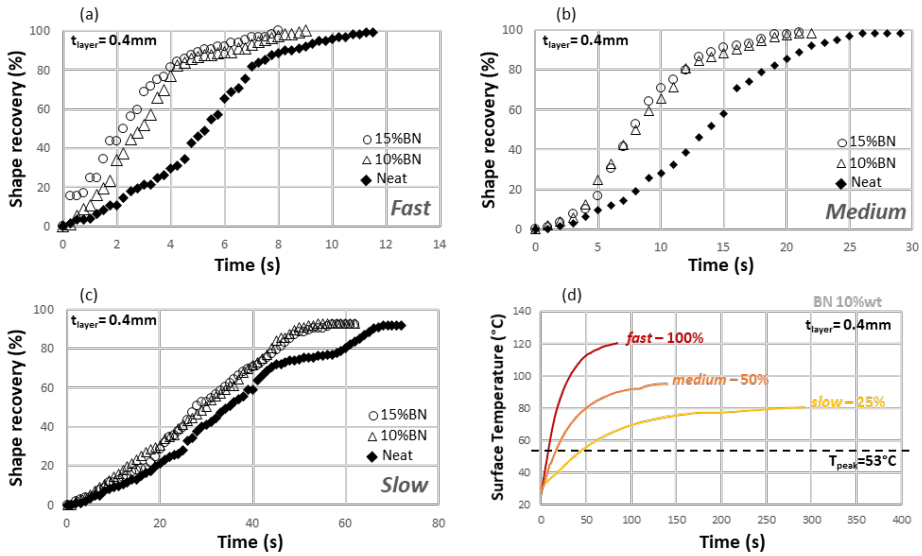

Figure 7.9. (a) Shape recovery ratio over time for the fast heating strategy; (b) Shape recovery ratio over time for the medium heating strategy; (c) Shape recovery ratio over time for the slow heating strategy; (d) Joule heating profiles of ERA loaded with 10 %wt of BN.

The In order to better understand the electro activated shape-recovery process, the time-dependent temperature profiles of 10 wt% of BN loaded ERA were determined for all heating strategies (**Figure 7.9.d**). Heating profiles were obtained by means of a PT100 temperature probe stuck on the SMP surface during heating. As expected, the heating rate strongly increase with the I_{heat} (from *slow* to *fast* strategy), as well as the maximum temperature reached in the surface of the ERA. Although the T_{set}=120°C was only reached by the *fast* strategy, all strategies are easily able to reach the actuation temperature. In particular, the ERA recovers the initial shape in the same temperature range for all heating strategies and at a temperature close to the T_{peak} found for 3°C/min recovery experiment in DMA.

The possibility to control the recovery process speed can be exploited to obtain different actuation strategies that can be adjusted to the final application. In bending mode, for constrained recovery process or partially constrained process the thickness of the actuator is a commanding parameter and higher recovery forces or higher work output

are obtained with higher thickness. The effect of increasing the t_{layer} of SMP with 10 wt% of BN was also tested with all heating strategies and the results are shown in **Figure 7.10**, where the induction time is defined as the time needed to get a 3% recovery rate. Thicker layers results in increasing recovery time and the appearance of an induction time which the sample takes to get heated from ambient to transition temperature. The more significant effect can be seen for the *slow* heating strategy (25%). The lower current intensity produces a less powerful joule heating which, combined with the higher layer thickness, results in a significant induction time between 20 and 40 s, depending on the thickness.

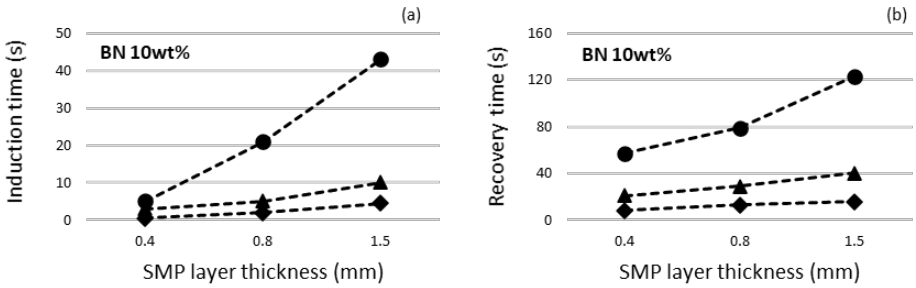

Figure 7.10. Variation of the induction time (a) and recovery time (b) with SMP thickness at three actuation strategies: slow (•),medium (Δ), fast (▪).

With respect to the results obtained when heating in oven, the electrical activated shape-recovery is enormously fast and efficient, even with thicker SMP layers: moderate energy level is employed to directly heat the material with almost no energy losses. On the other hand, for traditional thermally activated actuation, extra heat power is always required to increase the whole ambient temperature, wasting much more energy than the actual heat needed by the sample [33].

High-speed actuation at relatively low voltage was obtained. The combined use of BN particles and conductive heater layer leads to recovery times lower than other electro-responsive actuators found in literature: PU-TiO_2 SMP composites developed by Liu et al. recovered their permanent shape in about 60 s under 70 V applied [20]; Epoxy based SMP composites by Lu et al. achieved complete recovery in 74s (4.8 V) [21]; PU composites incorporating printed carbon nanotube layers proposed by Wang et al. recover the shape in about 30 s [34]. Bilayer shape-memory composites developed by Zheng et al. [35] took around 220s to recover their shape under 5 V voltage applied. Higher speed of actuation can be found in literature but at significantly higher voltage (around 20-40 V) [17,36,37]. The comparison in terms of power (W) is not always

possible due to insufficient data available. In this investigation, electro activated SM experiments were conducted applying 0.84, 1.8 and 3.5 W (respectively *slow*, *medium* and *fast*) depending on the heating strategies. Similar values of electric power were found for RGOP/epoxy composites [36] which recovered the shape in 5 s when 3.6 W were applied. Lu et al. [21] shape-memory nanocomposites recovered the initial shape in 72 s when 2.3 W were applied, while, with *medium* heating strategy (1.8 W), our actuator showed a significantly faster recovery. Recently, electroactive polymer composites developed by An et al. [38] reached similar recovery times (7 s) with a lower electric power (less than 1 W) applied.

As it can be concluded, the voltage supplied to our thermoelectric control is the USB standard voltage and the value of current are well below the maximum value provided by a commercial USB charger. The flexibility in terms of power source is a strong point in favor of the applicability of our system.

4. Conclusions

Novel electro-responsive shape-memory actuators were developed combining dual-cured SMPs and flexible conductive heaters. The dual-curing processing was exploited to incorporate the conductive heater in the thermo-responsive SMP. First of all, 10 and 15% of Boron Nitride (BN) agglomerates were added to the SMP matrix in order to increase the thermal conductivity. The addition of BN fillers led to almost to a 300% increase of thermal conductivity and an increase of flexural modulus around 70%, while the relaxation process is not significantly affected.

A thermoelectric controlling unit was designed in order to characterize the electrical activation of the SME. The shape-memory behavior of the thermo-responsive and the electro responsive actuator was characterized in order to determine the advantages of the electrically driven Joule heating with respect to the traditional external heating. In both activation mechanisms the SME was tested at different heating rates or heating strategies. The electro-responsive actuators demonstrated extremely higher recovery velocity with respect to traditional thermo-responsive actuators; the lowest recovery time achieved was the 8 s reached by the 15% BN actuator with the *fast* heating strategy.

The effect of the increased thermal conductivity was also visible since the increase of BN% led to faster recovery with all heating strategy. Finally, the controlling unit proposed in this work allowed an excellent control on the recovery process by providing different heating strategy maintaining a fixed and low value of voltage (5 V).

Acknowledgements

The authors would like to thank MCIU (Ministerio de Ciencia, Innovación y Universidades) and FEDER (Fondo Europeo de Desarrollo Regional) (MAT2017-82849-C2-1-R and MAT2017-82849-C2-2-R) and Generalitat de Catalunya (2017-SGR-77 and Serra Húnter programme) for the financial support.

5. References

[1] D.L. Safranski, Introduction to Shape-Memory Polymers, Elsevier Inc., 2017. https://doi.org/10.1016/B978-0-323-37797-3.00001-4.

[2] A. Lendlein, S. Kelch, Shape-Memory Polymers, Angew. Chemie Int. Ed. 41 (2002) 2034. https://doi.org/10.1002/1521-3773(20020617)41:12<2034::AID-ANIE2034>3.0.CO;2-M.

[3] M. Balk, M. Behl, C. Wischke, J. Zotzmann, A. Lendlein, Recent advances in degradable lactide-based shape-memory polymers, Adv. Drug Deliv. Rev. 107 (2016) 136–152. https://doi.org/10.1016/j.addr.2016.05.012.

[4] C.M. Yakacki, R. Shandas, C. Lanning, B. Rech, A. Eckstein, K. Gall, Unconstrained recovery characterization of shape-memory polymer networks for cardiovascular applications, Biomaterials. 28 (2007) 2255–2263. https://doi.org/10.1016/j.biomaterials.2007.01.030.

[5] D.J. Maitland, M.F. Metzger, D. Schumann, A. Lee, T.S. Wilson, Photothermal properties of shape memory polymer micro-actuators for treating stroke, Lasers Surg. Med. 30 (2002) 1–11. https://doi.org/10.1002/lsm.10007.

[6] J. Sun, Q. Guan, Y. Liu, J. Leng, Morphing aircraft based on smart materials and structures: A state-of-the-art review, J. Intell. Mater. Syst. Struct. 27 (2016) 2289–2312. https://doi.org/10.1177/1045389X16629569.

[7] H. Tobushi, S. Hayashi, K. Hoshio, Y. Ejiri, Shape recovery and irrecoverable strain control in polyurethane shape-memory polymer, Sci. Technol. Adv. Mater. 9 (2008) 015009. https://doi.org/10.1088/1468-6996/9/1/015009.

[8] S. Gopinath, S. Mathew, P.R. Nair, Shape Memory Actuators, in: Actuators, Wiley, 2020: pp. 139–158. https://doi.org/10.1002/9781119662693.ch6.

[9] A. Lendlein, T. Sauter, Shape-Memory Effect in Polymers, Macromol. Chem. Phys. 214 (2013) 1175–1177. https://doi.org/10.1002/macp.201300098.

[10] M. Heuchel, T. Sauter, K. Kratz, A. Lendlein, Thermally induced shape-memory effects in polymers: Quantification and related modeling approaches, J. Polym. Sci. Part B Polym. Phys. 51 (2013) 621–637. https://doi.org/10.1002/polb.23251.

[11] C.M. Yakacki, R. Shandas, D. Safranski, A.M. Ortega, K. Sassaman, K. Gall, Strong, tailored, biocompatible shape-memory polymer networks, Adv. Funct. Mater. 18 (2008) 2428–2435. https://doi.org/10.1002/adfm.200701049.

[12] D.P. Nair, N.B. Cramer, T.F. Scott, C.N. Bowman, R. Shandas, Photopolymerized thiol-ene systems as shape memory polymers, Polymer (Guildf). 51 (2010) 4383–4389. https://doi.org/10.1016/j.polymer.2010.07.027.

[13] A. Belmonte, C. Russo, V. Ambrogi, X. Fernández-Francos, S.D. la Flor, Epoxy-based shape-memory actuators obtained via dual-curing of off-stoichiometric “thiol-epoxy” mixtures, Polymers (Basel). 9 (2017). https://doi.org/10.3390/polym9030113.

[14] C.O. Correia, Á.J. Leite, J.F. Mano, Chitosan/bioactive glass nanoparticles scaffolds with shape memory properties, Carbohydr. Polym. 123 (2015) 39–45. https://doi.org/10.1016/j.carbpol.2014.12.076.

[15] A.J. Boyle, A.C. Weems, S.M. Hasan, L.D. Nash, M.B.B. Monroe, D.J. Maitland, Solvent stimulated actuation of polyurethane-based shape memory polymer foams using dimethyl sulfoxide and ethanol, Smart Mater. Struct. 25 (2016) 075014. https://doi.org/10.1088/0964-1726/25/7/075014.

[16] H. Yang, W.R. Leow, T. Wang, J. Wang, J. Yu, K. He, D. Qi, C. Wan, X. Chen, 3D Printed Photoresponsive Devices Based on Shape Memory Composites, Adv. Mater. 29 (2017) 1701627. https://doi.org/10.1002/adma.201701627.

[17] X. Luo, P.T. Mather, Conductive shape memory nanocomposites for high speed electrical actuation, Soft Matter. 6 (2010) 2146–2149. https://doi.org/10.1039/c001295e.

[18] P. Slobodian, P. Riha, R. Olejnik, J. Matyas, Accelerated Shape Forming and Recovering, Induction, and Release of Adhesiveness of Conductive Carbon Nanotube/Epoxy Composites by Joule Heating, Polym. 2020, Vol. 12, Page 1030. 12 (2020) 1030. https://doi.org/10.3390/POLYM12051030.

[19] X.F. Sánchez-Romate, A. Sans, A. Jiménez-Suárez, M. Campo, A. Ureña, S.G. Prolongo, Highly Multifunctional GNP/Epoxy Nanocomposites: From Strain-Sensing to Joule Heating Applications, Nanomater. 2020, Vol. 10, Page 2431. 10 (2020) 2431. https://doi.org/10.3390/NANO10122431.

[20] W. Liu, H. Chen, M. Ge, Q.Q. Ni, Q. Gao, Electroactive shape memory composites with TiO2 whiskers for switching an electrical circuit, Mater. Des. 143 (2018) 196–203. https://doi.org/10.1016/j.matdes.2018.02.005.

[21] H. Lu, W.M. Huang, J. Leng, Functionally graded and self-assembled carbon nanofiber and boron nitride in nanopaper for electrical actuation of shape memory nanocomposites, Compos. Part B Eng. 62 (2014) 1–4. https://doi.org/10.1016/j.compositesb.2014.02.003.

[22] H. Lu, J. Yin, B. Xu, J. Gou, D. Hui, Y. Fu, Synergistic effects of carboxylic acid-functionalized carbon nanotube and nafion/silica nanofiber on electrical actuation efficiency of shape memory polymer nanocomposite, Compos. Part B Eng. 100 (2016) 146–151. https://doi.org/10.1016/j.compositesb.2016.06.072.

[23] C. Russo, À. Serra, X. Fernández-Francos, S. De la Flor, Characterization of sequential dual-curing of thiol-acrylate-epoxy systems with controlled thermal properties, Eur. Polym. J. 112 (2019) 376–388. https://doi.org/10.1016/j.eurpolymj.2018.12.048.

[24] C. Russo, X. Fernandez-Francos, S. De la Flor, Shape-memory actuators based on dual-curing thiol-acrylate-epoxy thermosets, Express Polym. Lett. 15 (2021) 58–71. https://doi.org/10.3144/expresspolymlett.2021.7.

[25] A. Belmonte, G.C. Lama, P. Cerruti, Motion control in free-standing shape- memory actuators, (2018).

[26] A. Belmonte, G.C. Lama, G. Gentile, P. Cerruti, V. Ambrogi, X. Fernández-Francos, S. De la Flor, Thermally-triggered free-standing shape-memory actuators, Eur. Polym. J. 97 (2017) 241–252. https://doi.org/10.1016/j.eurpolymj.2017.10.006.

[27] A. Belmonte, G.C. Lama, G. Gentile, P. Cerruti, V. Ambrogi, X. Fernández-Francos, S. De la Flor, Thermally-triggered free-standing shape-memory actuators, Eur. Polym. J. 97 (2017) 241–252. https://doi.org/10.1016/j.eurpolymj.2017.10.006.

[28] M. Alvarado, S. De La Flor, E. Llobet, A. Romero, J.L. Ramírez, Performance of flexible chemoresistive gas sensors after having undergone automated bending tests, Sensors (Switzerland). 19 (2019). https://doi.org/10.3390/s19235190.

[29] M. Alvarado, È. Navarrete, A. Romero, J. Ramírez, E. Llobet, Flexible Gas Sensors Employing Octahedral Indium Oxide Films, Sensors. 18 (2018) 999. https://doi.org/10.3390/s18040999.

[30] I. Isarn, F. Gamardella, L. Massagués, X. Fernàndez-Francos, À. Serra, F. Ferrando, New epoxy composite thermosets with enhanced thermal conductivity and high Tg obtained by cationic homopolymerization, Polym. Compos. 39 (2018) E1760–E1769. https://doi.org/10.1002/pc.24774.

[31] I. Isarn, L. Bonnaud, L. Massagués, À. Serra, F. Ferrando, Enhancement of thermal conductivity in epoxy coatings through the combined addition of expanded graphite and boron nitride fillers, Prog. Org. Coatings. 133 (2019) 299–308. https://doi.org/10.1016/j.porgcoat.2019.04.064.

[32] A. Belmonte, D. Guzmán, X. Fernández-Francos, S. De la Flor, Effect of the network structure and programming temperature on the shape-memory response of thiol-epoxy “click” systems, Polymers (Basel). 7 (2015) 2146–2164. https://doi.org/10.3390/polym7101505.

[33] N.J. Petersen, R.P.H. Nikolajsen, K.B. Mogensen, J.P. Kutter, Effect of Joule heating on efficiency and performance for microchip-based and capillary-based electrophoretic separation systems: A closer look, Electrophoresis. 25 (2004) 253–269. https://doi.org/10.1002/elps.200305747.

[34] X. Wang, J. Sparkman, J. Gou, Electrical actuation and shape memory behavior of polyurethane

composites incorporated with printed carbon nanotube layers, Compos. Sci. Technol. 141 (2017) 8–15. https://doi.org/10.1016/j.compscitech.2017.01.002.

[35] Y. Zheng, J. Qin, J. Shen, S. Guo, Controllable distribution of conductive particles in polymer blends via a bilayer structure design: a strategy to fabricate shape-memory composites with tunable electro-responsive properties, J. Mater. Chem. C. 8 (2020) 9593–9601. https://doi.org/10.1039/D0TC01854F.

[36] W. Wang, D. Liu, Y. Liu, J. Leng, D. Bhattacharyya, Electrical actuation properties of reduced graphene oxide paper/epoxy-based shape memory composites, Compos. Sci. Technol. 106 (2015) 20–24. https://doi.org/10.1016/j.compscitech.2014.10.016.

[37] F. Quadrini, L. Iorio, D. Bellisario, L. Santo, Shape memory polymer composite unit with embedded heater, Smart Mater. Struct. 30 (2021) 075009. https://doi.org/10.1088/1361-665x/ac00cb.

[38] Y. An, H. Okuzaki, Novel electro-Active shape memory polymers for soft actuators, Jpn. J. Appl. Phys. 59 (2020) 061002. https://doi.org/10.35848/1347-4065/ab8e08.

Chapter 8

Developing electro-responsive free-standing actuators

DUAL-CURING THIOL-ACRYLATE-EPOXY
THERMOSETS FOR FUNCTIONAL APPLICATIONS
Claudio Russo

Chapter 8 : DEVELOPING ELECTRO-RESPONSIVE FREE-STANDING SOFT ACTUATORS

8.1. Preliminary overview

8.1.1. Introduction

Soft actuators can be defined as highly deformable materials or composites that can be activated by external stimuli to generate desired motions and forces/torques [1]. Recently, their attracting a growing interest due to their ability to mimic nature and its motions (i.e., gripping, crawling, walking)[2–4]. Actively moving polymers (AMPs), exhibiting the ability to change their shape upon the application of an external stimulus, are good candidates for soft actuators. Polymers with shape-changing capability (SCC) and shape-memory polymers (SMPs) are the main classes of AMPs [5]. Both mechanisms are based on certain elements of the polymer structure that act as switches. The shape transformation starts upon triggering these switches by exposing them to a compatible external stimulus. The key differences between SM and SCC arise from the reversibility of the shape changes, the different degree of freedom that influences the final geometry of the shape, and the effect of the stimulus. They can use extremely diverse stimuli for actuation, such as heat, light, solvent or electric field [6–9]. Moreover, other attractive features are: the possibility of tuning their mechanical properties by the addition of fillers and the creation of composites; they have potential to be lightweight, biocompatible [10] and biodegradable [11]; they can be obtained by uncomplicated manufacturing processes.

Among shape-changing polymers, liquid crystalline networks (LCNs), or liquid crystalline elastomers (LCEs), are highly used as thermoresponsive actuators [12,13]. These materials have a lightly crosslinked semicrystalline structure, and they owe their SCC to a combination of entropic effects and liquid crystal order [14]. Besides most of LCEs types are capable to produce a two-way SME, the actuation performance depends on the network structure and the thermal transitions (glass transitions and isotropization) resulting from the complex process of LCE developing. One of the major applications of LCEs are in the field of stimuli responsive smart actuators. Besides, the need of a constant load applied in the actuation direction, represent a major drawback to produce the bidirectional actuators. Recently, some strategies to overcome this limitation and

produce autonomous 2W-SMPs have been proposed. Those strategies rely on the retention of the LCN stressed network by a stress applying element that can be both internal to the polymeric structure or even an external rigid layer adhered to the LCN surface [15–17]. A novel approach based on dual-curing processing was proposed by Belmonte et al. [18]; Dual-curing glassy thermoset was used to embed the pre-stretched LCN films taking advantage of the intermediate stable materials obtained after the first curing stage.

Although direct heating is commonly used to trigger the shape transformation, other approaches for internal heating are present in literature. Photothermally driven actuation can be obtain by loading an LCE with a variety of photothermal agents, such as carbon nanotubes (CNTs), graphene or metallic nanoparticle. They can absorb visible and/or NIR light and convert optical energy into thermal energy by releasing heat into the polymer matrix to trigger the LC–isotropic phase transition [19]. As compared to direct bulk heating, using light to control the LC – isotropic phase transition enables localized heating and thus actuation in spatially selected regions, which can be controlled remotely and switched on/off rapidly [20]. The incorporation of magnetic fillers, such as magnetite [21] and Fe_3O_4 nanoparticles [22], into the SMP results in inductive heating of the polymeric matrix triggered by electromagnetic fields that can be used to activate the shape transformation. Electroactive SMPs have been fabricated loading the SMP with electrically conductive fillers, such as CNTs, graphene oxide (GO) or conductive polymer particles [23,24]. The presence of those fillers increases the electrical conductivity and enables the Joule heating effect when a voltage is applied. The challenging part of this approach is the high amount of filler required to reach the percolation threshold, which can result in high viscosity and, consequently, difficulties in material processing. To avoid these issues other approaches can be followed. In particular, a conductive element or layer can be used to provide the joule heating necessary to trigger the SME (or SCC) [4,25,26].

8.1.2. Background

In this investigation (see Chapter 7), electro-responsive shape-memory composites (SMPC) were obtained by taking advantages of dual-curing SMP. The dual-curing system was based on the combination of thiol-acrylate Michael addition and epoxy-thiol “click” reactions (see Chapter 1). A conductive heater layer made of a silver ink track printed on a Kapton® substrate was incorporated between two intermediate materials layers and then the second curing stage was performed to obtain the final assembly.

Previously our research group developed a thermally-triggered self-standing actuator [18,27] exploiting the dual-curing processing to incorporate a shape-changing film between two glassy thermosets (GT) layer. The actuation extent, rate and time were studied by varying the GT and the heating rate in thermo-actuation with an experimental approach. The results demonstrate that it is possible to tailor the actuation rate and time by designing GT materials with a glass transition temperature close to that of the liquid-crystalline-to-isotropic phase transition of the LCN, thus making it possible to couple the two processes. A crucial design aspect that needs to be considered is that the isotropization temperature must be significantly higher than the second stage curing temperature, in order to prevent accidental triggering of the LCN isotropization. Moreover, the researchers demonstrated a high level of motion control by analytical model prediction.

In order to further develop such actuators design and enhance their applicability, an alternative to direct heating should be provided. Combining the actuator design developed by Belmonte et al. and the electro-responsive SMPC presented in Chapter 7, we could be able to prepare a multi-layer actuator, in which the shape-changing movement-engine is started by the joule heating produced by the conductive heater when a voltage is applied. A scale-down of the characteristic transition temperatures of the GT and LCN would be also beneficial to the overall functioning. This potential design up-grade would result in a further step towards a more efficient and autonomous functioning of the actuator.

8.1.3. Objectives

The final aim of this work is the development of an electro-responsive self-standing actuator based on the multi-layered structure represented in **Figure 8.1**. The designed assembly would be made of four functional layers: (1) two GT layers obtained by a thiol-acrylate-epoxy dual-curing system; (2) a suitable LCN film; (3) a conductive layer consisting of 50 µm Kapton® film on which the silver conductive net is printed.

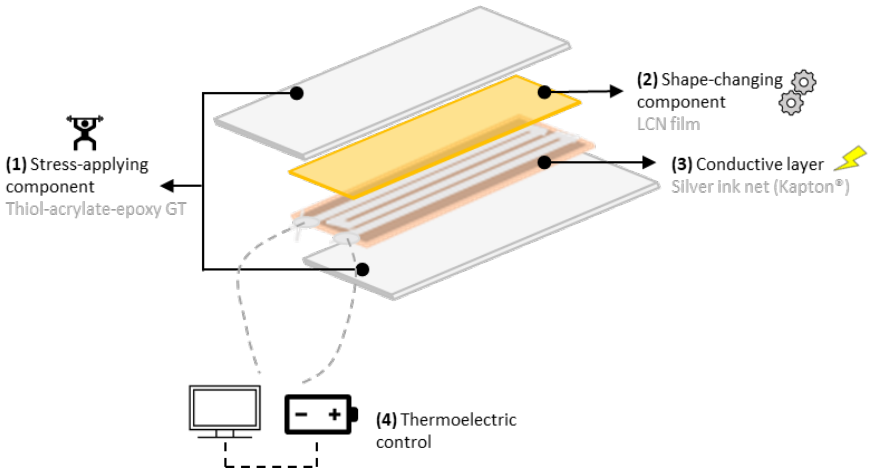

Figure 8.1. Schematic representation of the actuator multi-layered structure.

The GT layers (1) will be made of the SMP, loaded with 15% of Boron Nitride (BN) particles, characterized in Chapter 7, as well as the conductive layer (3) and the thermoelectric control (4). Therefore, the preliminary objective of this investigation is to develop a suitable LCN. In particular, the LCN must be able to retain its stretched shape during the embedding process, which takes place at 70-80°C (curing temperature of the thiol-epoxy stage). Consequently, a crosslinking system leading to an LCN with isotropization temperature (T_{iso}) above 90°C is required in order to safely embed the LCN film. In addition, considering that the thermoelectric control was proved to reach a maximum temperature (T_{set}) of 120°C, the T_{iso} has not to exceed this upper limit.

Considering the above, in this part of the investigation liquid-crystalline elastomers were prepared by curing an epoxy-based mesogen, the 4'-(2,3-epoxypropoxy)phenyl-4-(2,3-epoxypropoxy)benzoate (PHBHQ) [28], with a dicarboxylic acid. The thermal, phase behaviour, and thermomechanical properties of the resulting LCN were investigated. The shape-changing capability was studied in terms of actuation strain through consecutive cycles in order to evaluate the quality of the SCC produced.

8.2. LCNs based on PHBHQ epoxy monomers

8.2.1. Experimental part

Materials

A dihydroxy compound 4'-hydroxyphenyl,4-hydroxybenzoate (iPHBHQ) supplied by Hoechst was used as precursor for the synthesis of the epoxy mesogen. Epichlorohydrin (99% purity, 1.183 g/mL, 92.52 g/mol), isopropyl alcohol, and sodium hydroxide have

been used for the epoxidation of the precursor. Dodecanedioic acid (DA, n=10, 230.30 g/mol, Sigma-Aldrich) was used as crosslinking agent. Tricaprylylmethylammonium chloride was used as catalyst (2% of the total epoxy mol). iPHBHQ was purified in ethanol twice prior to use in order to ensure an adequate level of purity.

Synthesis of the Epoxy-based Mesogen (PHBHQ)

The epoxy-based mesogen was synthesized by epoxidation of the iPHBHQ according to the procedure described by Giamberini et al. [29]. The epoxidation was carried out using epichlorohydrin in the presence of NaOH in a two-step reaction mechanism (**Figure 8.2.a**): the formation of a chlorohydrin intermediate and the dehydrohalogenation of the intermediate to the diglycidyl ether. Then, NaOH catalyses the reaction to produce the intermediate, acts as a dehydrohalogenation agent, and neutralizes the formed HCl. In order to achieve a satisfactory degree of purity, synthesized monomer is recrystallized from ethanol. Dynamic scanning calorimetry (DSC) confirmed the formation of the epoxy-based mesogen with a melting temperature of 113°C.

Preparation of the Liquid-crystalline Network (LCN)

LCN films were prepared by mixing PHBHQ with Dodecanedioic acid (**Figure 8.2.b**) using TCAC as catalyst (2% with respect to epoxy mol). LCN films of around 0.2-0.3 mm thickness and 50 × 50 mm^2 surface area were prepared in an oven as follows: first, melting the epoxy-acid mixture at 140 °C under magnetic stirring during 5 min, then, pouring the catalyst in and mixing under stirring during 30 s to ensure homogeneity, and finally, pouring the mixture into a preheated mould and placing it inside the oven at 180 °C for 120 min, to ensure the completion of the polymerization. Sample obtained was named PHDA.

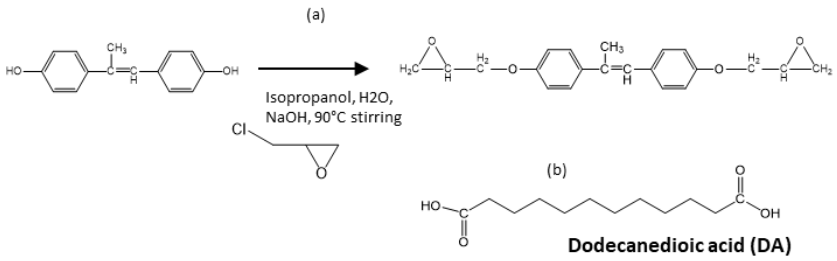

Figure 8.2. (a) Schematic representation of the iPHBHQ epoxidation process by epichlorohydrin; (b) molecular structure of Dodecanedioic Acid.

Characterization of the LCN film

PHDA samples were analysed by dynamic DSC analysis using a TA Instruments DSC Q2000 calorimeter, under N_2 atmosphere with heating and cooling ramps from 0 up to 200 °C at 10 °C/min. The nominal values of the temperatures corresponding to the glass transition, isotropization and anisotropization process (T_g, T_{iso} and T_{aniso}) were determined as the peak of the heat flow, while the temperature corresponding to Tg was determined as the midpoint of the step change in the heat flow. The enthalpy change associated to the isotropization (ΔH_{iso}) were measured by integrating the corresponding peak area of the heat flow signal.

Dynamic-mechanical analyses were performed using a TA Instruments DMA Q800 equipment operating in oscillation mode and equipped with a tension film clamp geometry. Strips with effective length × width × thickness of 12 × 4 × 0.25 mm^3 were cut from the film and tested in the apparatus at a frequency of 1 Hz, strain amplitude of 0.1%, and a heating rate of 3 °C/min from 30 up to 180 °C. T_g and T_{iso} temperatures were determined as the peak of the tanδ curve in the corresponding transition region. Values of the glassy modulus E'_g and rubbery modulus E'_r were determined from the storage modulus curves. In particular, E'_r was measured at T_{iso}+20°C.

Tensile test at T_{iso}+20°C were performed on 12 × 4 × 0.25 mm^3 LCN film using the DMA apparatus equipped with a tension film clamp in Force controlled mode. Sample were tested with a loading rate of 10 mN/min in order to determine the σ_{break} and consequently the programming limit of the LCN. At least three samples were used, and the average values was calculated.

Shape-memory Characterization

Thermomechanical experiments were performed using a TA DMA Q800 apparatus equipped with a tension film clamp and operating in force-controlled mode. In order to evaluate the shape-memory actuation capacity, two-way shape-memory experiments were carried out at different level of programming stress (σ_{max} = 5, 10, 15, 25, 50% of σ_{break}). The experiment was conduct as follow: programming the sample by heating up to T_{iso}+20 °C, holding during 5 min for thermal stabilization, loading at 10 mN/min up to σ_{max}. Then the sample is cooled to 10°C at 2°C/min. After thermal stabilizations (5 min isotherm), the sample is heated at 2°C/min to T_{iso}+20 °C. The level of actuation was obtained as the effective elongation produced by the LC transition.

Moreover, in order to evaluate the strain actuation and creep response evolution during cyclical shape-changing actuation, shape-memory cycle under a constant load (25% and 50% of σ_{break}) were performed as follows: first, programming the sample by heating up

to T_{iso}+20 °C, holding during 5 min for thermal stabilization, loading at 10 mN/min up to 25% or 75% of σ_{break}, and cooling to 10°C while keeping the load applied (elongation induced by the ordering of the liquid crystalline domains). Afterward, the SME was triggered by heating−cooling steps at 2 °C/min while maintaining the load applied (each cycle is defined by one heating−cooling step). The creep response is determined by the residual strain after each cycle.

8.2.2. Results

Reaction Mechanism

The reaction scheme between epoxy monomer and carboxylic acids proposed by Giamberini et al. [29,30] is reported in **Scheme 8.1**. It proceeds via opening of the epoxy ring by the carboxyl group (1). The hydroxyl groups produced are subsequently involved in the reaction with carboxylic acid, resulting in the formation of ester linkages by condensation (2), or in the etherification through the reaction with unreacted epoxy groups (3). On the other hand, at 180 °C, a competitive reaction path, consisting on the diglycidyl derivative homopolymerization, is also a present (see **Scheme 8.2**), since epoxies are reactive towards self-polymerization to polyethers [31,32].

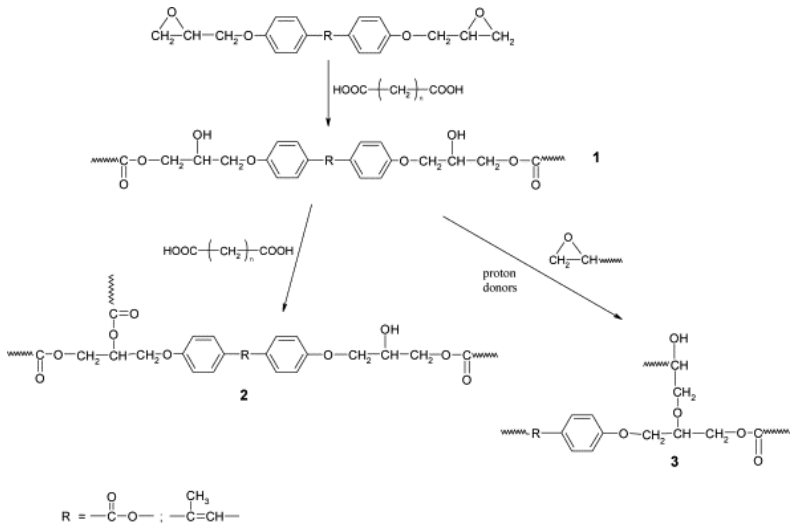

Scheme 8.1. Reaction scheme between epoxy monomers and carboxylic acids as reported in [33].

Besides both epoxy monomer and crosslinking agent are bifunctional, the formation of a crosslinked structure is expected. The hydroxyl group in the ether dimer (4), can undergo both esterification with acid (5), or further etherification with an epoxy (6).

Hydroxyl groups are, therefore, responsible for the formation of a lightly crosslinked elastomeric network. This was confirmed by reacting epoxies and acids in the presence of inhibitors of the reaction between epoxy and hydroxyl groups, such as aromatic amines. In such conditions, only linear polymers containing hydroxy side groups were obtained [34]. The prevailing reaction path depends on the experimental conditions (reaction temperature, epoxy/acid molar ratio, nature of monomers and acids selected).

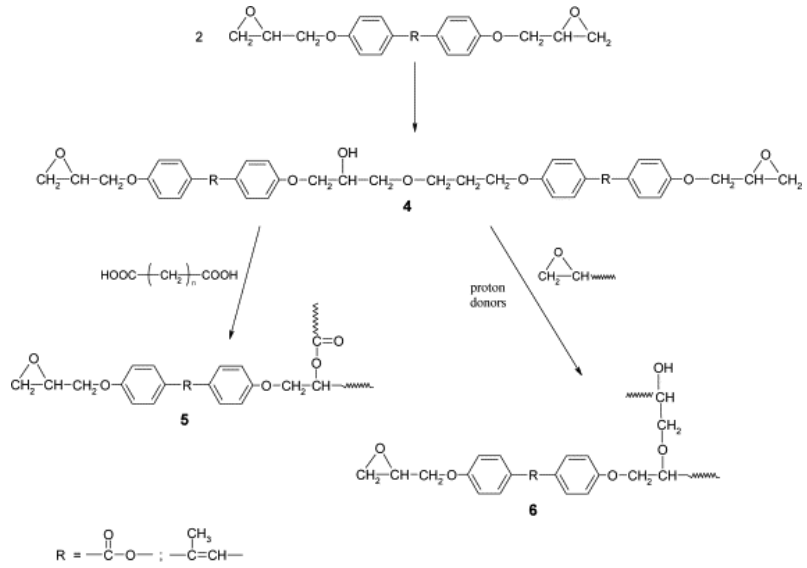

Scheme 8.2. Alternative homopolymerization reaction in the epoxy/acid mixture as reported in [33].

Differential scanning calorimetry (DSC)

As stated in the Experimental part, main-chain LCN film was prepared by using Dodecanedioic acid (n=10) as crosslinking agent. The thermal behaviour of curing systems was evaluated after an isothermal cure in oven at 180°C for 2h. The results of the second heating and cooling scan are shown in **Figure 8.2**. No residual heat was detected in the first curing scan, therefore, the cure of the LCN can be considered completed. The curing reaction led to the formation of a LCN as deduced by the presence of liquid-crystalline transitions on both cooling and heating, with an enthalpy around 16-17 J/g.

Table 8.1. Thermal properties of the PHDA film.

	T_g (°C)	T_{iso} (°C)	T_{aniso} (°C)	ΔH_{iso} (J/g)	ΔH_{aniso} (J/g)
PHDA	33	103	92	16.98	16.39

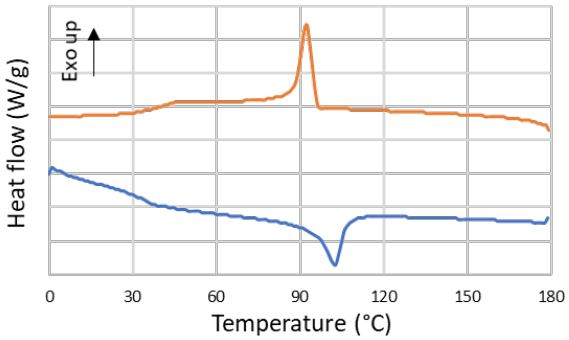

Figure 8.3. DSC cooling-heating traces of PHDA sample.

Looking at the LC phase parameters (T_{iso}, ΔH_{iso}) the obtained film seems to fit our requirements: The isotropization peak is far higher than the actuator assembling temperature (70-80°C) and the value of ΔH_{iso} is in line with the value obtained by Belmonte et al. [35] for similar LCN films with excellent SCC. Such enthalpy values indicates that a good degree of liquid-crystallinity and a stable mesophase are obtained. This are crucial aspect to obtain a high quality SCC and high strain actuations.

Dynamic mechanical analysis

In **Figure 8.4** the results of DMA oscillatory analysis on PHDA sample are presented. At temperatures below T_g the material is in the glassy region, the response is completely elastic, and E' remains stable with values around 1 GPa. When the materials approach its glass transition, the mechanical relaxation of the network takes place, E' falls down to 50-5 MPa, and tan δ reaches a maximum peak associated with the nominal T_g value. After the glass transition peak, tan δ remains constant and higher than 0 pointing out the presence of a liquid-crystalline mesophase, while E' slowly decreases on approaching the isotropization. Finally, a drastic decrease of E' (called dynamic softening elasticity) takes place during the isotropic transition, and E' reaches a stable plateau (rubbery region). The thermomechanical data are summarized in **Table 8.2**, together with the values of ε_{break} and σ_{break} obtained at T_g+20°C. The values of T_g and T_{iso} are in good agreement with the values obtained by DSC.

Table 8.2. Thermomechanical data and programming limits.

	E'_g (MPa)	E'_r (MPa)	FWHM (°C)	T_g (°C)	T_{iso} (°C)	σ_{break} (kPa)	ε_{break} (%)
PHDA	1062	0.96	18.2	41	104	170	24.2

The main issue is represented by the low value of storage modulus found for PHDA film. In particular, the E'_r is lower than 1 MPa probably due to a crosslinking density lower than the expected. This result does not fit well the requirements of an application as shape-changing layer in self-standing actuator. Similar actuators assembled by Belmonte et al. [36] presented a $E'_r{}^{GT}/ E'_r{}^{LC}$ ratio of around 5. In our case, taking into account the values of E'_r obtained in Chapter 7, the $E'_r{}^{GT}/ E'_r{}^{LC}$ will be around 25-29 that could result in in the impossibility of the LCN to move the entire assembly.

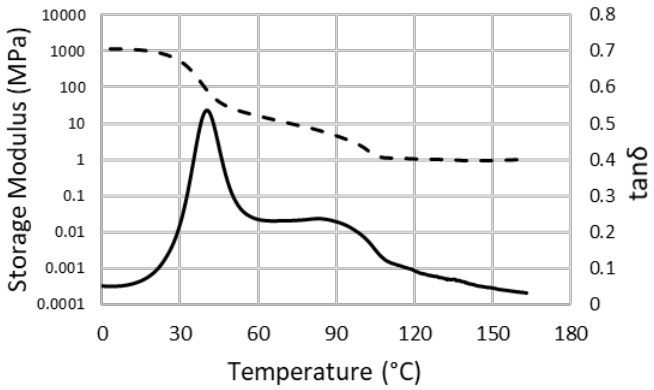

Figure 8.4. DMA oscillatory analysis on PHDA film.

Shape-changing behaviour

Although the obtained LCN appears to not meet our requirements, the shape-changing behaviour was studied anyway. First of all, two-way experiments were performed to understand the strain actuation variation with the programming stress.

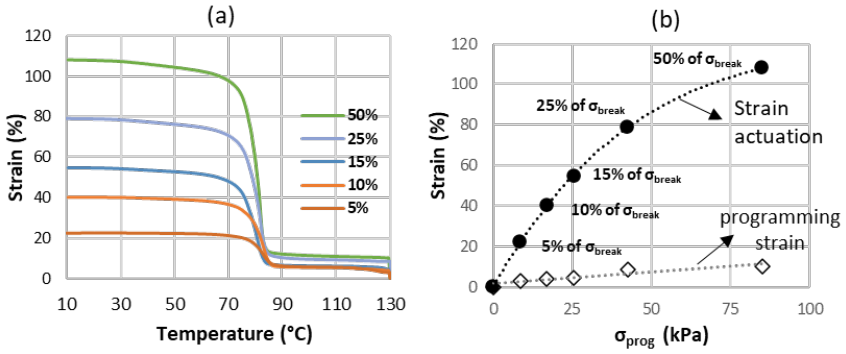

Figure 8.5. LCN strain actuation at different programming levels (cooling): (a) Strain Vs temperature plots; (b) Strain actuation variation with σ_{prog}.

In **Figure 8.5.a**, the strain evolution is plotted as a function of the temperature during the cooling step, whereas in **Figure 8.5.b**, the relation between the programming stress, σ_{prog}, and actuation strain, ε_{act}, is presented. The strain actuation increases almost linearly until the 15% of σ_{break} then a progressive deviation is visible. Besides the value ultimate stress of PHDA at high temperature is low (170 kPa), a wide range of actuation values can be obtained. The deviation from the linearity can be attributed to relaxation phenomenon taking place at higher stretching levels [37].

In order to investigate the shape-memory cycling stability, cycle experiments were carried out at 25% and 50% of σ_{break}. The results are presented in **Figure 8.6**. The strain actuation increases with programming level, as shown in **Figure 8.5**, but it slightly decreases with the number of cycles. With both programming level around 3% loss in elongation (associated to the LC phase ordering) were found at each cycle. It could be ascribed to some damage produced in the LC network structure due to the high strain levels that results in progressive reduction of the actuation capability. Further studies, increasing the number of cycles, should be performed in order to determine if the strain actuation can be stabilized increasing the number of cycles. On the other hand, the creep response is almost null; a maximum value of creep around 0.6% and 0.8 % was found, respectively, for 25% and 50% programming level.

In conclusion, besides wide range of strain actuation is achievable even within a low programming limit, the cyclic behaviour appears to be not perfectly stable and further analysis are required to better understand the phenomenon.

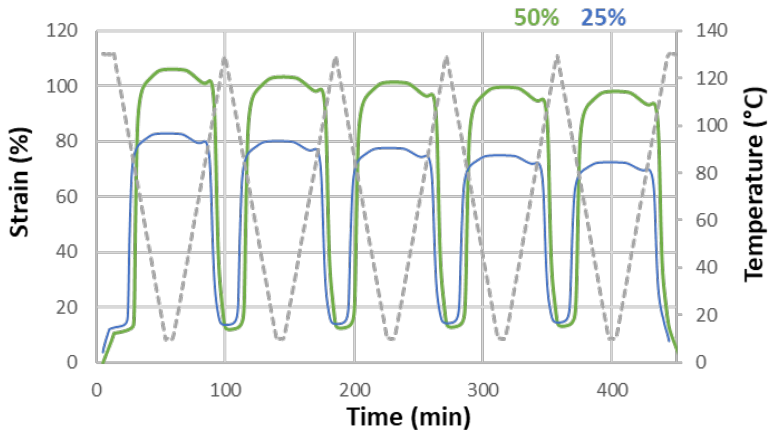

Figure 8.6. Shape-memory five cycles of the PHDA at 25% and 50 of σ_{break}.

8.3. Final considerations and future prospective

Epoxy-based LCN as potential materials for the development of autonomous electro-responsive actuators have been synthesized starting from *Dodecanedioic acid* and PHBHQ epoxy-based mesogen. A LC phase with a T_{iso} safely higher than 80°C was obtained after curing. Moreover, from the enthalpy associated to the isotropic transitions, an optimal degree of liquid-crystallinity was found. Unfortunately, thermomechanical analysis on the PHDA films revealed a low value of storage modulus that is not compatible with the desired application. The shape-changing capability was also evaluated. Overall, the LCN film showed a good SCC even if a slightly unstable strain actuation was found.

At this point, two different paths can be followed: (i) the enhancement of the thermomechanical properties of the PHDA film; (ii) synthesis of a new LC monomer or move to alternative curing systems. The enhancement of the thermomechanical properties could be the less time consuming option. Network properties could be improved by including small proportion of a higher functionality acid (i.e., citric acid) in order to increase the crosslinking density. Although, the increase of monomer functionality is an effective way to increase properties in the rubbery state, in LC systems it could backfire. High crosslinking density cold results in significant reduction in network mobility and resulting in no mesophase formation after curing. Another way to increase the crosslinking density could be the unbalancing of the stoichiometry. Low percentage of crosslinking agent excess can lead to a moderate increase of the crosslinking density and, consequently, of the E'_r. This effect was reported by Marotta et al. for epoxy/anhydrides thermosets [38].

Another viable way could be the modification of the PHBHQ structure by the addition of more rigid block. For example, it could be achieved by introducing a pre-polymerization step, prior to epoxy-acid curing, during which PHBHQ can react with a short and rigid compound (such as aromatic diamino compounds). The pre-polymerization step can result in a mixture of oligomers incorporating rigid blocks that can be crosslinked with a dicarboxylic acid. No evidence of the viability of this process were found in literature. In addition, reactivity issues can result from the presence of prepolymer chains with different functional groups at the two chain ends.

8.4. References

[1] L. Hines, K. Petersen, G.Z. Lum, M. Sitti, Soft Actuators for Small-Scale Robotics, Adv. Mater. 29 (2017) 1603483. https://doi.org/10.1002/adma.201603483.

[2] S. Kim, C. Laschi, B. Trimmer, Soft robotics: A bioinspired evolution in robotics, Trends Biotechnol. 31 (2013) 287–294. https://doi.org/10.1016/j.tibtech.2013.03.002.

[3] M. Wehner, R.L. Truby, D.J. Fitzgerald, B. Mosadegh, G.M. Whitesides, J.A. Lewis, R.J. Wood, An integrated design and fabrication strategy for entirely soft, autonomous robots, Nature. 536 (2016) 451–455. https://doi.org/10.1038/nature19100.

[4] C. Yuan, D.J. Roach, C.K. Dunn, Q. Mu, X. Kuang, C.M. Yakacki, T.J. Wang, K. Yu, H.J. Qi, 3D printed reversible shape changing soft actuators assisted by liquid crystal elastomers, Soft Matter. 13 (2017) 5558–5568. https://doi.org/10.1039/c7sm00759k.

[5] A. Lendlein, S. Kelch, Shape-Memory Polymers, Angew. Chemie Int. Ed. 41 (2002) 2034. https://doi.org/10.1002/1521-3773(20020617)41:12<2034::AID-ANIE2034>3.0.CO;2-M.

[6] A. Belmonte, C. Russo, V. Ambrogi, X. Fernández-Francos, S.D. la Flor, Epoxy-based shape-memory actuators obtained via dual-curing of off-stoichiometric “thiol-epoxy” mixtures, Polymers (Basel). 9 (2017). https://doi.org/10.3390/polym9030113.

[7] G.C. Lama, P. Cerruti, M. Lavorgna, C. Carfagna, V. Ambrogi, G. Gentile, Controlled Actuation of a Carbon Nanotube/Epoxy Shape-Memory Liquid Crystalline Elastomer, J. Phys. Chem. C. 120 (2016) 24417–24426. https://doi.org/10.1021/acs.jpcc.6b06550.

[8] D. Habault, H. Zhang, Y. Zhao, Light-triggered self-healing and shape-memory polymers, Chem. Soc. Rev. 42 (2013) 7244–7256. https://doi.org/10.1039/c3cs35489j.

[9] C. Wang, B. Kou, Z. Hang, X. Zhao, T. Lu, Z. Wu, J.P. Zhang, Tunable shape recovery progress of thermoplastic polyurethane by solvents, Pigment Resin Technol. 47 (2018) 7–13. https://doi.org/10.1108/PRT-03-2017-0021.

[10] C.M. Yakacki, R. Shandas, D. Safranski, A.M. Ortega, K. Sassaman, K. Gall, Strong, Tailored, Biocompatible Shape-Memory Polymer Networks, Adv. Funct. Mater. 18 (2008) 2428–2435. https://doi.org/10.1002/adfm.200701049.

[11] G.I. Peterson, A. V. Dobrynin, M.L. Becker, Biodegradable Shape Memory Polymers in Medicine, Adv. Healthc. Mater. 6 (2017) 1700694. https://doi.org/10.1002/adhm.201700694.

[12] C. Ohm, M. Brehmer, R. Zentel, Liquid crystalline elastomers as actuators and sensors, Adv. Mater. 22 (2010) 3366–3387. https://doi.org/10.1002/adma.200904059.

[13] H. Jiang, C. Li, X. Huang, Actuators based on liquid crystalline elastomer materials, Nanoscale. 5 (2013) 5225–5240. https://doi.org/10.1039/c3nr00037k.

[14] A.R. García-Márquez, B. Heinrich, N. Beyer, D. Guillon, B. Donnio, Mesomorphism and shape-memory behavior of main-chain liquid-crystalline co-elastomers: Modulation by the chemical composition, Macromolecules. 47 (2014) 5198–5210. https://doi.org/10.1021/ma501164u.

[15] M.O. Saed, A.H. Torbati, C.A. Starr, R. Visvanathan, N.A. Clark, C.M. Yakacki, Thiol-acrylate main-chain liquid-crystalline elastomers with tunable thermomechanical properties and actuation strain, J. Polym. Sci. Part B Polym. Phys. 55 (2017) 157–168. https://doi.org/10.1002/polb.24249.

[16] C.L. Lewis, E.M. Dell, A Review of Shape Memory Polymers Bearing Reversible Binding Groups, J. Polym. Sci., Part B Polym. Phys. 54 (2016) 1340–1364. https://doi.org/10.1002/polb.23994.

[17] W. Wang, Y. Liu, J. Leng, Recent developments in shape memory polymer nanocomposites: Actuation methods and mechanisms, Coord. Chem. Rev. 320–321 (2016) 38–52. https://doi.org/10.1016/j.ccr.2016.03.007.

[18] A. Belmonte, G.C. Lama, G. Gentile, P. Cerruti, V. Ambrogi, X. Fernández-Francos, S. De la Flor, Thermally-triggered free-standing shape-memory actuators, Eur. Polym. J. 97 (2017) 241–252. https://doi.org/10.1016/j.eurpolymj.2017.10.006.

[19] L. Dong, Y. Zhao, Photothermally driven liquid crystal polymer actuators, Mater. Chem. Front. 2 (2018) 1932–1943. https://doi.org/10.1039/c8qm00363g.

[20] J.E. Marshall, Y. Ji, N. Torras, K. Zinoviev, E.M. Terentjev, Carbon-nanotube sensitized nematic elastomer composites for IR-visible photo-actuation, Soft Matter. 8 (2012) 1570–1574. https://doi.org/10.1039/c1sm06656k.

[21] M.Y. Razzaq, M. Behl, U. Nöchel, A. Lendlein, Magnetically controlled shape-memory effects of hybrid nanocomposites from oligo(ω-pentadecalactone) and covalently integrated magnetite nanoparticles, Polymer (Guildf). 55 (2014) 5953–5960. https://doi.org/10.1016/j.polymer.2014.07.025.

[22] Q. Ze, X. Kuang, S. Wu, J. Wong, S.M. Montgomery, R. Zhang, J.M. Kovitz, F. Yang, H.J. Qi, R. Zhao, Magnetic Shape Memory Polymers with Integrated Multifunctional Shape Manipulation, Adv.

Mater. 32 (2020) 1906657. https://doi.org/10.1002/adma.201906657.

[23] X. Luo, P.T. Mather, Conductive shape memory nanocomposites for high speed electrical actuation, Soft Matter. 6 (2010) 2146–2149. https://doi.org/10.1039/c001295e.

[24] Y. An, H. Okuzaki, Novel electro-Active shape memory polymers for soft actuators, Jpn. J. Appl. Phys. 59 (2020) 061002. https://doi.org/10.35848/1347-4065/ab8e08.

[25] F. Quadrini, L. Iorio, D. Bellisario, L. Santo, Shape memory polymer composite unit with embedded heater, Smart Mater. Struct. 30 (2021) 075009. https://doi.org/10.1088/1361-665x/ac00cb.

[26] H. Lu, W.M. Huang, J. Leng, Functionally graded and self-assembled carbon nanofiber and boron nitride in nanopaper for electrical actuation of shape memory nanocomposites, Compos. Part B Eng. 62 (2014) 1–4. https://doi.org/10.1016/j.compositesb.2014.02.003.

[27] A. Belmonte, G.C. Lama, P. Cerruti, Motion control in free-standing shape- memory actuators, (2018).

[28] V. Ambrogi, M. Giamberini, P. Cerruti, P. Pucci, N. Menna, R. Mascolo, C. Carfagna, Liquid crystalline elastomers based on diglycidyl terminated rigid monomers and aliphatic acids. Part 1. Synthesis and characterization, Polymer (Guildf). 46 (2005) 2105–2121. https://doi.org/10.1016/j.polymer.2005.01.007.

[29] M. Giamberini, E. Amendola, C. Carfagna, Liquid crystalline epoxy thermosets, Mol. Cryst. Liq. Cryst. Sci. Technol. Sect. A. Mol. Cryst. Liq. Cryst. 266 (1995) 9–22. https://doi.org/10.1080/10587259508033628.

[30] M. Giamberini, P. Cerruti, V. Ambrogi, C. Vestito, F. Covino, C. Carfagna, Liquid crystalline elastomers based on diglycidyl terminated rigid monomers and aliphatic acids. Part 2. Mechanical characterization, Polymer (Guildf). 46 (2005) 9113–9125. https://doi.org/10.1016/j.polymer.2005.04.093.

[31] M. Galiá, A. Mantecón, V. Cádiz, A. Serra, 13C NMR study of the reaction of unsymmetrical diacids with 4,4′-bis(2,3-epoxypropoxy)biphenyl, Die Makromol. Chemie. 191 (1990) 1111–1118. https://doi.org/10.1002/macp.1990.021910513.

[32] M.S. Wang, T.J. Pinnavaia, Clay-Polymer Nanocomposites Formed from Acidic Derivatives of Montmorillonite and an Epoxy Resin, Chem. Mater. 6 (1994) 468–474. https://doi.org/10.1021/cm00040a022.

[33] V. Ambrogi, M. Giamberini, P. Cerruti, P. Pucci, N. Menna, R. Mascolo, C. Carfagna, Liquid crystalline elastomers based on diglycidyl terminated rigid monomers and aliphatic acids . Part 1 . Synthesis and characterization, 46 (2005) 2105–2121. https://doi.org/10.1016/j.polymer.2005.01.007.

[34] B. Hirn, C. Carfagna, R. Lanzettab, Linear precursors of liquid crystalline thermosets, n.d. https://pubs.rsc.org/--/content/articlehtml/1996/jm/jm9960601473?casa_token=KX-nG0VaZXUAAAAA:UAGxUwK9VqArhBeAQUpQ8YaDKJY8kofWTzWOwyOT1iHiB1mfk5xXHSC4q9ljdUgwR0S6kVRcmAuRng (accessed June 17, 2021).

[35] A. Belmonte, G.C. Lama, G. Gentile, X. Fernández-Francos, S. De La Flor, P. Cerruti, V. Ambrogi, Synthesis and Characterization of Liquid-Crystalline Networks: Toward Autonomous Shape-Memory Actuation, J. Phys. Chem. C. 121 (2017) 22403–22414. https://doi.org/10.1021/acs.jpcc.7b04610.

[36] A. Belmonte, G.C. Lama, G. Gentile, P. Cerruti, V. Ambrogi, X. Fernández-Francos, S. De la Flor, Thermally-triggered free-standing shape-memory actuators, Eur. Polym. J. 97 (2017) 241–252. https://doi.org/10.1016/j.eurpolymj.2017.10.006.

[37] A. Belmonte, G.C. Lama, G. Gentile, P. Cerruti, V. Ambrogi, X. Fernández-Francos, S. De la Flor, Thermally-triggered free-standing shape-memory actuators, Eur. Polym. J. 97 (2017) 241–252. https://doi.org/10.1016/j.eurpolymj.2017.10.006.

[38] A. Marotta, N. Faggio, V. Ambrogi, P. Cerruti, G. Gentile, A. Mija, Curing Behavior and Properties of Sustainable Furan-Based Epoxy/Anhydride Resins, Biomacromolecules. 20 (2019) 3831–3841. https://doi.org/10.1021/ACS.BIOMAC.9B00919.

Chapter 9

General conclusions and Future works

DUAL-CURING THIOL-ACRYLATE-EPOXY
THERMOSETS FOR FUNCTIONAL APPLICATIONS
Claudio Russo

Chapter 9 : *GENERAL CONCLUSIONS AND FUTURE WORKS*

9.1. Conclusions

In this investigation, a novel dual-curing system based on the combination of thiol-acrylate Michael addition and thiol-epoxy "click" reaction was successfully developed. A controlled curing sequence was guaranteed by the significant differences in reaction kinetic of the two polymerization process. Thermosets obtained with this curing system were proved to be suitable for functional applications. In particular, these materials demonstrated excellent shape-memory properties and therefore where successfully employed in the developing of electroresponsive shape-memory polymers. In addition, they were proved to be suitable for two-stage adhesive applications, allowing an accurate control of bondline thickness and higher adhesive strength than one-step curing joint.

Secondary conclusions of this investigation were arranged in different categories according to the secondary objectives listed in section 1.7.

1° step) Development and characterization of a dual-curing mechanism based on thiol-acrylate Michael addition and thiol-epoxy "click" reaction:

- DSC and FTIR analysis of the curing kinetics of pure thiol-acrylate and thiol-epoxy systems showed substantially different kinetic behaviour ascribed to: (i) the faster kinetics of the nucleophile-mediated thio-Michael addition to acrylates; (ii) a slow initiation kinetics of thiol-epoxy reaction resulting from its autocatalytic character; (iii) the weak temperature dependence of the thiol-acrylate reaction in comparison with the thiol-epoxy reaction.
- Dual-curing mechanism analysis revealed the almost sequential character of the dual-curing system, with little or no overlapping at all between the thiol-acrylate and thiol-epoxy reactions under suitable reaction conditions.
- Intermediate materials showed a remarkable stability at room temperature. In addition, they were easily conformed or die-cut in complex shapes prior to the activation of the second curing stage. Their potential application as adhesive layer was qualitatively demonstrated.

2° step) Rheological and mechanical characterization of dual-curing thiol-acrylate-epoxy thermosets varying the ratio between acrylate and thiol equivalent (r_a):

- Rheological analysis of the curing process showed that the critical ratio (r_c) of the system is around 0.45–0.5, while theoretical calculation predicted a lower r_c of 0.33. This was caused by departures from the ideal step-growth behaviour such as intra-molecular cyclization.
- Thermomechanical characterization showed a network softening effect (decrease in flexural modulus and rubbery modulus E'_r) together with a rigidity increase in the glassy state (E'_g) with the increase of thiol-acrylate portion. Mechanical analysis revealed an interesting combination of the properties of the two network is obtained with r_a=0.6.
- Thermal and mechanical stability of intermediate materials were also evidenced, in agreement with the results of the previous characterization. This enabled a sufficiently long working window in which the properties and processing ability of the materials were hardly affected. Materials with higher contribution of the thiol-acrylate reaction were more stable than those richer in thiol-epoxy.

3° step) To obtain thiol-acrylate-epoxy dual-curing thermosets with thermomechanical properties suitable for shape-memory (SM) applications:

- The thermomechanical properties of the final materials were successfully enhanced by the modification of the network structure using suitable monomers. The synergistic effect of *bisphenol A glycerolate (1 glycerol/phenol) diacrylate* (BAGA) and *tri(2,3-epoxypropyl)isocyanurate* (ISO) led to T_g between 48 and 56°C together with narrow network relaxation, suitable for SM application.
- Excellent SME in unconstrained conditions was found for all materials tested. Moreover, these materials proved high capability of generate stress (up to 7 MPa) and generate a Work output (up to 1300 kJ/m^3) under respectively constrained and partially constrained conditions.

4° step) Investigation of the potentiality of dual-curing processing in two-stage adhesives applications:

- Samples loaded with BN particles showed a slight increase of T_g together with increased values of E'_g and flexural modulus. Moreover, increasing the BN particles content, a decrease of CTE is obtained.
- Stronger joints were obtained with liquid-like intermediate materials while a more accurate bondline thickness control was obtained with solid-like intermediate ones. The lightly crosslinked network of solid-like intermediate

allows a better shape retention during curing with no adhesive leakage. The increase of bondline thickness leads to a general decrease of adhesive strength, while the increase of BN fillers content has a beneficial effect on adhesive performance.

- Dual-curing procedures appears to be promising for adhesive applications for several reasons: (i) the accurate dimensional control of the adhesive layer obtained with gelled intermediate materials; (ii) the significant reduction of adhesive shrinkage or leakages during curing thanks to the dual-process. (iii) joints prepared by one-step curing (same reactive systems) showed worse adhesive behaviour than joints obtained with liquid-like intermediate adhesives.

5° step) Development of an electroresponsive shape-memory composites stacking up together different functional layers exploiting dual-curing thermoresponsive thermosets:

- Loading with the BN particles the SMP developed in the third step of present work leads to significant increase of thermal conductivity (almost 300% increase) without affecting the thermomechanical behaviour.
- The electro-activated SME leads to extremely faster shape recovery with recovery times in the order of seconds. The best results obtained for direct heating and joule heating activation were, respectively, 1.5 min and 8 s, both obtained with the highest heating rate tested. The increase in thermal conductivity obtained by BN fillers results in an early and higher recovery rate for the electro activated devices due to enhanced heat transmission.
- LCN films were prepared by curing a synthetized epoxy LC monomer (PHBHQ) with dodecanedioic acid. The resulting LCN showed a good SCC but an excessively low value of E'_r, limiting is application as shape-changing layer in electroresponsive free-standing actuators. Further studies are needed to enhance the stiffness in the rubbery state without adversely affect the LC phase.

9.2. Future Works

In recent years a strong concern about sustainability issue is arising. The research efforts are being directed through a polymer science with less environmental impact, trying to replicate and overpass all the extraordinary achievements obtained so far but with

renewable resources. A fast growing industrial demand of effective recycling procedures has also oriented the efforts of the scientific community in this matter. In particular, the revolutionary discovery of Vitrimers by Liebler has been a big breakthrough in the field of thermosets. This new technology has opened the possibility of the thermosets recycling, gathering the interest of the plastic industry and, consequently, the academic research efforts.

In light of this consideration, we strongly believe that a significant progress for this line of investigation would be the inclusion of more sustainable materials. As an example, there is a wide range of bio-based epoxy monomers available that could be used to replace the DGEBA. Moreover, in literature the number of shape-memory materials exhibiting vitrimeric behaviour are multiplying. Thiol-epoxy networks have recently been reported to show interesting vitrimeric properties. Therefore, thiol-acrylate-epoxy thermosets might benefit from enhanced processing flexibility.

Alongside this effort towards sustainability, the next short-term step of this investigation is, of course, addressed to the final development of the free-standing electroresponsive actuator. Both the properties of the dual thermoset and LC components should be further improved and tailored for that purpose. In addition, other methods of indirect heating enabling fast actuation should be considered. In this research line, the final aspiration could be the development of a reconfigurable actuator by the reproducing the multi-layer design with vitrimeric components. Exploiting the vitrimeric behaviour, a shape reconfiguration, or even the actuator recycling, could be obtained when desired. The tricky challenge in this pursuit would be the activation method that needs to be redesigned to meet the new requirements.

The use of dual-curing processing in adhesive applications appeared to be extremely promising. As mentioned in Chapter 6, further studies could be carried out in order to go deeper in this application. The wide range of dual-curing systems available nowadays can be exploited to obtain high-performance adhesives.

DUAL-CURING THIOL-ACRYLATE-EPOXY
THERMOSETS FOR FUNCTIONAL APPLICATIONS
Claudio Russo

DUAL-CURING THIOL-ACRYLATE-EPOXY
THERMOSETS FOR FUNCTIONAL APPLICATIONS
Claudio Russo